Ruperto-Carola University Heidelberg
Combined Faculties for Natural Sciences
and for Mathematics

Measurement of Open Charm in 158 AGeV/c Pb-Au Collisions

Dissertation
submitted by
Dipl.-Phys. Wilrid Ludolphs
born in
Königstein im Taunus

February 2006

Referees:

Prof. Dr. Johanna Stachel

Prof. Dr. Franz Eisele

Abstract

Measurement of Open Charm in 158 AGeV/c Pb-Au Collisions

This thesis presents a measurement of an upper limit for the open charm yield in 158 AGeV/c Pb-Au collisions with the CERES spectrometer at 7% centrality. A secondary particle reconstruction scheme, based on the reconstruction of the decay vertex, is developed and tested using the decay $K^0_S \to \pi^+\pi^-$ as a reference measurement. An integrated K^0_S rapidity density of $dN/dy = 19.75 \pm 0.23\,(\text{stat}) \pm 1.70\,(\text{syst})$ is measured in the rapidity region $2.0 < y < 2.6$ and compared to results from an alternative analysis of the CERES data and results from the NA49 and NA57 collaborations.

The analysis of the decay $\overline{D}^0 \to K^+\pi^-$ requires careful study of the combinatorial background and resonances contributing to the invariant mass spectrum. An open charm enhancement of more than a factor 22 can be excluded at 98% confidence level. The enhancement is calculated with respect to the expected open charm yield in nucleus-nucleus collisions of $\langle \overline{D}^0 \rangle = 0.21$ per event, obtained by scaling the charm cross-section in proton-proton collisions with the number of binary collisions.

The first part of this thesis is devoted to the development of a hit finding algorithm for the CERES TPC. Furthermore, a detailed description of the calibration of the TPC is presented. A position resolution of $\sigma_{r\Delta\phi} \approx 340$ μm and $\sigma_{\Delta r} \approx 640$ μm is achieved with the new calibration, with a momentum resolution of $\Delta p/p = 5.4\%$ at $p = 5$ GeV/c, the momentum region relevant for the $\overline{D}^0$ meson.

Open Charm Analyse in 158 AGeV/c Pb-Au Kollisionen

Diese Doktorarbeit beinhaltet die Messung einer oberen Grenze für die Produktionsrate von Open Charm Mesonen in 158 AGeV/c Pb-Au Kollisionen mit dem CERES Spektrometer bei einer Zentralität von 7%. Es wird die Entwicklung einer Rekonstruktionsmethode für Sekundärteilchen vorgestellt, die auf der Rekonstruktion des Zerfallsvertex beruht. Die Methode wird mit dem Zerfall $K^0_S \to \pi^+\pi^-$ als Referenzmessung getestet. Eine integrale Rapiditätsdichte von $dN/dy = 19.75 \pm 0.23\,(\text{stat}) \pm 1.70\,(\text{syst})$ wird für das K^0_S Meson im Rapiditätsbereich $2.0 < y < 2.6$ gemessen und mit den Ergebnissen einer alternativen CERES Messung und den Messungen der NA49 und NA57 Kollaborationen verglichen.

Eine genaue Untersuchung des kombinatorischen Untergrundes und der Resonanzen, die zusätzlich zu dem invarianten Massenspektrum beitragen, ist für die Analyse des Zerfalls $\overline{D}^0 \to K^+\pi^-$ unerlässlich. Eine vermehrte Open Charm Produktionrate von mehr als einem Faktor 22 kann bei einem Konfidenzniveau von 98% ausgeschlossen werden. Dieser Faktor bezieht sich auf die in Kern-Kern Stößen erwartete Open Charm Produktionsrate von $\langle \overline{D}^0 \rangle = 0.21$ pro Ereignis, die durch Skalierung des Charm Wirkungsquerschnitts in Proton-Proton Stößen mit der Anzahl der binären Kollisionen gegeben ist.

Der erste Teil dieser Doktorabeit befasst sich mit der Entwicklung eines Algorithmus zur Mustererkennung in der CERES TPC. Ferner wird eine detaillierte Beschreibung der Kalibration der TPC präsentiert. Mit der neuen Kalibration wird eine Ortsauflösung von $\sigma_{r\Delta\phi} \approx 340$ μm und $\sigma_{\Delta r} \approx 640$ μm erreicht, sowie eine Impulsauflösung von $\Delta p/p = 5.4\%$ bei einem für das $\overline{D}^0$ Meson relevanten Impuls von $p = 5$ GeV/c.

Contents

List of Figures

List of Tables

Chapter 1

Introduction

Heavy-ion collisions at ultra-relativistic energies offer the possibility to study the behavior of nuclear matter at high density and temperature where one expects the existence of the **Q**uark **G**luon **P**lasma (QGP). In this new state of matter the quarks are no longer confined inside individual hadrons, but they are free to move within the interaction region. At the same time the quarks lose their dynamical mass leading to the restoration of chiral symmetry, an approximate symmetry of QCD in the sector of light quarks.

Many different signatures have been proposed for the formation of a QGP phase. According to the type of final state particles, they can be divided into two main groups: the hadronic probes and the electromagnetic probes. Hadronic probes have the advantage of having large cross-sections. However, they undergo a substantial evolution through strong reinteractions in the period between their formation and the detection. Therefore, the momentum distribution and the final particle composition can be affected by later stages of the heavy-ion collision. Nevertheless, it is still possible to extract valuable information about the initial stage of the collision by studying final state hadrons. Electromagnetic probes have a negligible cross-section for the interaction with hadronic matter. They are a direct tool for the investigation of the first stages of the heavy-ion collision. The drawback of this kind of probe is that the production cross-section is very small, and the detection in a high background environment becomes a difficult task.

CERES is one of the experiments at the CERN **S**uper **P**roton **S**ynchroton (SPS) dedicated to the study of electromagnetic probes. Its main objective is the measurement of low mass electron-positron pairs produced in p-A and A-A collisions. Systematic studies have been done with S-Au in 1992 [1] and the proton-induced reactions p-Be and p-Au in 1993 [2]. An energy scan has been performed during the years 1995 to 2000 using the system Pb-Au [3, 4, 5]. While the p-A collisions could be well explained by a cocktail of the hadronic sources π^0, η, η', ρ, ω and ϕ, the S-Au and Pb-Au spectra showed a significant enhancement in the mass range $0.2 < m_{e^+e^-} < 1.5$ GeV/c^2. A comparison between the p-Au and S-Au data sets is shown in figure 1.1. A dilepton enhancement was also observed by the HELIOS/3 experiment in 200 AGeV/c S-W collisions [6, 7] and by the NA38/NA50 experiment in 158 AGeV/c Pb-Pb collisions [8]. The observation of this excess also led to an enormous theoretical activity. It might be explained by direct thermal radiation of the fireball, dominated by the two-pion annihilation $\pi^+\pi^- \rightarrow \rho \rightarrow e^+e^-$

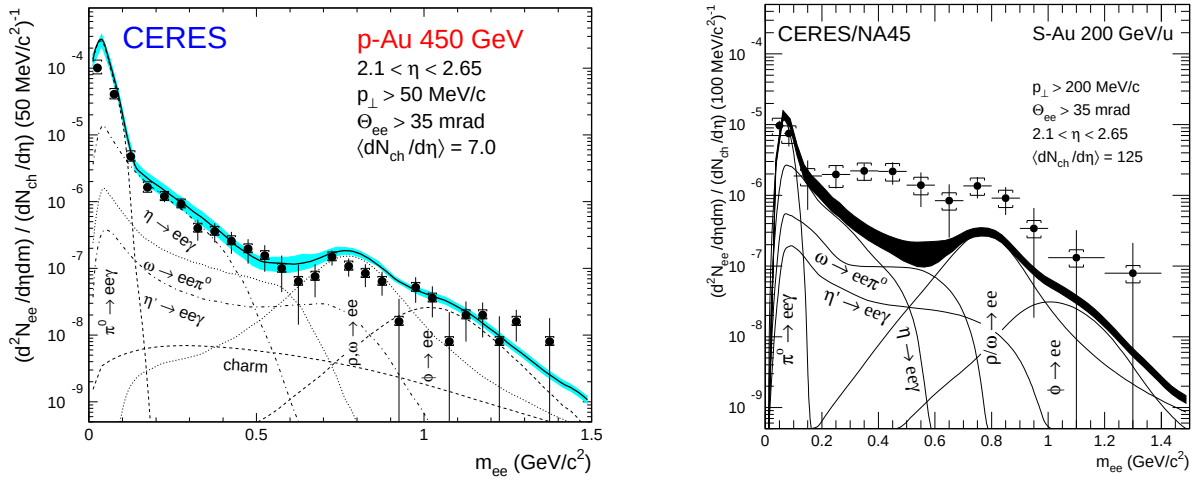

Figure 1.1: **Low-mass electron pair enhancement in nucleus-nucleus collisions.** *The left figure shows the inclusive e^+e^- mass spectra in 450 GeV/c p-Au collisions. The shape of the spectra is in good agreement with the predicted contributions from hadronic decays. The right figure shows the corresponding spectra for S-Au at 200 AGeV/c. In the mass range between 0.2 and 1.5 GeV/c^2 an enhancement by a factor of* $5.0 \pm 0.7\,(\text{stat}) \pm 2.0\,(\text{syst})$ *[1] is observed with respect to expectations from the hadronic cocktail.*

with an intermediate ρ vector meson. Compared to the lighter vector mesons ω and ϕ the ρ is of particular interest. Because of its short lifetime of 1.3 fm/c it samples the evolution of the fireball as a function of time. Furthermore, due to its link to chiral symmetry restoration [9], it is assumed that the intermediate ρ suffers strong in-medium modifications. The two main theoretical alternatives for this modification predict a shift of the ρ peak to lower masses (Brown-Rho scaling [10]) or a spreading of its width based on calculations of the ρ spectral density within the dense hadronic medium [11]. The upgrade of the CERES experiment in 1998 with a **T**ime **P**rojection **C**hamber (TPC) opened the additional possibility to study hadronic channels. Many interesting topics have been addressed since then [12, 13, 14, 15, 16].

The aforementioned dilepton enhancement in the low and intermediate mass region gave rise to several speculations. One often discussed possibility proposes an abnormally enhanced open charm production in nucleus-nucleus collisions [17]. However, such an increase is not easily justified theoretically [18], and would also be difficult to reconcile with the current understanding of the observed J/Ψ suppression. Another explanation argued that D meson rescattering in hot and dense matter might generate a transverse momentum broadening which can enrich the $\mu^+\mu^-$ phase space covered by the NA50 experiment [19]. But the resulting increase was to small to explain the excess [20]. Furthermore, the role of secondary Drell-Yan processes in hadronic rescatterings has been investigated within the UrQMD transport model [21]. It has been found that in the **i**ntermediate **m**ass **r**egion (IMR) this contribution may constitute up to 30% of the primordial Drell-Yan yield and thus far from explaining the experimental findings. An attempt to explain the HELIOS-3 data used a transport model incorporating dilepton production through secondary hadronic annihilation processes [22, 23]. It was found that the enhancement in S-W collisions could indeed be explained. Unfortunately, the statistics of the HELIOS-3

data for $m_{\mu^+\mu^-} > 2$ GeV is poor. Finally, the significance of thermal dilepton radiation has been investigated [24]. The evaluation of the dilepton spectra in Pb-Pb collisions as measured by NA50 showed that the IMR can be composed of 3 major components: open charm decays, Drell-Yan and thermal radiation. It was shown that the dilepton excess could indeed be explained without invoking any anomalous enhancement in the charm production. Furthermore, the low-mass dilepton spectra from the CERES experiment could be explained in the same framework when medium effects in the low-lying vector mesons are included. Therefore, a consistent picture of dilepton production at the full CERN SPS energy seems to emerge. To test this result against open charm enhancement a direct measurement of the D meson contribution is needed.

The subject of this thesis is the measurement of the open charm yield in 158 AGeV/c Pb-Au collisions. Due to the low production cross-section the measurement is difficult. The expected yield per event for central Pb-Pb collisions at SPS is ~ 0.03 for D^+/D^- and ~ 0.1 for $D^0/\overline{D}^0$ [25, 26]. However, the CERES experiment has the possibility to distinguish between primary and secondary tracks by cutting on the secondary vertex. Moreover, the upgrade of the experiment with a TPC and its extensive calibration provides a reasonable momentum resolution ($\Delta p/p = 5.4\%$ at $p = 5$ GeV/c). Finally, the large data sample of 30 million events taken during the beam time of the year 2000 is enough statistics to make such a measurement tempting.

The thesis is structured as follows. Chapter 2 gives a brief historical overview of the heavy-ion program and elucidates the most relevant features of the Quark Gluon Plasma. Chapter 3 presents the experimental findings of the NA38/NA50 experiment concerning the excess in the intermediate mass muon pair continuum in 158 AGeV/c Pb-Pb collisions. Furthermore, its most discussed sources, open charm enhancement and thermal radiation, are presented. The overall experimental setup of the CERES experiment together with its individual detector components are described in chapter 4. Chapter 5 is devoted to the reconstruction scheme of the raw data. Special emphasis is given to software components developed in the framework of this thesis. Another important contribution during this work was the calibration of the TPC, described in detail in chapter 6. Chapter 7 presents the analysis scheme for the measurement of open charm. It is mainly based on the reconstruction of the secondary vertex using two **S**ilicon **D**rift **C**ounters (SiDC) and the TPC. A cut on the longitudinal distance between the secondary vertex and the primary interaction region allows to separate secondary particles from target tracks and thus makes an almost background free particle reconstruction possible. In chapter 8 the feasibility of the analysis is demonstrated for the more abundant strange particles. The studies are performed on the two body decay $K^0_S \rightarrow \pi^+\pi^-$. The efficiency is tested against an alternative CERES measurement using only the TPC and measurements from the NA49 and NA57 experiments. The same analysis scheme is applied to the reconstruction of open charm in chapter 9. An upper limit on the open charm cross-section is obtained. Finally, chapter 10 contains the conclusions.

Chapter 2

Quark Gluon Plasma

Several experimental discoveries in particle physics revealed the hierarchical nature of matter. The constituents of macroscopic matter were found to be molecules and atoms. The atoms consist of a nucleus surrounded by an electron cloud. The components of the nuclei are the nucleons which in turn are formed of quarks, antiquarks and gluons (partons). To this date no further substructure of quarks was observed. They are regarded as pointlike particles. The properties of the 6 known quark flavors are listed in table 2.1. Isolated quarks have never been detected and thus it is conjectured that they are confined together with other quarks to form hadrons. The gluons are the intermediators of the strong color force between the quarks. The physics of the strong interaction is described by the theory of **Q**uantum **C**hromo**d**ynamics (QCD). It is the SU(3) gauge symmetric part of the Standard Model of particle physics.

In deep-inelastic scattering experiments the individual scattered partons fly away practically freely, dress with a gluon cloud and rapidly form color singlet bound states, the hadrons. However, if the number of partons scattering simultaneously into the same volume element is sufficiently increased, the situation may change radically. A dense medium of partons is formed, where the interactions of quarks, antiquarks and gluons are screened such that the formation of bound states is inhibited. This new state of matter is called Quark Gluon Plasma.

The ultimate aim of ultra-relativistic heavy-ion collisions is to prove the existence of this new state of matter and to investigate its particular properties. The topic is also relevant to other fields, like cosmology and astrophysics. Firstly, the transition from hadronic matter to a QGP may happen in the inner core of neutron stars, where mass densities are likely to exceed 10^{15} g/cm^3 (about four times the central density of nuclei) while surface temperatures are as low as 10^5 K or less [11]. Secondly, it is believed that the inverse transition (hadro-synthesis) had to occur a few tens of microseconds after the Big Bang. The following sections will give a brief historical overview over the heavy-ion program and elucidate the most interesting features of the phase transition.

quark flavor	charge Q/e	current mass m_q [MeV/c^2]	dynamical mass M_q [MeV/c^2]
d (down)	$-1/3$	9.9 ± 1.1	310
u (up)	$+2/3$	5.6 ± 1.1	310
s (strange)	$-1/3$	199 ± 33	500
c (charm)	$+2/3$	1350 ± 50	1800
b (bottom)	$-1/3$	$\simeq 5000$	4500
t (top)	$+2/3$	> 90000	> 176000

Table 2.1: **Quark properties.** *Quarks are fermions (spin 1/2) and are characterized by the flavor degree of freedom d, u, s, c, b or t. The current quark masses listed in the table were taken from reference [27], the dynamical masses from [28]. A current mass is the mass of a quark in the absence of confinement. When the quark is confined in a hadron, it may acquire an effective mass which includes the effect of the zero-point energy of the quark in the confining potential. This so called dynamical mass is typically a few hundred MeV in magnitude.*

2.1 Historical Overview

The heavy-ion program started with fixed target experiments in 1986 at the **A**lternating **G**radient **S**ynchroton (AGS) of the **B**rookhaven **N**ational **L**aboratory (BNL) and the **S**uper **P**roton **S**ynchroton (SPS) of the **C**entre **E**uropéen pour la **R**echerche **N**ucléaire (CERN). The center of mass energy reached with these two facilities is $\sqrt{s} = 5$ AGeV and $\sqrt{s} = 17$ AGeV, respectively. Data was taken using a beam of relatively light ions of 14.6 AGeV ^{16}O and ^{28}Si at the AGS and 60-200 AGeV ^{16}O and ^{32}S beams at the SPS. It was observed that the colliding nuclear matter loses a substantial fraction of its energy in the collision process [29]. This proved the possibility to create hot and dense matter in heavy-ion collisions.

The program continued with heavier nuclei, 10.8 AGeV ^{197}Au at the AGS and 40, 80 and 158 AGeV ^{208}Pb at the SPS. The high energy Pb data provided circumstantial evidences that a new state of matter had been produced [30], and the official announcement from CERN soon followed in the year 2000 [31].

The QGP formed at SPS energies is not expected to be net-baryon-free. The net-baryon content in the QGP is small, if the separation between the beam and the target rapidity stays far away from the central rapidity region. For nucleus-nucleus collisions at an energy of $\sqrt{s} = 100$ AGeV, the separation between the projectile and the target rapidity is 10.7 units. On the other hand, the average rapidity loss of the baryons in the central collision of Au on Au is roughly 2 to 4 units [27]. Thus, for those high energy collisions a net-baryon-free Quark Gluon Plasma would be expected. This triggered the set of experiments, which began to run in the year 2000 at the **R**elativistic **H**eavy **I**on **C**ollider (RHIC), also located at BNL. These were collider experiments, able to reach even higher energies of about $\sqrt{s} = 200$ AGeV necessary to produce a net-baryon-free Quark Gluon Plasma.

An even clearer result will be obtained with a new collider being built at CERN, the **L**arge **H**adron **C**ollider (LHC). This machine will be capable to reach energies of about $\sqrt{s} = 5.5$ ATeV. At this highest energy all parameters relevant for the formation of the

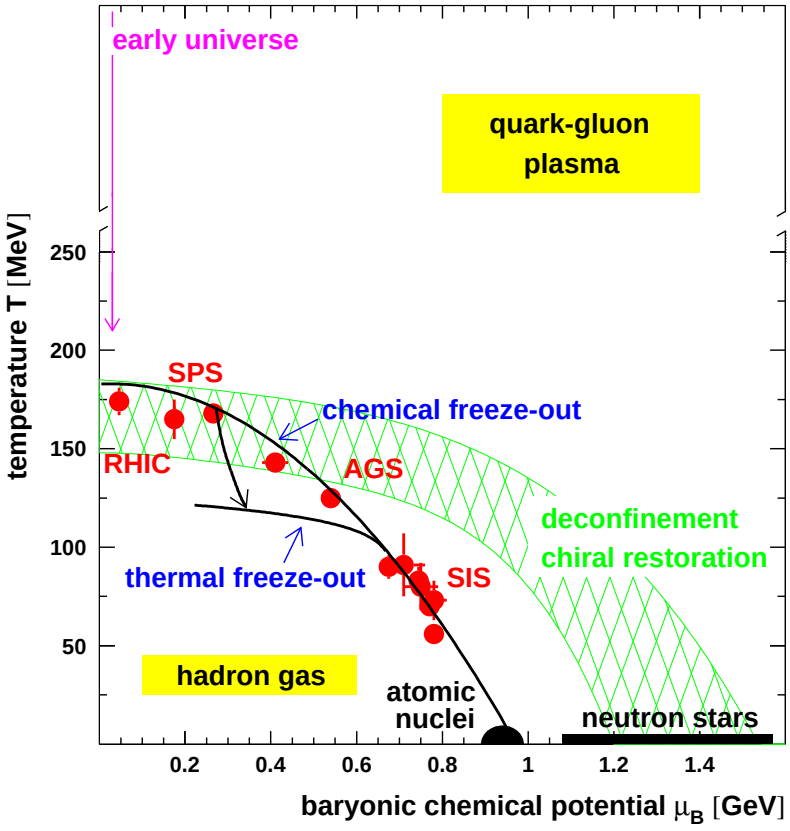

Figure 2.1: **Phase diagram of matter.** *Lattice QCD calculations predict a deconfinement phase transition, and an accompanying chiral phase transition, both at high temperature and/or high density. The expectation for the phase boundary [35], based on calculation for $\mu_B = 0$, is indicated by the hatched region. The chemical potentials μ and temperatures T resulting from thermal analyses place the chemical freeze-out (black line) very close to the phase boundary between plasma and hadrons.*

QGP, such as energy density, size and lifetime of the system and relaxation time, will be more favorable. The experiment dedicated to heavy-ion collisions at LHC will be ALICE (**A** **L**arge **I**on **C**ollider **E**xperiment) [32]. First runs are planned for the year 2007.

2.2 Phase Diagram of Nuclear Matter

Recent theoretical predictions estimate that the phase transition between the confined and the deconfined phases of QCD occurs at a critical energy density of $\epsilon_c = 0.70 \pm 0.35$ GeV/fm^3 [33]. This energy density can be reached by changing one or both of the two essential thermodynamical quantities: the temperature T and the density ρ. The QCD phase diagram in figure 2.1 can thus map out regions in the plane of temperature T and baryochemical potential μ_B [34], with the latter specifying the mean

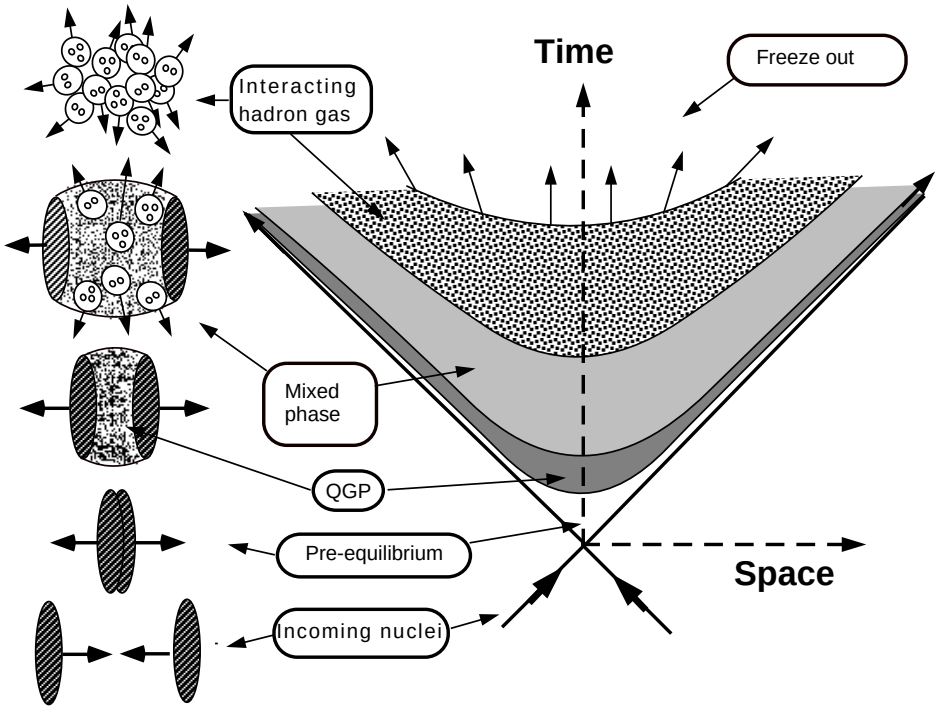

Figure 2.2: **Space-Time Evolution of a Heavy-Ion Collision.** *The invariant hyperbola in the space-time diagram allocate the individual stages passed during a heavy-ion collision.*

baryon number density ρ_B (baryon minus antibaryons).

If ordinary nuclear matter is compressed to the extent that nucleons overlap, a cold QGP is formed. It is believed that this situation may take place inside neutron stars [36]. At $T = 0$ the critical density for the transition can be estimated to be $\rho_c \simeq 0.72/\text{fm}^3$ [27]. ρ_c is about 5 times the nucleon number density $\rho_B = 0.14/\text{fm}^3$ for normal nuclear matter at equilibrium. Experimentally, the QGP can be accessed by a combination of heating and compression, colliding heavy nuclei with velocities close to the speed of light. The energy brought into the system is dissipated for the creation of quark-antiquark pairs and gluons. Assuming equilibration, the system becomes deconfined at sufficiently high density and temperature to form a hot QGP.

The space-time scenario of a high-energy nucleus-nucleus collision was suggested by Bjorken [37] as illustrated in figure 2.2. The trajectories of the projectile and the target nucleus are drawn as thick lines in the diagram. The nuclei are Lorentz contracted in longitudinal direction and therefore represented by two thin disks. During the collision process the baryons lose a substantial fraction of their energy, which is deposited in the vicinity of the center of mass. After the collision the slowed-down baryons can still have enough momentum to recede from each other. The energy deposition is approximately additive in nature and might be sufficient to create a system of quasi-free quarks and gluons in the central rapidity region. After a short moment of incomplete thermal equilibration (pre-equilibration), the plasma may reach local equilibration (QGP) at the formation time

$\tau_0 \approx 1$ fm/c [37]. The subsequent evolution of the fireball can be described in terms of the laws of hydrodynamics. The pressure inside the hot and dense medium leads the system to expand. Its temperature drops and the plasma starts to hadronize (mixed phase). The hadrons will stream out of the collision region when the temperature falls below the temperature of chemical freeze-out. At this stage all inelastic interactions stop and the yield of each hadron species is fixed. As the temperature further decreases to reach the point of thermal freeze-out, also the elastic collisions cease.

The relative abundance of produced hadrons in heavy-ion collisions can be compared with expectations for a statistical ensemble [34]. This allows two parameters to be adjusted to the data: the temperature T and the baryochemical potential μ_B. At present, data exists for a variety of energy regimes, accessible by different accelerators (SIS, AGS, SPS and RHIC). This allowed the determination of hadrochemical freeze-out points, shown in figure 2.1 as red circles. The empirical curve connecting the freeze-out points corresponds to a constant energy per hadron of 1 GeV [38]. The information about the thermal freeze-out can be extracted from the analysis of momentum spectra and is also shown in the figure.

2.3 Chiral Symmetry Restoration

A fundamental symmetry of QCD is chiral symmetry. It is broken in the vacuum, but lattice QCD predicts that chiral symmetry is restored at the same temperature as the deconfinement of the quarks and gluons occurs. An important goal in heavy-ion physics is therefore to look for evidences for this fundamental prediction of the Standard Model. This issue will briefly be elucidated in the present section. A comprehensive introduction to this topic can also be found in [39].

Chiral symmetry involves the handedness of particles, i.e. the information of the spin orientation versus its direction of motion. The ability to define the handedness in an absolute way depends on weather or not a particle has mass, since a particle with mass moves with less than the speed of light. For right-handed particles, the spin is pointing in the same direction as its velocity. But for an observer moving faster than the particle, it would appear to move backwards, while its spin would still remain unchanged. For that observer the particle would seem to be left-handed. In contrast, a massless particle moves at the speed of light in all frames, and all observers would agree on its handedness.

As indicated in table 2.1 the masses of the quarks are not fixed constants but are rather generated by interactions with other particles. The current mass m_q can be associated with the weak interaction. The dynamical mass M_q arises from the strong interaction. It is believed that the current masses are generated by the coupling to the still undiscovered Higgs field. The Higgs field has a finite average value in the ground state, generally known as vacuum. Particles interact with the vacuum Higgs field, which modifies their properties and gives rise to their masses. In the limit $m_q \to 0$ the QCD Lagrangian for light quarks (u,d, and s) reveals SU(3) flavor symmetry independently for left-handed and right-handed quarks, i.e. it has chiral symmetry $\mathrm{SU(3)_L} \times \mathrm{SU(3)_R}$. In this limit the helicity becomes a good quantum number. Since the actual current masses of the light quarks

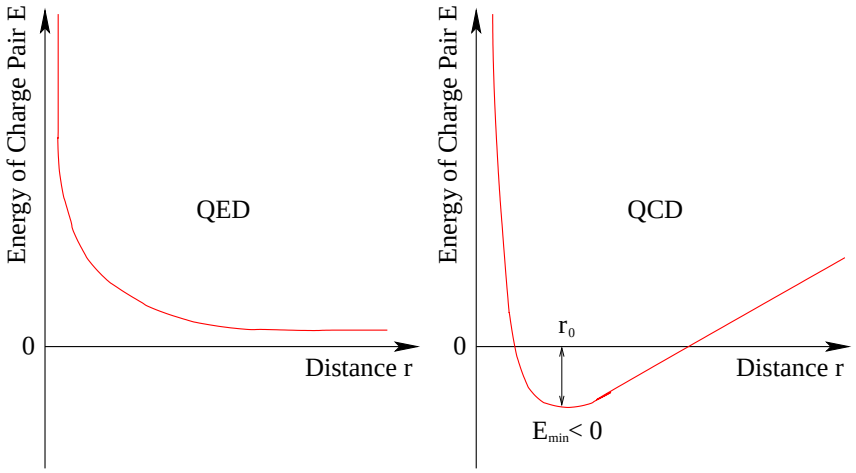

Figure 2.3: **Energy dependence of a charge singlet pair.** *Due to quantum fluctuations the vacuum is filled with pairs of charged particles in a singlet state. Charge means electric charge in the case of QED (**Q**uantum **E**lectro**d**ynamics) and color charge in the case of QCD (**Q**uantum **C**hromo**d**ynamics). If a e^+e^- pair is created from the QED vacuum, it will annihilate within the time scale $1/E_{pair}$ given by the uncertainty relation. These are virtual pairs. In contrast to this scenario, the total energy in QCD exhibits a minimum at negative energy. The empty vacuum at $E = 0$ becomes unstable and the pairs become real.*

are small compared to the typical few hundreds of MeV for strongly interacting particles, they can to a good approximation be regarded as massless and QCD as approximately invariant under the chiral version of isospin symmetry.

As is schematically illustrated in figure 2.3, the total pair energy in QCD has a minimum at some distance $r_0 \sim 1$ fm. Moreover the value of this minimum is negative. As a consequence, an empty ($E = 0$) vacuum becomes unstable because there exists a configuration with lower energy. Pairs of color charge are created and stay there forever. The QCD vacuum is filled with real color charge pairs. Because the gauge field (gluons) is a vector field, due to the helicity conservation for $m_q \to 0$ a left-handed quark can only couple with a left-handed antiquark and vice versa. This means that the $q\bar{q}$ pairs in the QCD vacuum have to be in the singlet state not only in color but also in spin. But already this means that chiral symmetry is broken in the vacuum, since there are $q\bar{q}$ pairs in a scalar state, i.e. containing q and $\bar{q}$ of opposite helicities, which in massless limit do not interact. A right-handed and massless test quark put into such a vacuum can only annihilate on a right-handed antiquark thus liberating a left-handed quark [40]. For an observer at some distance this will look like the test quark, being in a vacuum, changes spontaneously its helicity. Therefore, it cannot move with the speed of light, and hence it had to acquire some dynamical mass. It is these interactions with the asymmetric vacuum that hide the approximate chiral symmetry of QCD.

If the temperature and therefore the kinetic energy is raised, at some critical value T_c of the order of the pion mass the energy stored in the strong field is overcome. At this stage the minimum of the total pair energy will become positive, and hence the real $q\bar{q}$ pairs would disappear from the vacuum. Above that temperature chiral symmetry will be restored and quarks will retain their zero mass in the chiral limit.

2.4 Equation of State

The equation of state describes the temperature dependence of the energy density ϵ and the pressure p. Obviously it is of great interest to estimate the hadron-quark transition temperature. The simplest picture is perhaps assuming the hadronic phase to be an ideal non-interacting **H**adron **G**as (HG) of massless pions, and the quark phase to be an ideal gas (QGP) of massless gluons and two-flavor quarks [41]. The energy density ϵ and the pressure p of an ideal gas are given by:

$$\epsilon_{ideal} = \frac{g}{30}\pi^2 T^4, \tag{2.1}$$

$$p_{ideal} = \frac{\epsilon_{ideal}}{3} = \frac{g}{90}\pi^2 T^4. \tag{2.2}$$

The degeneracy factor g is defined by the boson degrees of freedom n_b and the fermion degrees of freedom n_f:

$$g = n_b + \left(1 - \frac{1}{2^3}\right) n_f. \tag{2.3}$$

With the boson degrees of freedom $n_b = 3$ for the three isospin pion states, and no fermions, the pressure of the ideal Hadron Gas would be:

$$p_{HG} = \frac{1}{30}\pi^2 T^4 \simeq \frac{1}{3}T^4. \tag{2.4}$$

In the QGP case, the boson degrees of freedom add up to $n_b = 16$ (8 color states $\times$ 2 spin states for gluons). The fermion degrees of freedom add up to $n_f = 24$ (2 flavors $\times$ 3 colors $\times$ 2 spins $\times$ 2 for quark-antiquark). The external pressure can be estimated using the bag model for hadrons [42]. It is equal to the bag constant B. As a result, the pressure for the QGP can be written as:

$$p_{QGP} = \frac{37}{90}\pi^2 T^4 - B \simeq 4T^4 - B. \tag{2.5}$$

For low temperatures, equation (2.4) yields the larger pressure. By increasing the temperature, the two pressures first become equal at a critical temperature T_c and thereafter the QGP pressure dominates. According to Gibbs criterion, the phase with the largest pressure is the stable one. This means that at low temperature the system will be in a HG phase and for high temperatures in the QGP phase. Assuming a bag constant of $B^{1/4} \simeq 200$ MeV [27], the transition will occur at a temperature:

$$T_c = \left(\frac{90B}{37\pi^2}\right)^{\frac{1}{4}} \approx 140 MeV \tag{2.6}$$

More detailed theoretical calculations are done in lattice QCD, a nonperturbative treatment of quantum chromodynamics formulated in a discrete lattice of space-time coordinates [43]. They have been performed at zero net-baryon charge. This has a pure technical reason, as some expressions that are in lattice Monte Carlo formulation interpreted as probabilities, are no longer positive definite at non-zero baryon densities.

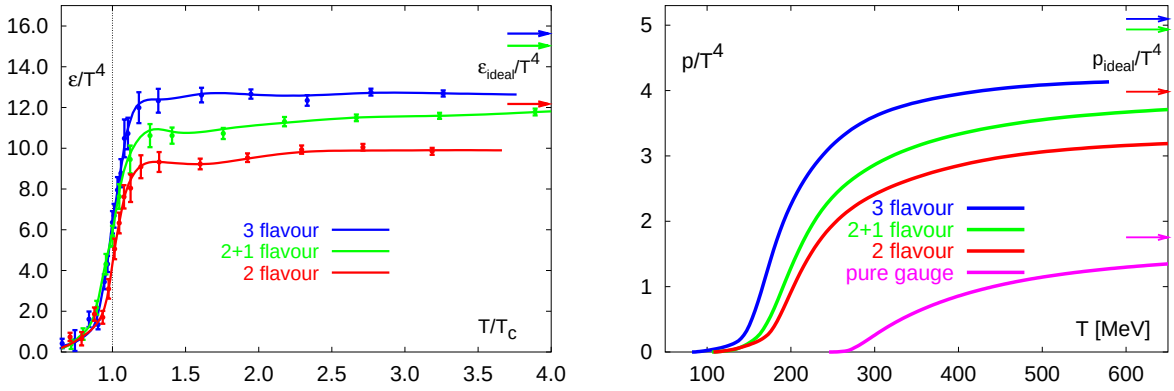

Figure 2.4: **Energy density and pressure as a function of temperature in lattice QCD.** *The calculations have been performed by the Bielefeld group [33] using 0, 2 and 3 light quarks as well as two light quarks and a heavier (strange) quark. At high temperature it is expected that ϵ/T^4 and p/T^4 will asymptotically approach the free gas limit for a gas of gluons and n_f quarks (equation 2.1 and 2.2). This is indicated by the arrows.*

Figure 2.4 shows a calculation for the energy density and the pressure. The rapid change in energy density within a narrow temperature interval indicates the change from confined hadrons to a QGP. However, the phase transition is found to be of the first or of the second order, or even a smooth cross-over, depending on the number of quark flavors and their masses. The critical temperature T_c obtained at zero baryon density is about 260 MeV for pure gauge theory, i.e. for systems consisting of gluons only. For theories with dynamical quarks T_c varies between 140-170 MeV.

Chapter 3

Dimuon Excess in the Intermediate Mass Region

Dileptons have the interesting property of not suffering strong interactions with the surrounding hadronic medium. Therefore, they are considered as ideal probes of the early stage of heavy-ion collisions, where the Quark Gluon Plasma formation is expected. The dilepton mass spectra can basically be divided into three regions [22]. The region below the ϕ meson ($\sim$ 1 GeV/c^2) is addressed as the low mass region. It is dominated by hadronic interactions and hadronic decays. In the intermediate mass region from about 1 to 2.5 GeV/c^2, the contribution from the thermalized QGP might be seen [44]. And finally, in the high mass region the J/ψ suppression has been a subject of great interest, since it was proposed as a signal of the deconfinement phase transition [45].

The most prominent observation in the low and intermediate mass region has been the dilepton enhancement seen by the experiments HELIOS/3, CERES and NA38/NA50. The NA50 experiment has proposed an enhanced open charm production in central Pb-Pb collisions by a factor of 3 [17]. Such a large enhancement is, however, difficult to explain theoretically. Another interpretation of the data is that the increase of the IMR dimuons is not from charm but is due to thermal dileptons [24]. This chapter summarizes the experimental findings and gives a brief confrontation of two possible explanations: open charm enhancement and thermal dilepton radiation.

3.1 Experimental Evidences

The NA38/NA50 experiment studied muon pair production in p-A, S-U and Pb-Pb collisions at the CERN SPS [8, 46]. The dominant contribution to the dimuon spectrum in the IMR is the combinatorial background due to the decays of π and K mesons. After its subtraction the invariant mass and transverse momentum spectra in p-A collisions are well described by a superposition of dimuons coming from leptonic and semi-leptonic charm decays and from Drell-Yan processes:

$$\frac{dN}{dm}^{\pm} - R\frac{dN}{dm}^{bg} = n^{J/\psi}\frac{dN}{dm}^{J/\psi} + n^{\psi'}\frac{dN}{dm}^{\psi'} + n^{D\overline{D}}\frac{dN}{dm}^{D\overline{D}} + n^{DY}\frac{dN}{dm}^{DY} \tag{3.1}$$

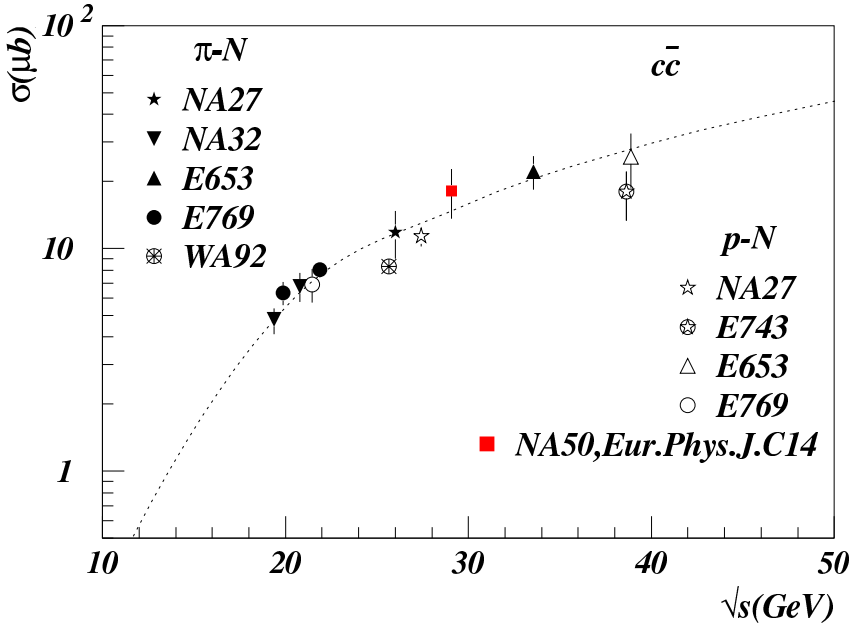

Figure 3.1: **Charm hadroproduction cross-section.** *The values refer to forward production ($x_F > 0$). The dotted curve shows the $\sqrt{s}-$dependence of $\sigma^{pp}_{c\overline{c}}$ obtained with PYTHIA and fitted to the measurements. The red square is the indirect measurement from the NA38/NA50 collaboration [17].*

In this equation R is a correction factor to account for charge correlation effects. The shape of the dimuon sources in the right part of equation (3.1) is evaluated by means of a Monte Carlo simulation. By fixing the shape of the dimuon sources, the p-A spectra are fitted leaving the yields n^i ($i = DY$, $D\overline{D}$, J/ψ, ψ') as free parameters.

The obtained total number of muon pairs from $D\overline{D}$ decays is translated into an open charm production cross-section $\sigma^{pA}_{D\overline{D}\to\mu\mu}$ for p-A collisions. To obtain the corresponding value for p-p collisions at 450 GeV/c a linear dependence on the mass number A is assumed:

$$\sigma^{pp}_{c\overline{c}} = \left(\frac{\sigma^{pp}_{c\overline{c}}}{\sigma^{pp}_{D\overline{D}\to\mu\mu}}\right)^{MC} \cdot \frac{\sigma^{pA,Data}_{D\overline{D}\to\mu\mu}}{A} = 36.2 \pm 9.1\ \mu\text{b}. \tag{3.2}$$

The Monte Carlo scaling ratio was obtained from a simulation with the event generator PYTHIA [47]. The NA38/NA50 compared their indirect measurement for the p-p open charm production cross-section to direct measurements from other experiments, as shown in figure 3.1. For this purpose the cross-section value was divided by a factor of 2 to consider only the $x_F > 0$ hemisphere. The agreement is satisfactory. It is possible to obtain the $\sigma^{pp}_{c\overline{c}}$ cross-section for different energies from a PYTHIA calculation fitted to the data.

The expected cross-section for A-A collisions $\sigma^{AA}_{c\overline{c}\to\mu\mu}$ is obtained by using a linear extrapolation of the p-A sources with the product $A_p \times A_t$ of the mass number of the projectile and target nuclei. This enables to calculate the expected number of $D\overline{D}$ dimuons in the centrality integrated S-U and Pb-Pb spectra. The Drell-Yan events are determined by a fit to the high mass region of the spectrum.

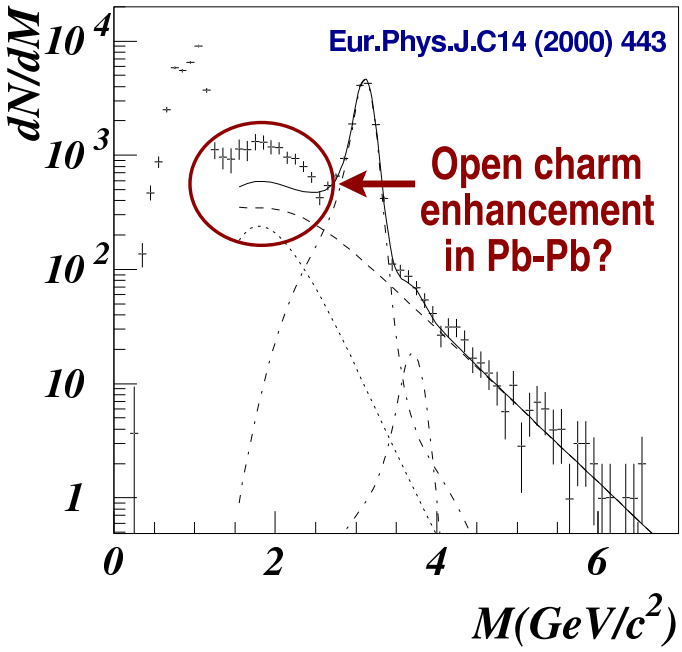

Figure 3.2: **Enhancement in the IMR dimuon spectra of Pb-Pb collisions.** *The figure shows the dimuon spectra from 158 AGeV/c Pb-Pb collisions [17]. The sum of expected sources is drawn as solid line. The contributions from Drell-Yan processes (dashed line), J/ψ and ψ' (dot-dashed lines), and from $D\overline{D}$ (dotted line) are also shown. The comparison to the data shows a dimuon excess in the IMR which might be assigned to an enhancement of open charm.*

The comparison of the expected sources in A-A collisions and the data points shows that the linear extrapolation from p-A collisions underestimates the dimuon yield in the IMR. As an example the spectrum for central Pb-Pb collisions ($N_{part} = 381$) is shown in figure 3.2. It is observed that the excess increases roughly linearly with the number of participant nucleons N_{part} as can be seen in figure 3.3. In order to describe the data with a simple superposition of DY and $D\overline{D}$, the expected open charm yield has to be scaled up by a factor reaching ~ 3.5 for central Pb-Pb collisions.

This excess has been interpreted as enhancement of open charm. It has been observed that the kinematical distributions (p_T, y and $\cos\theta_{cm}$) of the measured dimuon excess are compatible with those expected from open charm but not with a wrong estimation of the background normalization.

Also the CERES collaboration has tested the hypothesis of open charm enhancement to explain their dilepton enhancement in the low mass region [25]. However, the data would require an enhancement factor of about 150, which is ruled out by the NA38/NA50 measurement. To bring clarity in the situation, a direct measurement of the open charm yield is presented in this work.

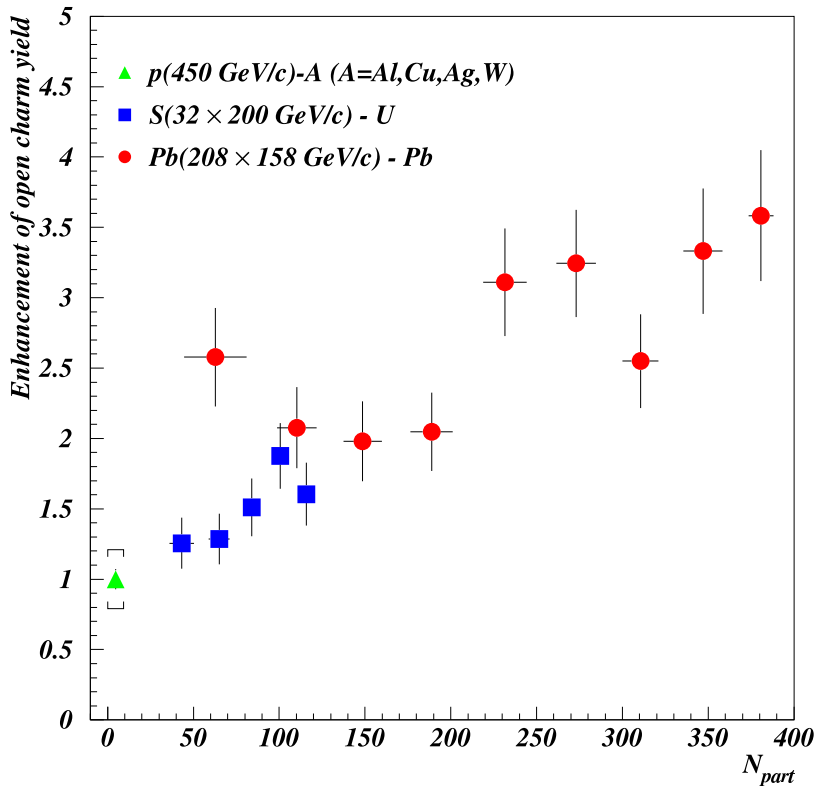

Figure 3.3: **Enhancement factor versus number of participants.** *The data points comprise the p-A and A-A collision measurements of the NA38/NA50 collaboration [17]. The bracket in the p-A point represents the systematic uncertainty.*

3.2 Open Charm Enhancement as QGP Signature

One possible explanation of the open charm enhancement is given within the **S**tatistical **C**oalescence **M**odel (SCM) [48]. In this approach it is assumed that the J/ψ meson is created at hadronization according to the available hadronic phase-space. Thus, within this model, the J/ψ yield is independent of the open charm yield.

The hypothesis for open charm enhancement is that in A-A collisions a charm pair below the D meson pair threshold ($m_{c\overline{c}} < 2m_D$) can hadronize into D mesons [49]. This picture can be clarified by first considering open charm production in e^+e^- annihilation. If the distance between the c and $\overline{c}$ quark reaches the range of the confinement forces, a string connecting these colored objects is formed. If the e^+e^- center of mass energy $\sqrt{s}$ lies above the D meson threshold $2m_D$, the c and $\overline{c}$ quarks break the string into two (or more) pieces. As a consequence charmed mesons or hadrons are produced. However, if $\sqrt{s}$ exceeds the charm quark threshold but lies below the D meson threshold ($2m_c < \sqrt{s} < 2m_D$), the string does not break and no open charm meson is formed.

Next, the $c\overline{c}$ formation is assumed to take place inside a deconfined medium. In this case no string is formed between the colored objects due to the Debye screening. The created c and $\overline{c}$ quarks can fly apart as if they were free particles. Thus, they will be able

to form a D meson at the stage of the QGP hadronization even if their initial invariant mass $m_{c\overline{c}}$ was below the corresponding meson threshold.

In N-N or A-A collisions the heavy flavor quark pairs are produced due to hard parton interactions. Leading order pQCD calculations show that a great fraction of $c\overline{c}$ pairs are created with $m_{c\overline{c}} < 2m_D$ even at the largest RHIC energies. In a deconfined medium, as expected for high energy A-A collisions, the hadronization of the created $c\overline{c}$ pair would be facilitated. This should lead to an enhancement of charmed meson production in A-A collisions compared to the result obtained by linear extrapolating the N-N data. Within the rapidity window of the NA50 spectrometer the SCM predicts an open charm enhancement factor of 2.5 to 4.5 [50].

3.3 Thermal Dilepton Radiation

A different approach to explain the dilepton excess is the assumption of a thermal source emission [24, 51, 52, 53]. The model is based on the observation that the dilepton emission rate from a hadron gas at a given temperature is fairly well described by the $q\overline{q}$ annihilation rate at the same temperature [11]. The so called quark-hadron duality is valid down to a mass of approximately 1 GeV/c^2. Such simplification makes it possible to parameterize the thermal source by a Boltzmann-like exponential function with effective temperature T_{eff} and a normalization factor N_{eff} which reflects the space-time volume occupied by the thermal source.

In this way the dilepton spectra from CERES in the low mass region and from NA50 in the intermediate mass region can be described at the same time by just using the two parameters $T_{eff} = 170$ MeV and $N_{eff} = 3.3 \cdot 10^4$ fm^4. The comparison is shown in figure 3.4. Even the direct photon data from the WA98 [54] is compatible with this picture.

The thermal source model is not able to decide if the matter which emits the dileptons has a deconfined or hadronic nature. However, the effective temperature parameter of $T_{eff} = 170$ MeV is in perfect agreement with the temperature needed to describe hadron species ratios [55]. Since T_{eff} is an average temperature, it can be concluded that the electromagnetic probes indeed point to temperatures above the expected deconfinement temperature. This corroborates the expectation that at CERN-SPS energies a QGP is formed.

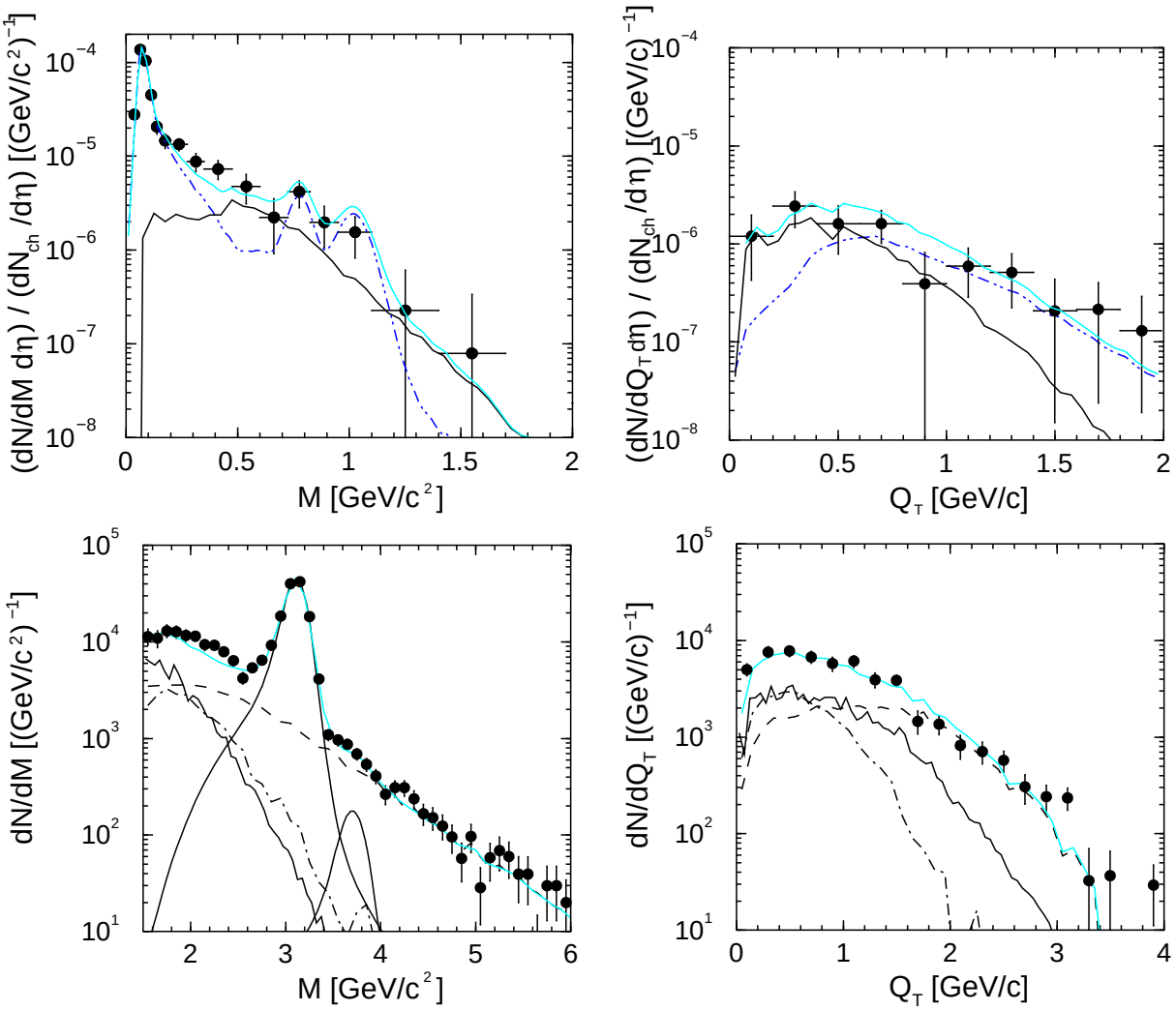

Figure 3.4: **Comparison of thermal model calculations to data.** *Preliminary CERES data (upper row) and NA50 data (lower row) can be described within thermal model calculations [53]. The thermal yields are drawn as black solid lines. The contribution from the hadronic decay cocktail is drawn as dot-dashed blue line in the CERES data. In the NA50 data the contribution from Drell-Yan processes is drawn as dashed line, the contribution from open charm as dot-dashed line, and the J/ψ and ψ' as black solid line. The blue solid line is the sum over all contributions.*

Chapter 4

CERES Experiment

The CERES (**Che**renkov **R**ing **E**lectron **S**pectrometer) experiment is part of the heavy-ion program at the CERN **S**uper **P**roton **S**ynchroton (SPS). It was designed for the measurement of low mass e^+e^- pairs in nucleus-nucleus collisions. The first version of the experiment consisted of a telescope of two **Si**licon **D**rift **C**ounters (SiDC1 and SIDC2) for precise vertex reconstruction and two **R**ing **I**maging **Ch**erenkov Detectors (RICH) for the electron identification. Originally, the momentum of the electrons was determined by measuring the deflection angle in the azimuthal symmetric magnetic field between the two RICH detectors. The experiment was upgraded in the year 1995. An additional Pad Chamber was positioned behind the second RICH detector to improve the momentum resolution and to cope with the high multiplicities of Pb-Au collisions [56].

In 1998 the Pad Chamber was replaced by a cylindrical **T**ime **P**rojection **C**hamber (TPC) [57] in order to improve the mass resolution in the range of the ρ, ω and ϕ mesons to $\Delta m/m = 3\%$. The differential energy loss dE/dx in the TPC is used to further improve the electron to pion separation. In addition, the TPC allows the study of final hadronic states. As all other subdetectors the TPC has full azimuthal coverage. The acceptance in polar angle is $8° < \theta < 14°$ which corresponds to a pseudorapidity range of $2.10 < \eta < 2.65$. At the time of the experimental upgrade the former magnetic system between the RICH detectors was disabled and a new system assembled around the TPC. The recent experimental setup of the CERES experiment is shown in figure 4.1. A detailed description of its individual components will follow in the next sections.

4.1 Target Area

The target system used during the beam time in 2000 consists of 13 gold disks. The gold is vacuum-metalized onto mylar foils which served as support structure. The thickness of the mylar foils is 1.5 μm, that of the gold layers is 25 μm. The mylar foils are glued onto iron rings of 350 μm. The distance between the targets is adjusted with spacers of 1.6 mm. A target diameter of 600 μm and a spacing between each disk of 1.98 mm is chosen to guarantee that each particle produced in the acceptance of the spectrometer does not pass additional target disks. This condition minimizes the amount of undesired

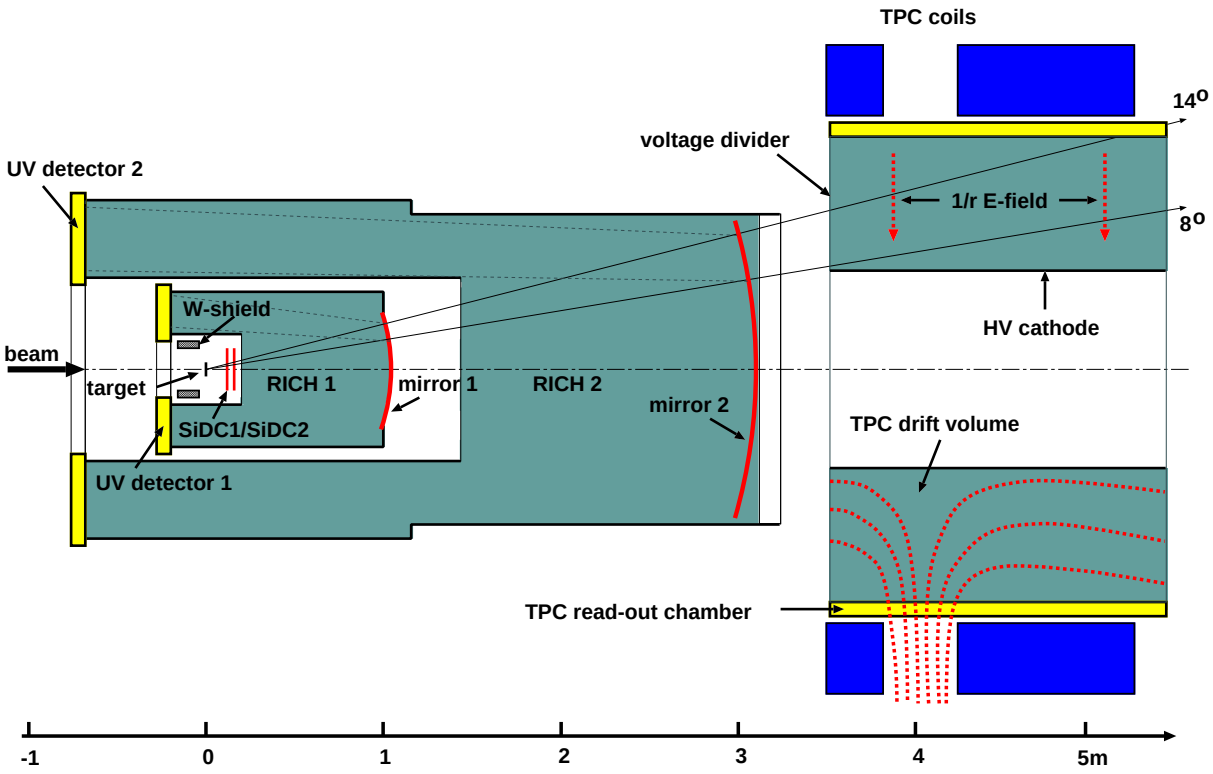

Figure 4.1: **Cross-section of the upgraded CERES experiment.** *Shown is the latest setup of the spectrometer used during the beam times in 1999 and 2000. The main components are two Silicon Drift Detectors (SiDC1/SiDC2) for the vertex reconstruction, two Cherenkov Counters (RICH1/RICH2) for electron identification and a Time Projection Chamber (TPC) for the measurement of the particle momentum.*

conversions of photons into e^+e^- pairs. The tungsten shield upstream the target system protects the UV-Counters of the RICH detectors against strongly ionizing particles from the target.

4.2 Trigger System

The trigger system of the CERES experiment starts the readout sequence of the detectors if a (central) collision between a beam and a target nucleus has been detected. The decision is based on the signals of three Cherenkov Counters with air as radiator gas (Beam Counters BC1, BC2, and BC3) and a 1 mm plastic scintillator for centrality (Multiplicity Counter MC).

The first two Cherenkov Counters are located 60 m and 40 mm upstream the target system, respectively. The beam trigger is defined by the coincidence between these two counters:

$$T_{beam} = BC1 \cdot BC2. \tag{4.1}$$

With an additional veto on BC3, located 69 mm downstream the target system, the

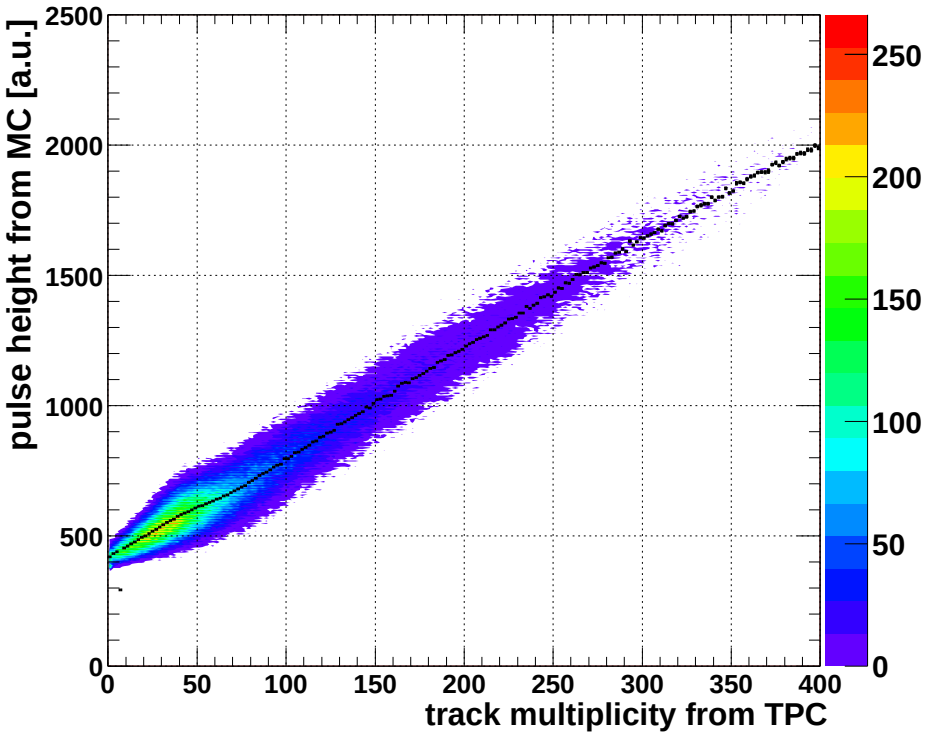

Figure 4.2: **Correlation between the pulse height of the MC and the TPC track multiplicity.** *The number of tracks for minimum bias runs is plotted on the horizontal axis. The vertical axis shows the pulse height information from the multiplicity detector of the trigger system. The plot was divided into vertical slices. To each slice a Gaussian function was fitted, and the mean value with its error is shown in black. Over the whole range the pulse height of the MC is proportional to the track multiplicity.*

minimum bias interaction trigger can be generated by:

$$T_{minbias} = BC1 \cdot BC2 \cdot \overline{BC3}. \tag{4.2}$$

Finally, the central trigger requires a signal from MC, located 77 mm downstream the target system:

$$T_{central} = BC1 \cdot BC2 \cdot \overline{BC3} \cdot MC. \tag{4.3}$$

The MC scintillator has an outer diameter of 14.7 mm. With a 4.9 mm diameter hole in the middle it has a mean pseudorapidity coverage of $2.3 < \eta < 3.5$. Its signal is roughly proportional to the number of charged particles hitting the scintillator and thus it is a good measure for centrality. The correlation between the MC pulse height and the track multiplicity measured with the TPC is shown in figure 4.2.

Additional beam particles passing through the target within several microseconds from the triggered event produce δ-electrons visible in the SiDC and the RICH detectors. These events are suppressed by the trigger system by requiring no other beam particle within ± 1 μs from the nuclear reaction triggered on.

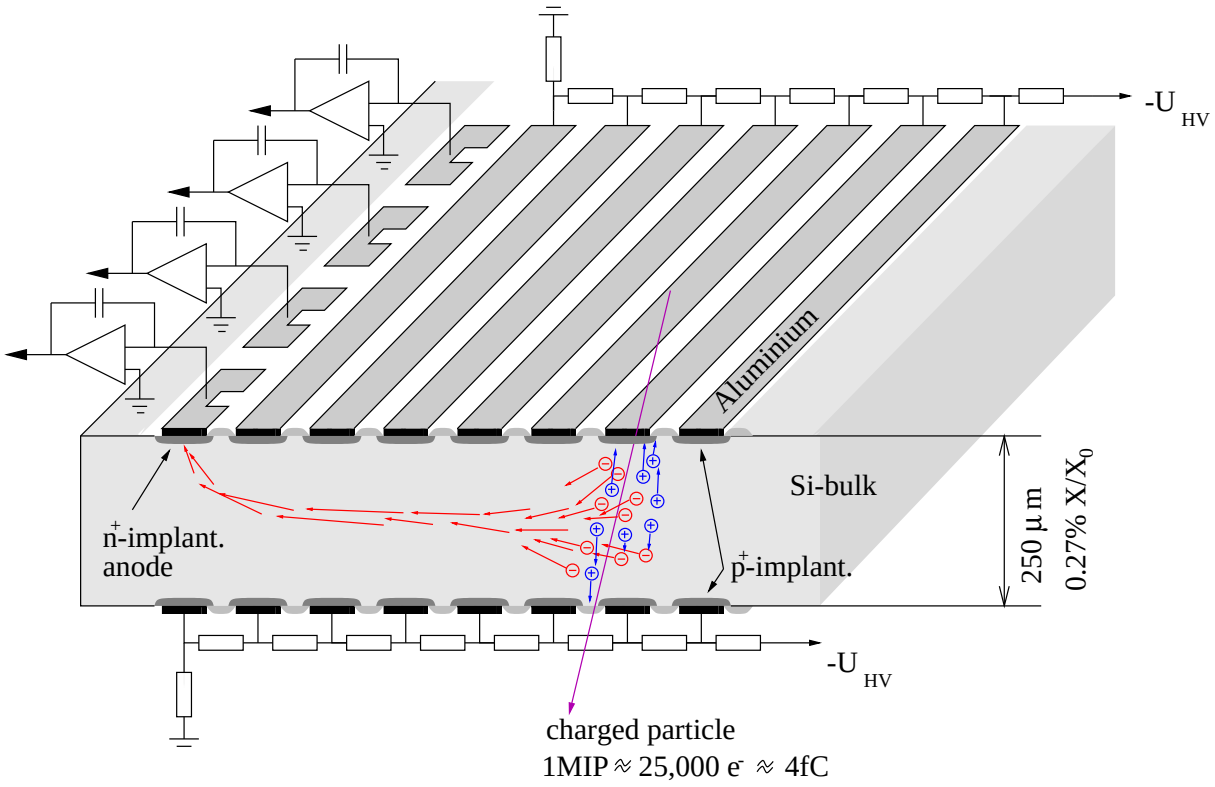

Figure 4.3: **Operation mode of the Silicon Drift Detectors used in the CERES spectrometer.** *A particle traversing the depletion zone of the detector creates electron-hole pairs. An electric drift field leads the electrons towards the anodes located at the edge of the wafer.*

4.3 Silicon Drift Detectors

Two radial Silicon Drift Counters (SiDC1, SiDC2) are located 10.4 cm and 14.3 cm respectively downstream the target system. Both detectors are 4″ wafers with a thickness of 250 μm. The active area ranges from 4.5 mm to 42 mm in radius.

The operation mode of the SiDC detectors is based on the sidewards depletion proposed by E. Gatti and R. Rehak in 1984 [58] and is illustrated in figure 4.3. The underlying idea is that a huge area of high resistive n-type doped silicon can be completely depleted from a tiny n^+-type doped contact by impressing a negative voltage on p^+-type implants on both side of the wafer. The minimum of the electric potential is located in the middle of the wafer and has a parabolic shape towards the surface.

If a particle traverses the depletion zone of a SiDC it produces electron-hole-pairs. The electrons are transported towards the n^+-anode via an electric drift field created by a voltage divider parallel to the wafer surface. For a typical drift field of 700 V/m the maximal drift time of the electrons is around 3.8 μs. This drift concept has the advantage that the surface of the anode can be kept small. A small anode surface implies a small capacitance which reduces electronic noise.

A total amount of 360 anodes are radially arranged at the edges of the SiDC detectors. They are connected with the readout chain. The measured pulse height is amplified by a

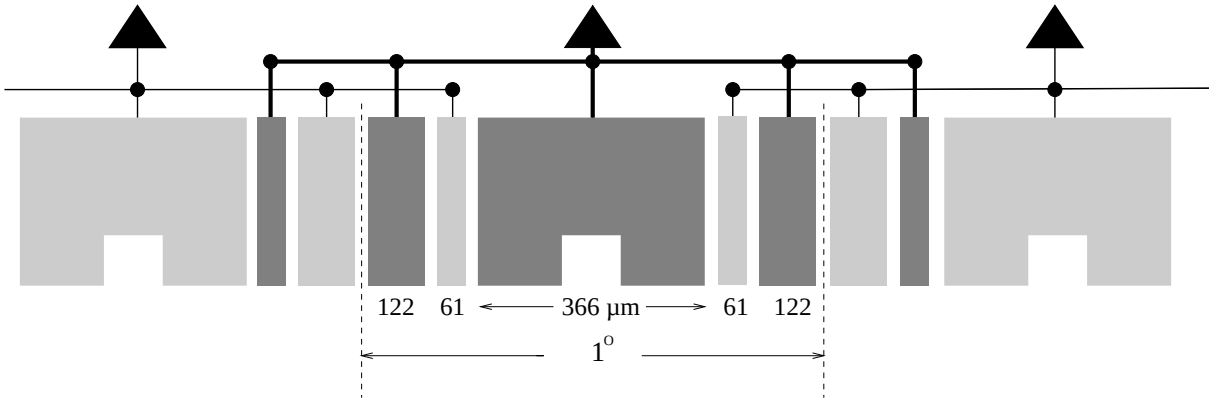

Figure 4.4: **Segmented anode structure of the SiDC detectors.** *The width of a 1° anode sector adds up to 732 µm. The central segment of 366 µm is connected to two main side segments of 122 µm. In addition each anode has two smaller side segments of 61 µm located in adjacent anodes. This design guarantees optimal charge sharing.*

charge sensitive amplifier and shaped in a quasi-Gaussian form. A FADC (**F**lash **A**nalog **D**igital **C**onverter) samples the analog signal with a frequency of 50 MHz and digitizes it with a 6 bit resolution.

Within the overall concept of the experiment the two SiDC detectors are used to determine the pseudorapidity density of charged particles $dN/d\eta$, suppress conversion electrons, and perform a precise vertex reconstruction. Knowing the drift velocity, the radial coordinate of a particle passing through the detector can be calculated by measuring the drift time of the electron cloud. The azimuthal coordinate ϕ can be accessed via the information which anode has been hit. Figure 4.4 shows a cross-section of an anode. The segmented structure improves the charge sharing between the anodes and therefore the azimuthal resolution of the detector [59].

4.4 Cherenkov Counters

The task of the two Ring Imaging Cherenkov Detectors (RICH1, RICH2) of the CERES spectrometer is the identification of electrons. These detectors take advantage of the Cherenkov radiation to measure the velocity β of the traversing particle. Combined with the knowledge of the particle momentum, β determines its mass.

Whenever charged particles pass through matter they polarize the molecules, which then turn back rapidly to their ground state emitting prompt radiation. If the velocity of the particle exceeds the velocity of light in the medium $v > c/n$, the emitted light forms a coherent wavefront. This so called Cherenkov light is emitted under a constant angle θ_c with respect to the particle trajectory:

$$\theta_c = \arccos\left(\frac{c/n}{v}\right) = \arccos\left(\frac{1}{\beta n}\right) \tag{4.4}$$

The lowest velocity where the emission of Cherenkov radiation is still possible is $v_{th} = c/n$.

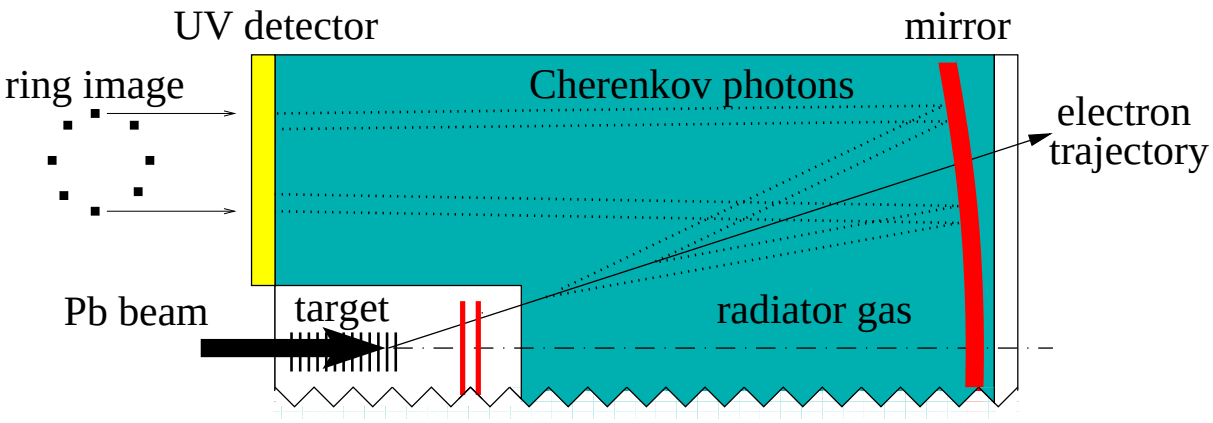

Figure 4.5: **Principle of the RICH detectors.** *Cherenkov photons are emitted under a constant angle to the trajectory of a particle, if its velocity exceeds the velocity of light in the radiator gas. The photons are focused by a mirror onto a ring at the surface of a position-sensitive photon detector. The radius of the ring is a measure for the particle velocity.*

This corresponds to a Lorentz threshold factor of:

$$\gamma_{th} = \frac{1}{\sqrt{1 - \frac{1}{n^2}}} \tag{4.5}$$

The concept of a RICH detector was proposed in 1977 by J. Séguinot and T. Ypsilantis [60] and is illustrated in figure 4.5. The Cherenkov photons, emitted at an angle θ_c by a particle passing the radiator of the detector, are focused by a mirror onto a ring of radius R at the surface of a position-sensitive photon detector. By measuring the ring radius the particle velocity, which is connected with the relativistic Lorentz factor γ, can be determined by:

$$R = R_\infty \sqrt{1 - \left(\frac{\gamma_{th}}{\gamma}\right)^2} \tag{4.6}$$

In this equation R_∞ is the asymptotic radius for particles with $\gamma \gg \gamma_{th}$. It is determined by the focal length f of the mirror and the Lorentz threshold factor:

$$R_\infty = f \cdot \frac{1}{\gamma_{th}} \tag{4.7}$$

The radiator gas used in the RICH detectors of the CERES spectrometer is CH_4 at atmospheric pressure. The high threshold of $\gamma_{th} = 32$ assures that only electrons and positrons emit Cherenkov light, whereas 95% of the hadrons do not produce any signal. Only pions with a momentum exceeding 4.5 GeV/c make an exception to the hadron blindness of the RICH detectors.

The spherical shape of the RICH1 mirror is manufactured out of a carbon fiber composite with a low radiation length of $X/X_0 = 0.4\%$. It is coated with aluminum, known for its high reflectivity in the UV region ($> 85\%$). The RICH2 mirror is a conventional 6 mm glass with a radiation length of $X/X_0 = 4.5\%$ at comparable UV-reflectivity [61].

The position-sensitive UV-detectors located in the focal plane of the mirrors are gas detectors filled with 94% He and 6% CH_4 at atmospheric pressure. To convert the incoming photons to electrons via photoionization TMAE (**T**etrakis-di-**M**ethyl-**A**mino-**E**htylen) vapor is added. It has a low ionization potential of 5.4 eV. The gas is heated to a temperature of 40° to increase the partial pressure of TMAE. At this working temperature the mean free path for photoabsorption is 5 mm. The conversion region of the UV-detectors of 15 mm adds up to a conversion probability of 95%. The electrons emitted after photoabsorption are amplified in an avalanche process. The signals are read out on 53800 individual pads in RICH1 and 48400 pads in RICH2. The pad size is 2.7×2.7 mm^2 in RICH1 and 7.6×7.6 mm^2 in RICH2, respectively. To separate the UV-detectors from the radiator gas of the RICH detectors UV-transparent windows are used (CaF_2 for RICH1 and Quartz for RICH2).

4.5 Time Projection Chamber

The measurement of the particle momentum is accomplished with a cylindrical Time Projection Chamber (TPC), located 3.8 m downstream the target system. Furthermore, particle identification is possible taking advantage of the differential energy loss dE/dx. As mentioned in the introduction of this chapter, the CERES experiment was originally conceived for the measurement of e^+e^- pairs. However, the spectrometer upgrade with the TPC renders the additional possibility to study final hadronic states.

Figure 4.6 shows a schematic view of the CERES TPC. Its sensitive volume is filled with gas. If a charged particle passes through the TPC the gas is ionized. An electric field forces the liberated electrons to drift outwards until they reach a plane of anode wires. In the vicinity of the anode wires the electrons are accelerated and produce secondary ionization in an avalanche process. The electrons are quickly collected by the anode wires and therefore contribute little to the induced signal. The heavier ion clouds remain and expand radially, inducing a signal on the pads, which are connected to the readout electronics.

The CERES TPC has an active length of 2 m and an outer radius of 130 cm. The inner barrel has a radius of 48.6 cm. The TPC is composed of 16 multiwire proportional chambers forming a polygonal structure. The segmented readout pads are arranged in groups of 48 in azimuthal direction on each chamber. Along the z axis the TPC is divided into 20 planes. The $16 \times 48 \times 20 = 15360$ readout channels of the TPC are sampled in 256 time bins, thus allowing a 3-dimensional reconstruction of a particle track.

The electric drift field inside the TPC is radial, pointing from the grounded cathode wires on the readout chambers to the inner barrel, supplied with a high voltage of -30 kV. Both sides of the TPC are closed by 50 μm capton foils with incorporated voltage dividers. The TPC is operated inside an inhomogeneous magnetic field, generated by two opposite-polarity solenoidal coils. The magnetic flux is indicated in figure 4.1 by red dotted lines. In the region between the two coils a field strength of 0.5 T is reached (compare figure 6.1).

In the presence of a magnetic and an electric field, the drift velocity vector $\vec{v}_{drift}$

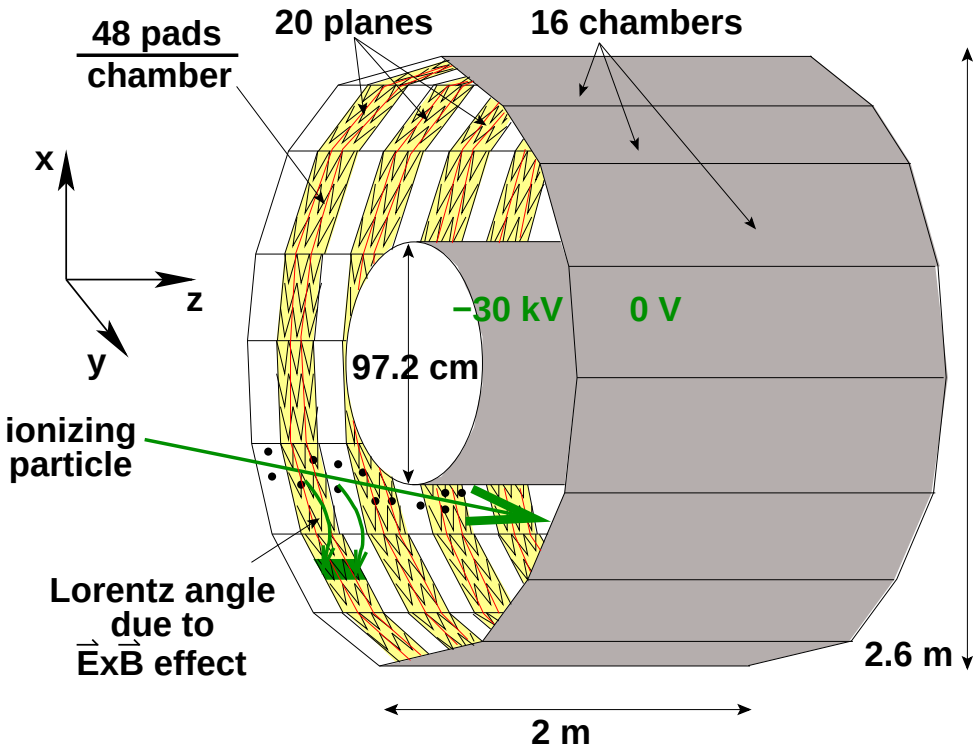

Figure 4.6: **Schematic view of the CERES TPC.** *A charged particle passing the active volume of the TPC ionizes the gas along its trajectory. The electrons drift towards the anode wires on the readout chambers. The angle between the radial electric field $\vec{E}$ and the drift velocity $\vec{v}_{drift}$ is given by the Lorentz angle α_L.*

of the electrons has non-zero components perpendicular to the the electric field vector $\vec{E}$ [62]:

$$\vec{v}_{drift} = \frac{\mu}{1+(\omega\tau)^2}\left(\vec{E} + \omega\tau\frac{\vec{E}\times\vec{B}}{B} + (\omega\tau)^2\frac{(\vec{E}\cdot\vec{B})\vec{B}}{B^2}\right) \tag{4.8}$$

In this equation τ is the mean time between two collisions. The cyclotron frequency ω is given by:

$$\omega\tau = \frac{e}{m}B\tau = B\mu \tag{4.9}$$

where μ is the mobility. It has to be pointed out that the mobility is a function of the electric field, gas composition, pressure, and temperature. As soon as the magnetic and the electric fields are not parallel to each other, the electrons do not follow any more the electric field lines. The angle between the drift velocity $\vec{v}_{drift}$ and the electric field $\vec{E}$ is called Lorentz angle α_L.

The CERES TPC has a large contribution of a magnetic field component perpendicular to the radial electric field, especially towards the edges. If μ, $\vec{E}$ and $\vec{B}$ are known, the drift velocity can be computed. Its value ranges from 0.7 cm/μs to 2.4 cm/μs with a maximal drift time of about 71 μs. However, to minimize uncertainties, the Lorentz angle should be kept small. Thus, a gas composition with low mobility has to be used. Beside this aspect, the radiation length, the number of created electron-ion pairs, the maximal drift time and the diffusion coefficients were taken into account and led to the choice of

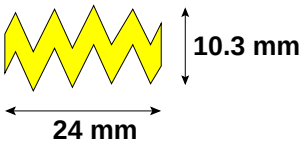

Figure 4.7: **Chevron structure of the cathode pads.** *The chevron structure results in an optimal charge sharing between adjacent pads and in a good linearity of the pad response.*

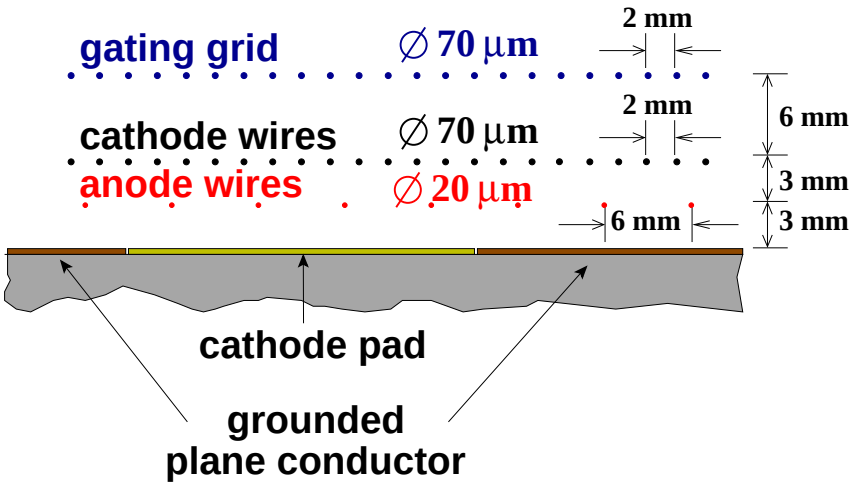

Figure 4.8: **Cross-section of a TPC readout chamber.** *Primary electrons coming from an ionizing particle are amplified in an avalanche process due to the strong electric field in the vicinity of the anode wires. The gating grid is responsible to protect the readout chambers from free charge. It is switched to a transparent mode as soon as a trigger signal has been given.*

a gas mixture of 80% Ne and 20% CO_2 [63].

The pads of the CERES TPC have a chevron-shaped structure, as plotted in figure 4.7. Compared to usual rectangular pads, the chevron shape results in a better charge sharing and linearity of the pad response [63].

The anode wires are strained in azimuthal direction 3 mm above the chamber surface. A cross-section of a chamber is shown in figure 4.8. Thin parallel and equally spaced anode wires are sandwiched between a cathode wire plane and the pads. The anodes are on positive potential of about 1.3 kV. The adjacent cathode wires are grounded. This creates a very strong electric field close to the anode wires where the electrons are multiplied by a factor of 10^4 in an avalanche process. The potential of the gating grid, located 6 mm above the cathode wire plane, is responsible to regulate the passage of electrons and ions. It impedes free charge inside the gas volume, which does not come from particles originating from a nucleus-nucleus collision, to reach the anodes. Secondly, it prevents the ions from floating back into the drift volume. The gating grid is operated at an offset potential of $U_{offset} = -140$ V. In the closed mode an additional bias potential of $U_{bias} = \pm 70$ V is superposed, alternating from wire to wire. This causes a strong inhomogeneous field and the charge is collected at the gating grid. Only after a signal from the trigger the gating grid is switched to a transparent mode at $U_{bias} = 0$ V.

4.6 Coordinate System

All subdetectors use their own specific coordinate system. However, a global polar coordinate system with the origin located in the center of the first Silicon Drift Detector

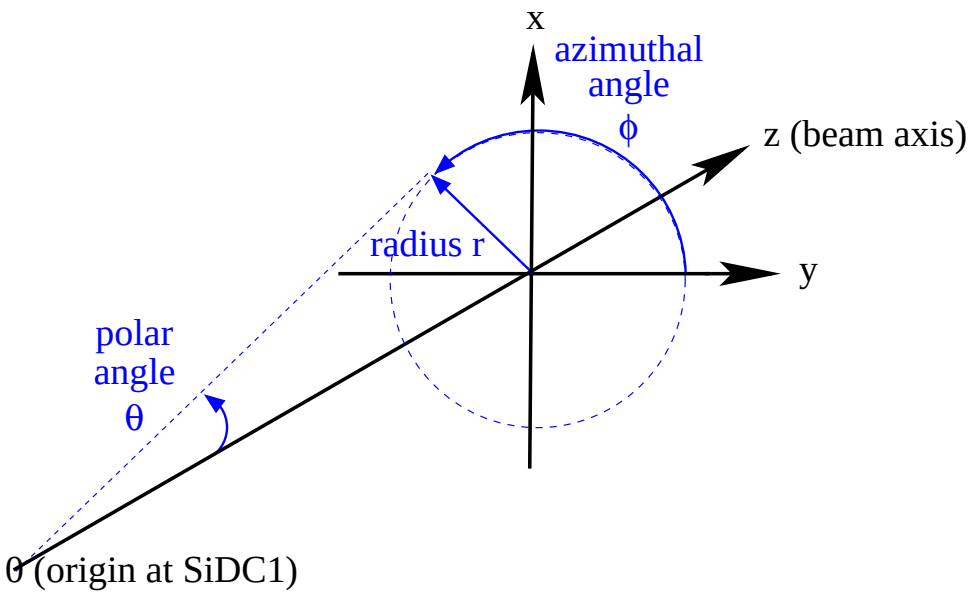

Figure 4.9: **Global coordinate system of the CERES experiment.** *It is a polar coordinate system (z,θ,ϕ) with the origin in the center of the first Silicon Drift Detector SiDC1. The z coordinate is parallel to the beam axis. For secondary particles a right handed Cartesian coordinate system (x,y,z) with origin in the interaction point is used.*

(SiDC1) combines all detectors. It is drawn in figure 4.9. The beam axis coincides with the z coordinate. Therefore each point is defined by its distance z to SiDC1, its polar angle θ, and its azimuthal angle ϕ.

Also frequently used are the so called event coordinates. Their origin is located in the interaction point of each event. For a segmented target, as it is used in the CERES spectrometer, this coordinate system is very convenient. It projects all target disk onto a single one which is specially important for the mixed events technique, described in section 8.3.1.

The polar coordinate system, as it is commonly used in the CERES experiment, is not suitable for the analysis of secondary particles arising from late decays. For this purpose a conversion into Cartesian coordinate is needed.

Chapter 5

Raw Data Reconstruction

This thesis is based on the analysis of data recorded during the beam time in the year 2000. The CERES experiment has taken a large data sample of about $30 \cdot 10^6$ Pb-Au collisions at 158 AGeV/c triggering on the 7% most central collisions. A second sample of $3 \cdot 10^6$ events was collected at 20% centrality. The typical beam intensity was 10^6 ions per burst. Each burst had a duration of 5 s with a 14 s pause in between. The data taking rate was 300-500 events per burst.

The raw data is stored on tape at the CERN computer center. Before being able to perform any physics analysis it has to be transformed into a suitable format. Therefore, the data is decompressed, the pedestals are subtracted, and an automatic calibration is performed. The signals are disentangled to form hits and the hits are combined in a meaningful way to form tracks. And finally, further information like the momentum is retrieved by fitting the curvature of the track in the magnetic field.

This chapter is focused to specific aspects of the data reconstruction, i.e. the hit and track reconstruction procedure in the SiDC detectors and the TPC. It is part of the C++ package COOL (**C**eres **O**bject **O**riented **L**ibrary). Special importance is given to developments in the framework of this thesis. These are the reconstruction of particles originating from late decays and the hit finding strategy in the TPC.

5.1 Reconstruction Procedure in the SiDC Detectors

5.1.1 Hit Finding

The raw data of the SiDC detectors consist of 6 bit nonlinear amplitudes on 360 anodes in azimuthal direction and 256 time bins in radial direction. Thus, a SiDC event consists of a grid of $360 \times 256 = 92160$ pixels. Figure 5.1 shows an example of an event display of SiDC1. A signature of a charged particle passing the detector and depositing energy is called a hit. It is a cluster of typically 8-12 time bins on 2-3 anodes.

The pattern recognition starts from a given pixel and searches for neighbors with non-zero amplitude which are not yet assigned to another hit. All pixels fulfilling these criteria are grouped together in a cluster. Also non-functioning (dead) anodes, if present,

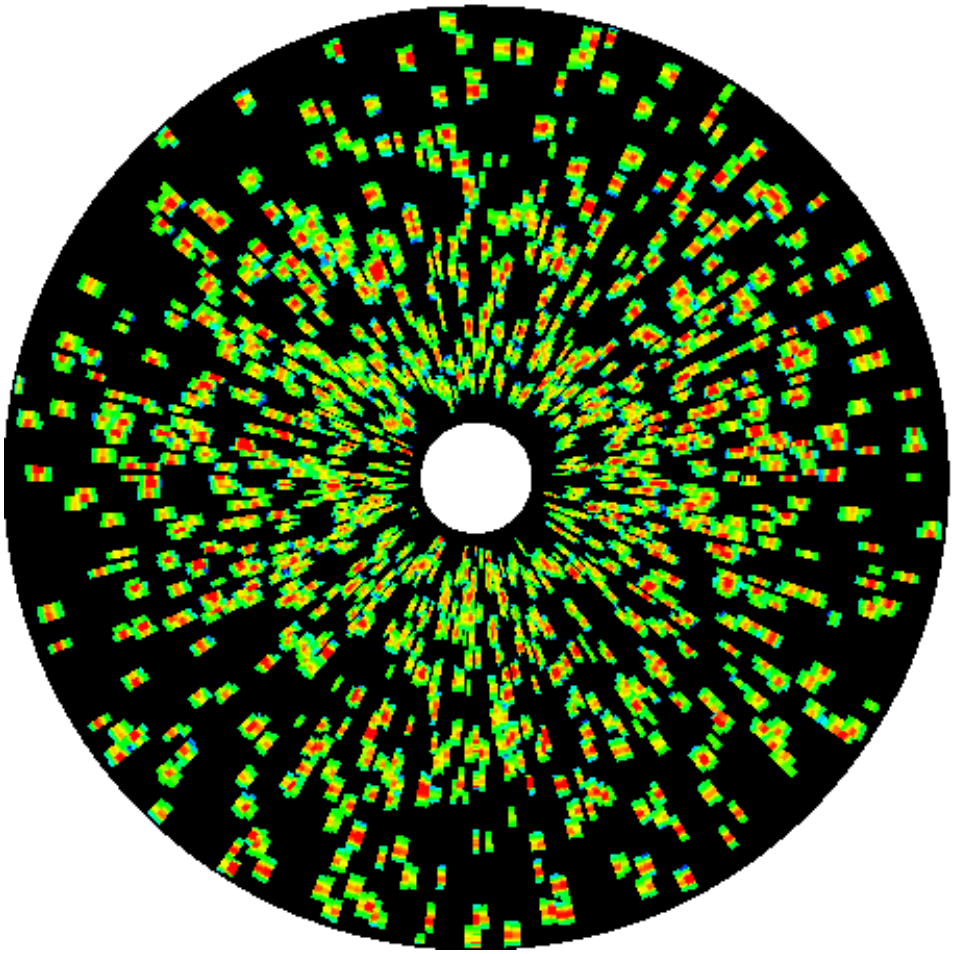

Figure 5.1: **Event display of SiDC1.** *The SiDC plane is divided into 360 anodes and 256 time bins. The amplitude height is displayed in a color code, going from the lowest values in blue to the highest in red.*

are considered to prevent additional cluster formation.

Each cluster is then divided into anode slices. These time pulses are scanned for local maxima and minima in the amplitude profile. If the amplitude of a minimum is less than 10% of one of the adjacent maxima, the pulse becomes a candidate to be split into two parts. The final decision about the splitting is based on several criteria concerning the width and the skewness [13].

The time position of a maximum is determined by calculating the center of gravity. Only in the cases where one or more time bins are in saturation, it is determined by fitting a Gaussian function. Overlapping pulses are fitted with a double-Gaussian. Within a window of ± 7 time bins the pulses are combined in anode direction to hits. Pulses with three or less time bins are discarded in this process.

If more than two time pulses are combined to a hit candidate, the amplitude profiles are scanned for a minimum in anode direction. If such a minimum is found the hit is split in two parts. The position of the hit in anode direction is obtained by calculating the center of gravity. In cases where a pixel has reached saturation a Gaussian regression is

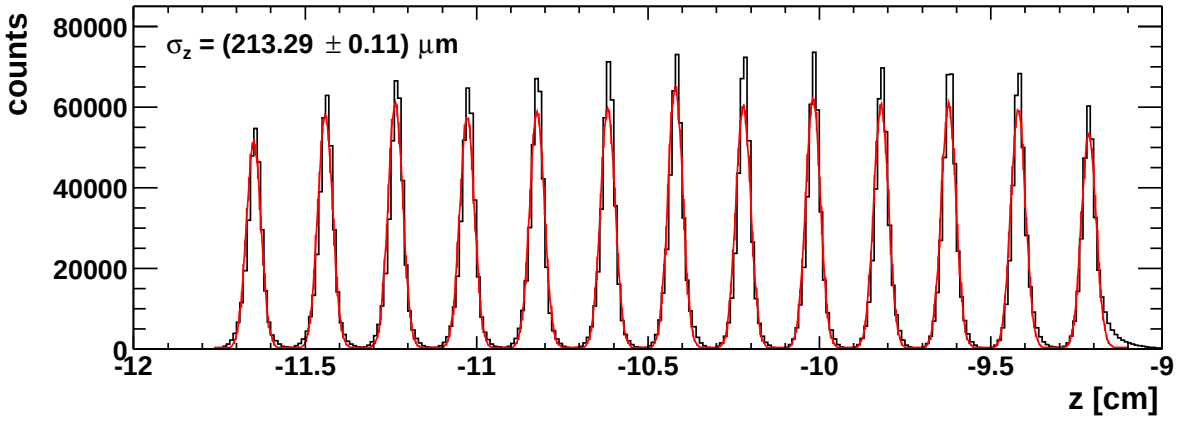

Figure 5.2: **Reconstructed target resolution.** *The 13 target discs are well resolved along the beam axis. The thickness of each gold disc of 25 μm is negligible as compared to the resolution.*

used for this purpose.

5.1.2 Track and Vertex Reconstruction

Once the hits in the two SiDC detectors are reconstructed a first estimate of the vertex position can be obtained using a robust vertex fitting approach [64]. It has the advantage of being an order of magnitude faster than a standard minimization package, at comparable accuracy. In this method each hit in SiDC1 is combined with each hit in SiDC2 into a straight track segment. Afterwards, the residual of the SiDC1 hit from the line through an assumed vertex and the SiDC2 hit is calculated. The same is done for the hit in SiDC2. The starting value of the vertex position is in the middle of the target region. The sum of the squared residuals are minimized using Tukey's bi-squared weights [65] to account for the fact that the data is highly contaminated with background. In this way a better estimate for the vertex position is obtained. The procedure is repeated until it converges after approximately five iterations. The reconstructed vertex distribution is shown in figure 5.2. The 13 target discs are resolved with an average resolution of about $\sigma_z \approx 210$ μm along the beam axis.

The knowledge of the vertex position is needed for the tracking strategy in the SiDC detectors. In the standard method used in the CERES experiment a SiDC track segment is created by searching for the closest SiDC2 hit in a narrow matching window around the hit in SiDC1. The matching window is defined in event coordinates. Thus, preferentially tracks pointing to the vertex are reconstructed.

For the special demands of the K^0_S and $\overline{D}^0$ analysis described in the chapters 8 and 9 this strategy had to be modified in order to enhance the number of tracks from secondary decays. To avoid the bias due to the fitted vertex the hits in SiDC2 are now projected onto the SiDC1 plane. In this projection all SiDC2 hits in the vicinity of a given SiDC1

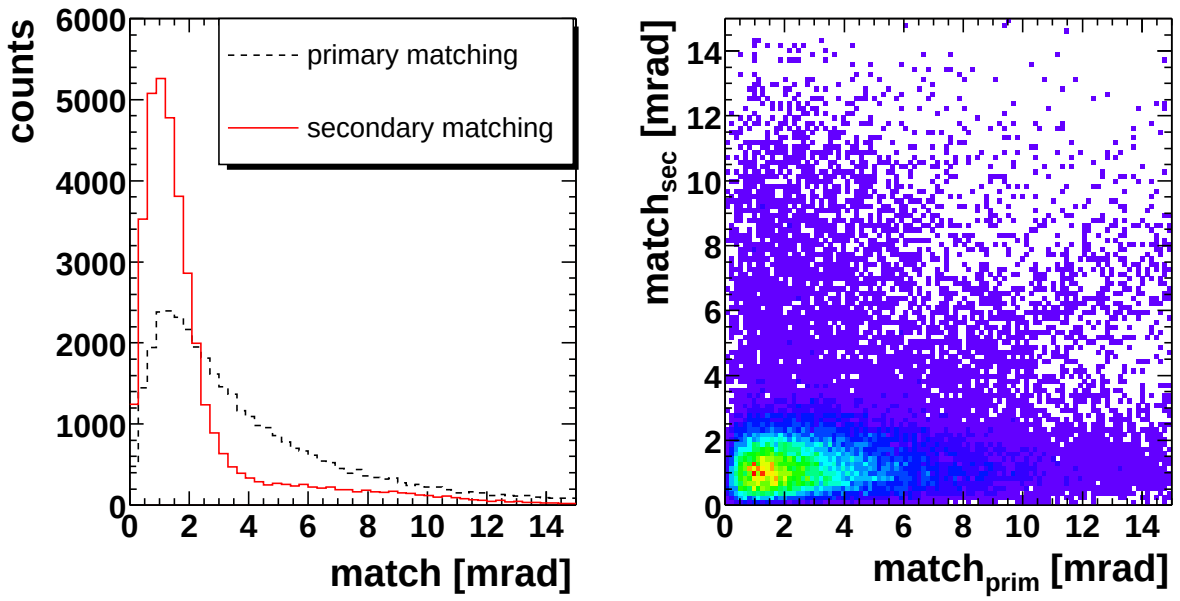

Figure 5.3: **Primary versus secondary matching.** *The comparison is based on a clean Monte Carlo sample of daughter particles from D^+ decays. The primary matching distribution is broad because it uses mean angles for the pointing. The secondary matching is based on local angles and thus yields better results for tracks originating from late decays.*

hit are accepted if they fulfill the following distance criteria:

$$d = \frac{\Delta r^2}{\sigma_r^2} + \frac{\Delta \phi^2}{\sigma_\phi^2} < 1 \tag{5.1}$$

In this equation Δr and $\Delta\phi$ are the radial and azimuthal distances between the SiDC1 hit and the projected SiDC2 hit. The values for σ_r and σ_ϕ define the cutoff and are given by 0.09 cm and 0.05 rad, respectively. The cutoff is tuned such that the amount of additional SiDC track segments does not exceed 30%.

Another change concerns the matching between a SiDC and a TPC track segment. The originally matching procedure favored tracks coming from the targets. It was defined using the average angles ϕ_{mean} and θ_{mean} of the two SiDC hits in order to improve the pointing resolution of the SiDC track segment to the TPC. This procedure is not applicable for tracks originating from late decays. In this case the two SiDC hits are directly connected with a straight line and extrapolated in the field free region to the plane of the RICH2 mirror. Also the TPC track segment is extrapolated to the RICH2 mirror, but now taking the magnetic fringe field into account. The RICH2 mirror is the main source of multiple scattering in the experiment and therefore a suitable place for the matching between the two track segments. A global track is obtained if the matching

$$match = \sqrt{(\Delta\theta)^2 + (\Delta\phi \cdot \sin(\theta_{SiDC}))^2} \tag{5.2}$$

between the two track segments is minimal as compared to other combinations. The azimuthal angle difference in this equation is defined as $\Delta\phi = \phi_{SiDC} - \phi_{TPC}$, and similar for $\Delta\theta$.

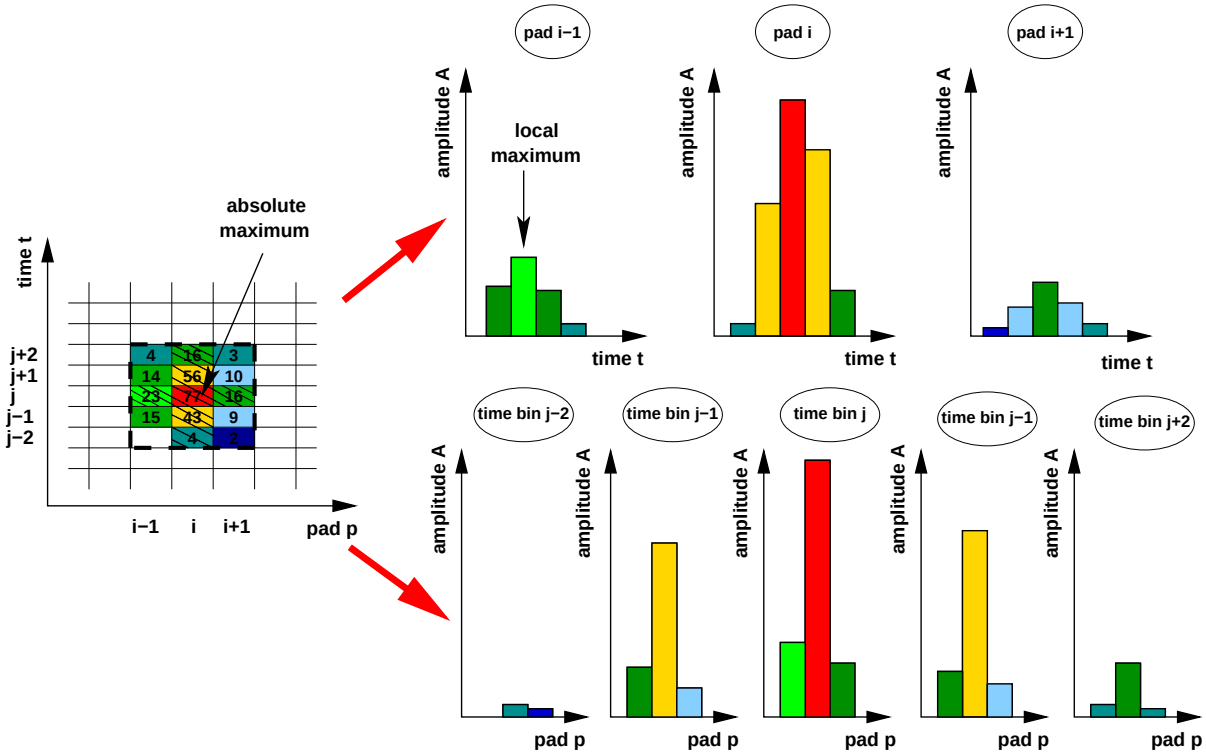

Figure 5.4: **Scheme of the hit finding procedure in the TPC.** *The pixel grid is searched for local maxima in time direction, followed by a search in pad direction. If a pixel is flagged as a local maximum in both coordinates it become an absolute maximum. The hit is defined as an area of 15 pixels around the absolute maximum.*

The two different matching procedures are optimized for either primary or secondary tracks, and will therefore be denominated as primary or secondary matching, respectively. The comparison between the two matching procedures, applied to a clean Monte Carlo sample of D^+ mesons, is shown in figure 5.3. The D^+ meson has a decay length of $c\tau = 311.8\ \mu$m [66] and thus decays in the vicinity of the targets. Nevertheless, the difference between the two matching procedures is remarkable. In spite of the fact that the secondary matching has a limited resolution, the figure shows that the pointing of the primary matching is even worse and might lead to a wrong track segment combination. The new matching procedure is implemented in the CERES code such, that the user can chose between primary and secondary matching, depending on the needs of his physics analysis.

5.2 Reconstruction Procedure in the TPC

5.2.1 Hit Finding

The TPC is divided into 20 planes, each of them containing 768 pads in azimuthal direction and 256 time bins in radial direction. Thus, the overall grid is composed of $20 \times 756 \times 256 \approx 4$ million pixels. The pixel contains the linear amplitude information

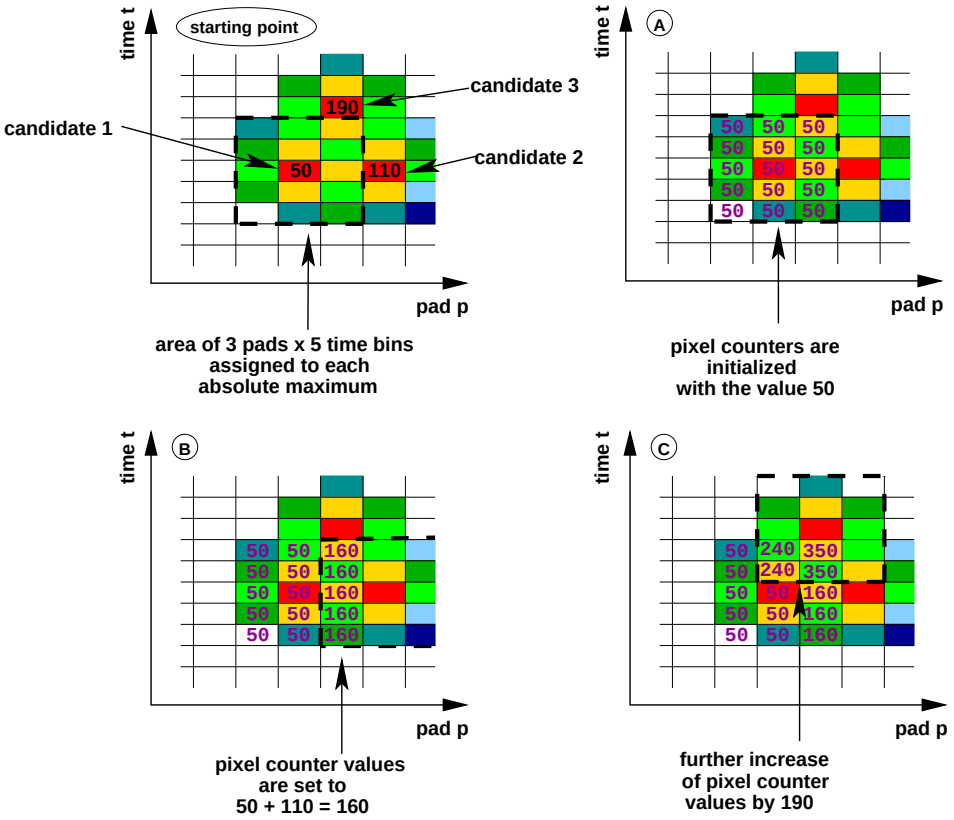

Figure 5.5: **Reconstruction of overlapping hits in the TPC.** *A counter variable memorizes the value of the absolute maximum of the regarded hit. If a pixel is assigned to several hits, the counter variable is augmented by the corresponding absolute maxima of the overlapping neighbors.*

from an 8 bit ADC.

The pixel grid of the TPC is scanned for hits individually in each plane. A schematic overview of the procedure is drawn in figure 5.4. In a first loop local maxima are searched in time direction for a given pad p. The same is repeated in pad direction for a given time bin t. The combination of both informations finally yields the position of absolute maxima. These are pixels which are flagged as a local maximum in time as well as in pad direction. They provide a first guess of the true hit position.

The search for local maxima might yield wrong results if several adjacent pixels in a time bin row have saturated amplitudes. As compromise the middle pixel of the saturated cluster is chosen as local maximum. For instance, if three pixels have saturated amplitudes $A_0 = A_1 = A_2$, the pixel with A_1 is flagged. A further problem appears if the number of adjacent saturated amplitudes is even. In this case the non saturated neighborhood is used for the decision. For instance, if two pixels have saturated amplitudes $A_1 = A_2$, and the amplitude A_3 is higher than A_0, than the pixel with A_2 is flagged as local maximum.

The area assigned to a hit is composed of 5 time bins and 3 pads. These 15 pixels are arranged around the absolute maximum. Hits containing only one time bin row are

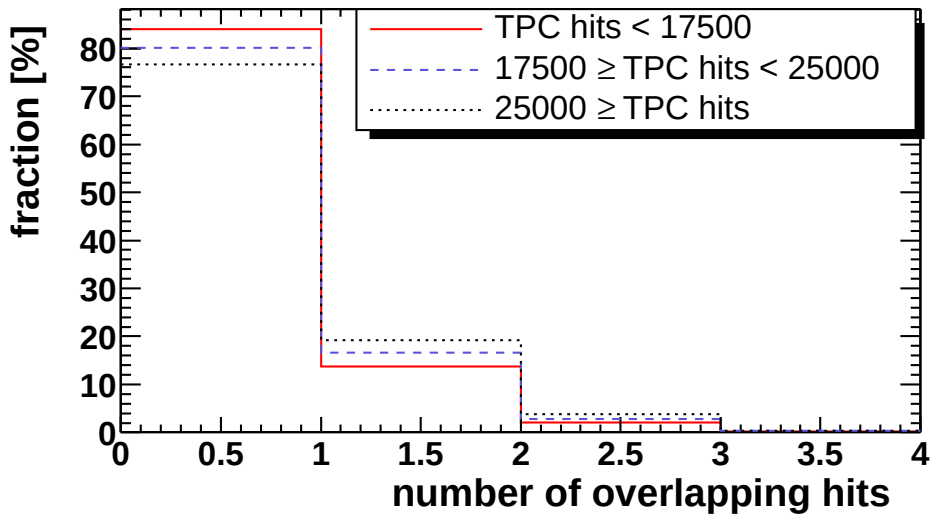

Figure 5.6: **Number of overlapping hits.** *The three different lines correspond to different multiplicity ranges. For the distribution of the hit multiplicity in the TPC compare figure 6.15.*

discarded. The same applies for one pad clusters, with the exception of a hit being localized at the edge of a chamber or adjacent to a dead front-end-board.

If a hit is isolated, its position in pad and time coordinates is given by the center of gravity comprising the area of the 15 pixels. However, many times the area assigned to a hit overlaps with other hit areas and the simple computation of the center of gravity is falsified. This problem is solved by allocating a counter variable f_i to each pixel i. It memorizes the amplitude of the absolute local maximum of the regarded hit. If a pixel can also be assigned to areas belonging to other hits, the counter f_i is augmented by the values of their absolute maxima. The operation method is clarified in figure 5.5. In this way it becomes possible to weight each pixel individually by the ratio of the absolute maximum A_{max} of the regarded hit and the counter variable f_i. The center of gravity is defined as

$$\overline{t} = \frac{\sum_i A_i \cdot \frac{A_{max}}{f_i} \cdot t_i}{\sum_i A_i} \quad \text{and} \tag{5.3}$$

$$\overline{p} = \frac{\sum_i A_i \cdot \frac{A_{max}}{f_i} \cdot p_i}{\sum_i A_i}$$

for the time and pad coordinates, respectively.

The information about the number of overlapping hits is stored. If the overlapping factor is zero the hit is isolated. The distribution of the overlapping factor is shown in figure 5.6 for different hit multiplicities in the TPC. About 80% of the hits are isolated, 17% are overlapping with one other hit and 3% are overlapping with two other hits. The fraction of hits overlapping with more than two hits is in the per mill range. The number of overlapping hits increases with the hit multiplicity in the TPC, though the effect is small.

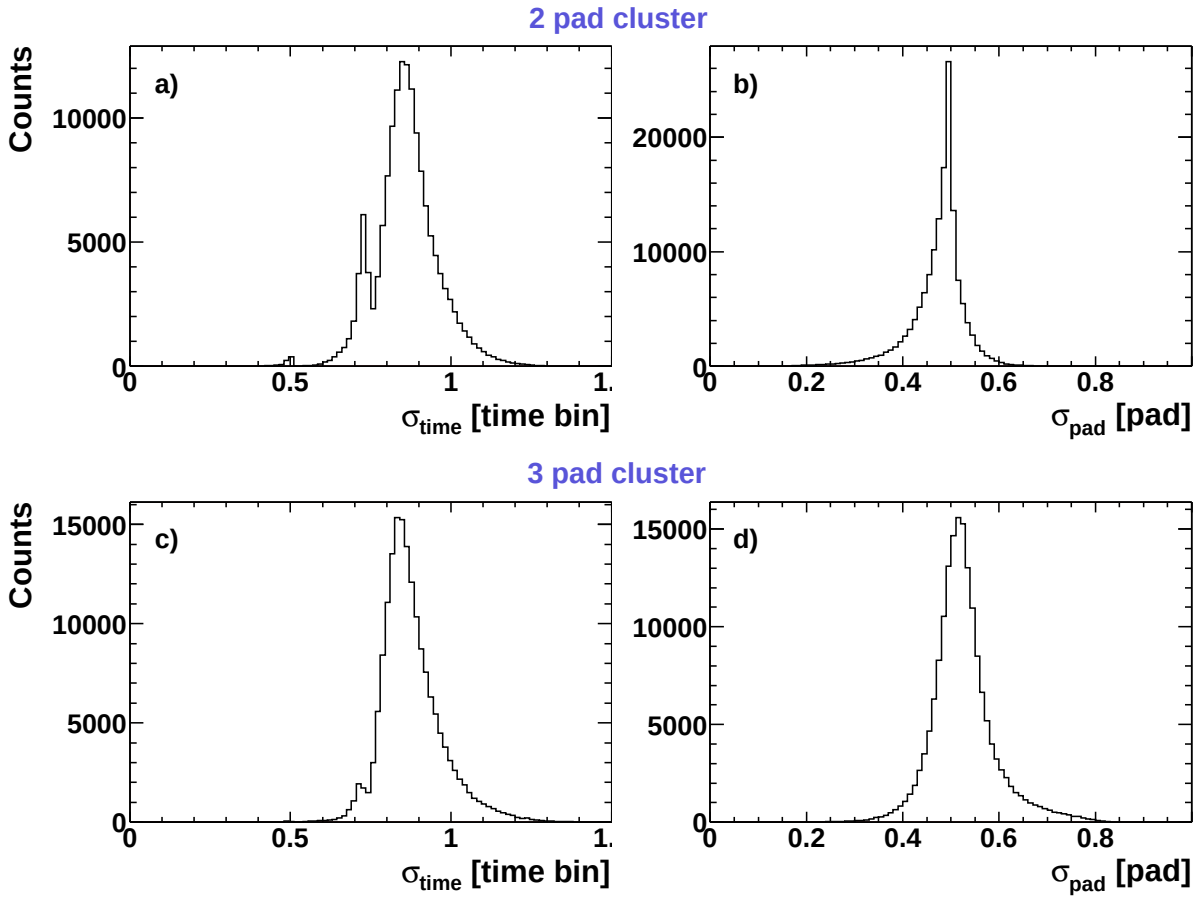

Figure 5.7: **Time and pad width distribution.** *Figures a) and c) show the distribution of the hit width expressed in units of time bins for 2 and 3 pad clusters, respectively. The same is shown in figures b) and d) in units of pads. Only isolated hits belonging to tracks are taken into account.*

Another useful quantity is the hit width in terms of time bins and pads. It is defined as:

$$\sigma_{time} = \sqrt{\overline{t^2} - \overline{t}^2} \quad \text{and} \quad \sigma_{pad} = \sqrt{\overline{p^2} - \overline{p}^2}. \tag{5.4}$$

Figure 5.7 shows the distribution of σ_{time} and σ_{pad} for isolated hits belonging to tracks. Three peaks are visible in the σ_{time} distribution. The tiniest one is at a value of 0.5 corresponding to half a time bin. It can be attributed to hits allocating only two time bin rows. A second peak can be seen at about 0.7. These are mostly hits which are well situated in an area containing three time bin rows. The rest of the cases belong to the main peak localized at 0.85. The σ_{pad} distribution peaks at a value of 0.5 regardless of the hit being a 2 or a 3 pad cluster. For the 2 pad clusters the charge is distributed almost equally over the two pads, while for a 3 pad cluster the bulk of the charge is localized on the center pad. Conspicuous is the long tail on the right hand side of the 3 pad cluster distribution. Here the contribution of unresolved double or even triple hits becomes important. This issue will be readdressed in section 6.5.

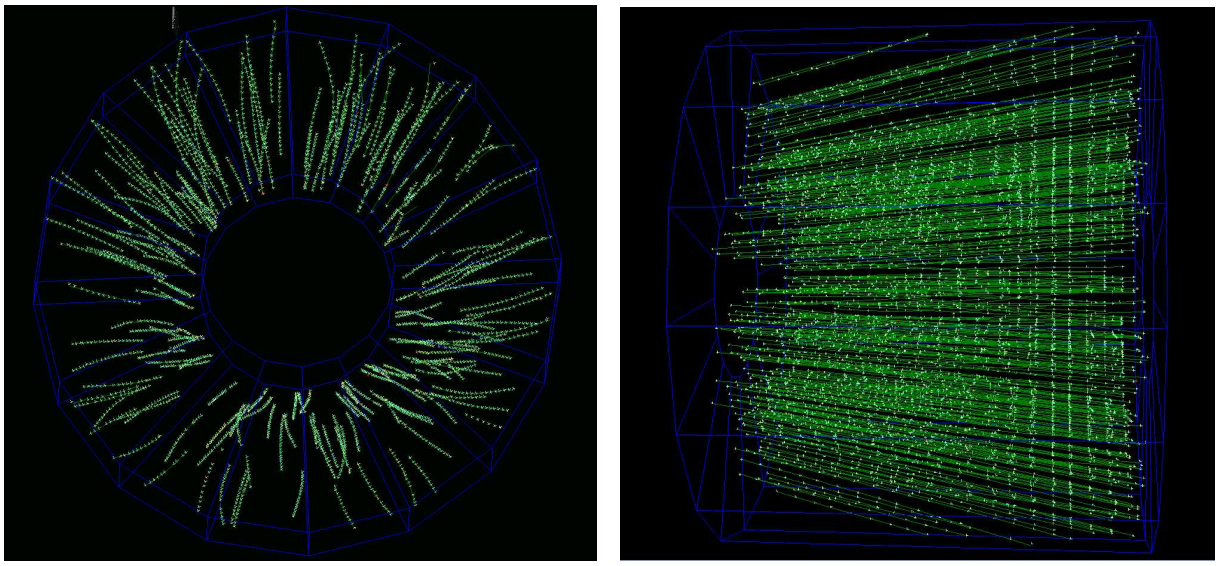

Figure 5.8: **Event display of the TPC.** *The left plot shows a front view of the TPC, the right plot the corresponding sight view. The reconstructed hits are connected to TPC track segments, represented as green lines.*

The detector specific hit coordinates $(pad, time, plane)$ are transformed to the spacial coordinates (x, y, z) with the help of look-up tables. This transformation contains the information about the transport process of the charged clusters in the electric and magnetic field inside the TPC. Furthermore, many calibration aspects enter already at this stage. The calibration of the TPC is described in detail in chapter 6.

5.2.2 Track Finding

The next task is to combine the reconstructed hits in the TPC to a track segment. The maximal number of hits per track is given by the 20 planes in the TPC. The minimal number is limited to 6 hits in order to reduce the contribution of deficient or fake tracks.

The tracking starts from a hit in one of the middle planes in the TPC. This hit is combined with its four closest neighbors in the two upstream and two downstream planes. These hits are used to determine the sign of the track curvature in azimuthal direction. The information is used to define a narrow window in which further hits are searched. The ϕ position of the next hit is predicted by a linear extrapolation of the deflection obtained from the previous hits. The procedure stops if no further hit is found. In order to find hits which are still missing, a second order polynomial fit with Tukey weights [65] is performed in the next step for the prediction. This is done in several iterations until no further hit is found. Special treatment is required for low momentum (soft) tracks. In this case a correction is applied to the prediction of the next hit. The correction depends on the curvature of the track and the z position of the next point. The result of the track finding procedure in the TPC is shown in figure 5.8. More details can be found in [67].

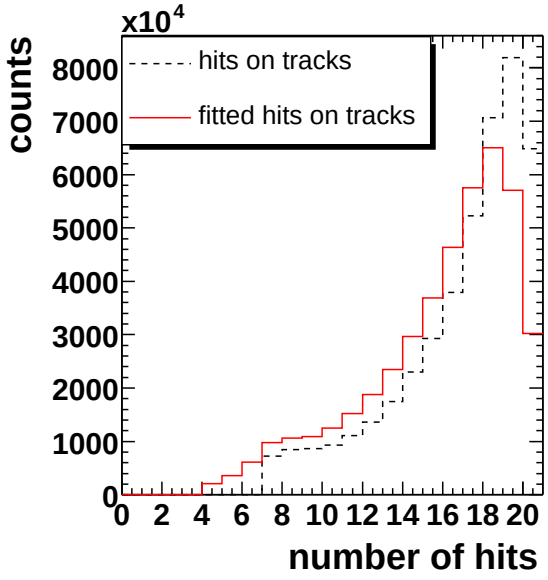

Figure 5.9: **Number of hits per track and fitted hits per track.** *The comparison of the two distributions shows that in average one hit is excluded from the track fit.*

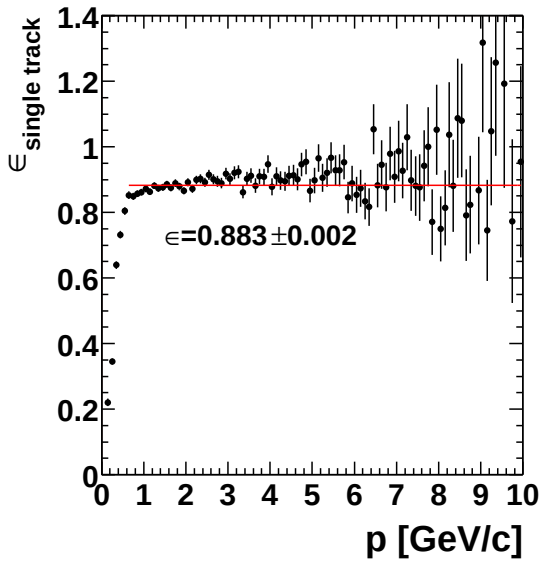

Figure 5.10: **Single track efficiency of TPC track segments.** *The single track efficiency is determined from an overlay Monte Carlo simulation.*

5.2.3 Track Fitting

The magnetic field in the TPC is very inhomogeneous and an analytical description of a trajectory is not possible. This problem is handled by using reference tables for the track fit in the ϕ-z and r-z planes. The reference tables contain the TPC hit coordinates of Monte Carlo tracks from a GEANT simulation [68] of the CERES experiment. The Monte Carlo tracks are generated in steps of 32 different ϕ angles in the range $-\pi < \phi < \pi$, 18 different η angles in the range $2.05 < \eta < 2.95$ and 8 different momentum values in the range $-2 < q/p < 2$ $(\mathrm{GeV/c})^{-1}$, where q is the charge of the simulated particle [69]. The track segments in the TPC are fitted with a two-parameter fit assuming that the tracks come from the vertex, and also with a three-parameter fit taking into account multiple scattering which happens mainly in the RICH2 mirror. After several iterations, hits with large residuals $\Delta r > 0.4$ cm and $r\Delta\phi > 0.2$ cm are excluded from the fit.

The distribution of the number of hits per track and fitted hits per track is plotted in figure 5.9 for the same number of events. The average number of hits per track is 16.5. The distribution peaks at a value of 19 hits. Once the track is fitted, in average one hit is excluded. The mean value of fitted hits per track is 15.3, the most probable value is 18 hits. The single track efficiency of TPC track segments is plotted in figure 5.10 as a function of momentum. The efficiency drops steeply for tracks with a momentum smaller than 0.6 GeV/c. Tracks with higher momentum are reconstructed with an efficiency of approximately 90%. It has to be mentioned that about 2% of the efficiency loss can be assigned to a row of dead front-end-boards in chamber 15 in all 20 planes which were disabled during the beam time in 2000.

In a first order approximation it is assumed that the track is only deflected in

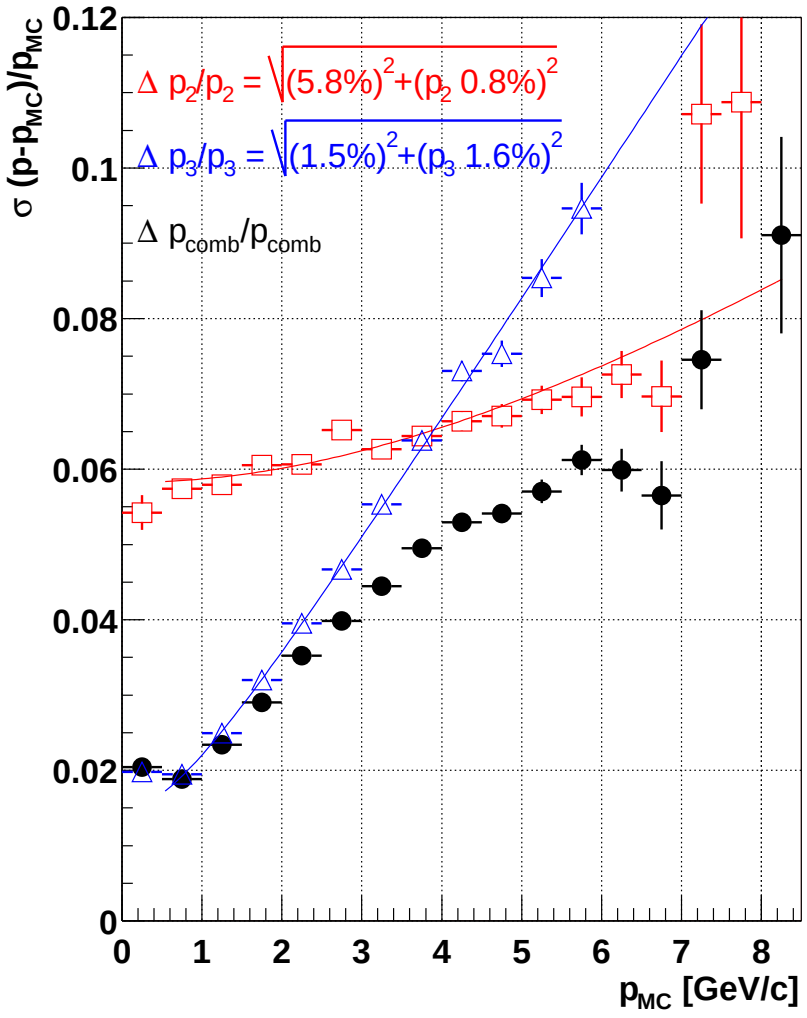

Figure 5.11: **Momentum Resolution.** *The momentum resolution is determined from an overlay Monte Carlo sample. Red squares are used for the two-parameter fit, blue triangle for the three-parameter fit. The black circles show the result for the combined momentum fit, which include the positive aspects of both.*

azimuthal direction. This allows to determine the polar angle θ from a straight line fit in the r-z plane. In the next step the track is fitted in the ϕ-z plane using the hits of the reference tracks for the given θ angle. The momentum of the track is determined from the deflection in ϕ-direction. The deflection in θ-direction caused by a second order field effect is considered by applying a small correction. In addition to the two-parameter fit, the three-parameter fit allows an azimuthal inclination of the track already at the entrance of the TPC.

The three-parameter fit yields an optimal result for low momentum tracks which often suffer multiple scattering. In contrast, high momentum tracks are better described by a two-parameter fit due to the additional vertex constraint. This is clearly seen in figure 5.11 which shows the momentum resolution as a function of the momentum. To exploit the positive aspect of both, a weighted combination is used. The combined momentum p_{comb}

is given by

$$p_{comb} = \frac{\frac{p_2}{\sigma_2^2} + \frac{p_3}{\sigma_3^2}}{\frac{1}{\sigma_2^2} + \frac{1}{\sigma_3^2}}, \tag{5.5}$$

where p_2 and p_3 denote the two-parameter and three-parameter fit, respectively, and $\sigma_2 = \Delta p_2/p_2$ and $\sigma_3 = \Delta p_3/p_3$ the corresponding resolution.

The relative momentum resolution is determined by the resolution of the detector and multiple scattering in the detector material [70]:

$$\left(\frac{\Delta p}{p}\right)^2 = \left(\frac{\Delta p}{p}\right)^2_{det} + \left(\frac{\Delta p}{p}\right)^2_{scat} \tag{5.6}$$

with

$$\left(\frac{\Delta p}{p}\right)_{det} \propto p \quad \text{and} \quad \left(\frac{\Delta p}{p}\right)_{scat} \propto \frac{1}{B}\sqrt{\frac{1}{L \cdot X_0}} = const. \tag{5.7}$$

Here L denotes the measured track length, X_0 is the radiation length, and B is the magnitude of the magnetic field. The multiple scattering term is constant and influences the resolution of low momentum tracks. The detector resolution deteriorates with momentum because the relative error of the momentum fit is smaller for large track deflections than for small ones. This term determines the momentum resolution of high momentum tracks. The relative momentum resolution of the TPC, as obtained from the combined momentum fit, is given by:

$$\frac{\Delta p}{p} = \sqrt{(1\% \cdot p)^2 + (2\%)^2}. \tag{5.8}$$

Chapter 6

Calibration of the CERES TPC

The CERES TPC is exceptional in terms of its radial electric field (see figure 4.1). The readout system is therefore not located at the end plates as for a usual TPC, but around the outer barrel. The magnetic field inside the CERES TPC is inhomogeneous to be almost parallel to the course of the tracks inside the spectrometer, except for the part at which the deflections of the tracks occur. Due to this complex field configuration the calibration of the CERES TPC poses a great challenge.

The different steps of the calibration are described in each section of this chapter. It has to be pointed out that most of the steps are not independent from each other and have to be determined after previous calibration steps are applied.

6.1 Electric and Magnetic Field and Mobility Calibration

The magnetic field of the upgraded CERES experiment is calculated with the POISSON program and shown in figure 6.1. The radial and longitudinal components B_r and B_z change as a function of r and z. The magnetic field has been measured before the installation of the TPC in the experimental area. The measurement deviates from azimuthal symmetry by few percent compared to the nominal calculation. The deviations are included as correction in the field map [67].

The electric field is predominantly radial with $E_r \sim 1/r$. Deviations from the radial symmetry occur due to the polygonal shape of the TPC. Furthermore, a small longitudinal component appears at both end plates. The electric field is calculated with a custom program based on the relaxation method. The exact knowledge of the field cage resistors, of field distortions caused by displaced chambers, and the leakage of the amplification field through the cathode wire plane is included in the calculation [12, 71].

The electron mobility μ depends on the electric field, pressure, gas composition, and temperature. The dependence on the electric field is calibrated using so called laser events in absence of a magnetic field [72]. For this purpose UV light of $\lambda = 266$ nm from a Nd:YAG laser was sent into the TPC, parallel to its axis and at different radii,

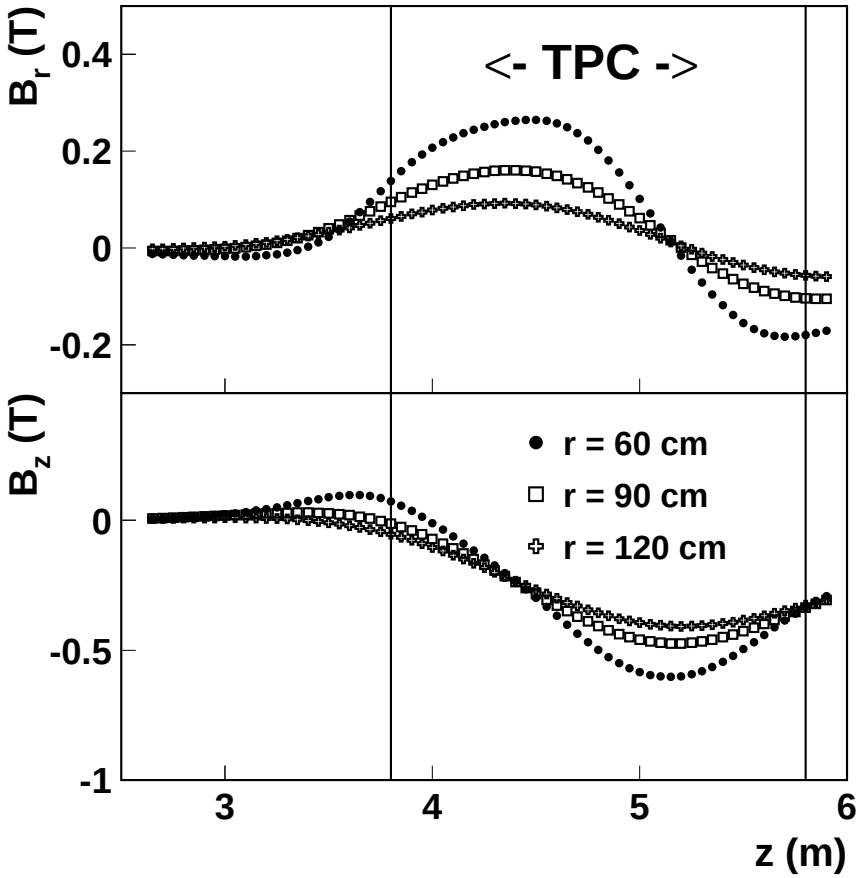

Figure 6.1: **Magnetic field in the TPC.** *The plots show the radial and longitudinal magnetic field components B_r and B_z as a function of z for different radii r. The region of the TPC from $z = 381.15$ m (plane 0) to $z = 572.55$ m (plane 19) is marked with two vertical lines. A magnetic fringe field is also present outside the TPC, starting to be negligible upstream the RICH2 mirror at a position $z = 329.73$ m.*

using a mirror system at the backplate of the TPC. The position of each laser ray was monitored with position sensitive diodes placed behind the semi-transparent mirrors. The estimated resolution of the measured laser ray position is $dr = 0.25$ mm and $rd\phi = 0.5$ mrad. In figure 6.2 an example of such a laser event can be seen. For a given set of gas parameters the reconstructed track position is compared to its nominal position known from the diodes. The mobility is adapted iteratively until both positions agree.

A further constraint is given by the position of the inner cylinder at a radius of $r = 486$ mm. The signal from the inner cylinder comes from photo electrons knocked out by UV stray light which falls onto the aluminum material. If no proper calibration is applied, this signal appears as semicircles, as can be seen in figure 6.2. It reflects the polygonal shape of the TPC due to the fact that the drift paths for electrons become longer and the drift velocities become smaller towards the edges of a chamber.

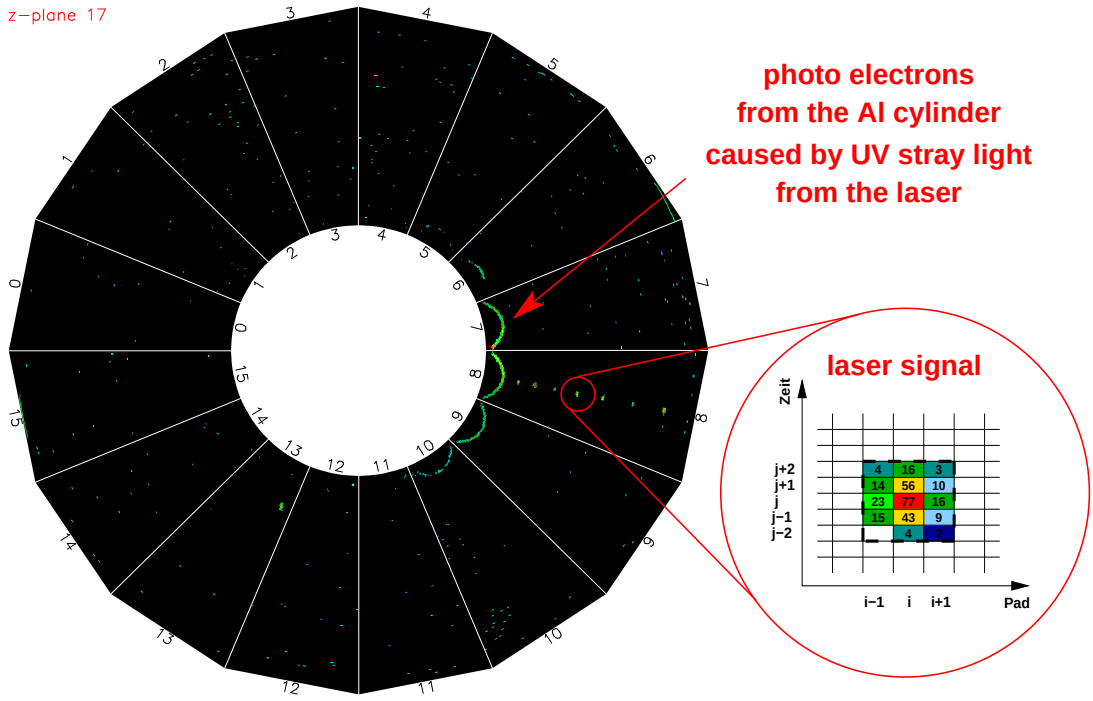

Figure 6.2: **Laser event in the TPC.** *The figure shows a display of plane 17 of the TPC for a laser event. The reconstructed hits in chamber 8 correspond to the radii 700, 800, 900, 1000, 1100 and 1200 mm. The semicircles at the inner cylinder are caused by photo electrons from UV stray light of the laser. This periodic structure reflects the polygonal shape of the TPC.*

The pressure, gas composition, and temperature were monitored during the beam time with the slow control system of the experiment as shown in figure 6.3. The data is divided in calibration units of roughly one hour. For each calibration unit the relative change of the mobility due to outside influences is calculated with the MAGBOLTZ program [73]. The transformation from detector specific coordinates (*plane*,*time*,*pad*) to Cartesian coordinates (x,y,z) is done via the drift velocity $\vec{v}_{drift}$ using a fourth-order Runge-Kutta method. The drift velocity is determined with equation (4.8). A higher precision is achieved using the drift option in MAGBOLTZ, but the computation is time consuming. Therefore, the drift option is only used to compute $\vec{v}_{drift}$ in a wide meshed grid. The components of the drift velocity from equation (4.8) parallel to the $\vec{E}$ and parallel to $(\vec{E} \times \vec{B})$ are then corrected to account for the obtained differences.

At last the information about the maximum drift time t_{drift}^{max} is required for the coordinate transformation. This quantity is extracted from the edge of the average radius distribution of the hits from the middle 16 pads of planes 9 and 10 using the drift velocity $\vec{v}_{drift}$. t_{drift}^{max} is determined for each calibration unit to account for different conditions in the TPC over the beam time [74].

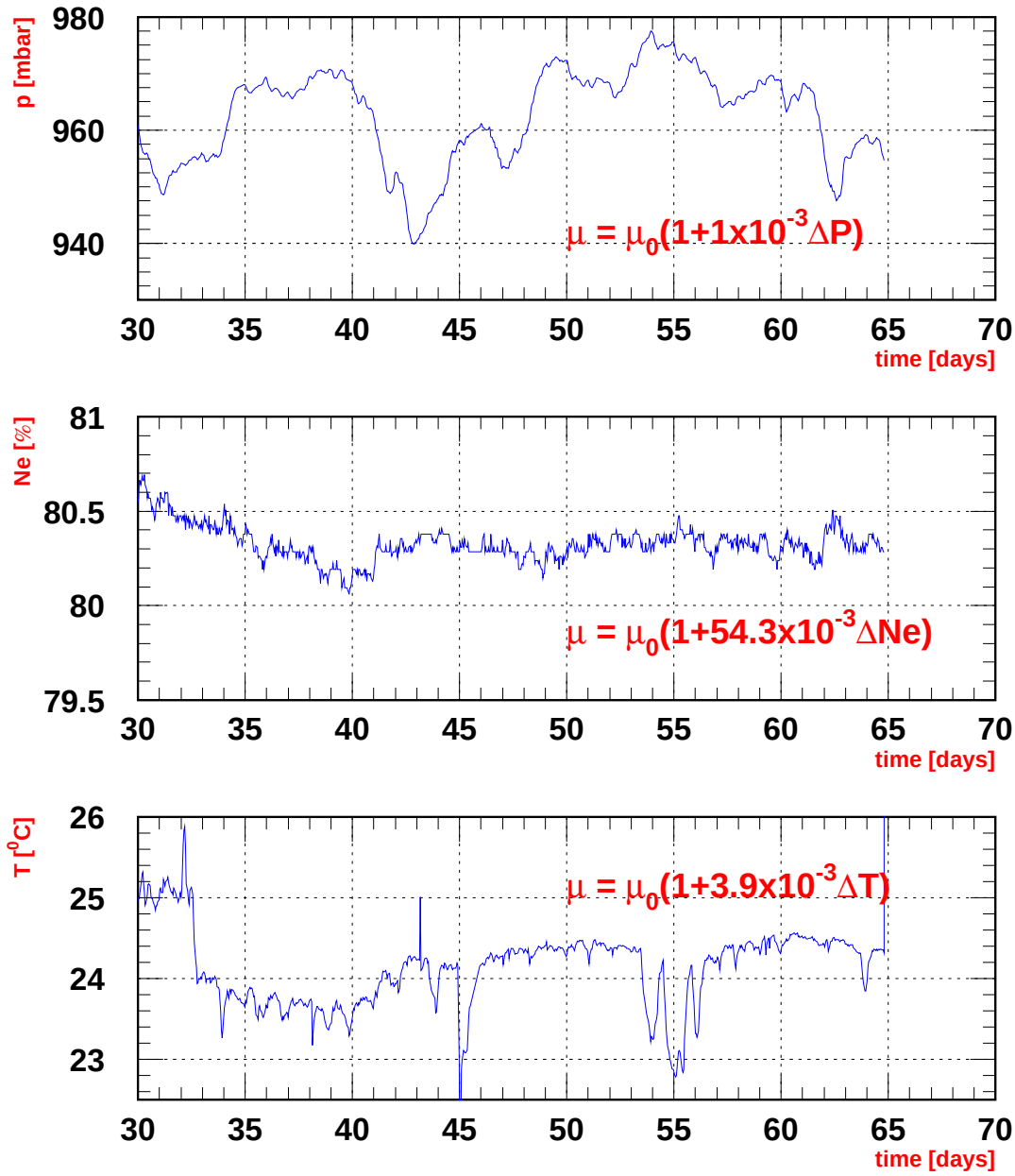

Figure 6.3: **Slow control.** *The slow control of the experiment monitored the pressure, gas composition, and temperature during the beam time. The changes of the nominal mobility value due to outside influences are in the percent range.*

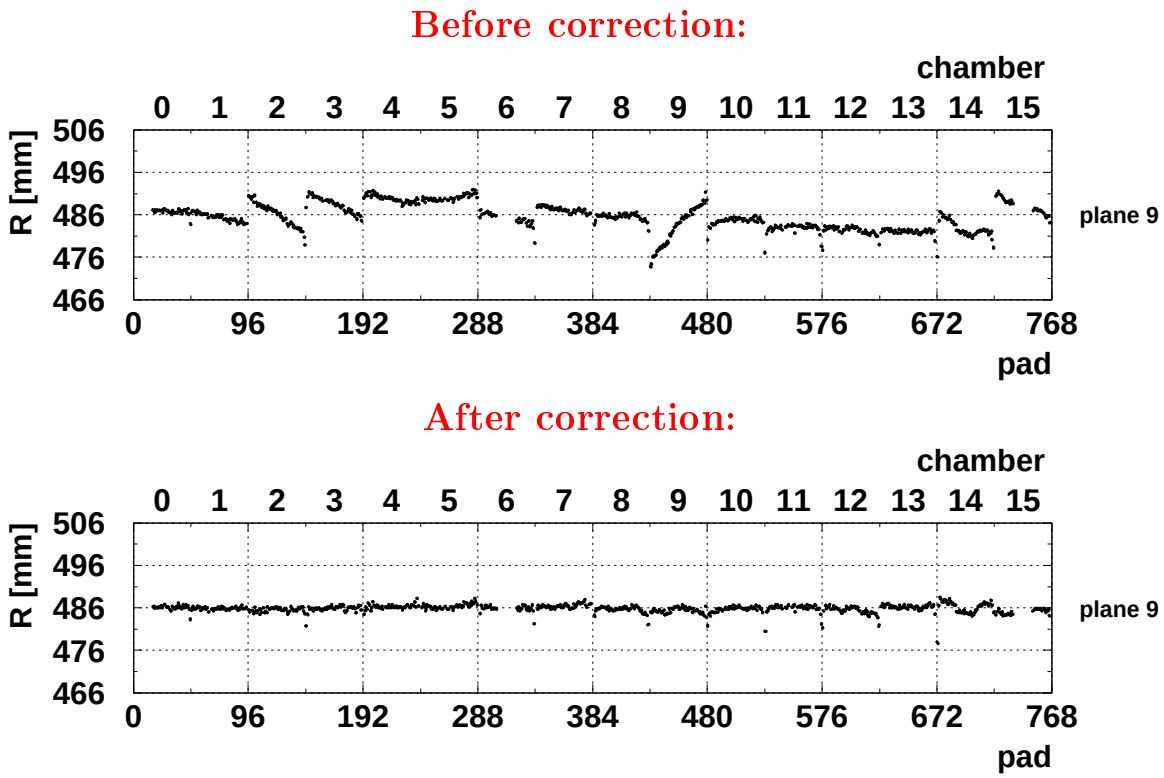

Figure 6.4: **Calibration of chamber positions.** *The plots show the reconstructed radius of the inner aluminum cylinder before and after calibration. The structures seen in the upper plot are caused by misaligned chambers. The three-fold structure within each chamber belongs to the three front-end-boards.*

6.2 Correction of Chamber Positions

The laser events taken in absence of a magnetic field can also be used to correct for tilts and shifts of the 16 readout chambers [72]. This is again done by using the signal from the inner cylinder, which was already mentioned in the previous section. Once the periodic structures seen in figure 6.2 have been corrected, the misalignment of the chambers becomes visible. This is shown in the upper plot of figure 6.4 for plane 9 of the TPC. The observed structures are ordered in groups of 48 pads corresponding to a chamber. Within each chamber a tinier three-fold structure of 16 pads is visible, related to the three front-end-boards. The reason is found in the different capacities of the connections between the pads and the preamplifiers and will be readdressed in section 6.8.

The chamber position affects the drift time via the drift path length and via the electric field. Thus, the correction has to be done iteratively. The corrected data is shown in the lower plot of figure 6.4.

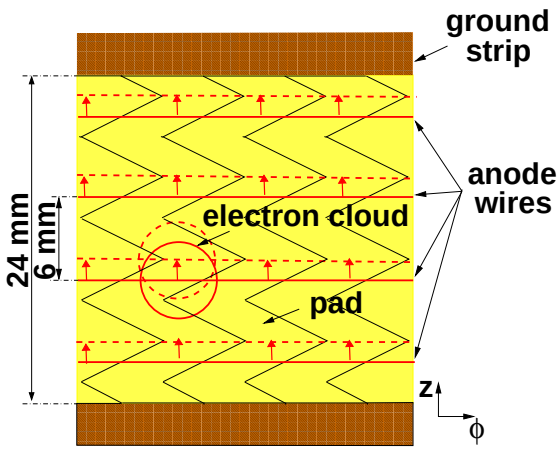

Figure 6.5: **Geometry of a readout board.** *The pads have a chevron-like structure oriented along the z coordinate and representing one plane. The planes are separated by ground strips from each other. The anode wires are mounted in azimuthal direction above the pads. The red circle represents electrons drifting towards the anode wire. A shift of the wire will influence the electron cloud in the indicated way.*

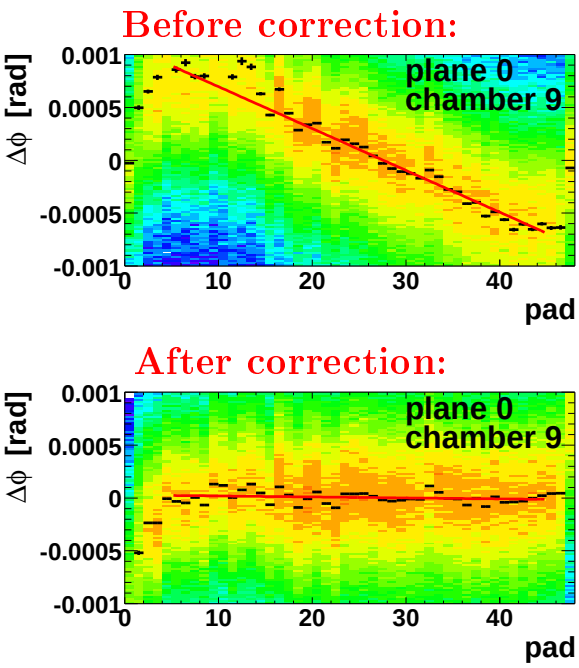

Figure 6.6: **Calibration of anode wire positions.** *Shifts of the anode wires result in a linear dependence of $\Delta\phi = \phi_{track} - \phi_{hit}$ versus pad number. This is corrected individually for each plane and each chamber via a look-up table.*

6.3 Correction of Anodes Wire Positions

The precision of the adjustment of the anode wires above the cathode pad planes is finite. Deviations from the nominal positions, as shown in figure 6.5, are calibrated using a sample of data taken in the absence of a magnetic field. For each plane and each chamber the difference of the azimuthal angle between the track and the hits $\Delta\phi = \phi_{track} - \phi_{hit}$ is plotted versus the pad number. Here ϕ_{track} is chosen as the best knowledge of the true azimuthal angle ϕ_{true}. This assumption is justifiable because the track is a fit to 12-20 hits and therefore a good measurand for ϕ_{true}.

In some cases systematic offsets of $\Delta\phi$ from zero are observed like the example in figure 6.6. These offsets depend linearly on the pad number and can be parameterized by a polynomial of first order. The linear dependence has its origin in the chevron-shaped structure of the cathode pads. If the position of an anode wire above the pads is shifted in beam direction (parallel to the z coordinate) the charge sharing between the pads must necessarily change. This in turn influences the determination of the center of gravity of a hit. The azimuthal hit position ϕ_{hit} is corrected with the help of a look-up table. The result can be seen in the lower plot of figure 6.6.

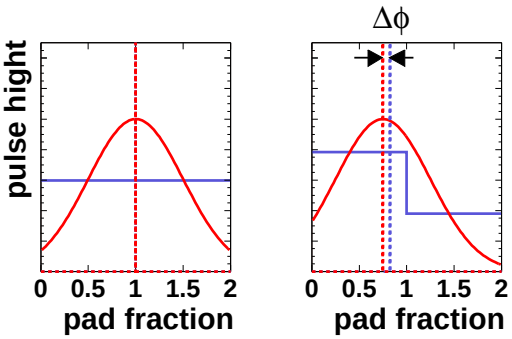

Figure 6.7: **Origin of nonlinearities.** *Nonlinearities are caused by the fact that a continuous charge distribution (red) is sampled by a discrete number of pads (blue). The center of gravity for both distributions differs by a small amount, depending on which pad fraction the mean of the charge distribution is located.*

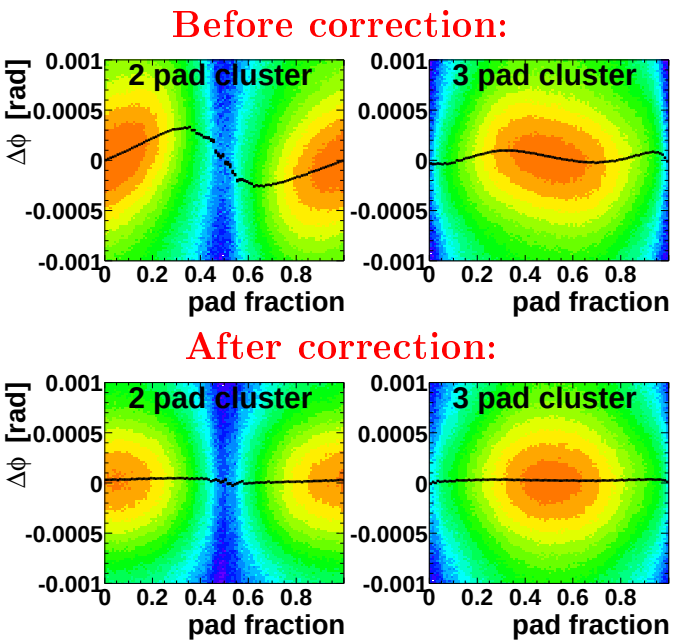

Figure 6.8: **Nonlinearity correction in the TPC.** *The nonlinearities can be seen by plotting $\Delta\phi = \phi_{track} - \phi_{hit}$ versus a fraction of a pad. They are corrected via look-up tables separately for 2 and 3 pad clusters. The shown example is plotted for a positive magnetic field in the TPC.*

6.4 Nonlinearities

The charge distribution from a track segment is sampled by a finite number of pads. This introduces a systematic error in the position resolution, as depicted in figure 6.7. As example a charge distribution, drawn as red curve, induces a signal in two adjacent pads. The continuous signal is transformed into a discrete one, and thus results in a nonlinearity of the pad response function. The error vanishes for symmetric configurations if the mean position of the charge distribution is located either in the middle or at the edge of a pad.

To minimize the nonlinearities a chevron shape has been chosen for the pads [63]. The advantage with respect to a rectangular shape is a better charge sharing and linearity of the pad response even at low pad granularity. The remaining nonlinearities can be corrected by plotting $\Delta\phi = \phi_{track} - \phi_{hit}$ versus a fraction of a pad, where ϕ_{track} is the best knowledge of the true value ϕ_{true}. The nonlinearities depend on the number of pads on which a signal is induced. In the upper row of figure 6.8 they are plotted separately for 2 and 3 pad clusters. The azimuthal position distortion is smaller than 0.5 mrad and thus a tiny effect. The correction of ϕ_{hit} is done via look-up tables, separately for positive and negative magnetic fields. The result of the correction is shown in the lower row of figure 6.8.

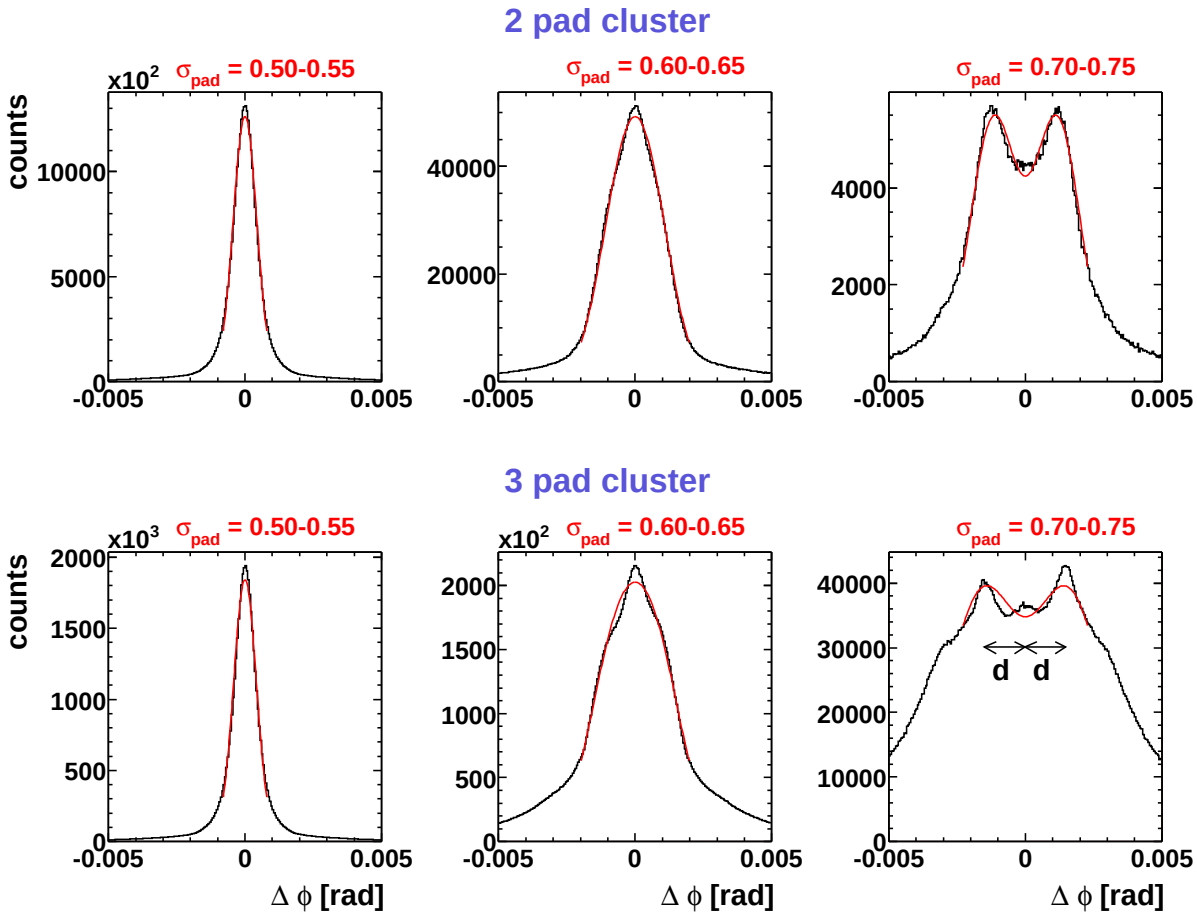

Figure 6.9: **Position correction for overlapping hits.** *The splitting of the $\Delta\phi = \phi_{track} - \phi_{hit}$ distribution in several peaks is due to unrecognized overlapping hits. The distance d of the peak to the center as a function of the pad width is used to derive a correction for the hit position.*

6.5 Position Correction for Overlapping Hits

The hit reconstruction procedure described in section 5.2.1 is able to separate overlapping hits as long as their absolute maxima are at least one pixel apart. If this is not the case, the merged clusters are assigned to a single hit. These hits can be recognized by their unusually large pad width of $\sigma_{pad} > 0.6$.

In figure 6.9 the azimuthal angle difference $\Delta\phi = \phi_{track} - \phi_{hit}$ is plotted for different values of σ_{pad}. With increasing pad width a double or even triple peak structure starts to appear. This can be used to derive a correction for unrecognized overlapping hits. The double peak structure is fitted with two Gaussian functions of same hight and width, but with the distance d from the center. The fits are performed separately for 2 and 3 pad clusters. The relationship between the distance d and the pad width σ_{pad} is linear and given by

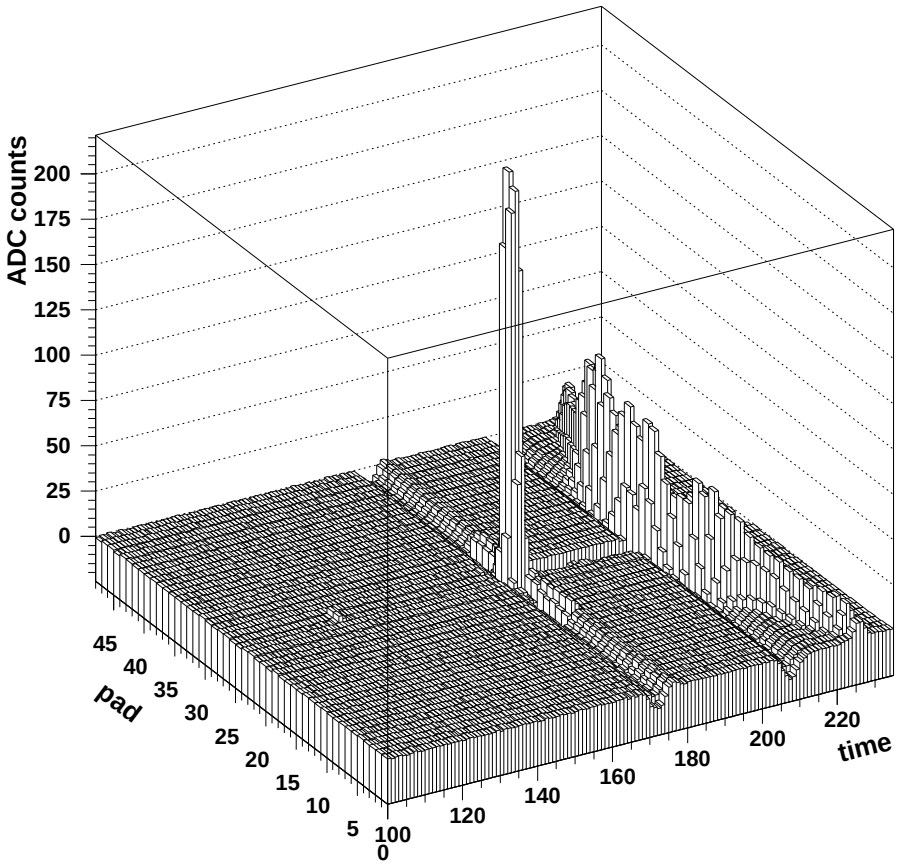

Figure 6.10: **Lateral crosstalk and signal undershoot.** *The figure shows an average over many laser events in the pad-time space. The laser pulse is accompanied by a signal undershoot and the lateral crosstalk. The broadly spread signal at high drift time is caused by stray light of the laser knocking out electrons at the inner cylinder of the TPC (compare figure 6.2).*

$$d_{2pdcl} = (3.569 \cdot \sigma_{pad} - 1.656) \text{ mrad}$$
$$d_{3pdcl} = (3.903 \cdot \sigma_{pad} - 1.543) \text{ mrad} \quad (6.1)$$

for 2 and 3 pad clusters, respectively. The triple peak structure is ignored in the correction. Assuming that ϕ_{track} is close to the true value ϕ_{true}, the hit position is shifted by the distance d towards the track. The track is refitted afterwards.

6.6 Lateral Crosstalk and Signal Undershoot

With the help of the laser it becomes possible to generate many events containing tracks at the same position and with similar signal amplitude. An average over several laser events can be seen in figure 6.10 [63]. The absence of surrounding tracks in laser events allows a detailed study of the pulse shape of the readout chamber.

Each gas amplification at an anode wire causes a drop of the wire voltage ΔU

according to

$$\Delta U = \frac{Q_{amp}}{C_{wire}}. \tag{6.2}$$

In this equation Q_{amp} is the deposited charge and C_{wire} is the capacitance of the anode wire grid with respect to the surrounding electrodes. On the other hand each pad has a capacitance C_{pad} with respect to the anode wire grid. A drop of the wire voltage therefore will induce a charge

$$Q_{crosstalk} = C_{pad} \cdot \Delta U = \frac{C_{pad}}{C_{wire}} \cdot Q_{amp} \tag{6.3}$$

on the readout pad. This effect is referred to as lateral crosstalk. It is a known feature of wire chambers [75]. The lateral crosstalk is seen in figure 6.10 as a sagging of the baseline in the same time bins as the laser hit, but on neighboring pads. The effect was reduced by a factor of 2.5 by adding additional capacitance of about 5 nF to each HV sector [63].

The second effect observed in figure 6.10 is the sagging of the baseline for time bins following the laser hit on a pad. The origin of this so called undershoot can be found in the usage of high-pass filters to suppress leakage currents. High-pass filters work as differentiators for frequencies below the threshold frequency [76]. Thus, a trailing edge of an incoming pulse will cause a negative outgoing pulse. This decreases the amplitude of pulses following in time.

For a given pad i and a local maximum l_0 the shape of the undershoot is well described by the sum of two exponential functions:

$$\sum_{l<l_0} A^l_{i,cor}(t) = \sum_{l<l_0} \left(C_{11} \cdot \sum_{j=t^l-2}^{t^l+2} A^l_{ij} \cdot e^{-C_{12}\cdot(t-t^l)} - C_{21} \cdot \sum_{j=t^l-2}^{t^l+2} A^l_{ij} \cdot e^{-C_{22}\cdot(t-t^l)} \right). \tag{6.4}$$

In this equation t^l is the time bin of pad i where a local maximum has been found. $\sum_j A^l_{ij}$ is the sum over the 5 time bins in pad i assigned to a hit l (for better understanding see also section 5.2.1). The coefficients C_{nm} have been determined in [77]. Finally, the sum $\sum_{l<l_0} A^l_{i,cor}(t)$ expresses that all undershoot corrections of hits preceding the local maximum l_0 in time have to be considered.

6.7 Electron attachment

Another important issue is a process which influences the number of primary produced electrons. The noble gas neon in the TPC has an admixture of 20% quench gas carbon dioxide. The CO_2 improves the drift properties [63] and prevents multiple discharges. It absorbs the photons emitted by excited atoms or de-excites the atoms directly through collisions. The energy mainly goes into rotational and vibrational excited molecular states and into ionization of the quencher.

However, the CO_2 molecules also interact with gas impurities like oxygen. Oxygen has the unwished property of attaching free electrons coming from primary ionization processes:

$$e^- + O_2 \rightarrow O_2^{-*}. \tag{6.5}$$

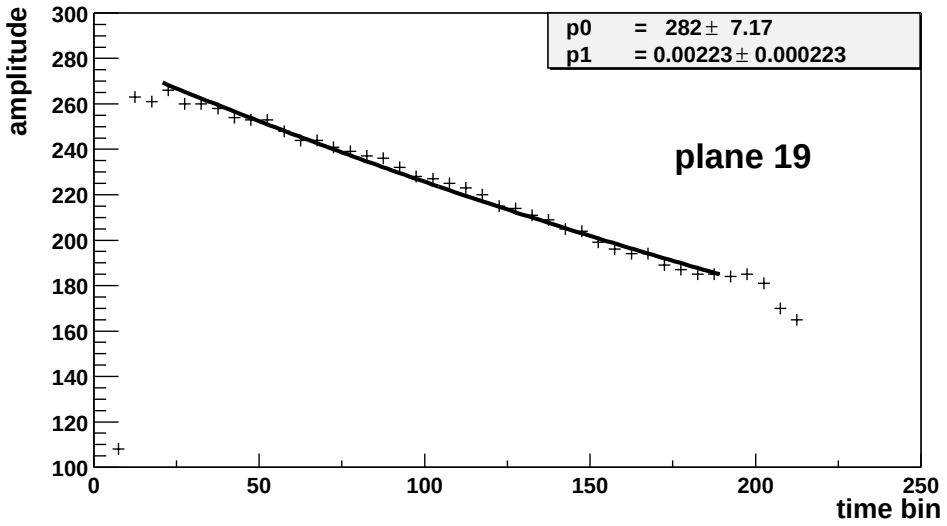

Figure 6.11: **Correction of electron attachment effects.** *The hit amplitudes decrease with drift time due to the attachment of free electrons to oxygen impurities in the fill gas of the TPC. The amplitudes are corrected for the polar angle θ of the track. This is important to account for the effect that a track segment projected onto a pad is longer for larger angles θ. Therefore, the amplitudes have to by multiplied by $\cos\theta$.*

In dilute media the oxygen loses its energy by the reemission of the electron or by radiation. Unfortunately, at the atmospheric pressure present in the TPC the dominating process is the interaction with another molecule M:

$$O_2 + M + e^- \tag{6.6}$$

$$O_2^{-*} + M \begin{array}{l} \nearrow \\ \searrow \end{array}$$

$$O_2^- + M^*. \tag{6.7}$$

In the lower case the electron is lost. The abundant excitation modes of CO_2 even enhance process (6.7). Therefore, high requirements for the oxygen purity of the gas mixture in the TPC are indispensable.

The electron attachment can be parameterized as a function of the drift time by

$$N(t) = N_0 \cdot e^{-p(M)p(O_2)Kt}, \tag{6.8}$$

where $p(M)$ is the operation pressure of the counting gas, $p(O_2)$ is the partial pressure of oxygen impurities and K is the electron attachment coefficient. The average value of $p(O_2)$ during the beam time in the year 2000 was 11 ppm. It is clear from equation (6.8) that the electron attachment increases with the drift path length.

The decrease of the amplitude with the drift time can be described by an exponential function:

$$A(t) = A_0 \cdot e^{-Ct}. \tag{6.9}$$

In this equation A_0 is the amplitude expected in absence of any electron attachment effect. An example is shown in figure 6.11 [77]. The coefficient C is determined individually for

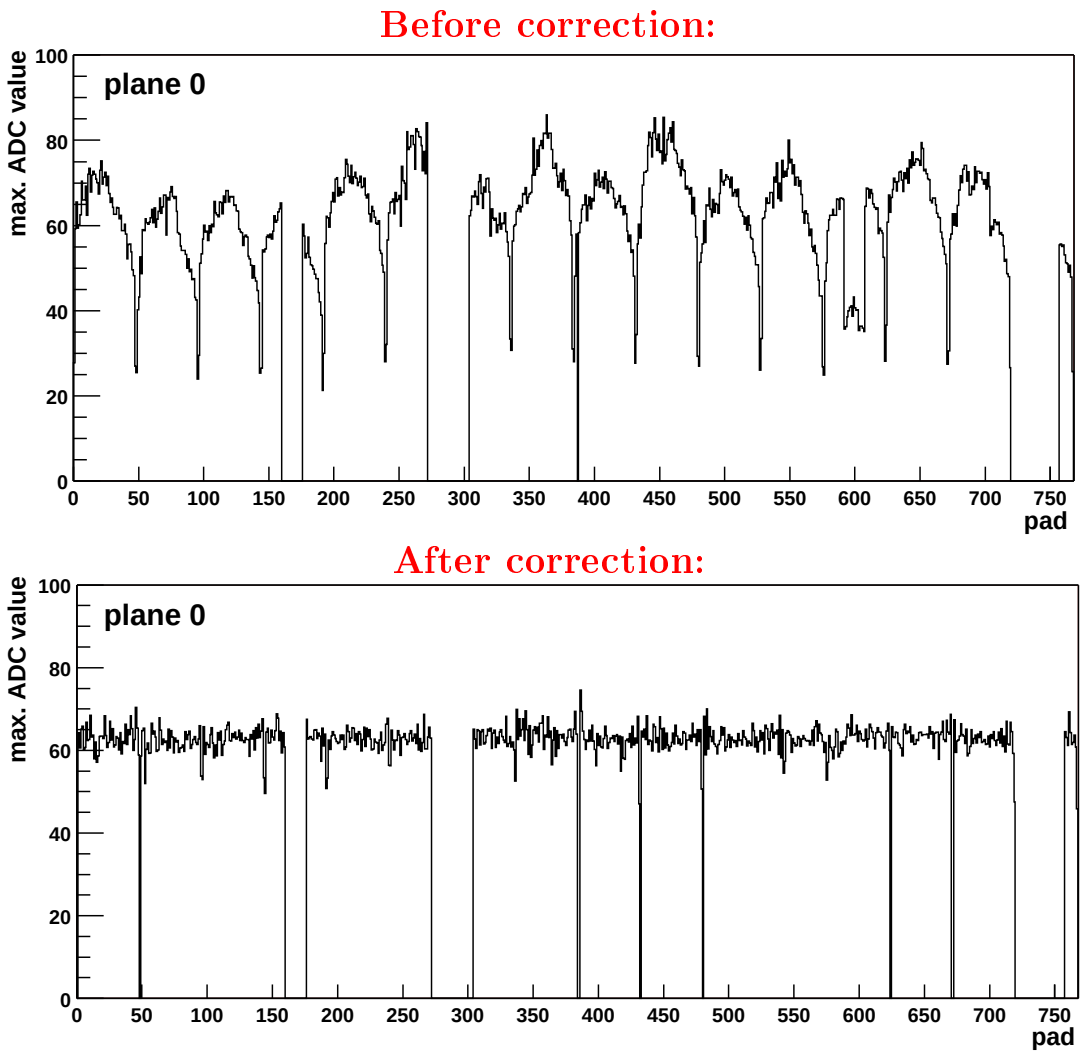

Figure 6.12: **Pad-to-pad gain correction.** *For the pad-to-pad gain correction the maximum ADC value of a hit is used, which is localized on a single pad. The maximum ADC value is corrected for the polar angle θ of the track.*

each of the 20 planes in time scales of calibration units. The different particle compositions as a function of the polar angle θ are taken into account. The correction is applied after the undershoot correction described in the previous section.

6.8 Pad-to-Pad Gain Variations

The pad-to-pad correction comprises all effects which cause gain variation from pad to pad, but also characteristics which extend over a whole electronic device. The upper plot of figure 6.12 shows the uncorrected pad-to-pad gain variation of the first plane of the TPC as an example.

The most noticeable structure extends over groups of 48 pads according to the chambers of the TPC. The periodic peaks can partly be explained by the bending of the anode wires. The wires are glued to the edge of a chamber. In between these two fixed points the wires might bend due to the electrostatic attraction towards the pad plane. This decreases the distance between the anode wires and the pads and thus a stronger signal is induced. The effect is strongest in the center of a chamber. It has also been observed that the gain drops at the end of the wires. Here the electric field differs from that of an infinite wire. Furthermore, the closing pads at the border of a chamber are smaller and have a different shape than the rest of the pads. This can be responsible for the dip at the edge of each chamber. Finally, the three-fold structure inside a chamber reflects the individual responding behavior of the front-end-boards.

The pad-to-pad gain variations have been studied in [77]. The correction is implemented in form of look-up tables and determined for each calibraton unit. The effect of the correction is demonstrated in the lower plot of figure 6.12.

6.9 Correction of Hit Positions

A fine tuning of the hit positions in the TPC can be achieved by using further information from the Silicon Drift Detectors. The upper row of figure 6.13 shows the polar angle difference $\Delta\theta = \theta_{SiDC,track} - \theta_{TPC,hit}$ between the SiDC track segment and the TPC hits versus the pads of the TPC [74]. The tiny structures seen in the plots reflect the 16 chambers. No periodic structure is seen in the distribution of $\theta_{SiDC,track}$. Using this knowledge the positions of the hits in the TPC are shifted by the amount $\Delta\theta_{cor}$, calculated with respect to the mean value $\Delta\theta$ obtained for each chamber. The correction is applied as a function of the polar angle θ to the individual pads and planes. The result can be seen in the lower row of figure 6.13.

For the next correction step it is important that the abundance of particles with opposite charge is similar. A convenient choice for this purpose are pions because the multiplicity of π^+ and π^- differs by only 10% [78]. A clean sample of high momentum pions ($p > 4.5$ GeV/c) can be selected with the help of the RICH detectors. This sample is used to plot the azimuthal angle difference $\Delta\phi = \phi_{R2M} - \phi_{TPC,hit}$ between the TPC track segment as measured at the RICH2 mirror and the hits in the TPC versus ϕ_{R2M} [69]. This is shown in figure 6.14. Clearly the deflection of the oppositely charged particles can be seen with increasing plane number. Tracks with infinite momentum do not suffer deflection. The minima of the distributions should therefore be centered at zero. However, a deviation from zero is seen as a function of ϕ_{R2M}. The deviation from zero is applied as correction to the hit positions of the TPC. The correction is done as a function of the azimuthal angle ϕ and as a function of the plane number. The procedure is repeated for the distribution $\Delta\theta = \theta_{R2M} - \theta_{TPC,hit}$.

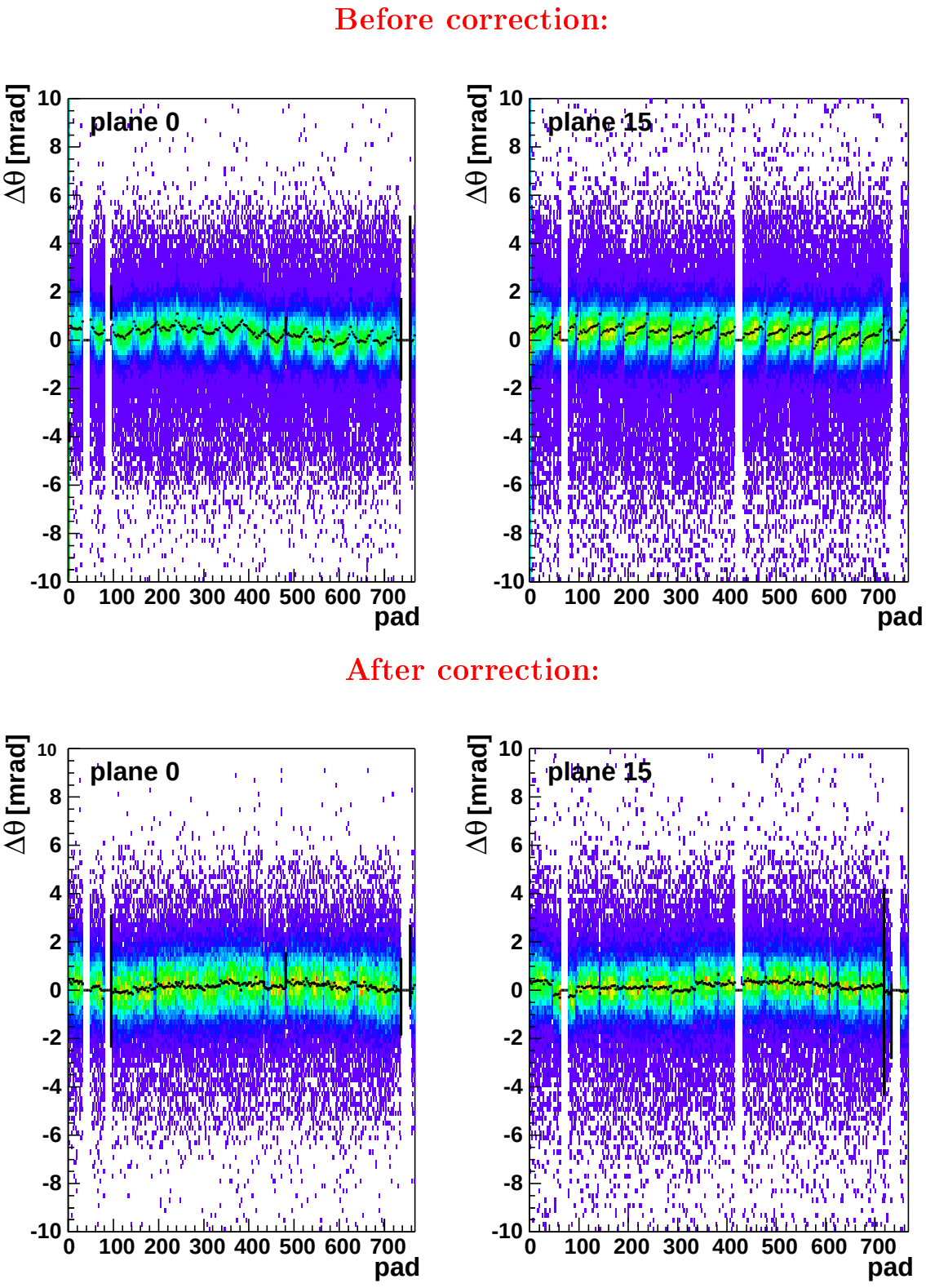

Figure 6.13: **Comparison between polar angles in SiDC and TPC.** *The distribution of* $\Delta\theta = \theta_{SiDC,track} - \theta_{TPC,hit}$ *plotted versus the pads in the TPC shows tiny structures (upper row). Applying a correction* $\Delta\theta$ *to the hits in the TPC results in a flat distribution (lower row).*

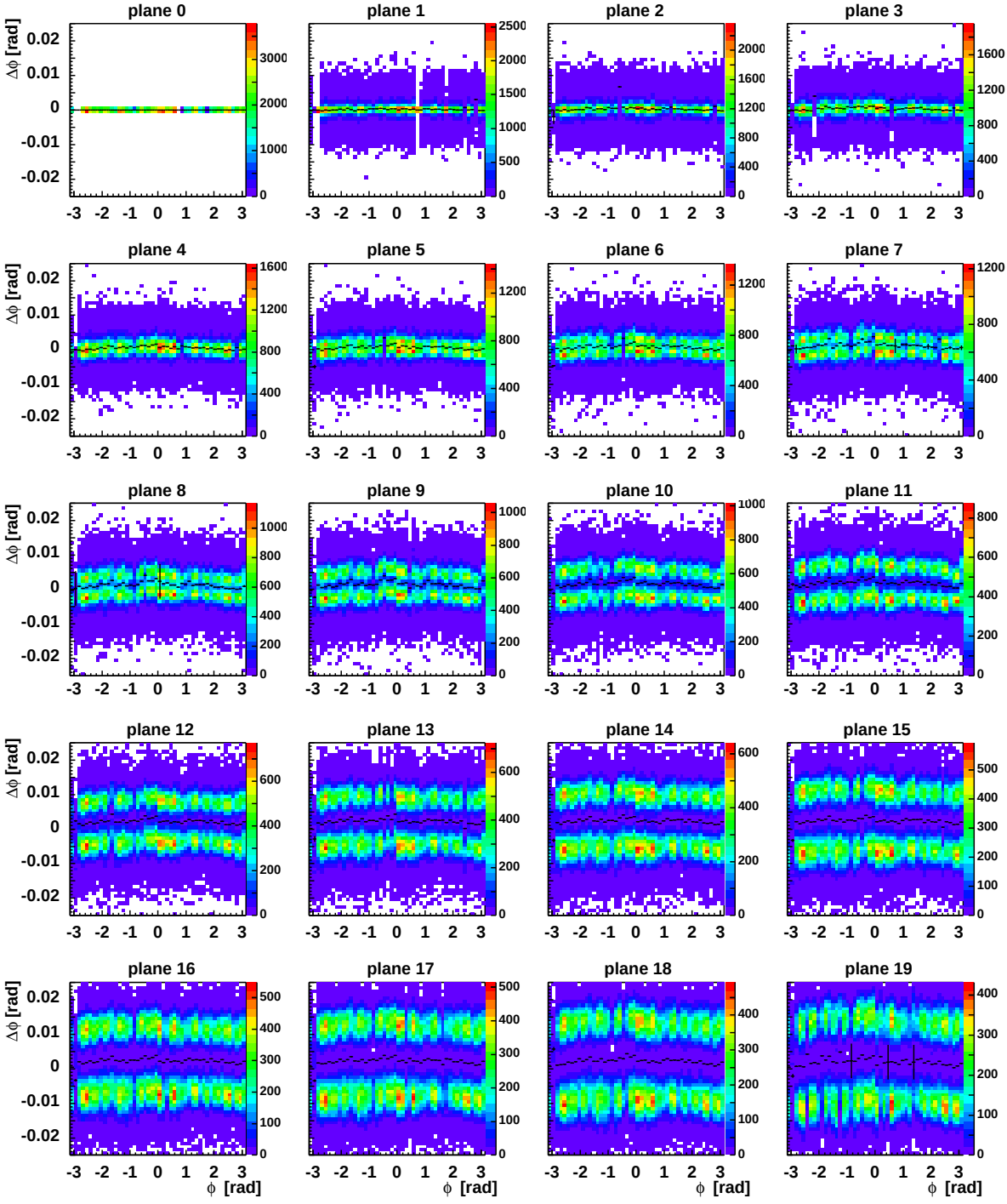

Figure 6.14: **Remaining deflection for infinite momentum tracks.** *For a sample of pion tracks the azimuthal angle difference* $\Delta\phi = \phi_{R2M} - \phi_{TPC,hit}$ *is plotted versus* ϕ_{R2M}*. Tracks with infinite momentum do not suffer deflection and should be centered at zero.*

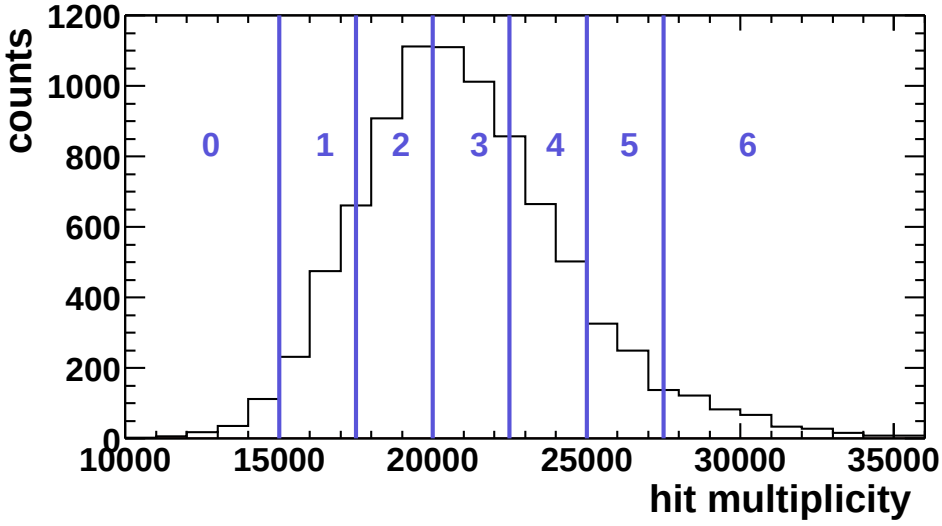

Figure 6.15: **Hit multiplicity in the TPC.** *The resolution is determined differentially for the seven multiplicity bins marked in the figure.*

6.10 Differential Resolution

The fitting of track segments in the TPC, as described in section 5.2.3, can be improved by switching from constant weights for all hits to a more sophisticated method by assigning individual weights to the hits according to their resolution. The weights contain the information about the hit position in the 3-dimensional space and about special hit characteristics. In this way remaining inaccuracies in the determination of the drift velocity are taken into account, as well as other dependencies like the hit amplitude or the hit multiplicity of the event.

The momentum of a particle is determined by the deflection of the trajectory in the magnetic field of the TPC. Thus, the important coordinate to obtain a good momentum resolution is the azimuthal angle ϕ. For this coordinate the differential resolution $\sigma_{r\Delta\phi}$ is determined as a function of

- the radius in steps of 4 cm,
- the 20 planes in the TPC,
- the hit amplitude in steps of 50 ADC units,
- the hit multiplicity in the TPC in steps according to figure 6.15,
- the number of responding pads, and
- the hit being isolated or not.

The differential resolution is shown in figure 6.16 for a selected set of hits. For a better understanding $\sigma_{\Delta\phi}$ is plotted instead of $\sigma_{r\Delta\phi}$. For isolated hits the 3 pad clusters have

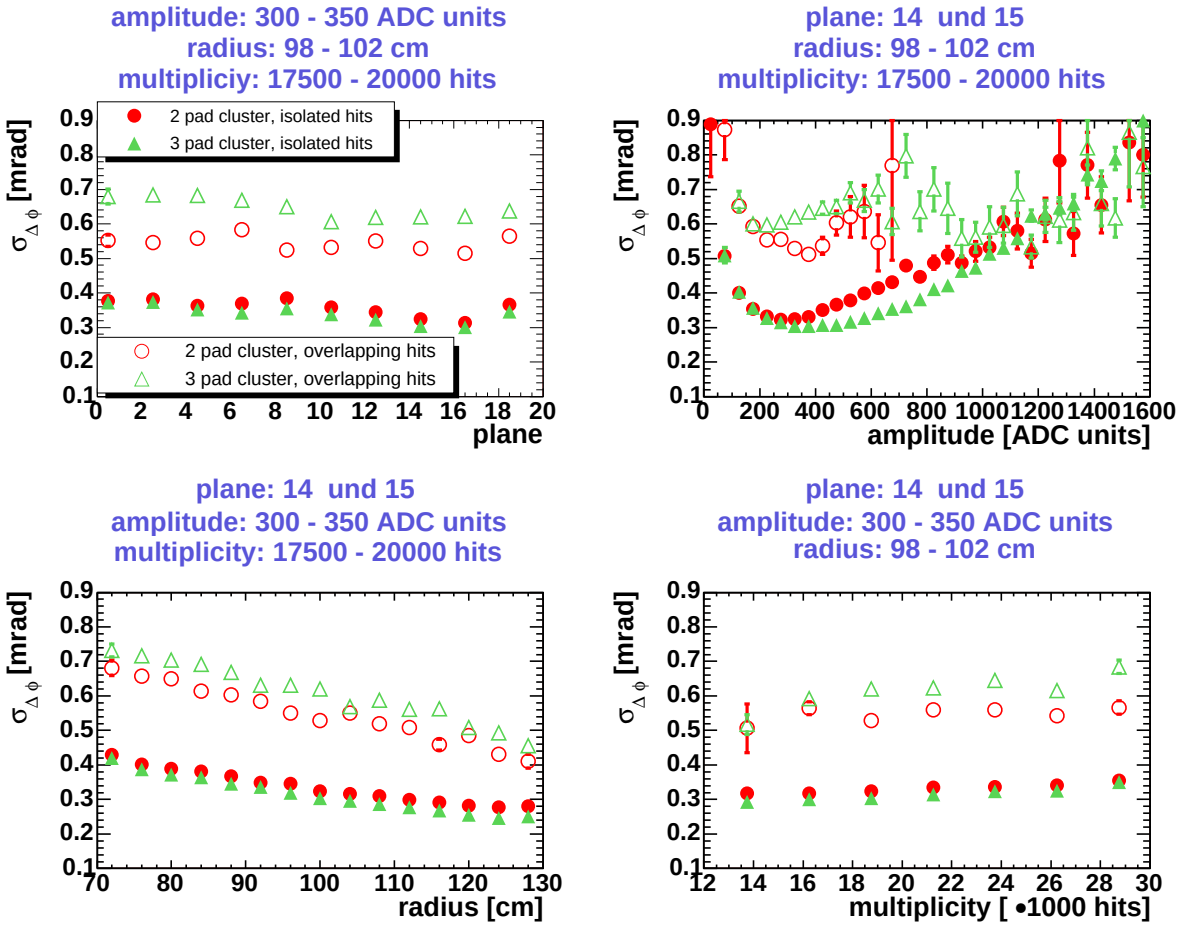

Figure 6.16: **Differential Resolution.** *The differential resolution is determined as a function of several hit characteristics. In this way it is possible to weight each hit individually in the fit of a TPC track segment.*

a somewhat better resolution than the 2 pad clusters due to the more favorable charge sharing. The resolution of overlapping hits deteriorates about a factor of two compared to isolated hits. Nevertheless the bulk of the hits are isolated, as can be seen in figure 5.6. Only 20% of the hits have an overlapping partner. Remarkable is also the strong dependence of the resolution on the amplitude. Firstly, the resolution increases with the amplitude. This effect can be ascribed to a better signal-to-noise ratio. Due to saturation effects the resolution deteriorates again at higher amplitudes. As expected, the resolution decreases with the number of hits in the TPC, though the effect only start to be important for very high multiplicities of more than 40000 hits. The number of events with such high multiplicities is small as can be judged from figure 6.15. The linear decrease of the resolution with the radius has its origin in the increasing influence of the diffusion with the drift length. The dependence on the plane number of the TPC is due to the higher occupancy in the first planes, but also due to remaining uncertainties in the knowledge of the electric or magnetic field.

Once the differential resolution has been determined, the weight of a hit is given by:

$$w = \frac{1}{\sigma^2_{r\Delta\phi}}. \tag{6.10}$$

Figures 6.17 and 6.18 show a small extract of the weights for isolated and overlapping 3 pad clusters, respectively. Each connected curve describes an amplitude scan at a fixed radius. The multiplicity in the TPC is between 25000 and 27500 hits. Only every second plane is displayed. The weights w can be parameterized as a function of the amplitude A by

$$w(A) = C_0 + C_1 \cdot A + \frac{C_2 \cdot A}{1 + e^{-\frac{A}{C_3}}} \tag{6.11}$$

or in the case of overlapping hits with three pads by

$$w(A) = C_0 + C_1 \cdot A + \frac{C_2 \cdot A}{1 + e^{-\frac{A}{C_3}}} + C_4 \cdot (A - C_5) + \frac{C_6 \cdot (A - C_5)}{1 + e^{\frac{(A-C_5)}{C_7}}}. \tag{6.12}$$

Unfortunately the weights have large error bars at high amplitudes or radii due to limited statistics. In some cases the fitting of the weights might fail, thus resulting in unreasonable coefficients C_n. To avoid this effect the coefficients C_n are also fitted, but now as a function of the radius. The used functions are polynomials. The functions shown in figures 6.17 and 6.18 are smoothed in the described way.

In order to keep the amount of data as small as possible, many runs were taken using a so called TPC mask. This means that only those hits in the TPC are written to tape which fall in the overall acceptance of the spectrometer. The mask window chosen for the beam time in 2000 is $6.5^o < \theta < 15^o$. Obviously, the information about the hit multiplicity needed to calculate the weights is wrong for runs with mask. The hit multiplicity has to be rescaled in those cases. The scaling factors are determined from runs taken without mask. The ratio

$$r_i = \frac{N^{mask}_{i,hit}}{N_{i,hit}} \tag{6.13}$$

is determined for each plane i, where $N^{mask}_{i,hit}$ and $N_{i,hit}$ are the hit multiplicities measured with and without mask application, respectively. The scaling factors rise continuously from ~ 0.6 for the first plane to 1.0 for the middle planes 9 and 10, and drop again to ~ 0.8 for the last plane.

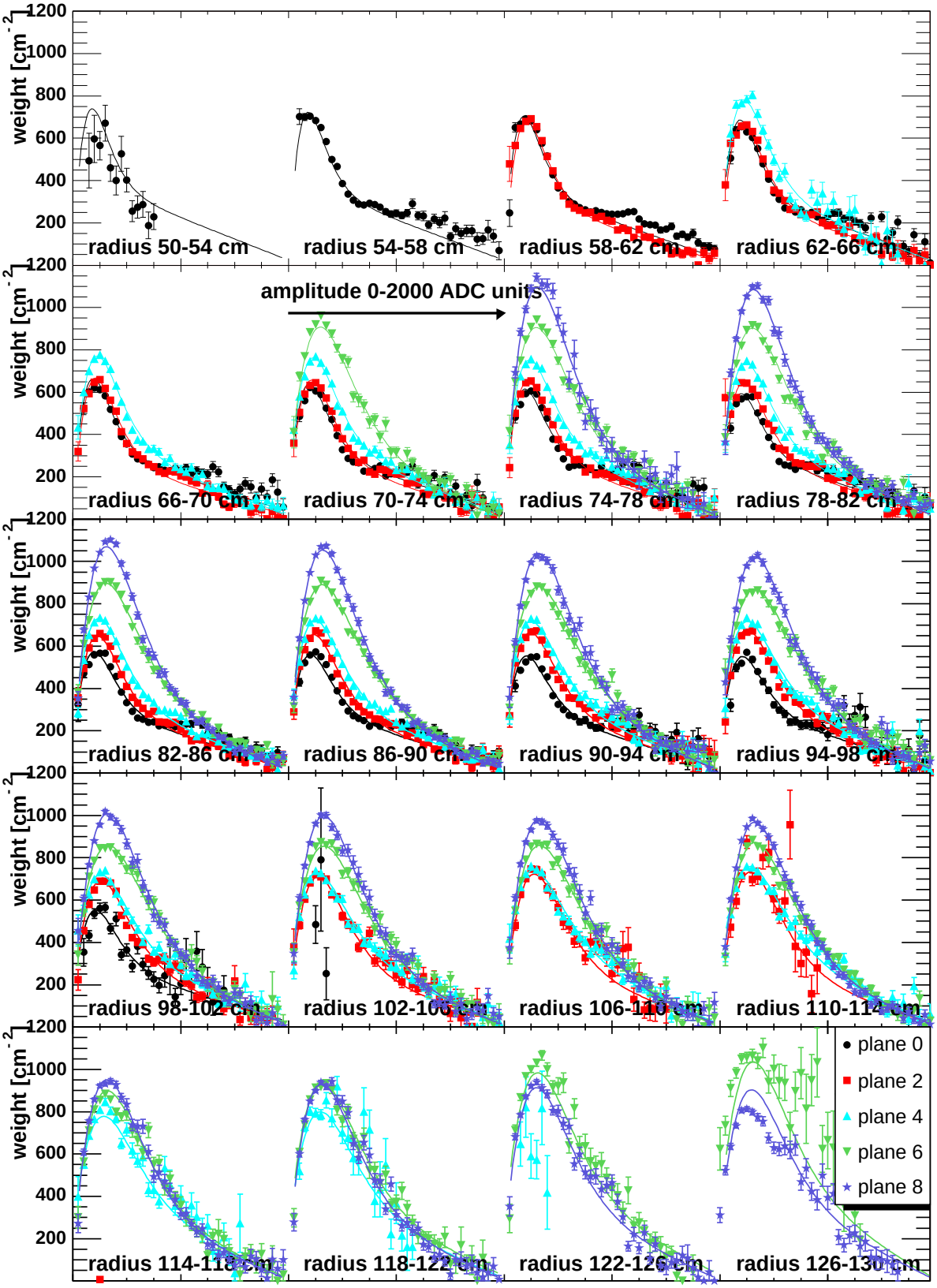

Figure 6.17: **Weight functions of isolated TPC hits.** *The plotted weights belong to isolated hits with three pads at a multiplicity of 22500-25000 hits. The lines are fits according to equation (6.11).*

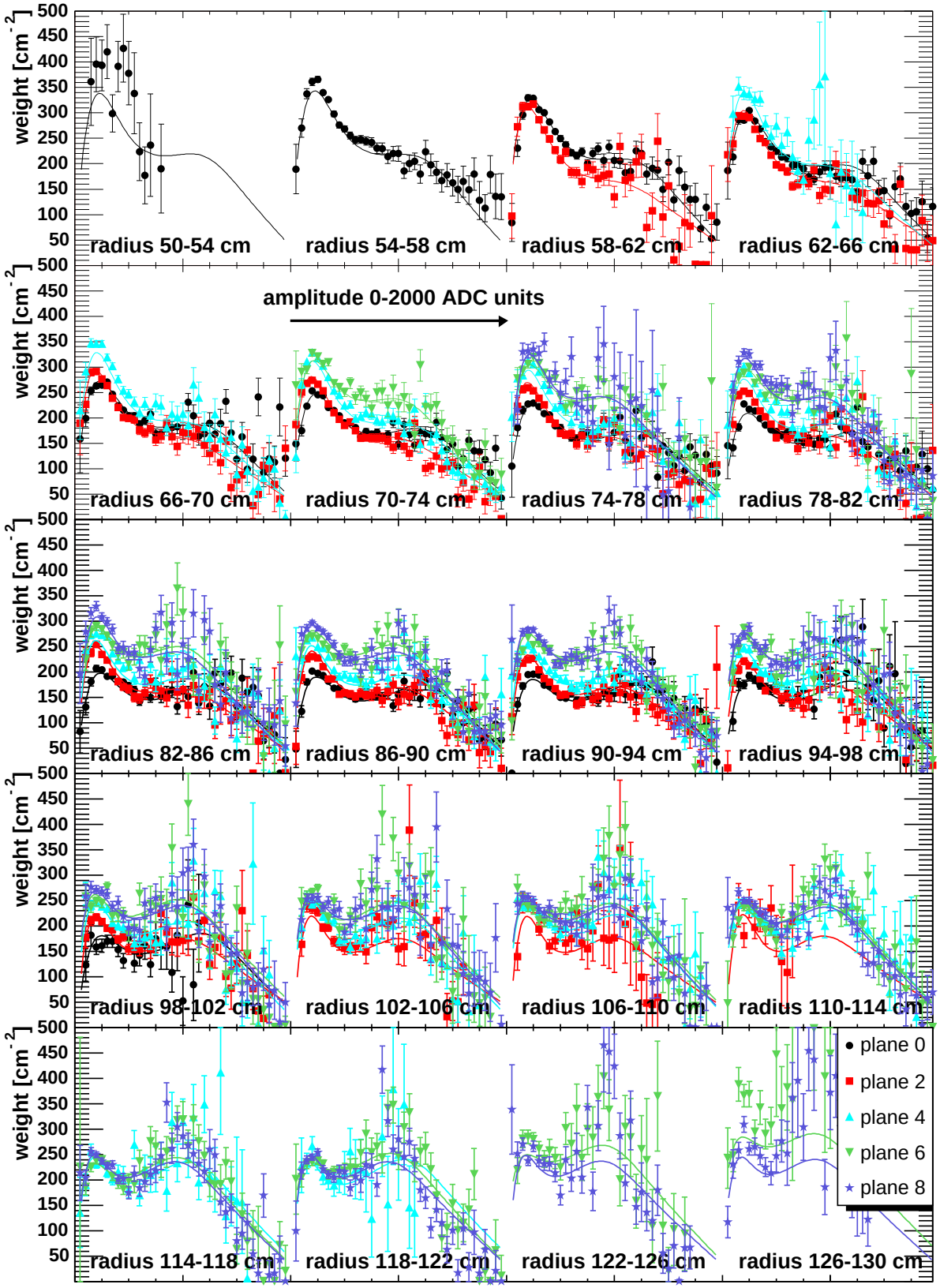

Figure 6.18: **Weight functions of overlapping TPC hits.** *The same as in figure 6.17 for overlapping hits. The lines are fits according to equation (6.12).*

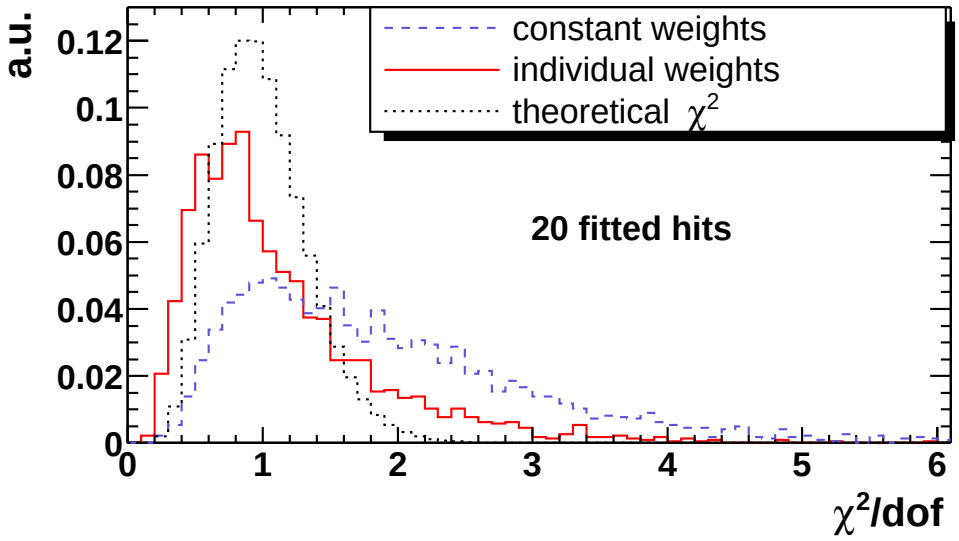

Figure 6.19: **χ^2 distribution for 20 fitted hits in the TPC.** *If the hits are weighted according to their individual characteristics the χ^2 distribution of the track fit in the TPC approaches the theoretical expectation.*

The benefit of using individual weights for the hits becomes obvious by plotting the χ^2 distribution of the track fits in the TPC. This is done is figure 6.19 for the case of 20 fitted hits. If all hits in the fit are weighted equally the fit result is inadequate and the χ^2 distribution is broad. If the hits are weighted according to their individual characteristics, the χ^2 distribution approaches the theoretical expectation. The remaining discrepancy is due to a contamination of the track sample with particles originating from decay vertices. However, the reference tracks used for the fits are calculated for particles coming from a target. The fit result for particles coming from another interaction point will therefore deliver an unsatisfactory result.

6.11 Inverse Momentum Correction

For a detector with infinite resolution the distribution of the charge times the inverse momentum q/p should be centered at zero. However, remaining uncertainties in the knowledge of the Lorentz angle might cause a shift, as sketched in figure 6.20. For instance, depending on the charge, a somewhat smaller or higher momentum might be reconstructed. It can even happen that particles at very high momentum are reconstructed with the wrong sign. If in addition the abundance of positive and negative charged particles is different, the shift of the minimum is even larger.

The shift can be used to correct remaining deviations in the momentum. A convenient particle choice for this measurement are pions. As already mentioned in section 6.9 the multiplicities of π^+ and π^- are similar and effects related to a different abundance of particles with opposite charge are therefore reduced.

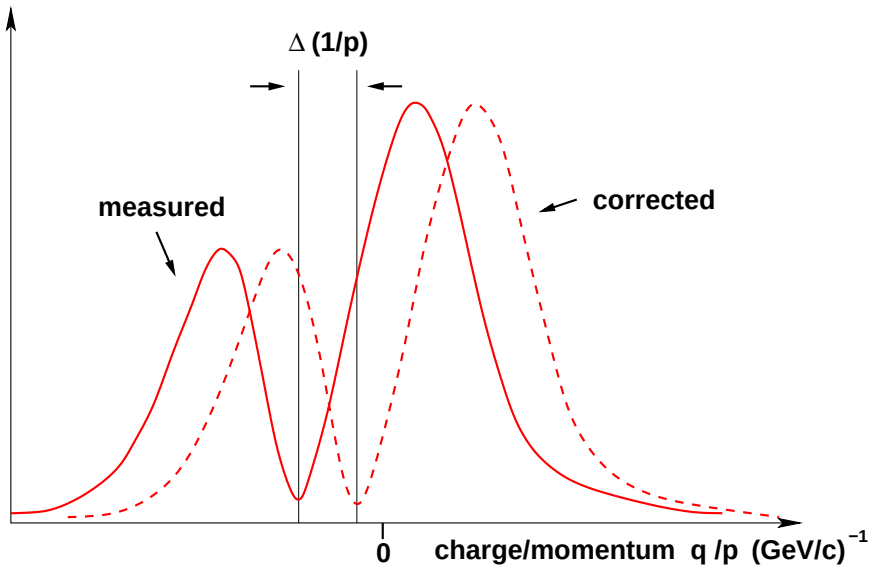

Figure 6.20: **Inverse momentum correction.** *If the knowledge of the Lorentz angle in the TPC is imprecise the particles are reconstructed at wrong momenta.*

The pions are selected with the RICH detectors by the ring radius. The determination of the shift of the minimum is done in four steps in order to optimize the statistics [79]. First, a coarse correction is calculated for each calibration unit. The data is then divided into three groups,

- positive magnetic field at the beginning of the beam time,
- negative magnetic field, and
- positive magnetic field at the end of the beam time.

A finer correction is calculated as a function of the azimuthal and polar angle ϕ and θ. In the following step the same is repeated as a function of θ, but now within each calibration unit. In this case the pions are selected via their differential energy loss in the TPC in order to increase statistics. Finally, a last correction is determined in even finer entities of 10 bursts, but integrated over ϕ and θ.

6.12 Test Results of the Calibration

The last section of this chapter is devoted to the benefits achieved with the calibration of the TPC. Figure 6.21 shows the e/π separation before and after calibration. In a momentum range between $0 < p < 1$ GeV/c the dE/dx resolution for electrons improved from 18.4% to 11.8% [77].

The position resolution is given by the width of the residuals $r\Delta\phi = r\phi_{track} - r\phi_{hit}$ or $\Delta r = r_{track} - r_{hit}$. Figure 6.22 shows the present position resolution as a function of

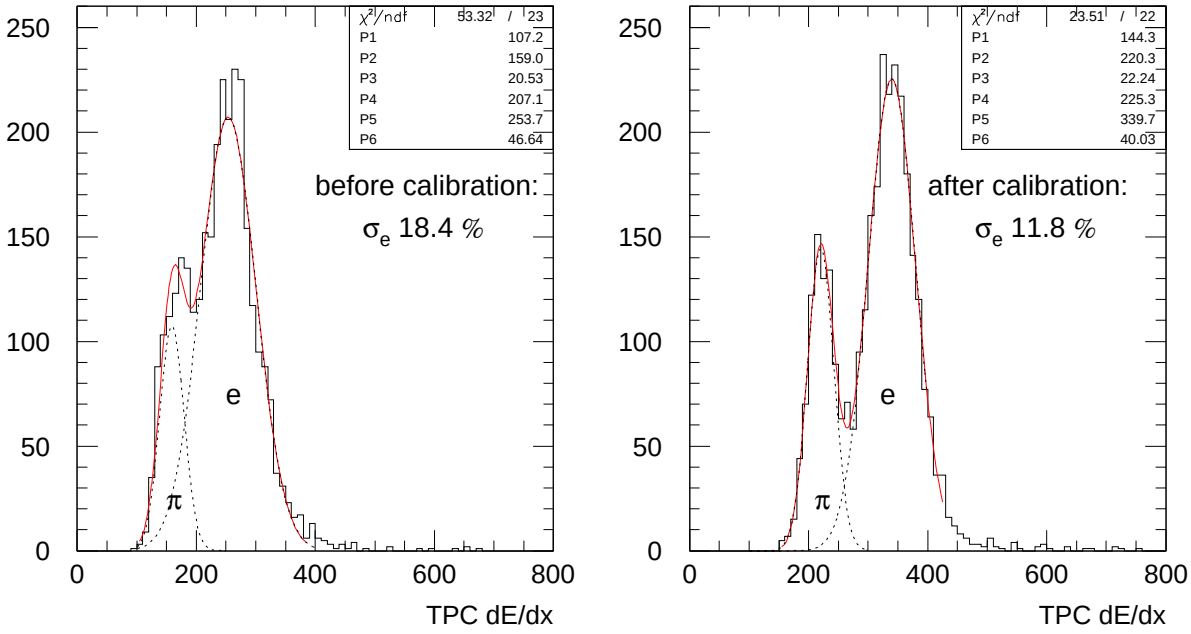

Figure 6.21: **dE/dx resolution in the TPC before and after calibration.** *The left plot shows the dE/dx resolution of electrons before the calibration of the TPC, the right plot shows the same after the calibration. The selected momentum range is* $0 < p < 1$ *GeV/c*^{2}*. Only tracks with at least 15 hits are used.*

the plane number in the TPC. The distortions in the azimuthal resolution are due to remaining uncertainties of the Lorentz angle. The higher occupancy in the first TPC planes is responsible for the deterioration of the radial resolution. Furthermore, the drift length is longer in the first planes due to the acceptance of the TPC, and thus diffusion plays a major role. The global position resolution achieved with the new calibration is $\sigma_{r\Delta\phi} \approx 340$ μm and $\sigma_{\Delta r} \approx 640$ μm. This has to be compared with the design resolution of $\sigma_{r\Delta\phi}^{design} = 250 - 350$ μm and $\sigma_{\Delta r} = 400 - 500$ μm [57]. The important coordinate for the momentum resolution is the azimuth. Here the design resolution is reached. The radial position resolution is worse than its design value. The main reason is, that the weight calculation described in the previous section is not performed for the radial component. The improvements of the new TPC calibration become visible by comparing the position resolution with the corresponding values $\sigma_{r\Delta\phi} \approx 500$ μm and $\sigma_{\Delta r} \approx 800$ μm [63], obtained with an earlier calibration version.

Another test is the comparison of the width of reconstructed particles like the Λ baryon or K_S^0 meson. Here, the previous calibration results in a width of 12.6 ± 0.3 MeV/c^2 for the decay $\Lambda \to p\pi^-$ and a width of 21.7 ± 0.3 MeV/c^2 for the decay $K_S^0 \to \pi^+\pi^-$ [63]. Figure 6.23 shows both particles reconstructed using the procedure described in chapter 7 and using the new calibration. The width of the Λ is significantly narrower, having now a value of 5.68 ± 0.17 MeV/c^2. The same applies for the K_S^0 which has now a width of 13.24 ± 0.05 MeV/c^2.

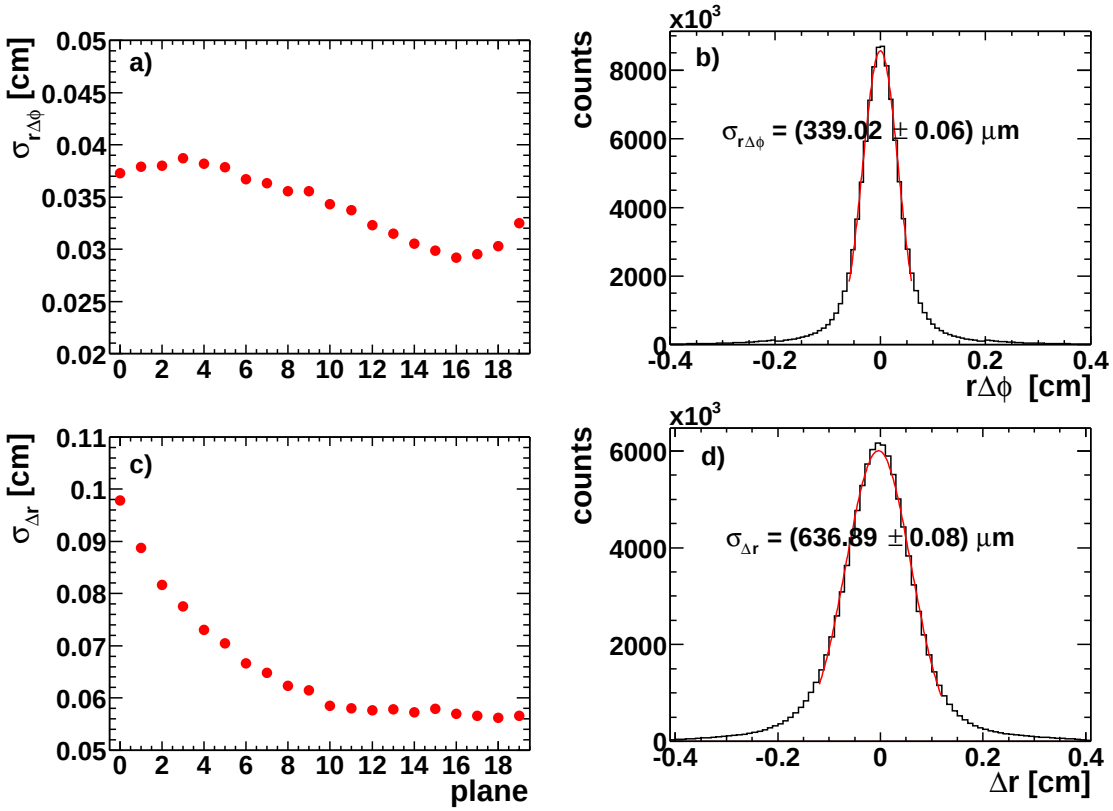

Figure 6.22: **TPC residuals.** *Plots a) and c) show the resolution as a function of the plane number in the TPC. Plots b) and d) show the residuals integrated over all planes.*

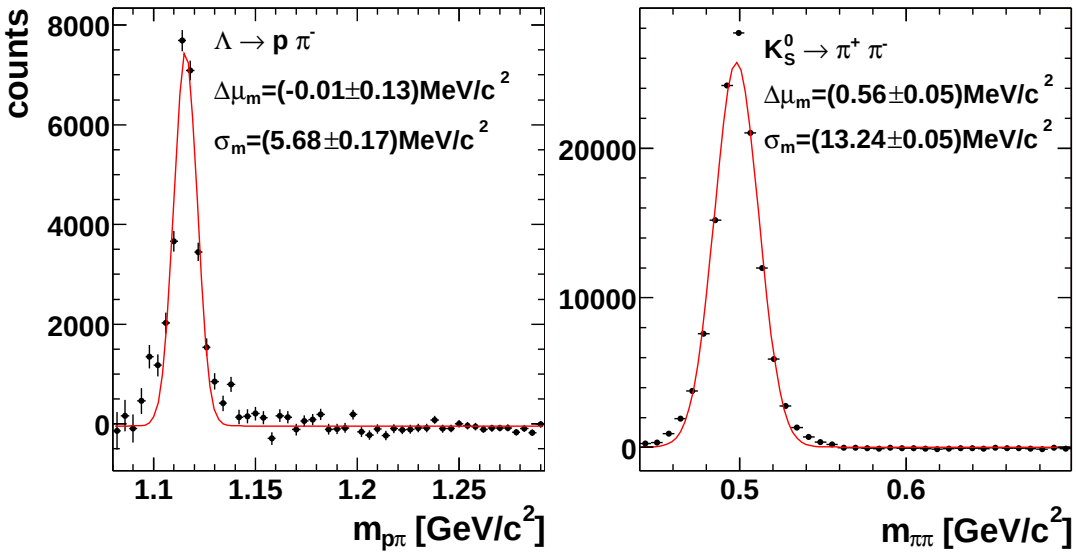

Figure 6.23: **Λ and K^0_S Width.** *The number of analyzed events is 3.4 million for the Λ and 15.9 million for the K^0_S. The width σ_m and the offset $\Delta\mu_m$ of the measured mass from its nominal value is written in the figures. For both analyses a secondary vertex cut of $z_{sv} > 1$ cm is used. Furthermore, a cut on the back extrapolated momentum vector of bep < 200 μm is applied. The χ^2 probability cut on the track and the secondary vertex fits is $P_{\chi^2} > 0.01$. The reconstruction procedure and the cut variables are explained in detail in chapters 7 and 8.*

Chapter 7

Secondary Particle Reconstruction Scheme

The two RICH detectors of the CERES experiment are optimized for the identification of electrons. Other particles can be identified using the differential energy loss dE/dx in the TPC, as shown in figure 7.1. In the CERES acceptance the momentum range of the K and π decay products of the D^0 meson is predominantly located between 2.5 and 7.5 GeV/c. In this momentum regime the dE/dx resolution of the CERES TPC is not sufficient to resolve the Bethe-Bloch lines of the decay products. In figure 7.2 a Monte Carlo simulation of the differential energy loss of the kaon and the pion are plotted as a function of the momentum. The $\pm 1\sigma$ bands correspond to $\sim 10\%$ of the mean dE/dx value. From 1 GeV/c on the bands for the kaon and the pion overlap. Furthermore, they are crossed by the Bethe-Bloch lines of other particles like protons and muons. Without particle identification the fraction of combinatorial background becomes extremely large. Thus, a combination of suitable cuts has to be applied to optimize the signal-to-background ratio.

A powerful tool for background suppression is provided by the reconstruction of the secondary vertex. This enables to separate tracks originating from the target from those coming from late decays. The detectors usable for this purpose are the two SiDC detectors and TPC. At first, each track of a particle is fitted by a straight line in the $\vec{B}$-field free region upstream the RICH2 mirror. The fits are based on three points. The first two are given by the hits in SiDC1 and SiDC2. To obtain the third point the TPC track segments are extrapolated to the RICH2 mirror taking the magnetic fringe field into account. The third point is then defined by the coordinates of this intercept. The fringe field upstream the RICH2 mirror is negligible as can be judged from figure 6.1. Nevertheless, deviations of the track from a straight line can still occur by multiple scattering between the two SiDC detectors and the TPC. This is accounted for by momentum dependent errors of the points. In a second step each two tracks are combined and the point of closest approach between them is calculated. The reconstruction scheme of the secondary vertex is illustrated in figure 7.3.

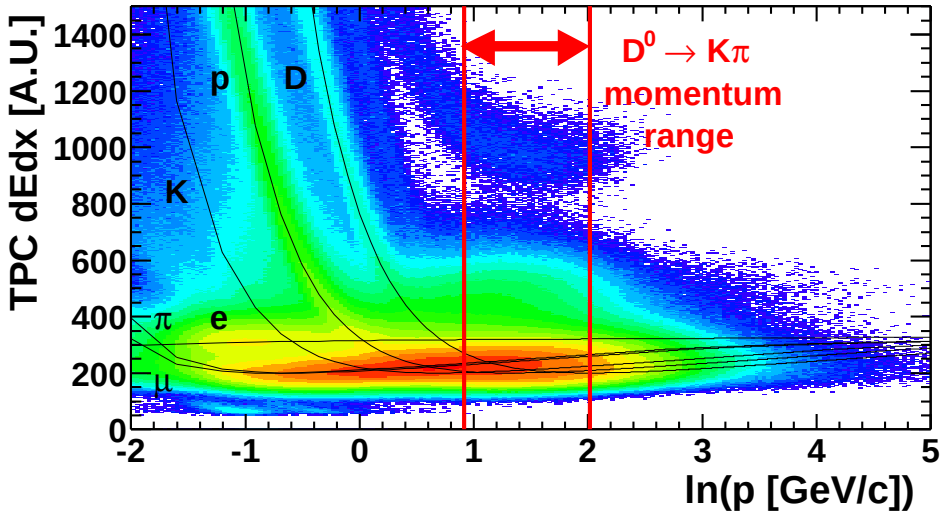

Figure 7.1: **Differential energy loss in the CERES TPC.** *The two vertical lines mark the momentum range of the decay products of the D^0 meson. In this region particle identification via the differential energy loss in the TPC is not applicable anymore.*

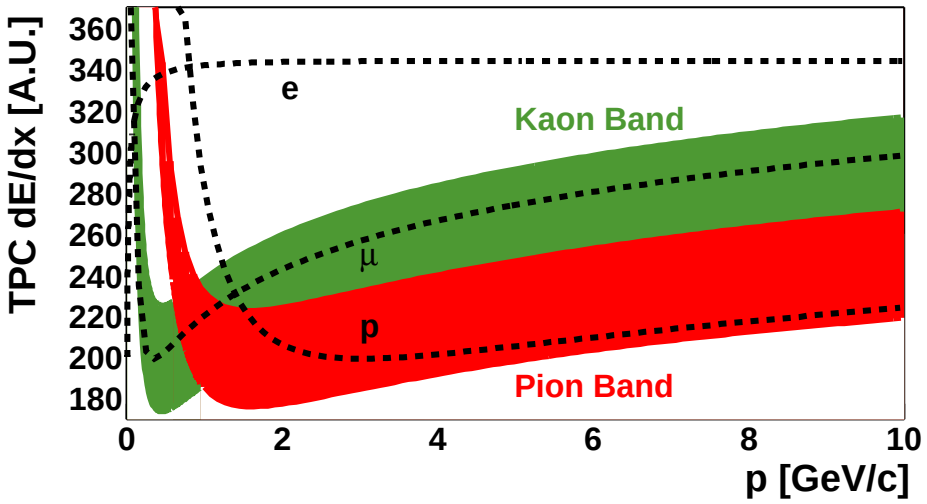

Figure 7.2: **Simulation of the kaon and pion dE/dx band.** *The red and green shaded regions correspond to the 1σ-dE/dx band of the pion and kaon, respectively. The bands overlap and are crossed by the Bethe-Bloch lines of other particles like protons and muons.*

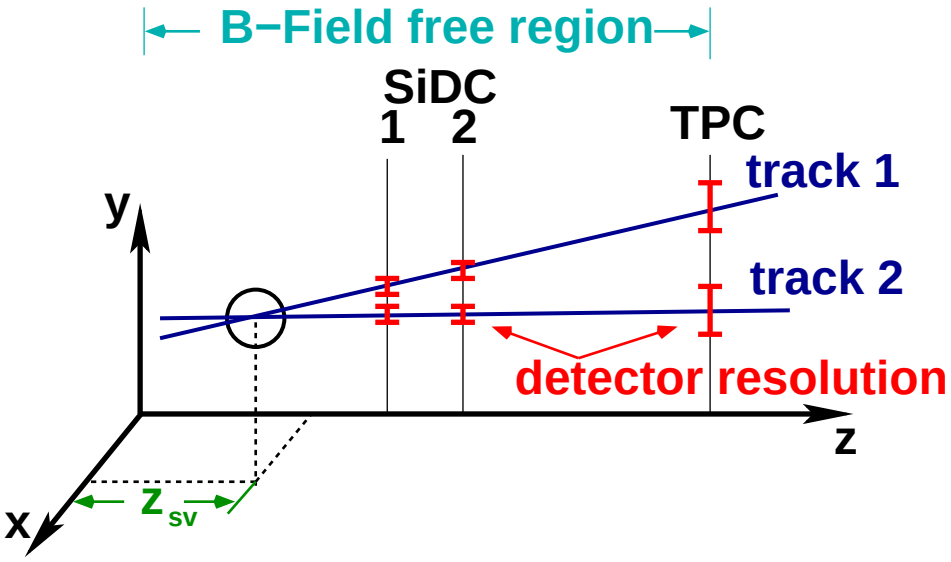

Figure 7.3: **Reconstruction scheme of the secondary vertex.** *The tracks are straight line fits through three points given by the SiDC detectors and the TPC. The errors of these points are determined from the resolution of the detectors. The secondary vertex is the point of closest approach between two tracks. A cut on its coordinates suppresses tracks originating from the targets. The picture is not drawn to scale.*

A possibility to suppress fake track combinations is given by a cut on the radial distance between the back extrapolated momentum vector of the D^0 candidate and the primary interaction point. In the following this distance will be denominated *bep* parameter. The momentum vector of the D^0 candidate is given by the sum of the momenta of the decay products $\sum \vec{p}_i$. For a true combination of tracks this momentum vector will point back to one of the targets. In this case the *bep* parameter will be small in contrast to the case of a fake combination of tracks. The meaning of the *bep* parameter is further clarified in figure 7.4.

The two following sections explain in more detail the track and the vertex fitting procedure and the error propagation. Afterwards the determination of the point errors needed for the straight line fits of the tracks is addressed. This is followed by a discussion of the *bep* parameter. The chapter will finish with additional corrections used in the analysis.

7.1 Track Fit

The tracks used in this analysis are obtained by fitting a straight line through two hits in the Silicon Drift Detector system, and an additional point obtained from the TPC. The fit is based on the Least Square Method and it is performed independently in the x-z and y-z planes. In this section the analytical solution of the problem will be discussed. Here, only the x-z plane will be considered. The treatment of the problem in the y-z plane is

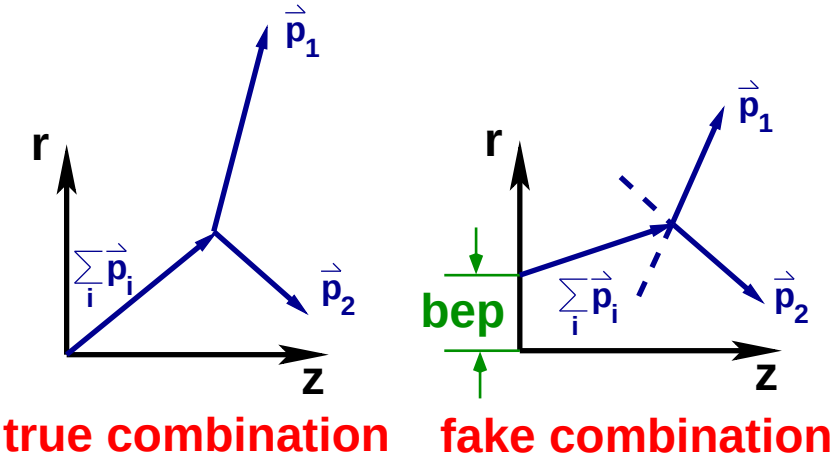

Figure 7.4: **Back extrapolated momentum vector.** *The momentum of a D^0 meson is the sum of its decay products $\sum \vec{p}_i$. This vector must point back to the primary interaction region for a true track combination. As a measurand the bep parameter is defined as the radial distance between the back extrapolated momentum vector and the primary interaction region.*

identical.

The general task is to describe a sample of N measured data points (x_i, z_i) by a function $f(z; a_1, a_2, \ldots, a_n)$ and to determine the unknown parameters $a_1, a_2, \ldots, a_n$. The number N of measured data points must be greater than the number n of parameters. Further, it is assumed that the measurement of the values x_i at the points z_i have the uncertainties σ_i. The method of least squares states that the best values of a_j are those for which the sum

$$\chi^2 = \sum_{i=1}^{N} \left[\frac{x_i - f(z_i; a_j)}{\sigma_i} \right]^2 \tag{7.1}$$

is minimal. Examining equation (7.1) it is clear that it just describes the sum of the squared deviations of the data points from the curve $f(z_i; a_j)$ weighted by the respective errors on x_i. To find the values of a_j, the system of equations

$$\frac{\partial \chi^2}{\partial a_j} = 0 \tag{7.2}$$

must be solved. In the case of functions linear in their parameters a_j, i.e. with no terms which are products or ratios of different a_j, equation (7.2) can be solved analytically. A straight line is one example of a linear function.

A straight line in the x-z plane is defined by slope x' and an intercept x_0:

$$x(z) = x'z + x_0. \tag{7.3}$$

Here x' and x_0 stand for the unknown parameters a_1 and a_2 to be determined. As mentioned at the beginning of this section, the number of data points N is 3 (two SiDC

hits and one TPC point). Equation (7.1) then can be written as

$$\chi^2 = \sum_{i=1}^{3} \left[\frac{x_i - x'z - x_0}{\sigma_i} \right]^2 . \tag{7.4}$$

Taking the partial derivatives with respect to x' and x_0 results in

$$\begin{aligned} \frac{\partial \chi^2}{\partial x'} &= -2 \sum_{i=1}^{3} \frac{(x_i - x'z_i - x_0) z_i}{\sigma_i^2}, \\ \frac{\partial \chi^2}{\partial x_0} &= -2 \sum_{i=1}^{3} \frac{(x_i - x'z_i - x_0)}{\sigma_i^2}. \end{aligned} \tag{7.5}$$

To simplify the notation, the following terms are defined:

$$\begin{aligned} B = \sum \tfrac{z_i}{\sigma_i^2}, \quad A = \sum \tfrac{1}{\sigma_i^2}, \quad C = \sum \tfrac{x_i}{\sigma_i^2}, \\ D = \sum \tfrac{z_i^2}{\sigma_i^2}, \quad E = \sum \tfrac{z_i x_i}{\sigma_i^2}, \quad F = \sum \tfrac{x_i^2}{\sigma_i^2}. \end{aligned} \tag{7.6}$$

Using these definitions, equation (7.6) becomes

$$E - x'D - x_0 B = 0, \tag{7.7}$$

$$C - x'B - x_0 A = 0, \tag{7.8}$$

and leads to the solutions

$$x' = \frac{AE - CB}{AD - B^2} \quad \text{and} \quad x_0 = \frac{DC - BE}{AD - B^2}. \tag{7.9}$$

Finally, assuming to have obtained the best estimates for the unknown parameters x' and x_0, it is necessary to determine their uncertainties. These can be extracted by inverting the Hessian matrix

$$\mathbf{H} = \begin{pmatrix} H_{11} & H_{12} \\ H_{21} & H_{22} \end{pmatrix}, \tag{7.10}$$

which contains the second derivatives:

$$H_{11} = \frac{1}{2}\frac{\partial^2 \chi^2}{\partial x'^2}, \quad H_{22} = \frac{1}{2}\frac{\partial^2 \chi^2}{\partial x_0^2}, \quad \text{and} \quad H_{12} = H_{21} = \frac{1}{2}\frac{\partial^2 \chi^2}{\partial x' \partial x_0}. \tag{7.11}$$

The inverse of the Hessian matrix is the covariance matrix,

$$\mathbf{V} = \mathbf{H}^{-1} = \frac{1}{H_{11}H_{22} - H_{12}^2} \begin{pmatrix} H_{22} & -H_{12} \\ -H_{12} & H_{11} \end{pmatrix}, \tag{7.12}$$

from which the variances $\sigma_{x'x'}$, $\sigma_{x_0 x_0}$ and the covariance $\sigma_{x'x_0}$ are obtained:

$$\begin{aligned} \sigma_{x'x'} &= \frac{A_{22}}{A_{11}A_{22} - A_{12}^2} = \frac{A}{AD - B^2} \\ \sigma_{x_0 x_0} &= \frac{A_{22}}{A_{11}A_{22} - A_{12}^2} = \frac{D}{AD - B^2} \\ \sigma_{x'x_0} &= \frac{-A_{12}}{A_{11}A_{22} - A_{12}^2} = \frac{-B}{AD - B^2} = \sigma_{x_0 x'}. \end{aligned} \tag{7.13}$$

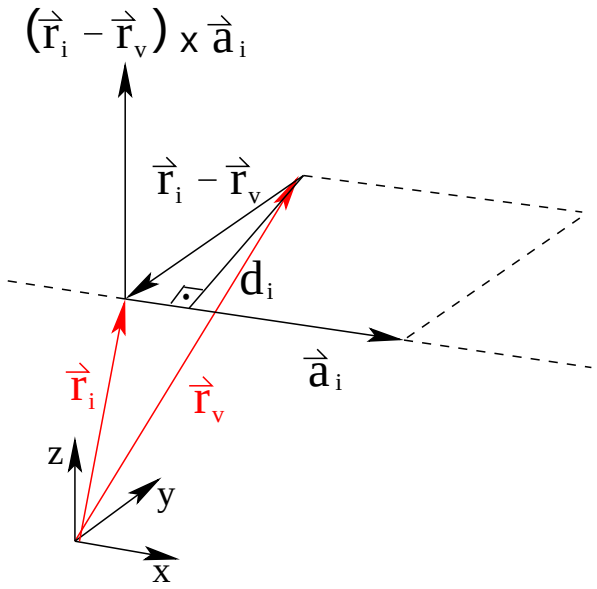

Figure 7.5: **Vectors used in the secondary vertex fit algorithm.** *$\vec{r}_i$ is the position vector of the i^{th} track, $\vec{a}_i$ is its direction vector. $\vec{r}_v$ is the vector pointing to the secondary vertex. d_i is the distance between the i^{th} track and the secondary vertex.*

7.2 Secondary Vertex Fit

The secondary vertex fit algorithm implemented within the framework of this thesis also uses the Least Square Method. It calculates the point of closest approach between a given number of N tracks in 3-dimensional space coordinates. A similar procedure was already used in the HADES experiment for the target reconstruction [80]. The mathematics behind it are described in the following.

Each track is defined by a straight line and can be written as:

$$\vec{x}_i = \vec{r}_i + t \cdot \vec{a}_i \quad \forall i : 1 \cdots N, \tag{7.14}$$

where $\vec{r}_i$ is the position vector of the i^{th} track, $\vec{a}_i$ is its direction vector and t is a parameter ($t \in \Re$). Let $\vec{r}_v$ be the vector pointing to the secondary vertex. The two vectors $(\vec{r}_i - \vec{r}_v)$ and $\vec{a}_i$ span a parallelogram with $|(\vec{r}_i - \vec{r}_v) \times \vec{a}_i|$ being equal to its area (see figure 7.5). On the other hand, the area of a parallelogram is also given by multiplying its base with its height, where the base is just $|\vec{a}_i|$ and the height is the distance d_i between the track and the secondary vertex. Hence, the distance is:

$$d_i = |(\vec{r}_i - \vec{r}_v) \times \hat{a}_i|, \quad \text{with} \quad \hat{a}_i = \frac{\vec{a}_i}{|\vec{a}_i|}. \tag{7.15}$$

The point of closest approach between all tracks is given as that point, where the distances d_i to each of the N tracks, normalized by their uncertainties σ_i, become minimal:

$$\frac{\partial \chi^2}{\partial x_v} = \frac{\partial \chi^2}{\partial y_v} = \frac{\partial \chi^2}{\partial z_v} = 0 \quad \text{with} \quad \chi^2 = \sum_{i=1}^{N} \frac{d_i^2}{\sigma_i^2} \tag{7.16}$$

The uncertainties σ_i assign a weight to the i^{th} track in the determination of the vertex. Assuming the uncertainties σ_i to be constant, the problem can be solved analytically.

The expression for d_i^2 can be extracted from equation (7.15):

$$\begin{aligned} d_i^2 = &[(y_i - y_v)a_{zi} - (z_i - z_v)a_{yi}]^2 + \\ &[(z_i - z_v)a_{xi} - (x_i - x_v)a_{zi}]^2 + \\ &[(x_i - x_v)a_{yi} - (y_i - y_v)a_{xi}]^2 \end{aligned} \tag{7.17}$$

Calculating the derivatives of equation (7.16) one obtains:

$$\begin{aligned} \frac{\partial\chi^2}{\partial x_v} &= \sum_{i=1}^{N} \frac{2}{\sigma_i^2}\{[(z_i - z_v)a_{xi} - (x_i - x_v)a_{zi}]a_{zi} - [(x_i - x_v)a_{yi} - (y_i - y_v)a_{xi}]a_{yi}\} = 0 \\ \frac{\partial\chi^2}{\partial y_v} &= \sum_{i=1}^{N} \frac{2}{\sigma_i^2}\{[(x_i - x_v)a_{yi} - (y_i - y_v)a_{xi}]a_{xi} - [(y_i - y_v)a_{zi} - (z_i - z_v)a_{yi}]a_{zi}\} = 0 \\ \frac{\partial\chi^2}{\partial z_v} &= \sum_{i=1}^{N} \frac{2}{\sigma_i^2}\{[(y_i - y_v)a_{zi} - (z_i - z_v)a_{yi}]a_{yi} - [(z_i - z_v)a_{xi} - (x_i - x_v)a_{zi}]a_{xi}\} = 0 \end{aligned} \tag{7.18}$$

By rearranging the variables in the system of equations (7.18), and by defining the following matrices

$$\mathbf{A} = \sum_{i=1}^{N} \frac{2}{\sigma_i^2}\mathbf{A}_i = \sum_{i=1}^{N} \frac{2}{\sigma_i^2} \begin{pmatrix} a_{yi}^2 + a_{zi}^2 & -a_{xi}a_{yi} & -a_{xi}a_{zi} \\ -a_{yi}a_{xi} & a_{xi}^2 + a_{zi}^2 & -a_{yi}a_{zi} \\ -a_{zi}a_{xi} & -a_{zi}a_{yi} & a_{yi}^2 + a_{xi}^2 \end{pmatrix} \tag{7.19}$$

and

$$\mathbf{B} = \mathbf{A} \begin{pmatrix} x_i \\ y_i \\ z_i \end{pmatrix}, \tag{7.20}$$

equations (7.18) can be written in matrix notation as

$$\mathbf{A} \begin{pmatrix} x_v \\ y_v \\ z_v \end{pmatrix} = \mathbf{B} \Rightarrow \begin{pmatrix} x_v \\ y_v \\ z_v \end{pmatrix} = \mathbf{A}^{-1}\mathbf{B} \tag{7.21}$$

and thus be solved to obtain the vertex coordinates.

A complication emerges with the fact, that the σ_i's in equation (7.18) are indeed not constant. One has to consider that the track fit, described in section 7.1, itself already comprises uncertainties. Thus, the values of σ_i are dependent on the distances d_i. They can be determined by error propagation:

$$\sigma_i^2(d_i) = \left(\frac{\partial d_i}{\partial x_0}, \frac{\partial d_i}{\partial y_0}, \frac{\partial d_i}{\partial x'}, \frac{\partial d_i}{\partial y'}\right) \begin{pmatrix} \sigma_{x_0x_0} & 0 & \sigma_{x_0x'} & 0 \\ 0 & \sigma_{y_0y_0} & 0 & \sigma_{y_0y'} \\ \sigma_{x'x_0} & 0 & \sigma_{x'x'} & 0 \\ 0 & \sigma_{y'y_0} & 0 & \sigma_{y'y'} \end{pmatrix} \begin{pmatrix} \frac{\partial d_i}{\partial x_0} \\ \frac{\partial d_i}{\partial y_0} \\ \frac{\partial d_i}{\partial x'} \\ \frac{\partial d_i}{\partial y'} \end{pmatrix} \tag{7.22}$$

In this notation x_0, y_0 denote the axis intercept of the track and x', y' the slopes. $\sigma_{kl} = \sigma_{lk}$ stand for the covariances of the track fit in the case of $k \neq l$ and for the variances in the

case of $k = l$. The track fit is performed independently for the x-z and y-z planes. Therefore the covariances $\sigma_{x_0y_0}$, $\sigma_{x_0y'}$, $\sigma_{x'y_0}$ and $\sigma_{x'y'}$ do not contribute to the covariance matrix in equation (7.22). The slopes x', y' can be expressed in terms of the unit direction vector $\hat{a}_i$:

$$x' = \tfrac{a_x}{a_z} \quad \text{and} \quad y' = \tfrac{a_y}{a_z}. \tag{7.23}$$

Using $\vec{\Delta}_i = (\vec{r}_i - \vec{r}_v)$ as abbreviation, equation 7.17 can be rewritten as:

$$\begin{aligned} d_i^2 &= [\Delta_{yi}a_{zi} - \Delta_{zi}a_{yi}]^2 + [\Delta_{zi}a_{xi} - \Delta_{xi}a_{zi}]^2 + [\Delta_{xi}a_{yi} - \Delta_{yi}a_{xi}]^2 \\ &= (\Delta_{zi}^2 - \Delta_{xi}^2)a_{xi}^2 + (\Delta_{zi}^2 - \Delta_{yi}^2)a_{yi}^2 + \Delta_{xi}^2 + \Delta_{yi}^2 \\ &\quad -2(\Delta_{yi}\Delta_{zi}a_{yi}a_{zi}) + \Delta_{xi}\Delta_{zi}a_{xi}a_{zi} + \Delta_{xi}\Delta_{yi}a_{xi}a_{yi}. \end{aligned} \tag{7.24}$$

The next concern are the derivatives $(\partial d_i/\partial x_0)$, $(\partial d_i/\partial y_0)$, $(\partial d_i/\partial x')$ and $(\partial d_i/\partial y')$. For simplicity first the derivatives with respect to a_x and a_y will be computed instead of x' and y'. Using the expressions

$$(d^2)' = 2dd' \Rightarrow d' = \frac{(d^2)'}{2d} \tag{7.25}$$

and

$$\frac{\partial a_z}{\partial a_x} = -\frac{a_x}{a_z}, \; \frac{\partial a_z}{\partial a_y} = -\frac{a_y}{a_z} \quad \text{with} \quad a_z^2 = 1 - a_x^2 - a_y^2 \tag{7.26}$$

one finally obtains:

$$\begin{aligned} \frac{\partial d_i}{\partial x_0} &= \frac{(1-a_{xi}^2)\Delta_{xi} - a_{xi}(\Delta_{zi}a_{zi} + \Delta_{yi}a_{yi})}{d_i} \\ \frac{\partial d_i}{\partial y_0} &= \frac{(1-a_{yi}^2)\Delta_{yi} - a_{yi}(\Delta_{zi}a_{zi} + \Delta_{xi}a_{xi})}{d_i} \\ \frac{\partial d_i}{\partial a_{xi}} &= \frac{(\Delta_{zi}^2 - \Delta_{xi}^2)a_{xi} + \frac{\Delta_{yi}\Delta_{zi}a_{yi}a_{xi}}{a_{zi}} + \frac{\Delta_{xi}\Delta_{zi}a_{xi}^2}{a_{zi}} - \Delta_{xi}\Delta_{zi}a_{zi} - \Delta_{xi}\Delta_{yi}a_{yi}}{d_i} \\ \frac{\partial d_i}{\partial a_{yi}} &= \frac{(\Delta_{zi}^2 - \Delta_{yi}^2)a_{yi} - \Delta_{yi}\Delta_{zi}a_{zi} + \Delta_{yi}\Delta_{zi}\frac{a_{yi}^2}{a_{zi}} + \Delta_{xi}\Delta_{zi}\frac{a_{xi}a_{yi}}{a_{zi}} - \Delta_{xi}\Delta_{yi}a_{xi}}{d_i}. \end{aligned} \tag{7.27}$$

The derivatives $\partial d_i/\partial x'$ and $\partial d_i/\partial y'$ can now be retrieved by:

$$\begin{aligned} \frac{\partial d_i}{x'} &= \frac{\partial d_i}{\partial a_{xi}}\frac{\partial a_{xi}}{\partial x'} + \frac{\partial d_i}{\partial a_{yi}}\frac{\partial a_{yi}}{\partial x'} = \frac{\partial d_i}{\partial a_{xi}}\frac{1-a_{xi}^2}{L} - \frac{\partial d_i}{\partial a_{yi}}\frac{x'y'}{L^3} \\ \frac{\partial d_i}{y'} &= \frac{\partial d_i}{\partial a_{xi}}\frac{\partial a_{xi}}{\partial y'} + \frac{\partial d_i}{\partial a_{yi}}\frac{\partial a_{yi}}{\partial y'} = -\frac{\partial d_i}{\partial a_{xi}}\frac{x'y'}{L^3} + \frac{\partial d_i}{\partial a_{yi}}\frac{1-a_{yi}^2}{L}, \end{aligned} \tag{7.28}$$

where

$$\begin{aligned} L^2 &= x'^2 + y'^2 + 1 \\ &= \frac{a_{xi}^2}{a_{zi}^2} + \frac{a_{yi}^2}{a_{zi}^2} + \frac{a_{zi}^2}{a_{zi}^2} \\ &= \frac{1}{a_{zi}^2} \end{aligned} \tag{7.29}$$

was used. The uncertainties σ_i can now be computed with equation (7.22). The fact that the vertex coordinates appear in the expression for σ_i has the consequence that the problem does not have an analytical solution anymore. Therefore an iterative minimization procedure is needed.

In the first iteration the values for the uncertainties σ_i are set to be constant. A first guess of the vertex position can then be obtained solving equation (7.21). Under the assumption that the σ_i change only slowly with the vertex, their values can be computed in the next iteration by using the vertex position from the previous one. This procedure is repeated until a convergence criterion is fulfilled. This criterion was chosen such that the computation stops if the changes in the vertex position become smaller than $\epsilon = 0,01$ μm. Typically three iterations are needed in order to reach this condition.

7.3 Resolution of the Detectors

The errors of the points needed as input for the straight line fits mentioned in section 7.1 are extracted from the matching between the track segments of each detector. The matching is performed in polar coordinates as most of the tracks come from the targets. Once the resolution of the detectors is determined, the point errors are determined by coordinate transformation $\sigma_x(\phi, \theta, z, \sigma_\phi, \sigma_\theta)$ and $\sigma_y(\phi, \theta, z, \sigma_\phi, \sigma_\theta)$.

The errors are extracted from the azimuthal angle difference $\Delta\phi = \phi_{SiDC1}^{hit} - \phi_{SiDC2}^{hit}$ between the hits in the two Silicon Drift Detectors and $\Delta\phi = \phi_{SiDC}^{track} - \phi_{TPC}^{track}$ between the SiDC and TPC track segments. The same applies for the polar angle difference $\Delta\theta$. These matching distributions are parameterized as a function of the momentum p and as a function of the polar angle θ. Furthermore the hits in the SiDC are classified in single anode (sgl) and multi anode (mlt) hits. The background was determined by a random rotation of the hits in SiDC2 and the track segments in the TPC, respectively. Figure 7.6 shows some examples of background subtracted matching distributions. They are fitted with a sum of two Gaussians. The width σ is defined as 68.3% of the total integral.

Under the assumption that the Silicon Drift Detectors have equal properties, the SiDC resolution is given by

$$\sigma_{SiDC}^{mlt} = \sqrt{\frac{1}{2}(\sigma_{SiDC1,SiDC2}^{mlt,mlt})^2} \tag{7.30}$$

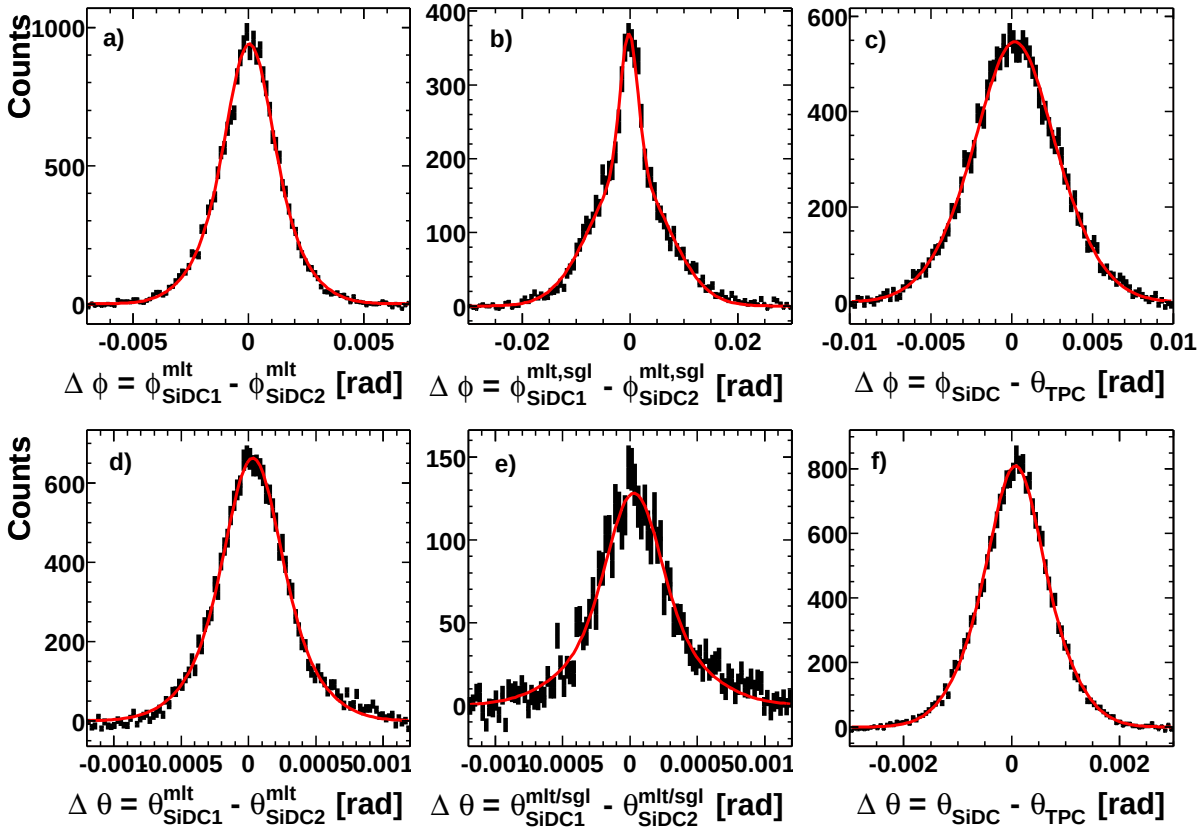

Figure 7.6: **Azimuthal and polar matching.** *The upper three plots a), b) and c) show the azimuthal matching distributions $\Delta\phi$ for a momentum range between 4 and 5 GeV/c and a range of the polar angle θ between 11° to 12°. The lower three plots d), e) and f) show the same for the polar matching distributions $\Delta\theta$. Plots a) and d) show the hit matching between the two SiDC detectors, only considering multi anode hits. The same is plotted for a combination of a multi with a single anode hit in b) and e). The track matching between the SiDC and the TPC is shown in c) and f).*

for multi anode hits, and by

$$\sigma^{sgl}_{SiDC} = \sqrt{(\sigma^{mlt,sgl}_{SiDC1,SiDC2})^2 - (\sigma^{mlt}_{SiDC})^2} \tag{7.31}$$

for single anode hits. The resolution of the TPC is

$$\sigma_{TPC} = \sqrt{(\sigma^{track}_{SiDC,TPC})^2 - \frac{1}{4}(\sigma^{mlt,mlt}_{SiDC1,SiDC2})^2} \tag{7.32}$$

if only SiDC track segments with multi anode hits are used.

The values for the detector resolution obtained in this way are summarized in figure 7.7. The resolution of the SiDC detectors is about $\sigma_\phi = 1$ mrad in the azimuthal coordinate and $\sigma_\theta = 0.2$ mrad in the polar coordinate for multi anode hits. As expected the resolution of single anode hits remains equal for σ_θ but deteriorates significantly for

		$\sigma_\phi : C_0$	$\sigma_\phi : C_1$	$\sigma_\theta : C_0$	$\sigma_\theta : C_1$
SiDC multi anode	$8° < \theta < 10°$	0.001160	0.000794	0.000198	0.000130
	$10° < \theta < 11°$	0.000995	0.000810	0.000192	0.000139
	$11° < \theta < 12°$	0.000916	0.000836	0.000190	0.000154
	$12° < \theta < 13°$	0.000848	0.000928	0.000189	0.000167
	$13° < \theta < 15°$	0.000863	0.000787	0.000193	0.000178
SiDC single anode	$8° < \theta < 10°$	0.006759	0.000794	0.000249	0.000130
	$10° < \theta < 11°$	0.005741	0.000810	0.000230	0.000139
	$11° < \theta < 12°$	0.005193	0.000836	0.000168	0.000154
	$12° < \theta < 13°$	0.004516	0.000928	0.000193	0.000181
	$13° < \theta < 15°$	0.003543	0.000787	0.000203	0.000178
TPC	$8° < \theta < 10°$	0.002487	0.010029	0.000659	0.001381
	$10° < \theta < 11°$	0.002176	0.008810	0.000588	0.001378
	$11° < \theta < 12°$	0.001943	0.008426	0.000543	0.001465
	$12° < \theta < 13°$	0.001794	0.007893	0.000498	0.001623
	$13° < \theta < 15°$	0.001738	0.007753	0.000669	0.001623

Table 7.1: **Fit parameters of the detector resolution.** *The table contains the values for the fit parameter C_0 and C_1 according to equation (7.33) and figure 7.7.*

σ_ϕ. The steep rise of the TPC resolution for low momenta has its origin due to multiple scattering in the RICH2 mirror. For high momenta the TPC can reach a resolution of $\sigma_\phi = 2.3$ mrad and $\sigma_\theta = 0.6$ mrad. The strong dependence of the TPC resolution on the polar angle θ is explained by diffusion, which affects electron clouds with long path length. Additionally the decreasing number of hits per tracks in the TPC has an impact on the resolution in the outer range $13° < \theta < 15°$.

The resolution was fitted with the function

$$\sigma = \sqrt{(C_0)^2 + \left(\frac{C_1}{p}\right)^2}. \tag{7.33}$$

The first term refers to the constant point resolution of the detector. The second term describes the deterioration of the resolution due to multiple scattering which predominantly effects the TPC at low momentum. The coefficients C_0 and C_1 are listed in table 7.1.

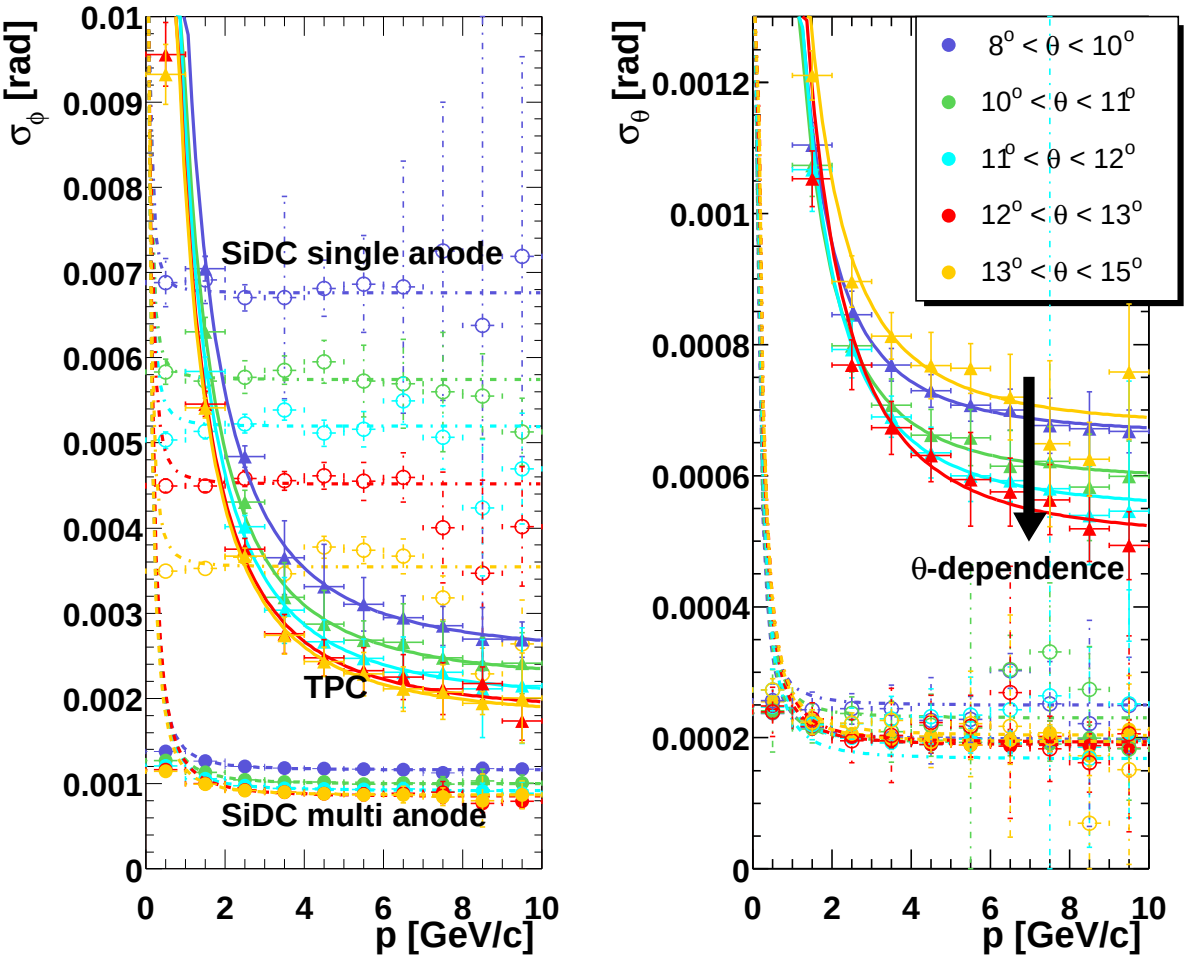

Figure 7.7: **Detector resolution versus momentum.** *The left plot shows the azimuthal angle resolution σ_ϕ of SiDC multi anode hits (filled circle), SiDC single anode hits (open circles) and of the TPC (filled triangles). The right plot shows the same for the polar angle resolution σ_θ. The resolution is plotted as a function of the momentum p and of the polar angle θ.*

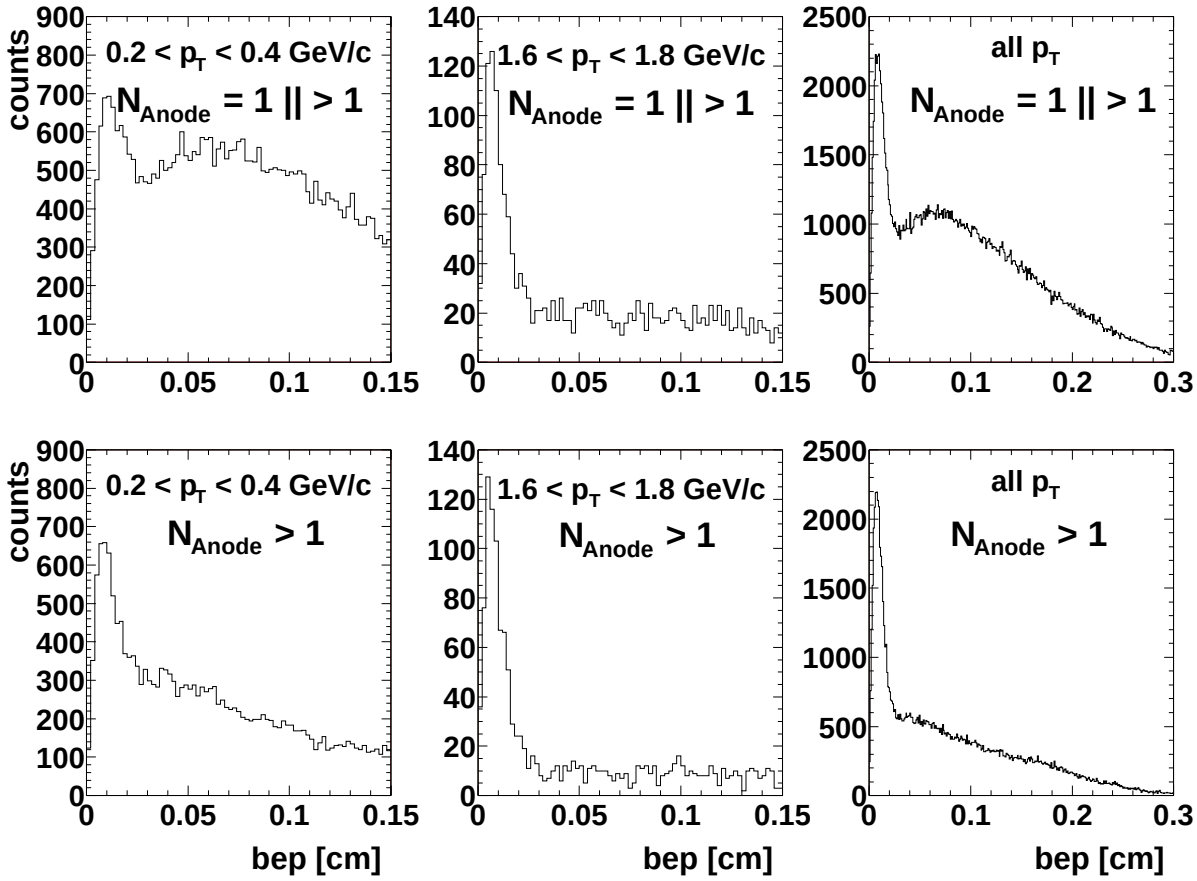

Figure 7.8: **bep parameter versus momentum and number of anodes.** *The figures show the bep parameter in overlay Monte Carlo for different pair p_T selections. The upper row is plotted for tracks with at least one single anode hit in the SiDC detectors. The lower row contains only tracks with multi anode hits.*

7.4 Back Extrapolated Momentum Vector

The momentum vector of a mother particle is given by the sum of the momentum vectors of its daughters. This vector should point back to the primary interaction region in one of the targets (compare figure 7.4). This is quantified by the radial distance between the back extrapolated momentum vector of the mother particle to the primary interaction region and denominated as *bep* parameter.

The measurement of the absolute momentum of a particle is performed with the TPC, as described in chapter 5. In this analysis the individual components p_x, p_y, and p_z are recalculated by multiplying the momentum with the unit slope vector obtained from the track fits. Thus the *bep* parameters depends strongly on the momentum resolution in the TPC and the pointing resolution of the track fits, as can be seen in figure 7.8.

A large fraction of 67% from all two track combinations contain tracks with at least one single anode hit in the Silicon Drift Detectors. It is thus clear that a cut excluding these tracks in order to improve vertex resolution implies a significant loss of statistics.

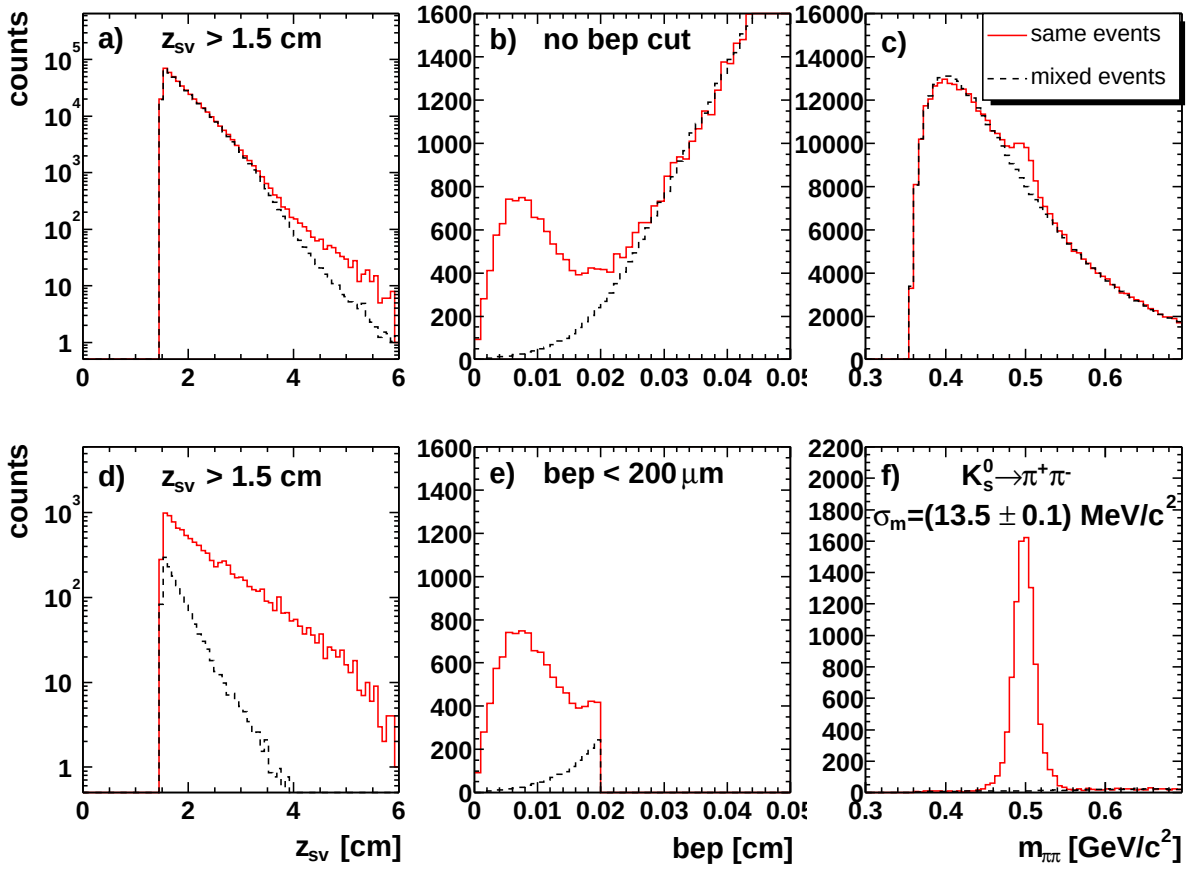

Figure 7.9: **Background suppression by a bep parameter cut.** *The plots show a* $K^0_S \to \pi^+\pi^-$ *analysis of* 3.4 *million events, once without using a bep parameter cut (upper row) and once requiring bep* < 200 *μm (lower row). Plots a) and d) show the distribution of the secondary vertex* z_{sv} *coordinate, b) and e) show the distribution of the bep parameter, and c) and f) the invariant mass spectra.*

The remaining 33% belong to tracks with multi anode hits. Of these only 28% have a *bep* parameter smaller than 200 μm. For the track combinations containing at least one single anode hit this number is 16%. The right part of the distribution with *bep* > 200 μm originates from mismatches between the TPC and the SiDC track segments or from mismatches between the hits in SiDC1 and SiDC2. It is removed by applying a cut on the χ^2 probability of the straight line fits of the tracks, which will be explained in detail in section 8.2.6.

The power of the *bep* parameter cut is demonstrated in figure 7.9. It shows a $K^0_S \to \pi^+\pi^-$ analysis once without a *bep* parameter cut and once with a cut of *bep* < 200 μm. For pairs of primary particles the *bep* parameter has by definition small values and therefore it is only a useful quantity if in addition a cut on the secondary vertex z_{sv} coordinate is applied. In figure 7.9 a cut of $z_{sv} > 1.5$ cm is chosen. Furthermore, a cut of $p_T > 200$ MeV/c was required on the single track transverse momentum and an opening angle cut of $\psi > 0.1$ rad. Only track and secondary vertex fits are considered which passed a χ^2 probability cut of $P_{\chi^2} > 0.01$. Contamination in the invariant

mass spectrum from misidentified Λ baryons is cleaned by an Armenteros-Podolanski cut of $q_T > 0.11$ MeV/c (see appendix A). Tracks containing single anode hits in the SiDC detectors are excluded. The background is drawn as dashed line and is obtained by the mixed events technique (see section 8.3.1 for more details). No particle identification via dE/dx in the TPC is used. The invariant mass spectra in figure 7.9 are plotted assuming that all tracks have the pion mass. For 3.4 million analyzed events the application of the *bep* parameter cut is able to improve the significance $S/\sqrt{B}$ from 31 to 733.

7.5 Additional Corrections

The present analysis is sensitive to the secondary vertex resolution. Therefore, two additional corrections are applied on top of the overall calibration. The first one is the determination of a matching correction between a TPC and a SiDC track segment [79]. The distribution $\Delta\phi = \phi_{SiDC} - \phi_{TPC}$ is plotted differentially as a function of the azimuthal and polar angle ϕ and θ, and as a function of the inverse momentum $1/p$ and the numbers of responding anodes in the SiDC detectors. The matching correction cor^{ϕ}_{match} is determined as the shift of the mean value of the distributions from zero. The same applies for cor^{θ}_{match}.

Under the assumption that the precision of the SiDC detectors is higher, the matching correction is added to ϕ_{TPC} and θ_{TPC}, respectively. The correctness of this statement can be judged from figure 7.10. It shows a comparison of the azimuthal angle distribution of the TPC before and after application of the matching correction. The tracks used for the plots are fitted according to section 7.1. It can be observed that the borders to dead pads or front-end-boards become sharper once the correction is applied. The slight valley in the distribution around $-2 < \phi_{TPC} < 0$ and $2.25 < \phi_{TPC} < 2.5$ rad can be ascribed to inefficiencies in the SiDC detectors. They develop if only multi anode hits are required.

The second correction is the determination of the nonlinearities in the SiDC detectors following the work described in section 6.4. Unfortunately, the SiDC track segment cannot be used as an approximation for the true value ϕ_{true} because it is obtained from only two hits. As a replacement the TPC track segment is used. The nonlinearities for the SiDC detector are derived by plotting $\Delta\phi = \phi_{TPC,track} - \phi_{SiDC,hit}$ versus a fraction of an anode. The correction is determined separately for SiDC1 and SiDC2, for positive and negative magnetic field and for 2 and 3 anode clusters. The correction needed for the hits is < 0.1 mrad for SiDC1 and < 0.2 mrad for SiDC2.

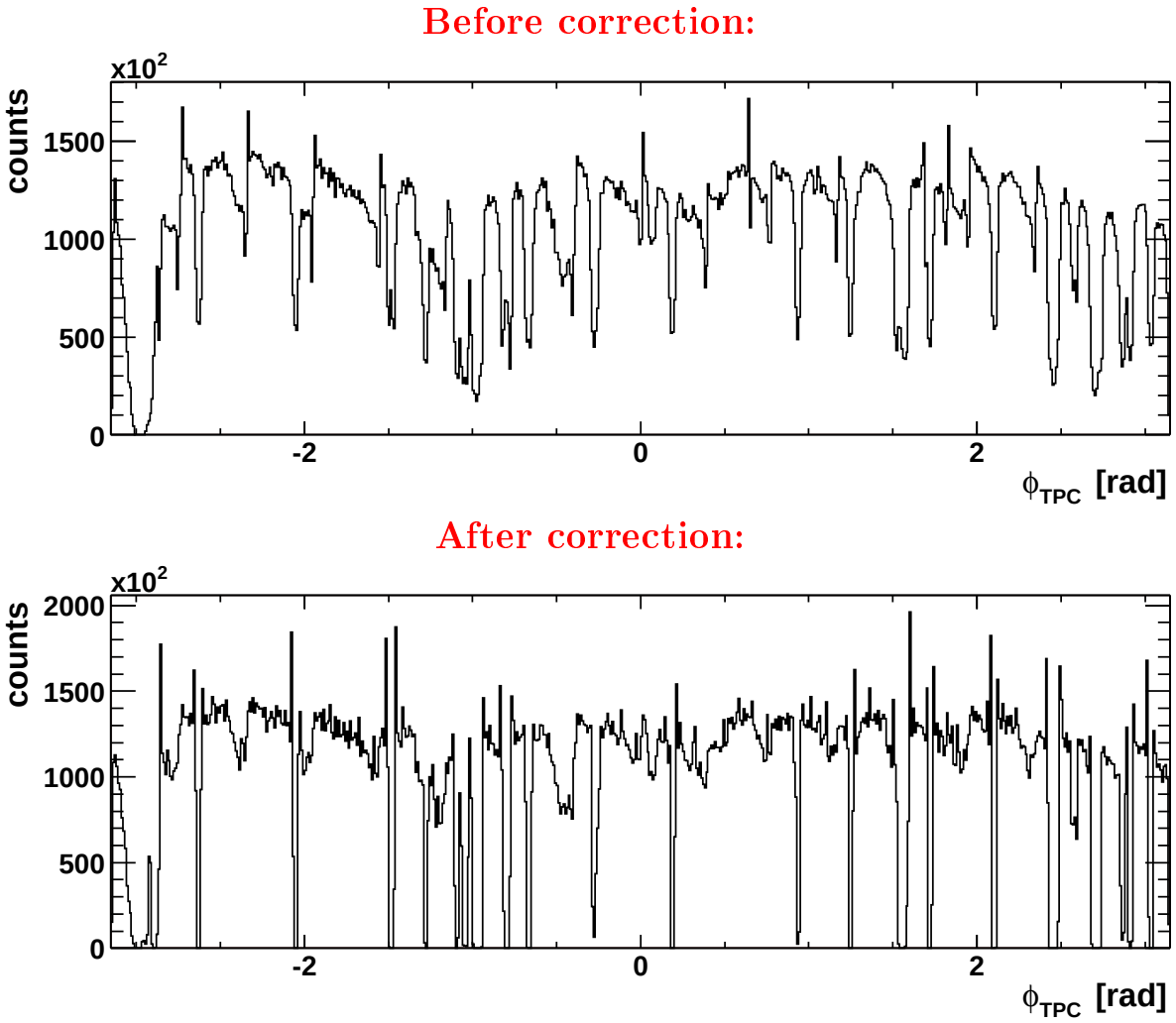

Figure 7.10: **Improvements due to matching correction.** *The azimuthal angle of the TPC is plotted for tracks constructed with the procedure described in section 7.1. If the matching correction is applied to the third fit point obtained from the TPC, the dips in the distribution become more pronounced.*

Chapter 8

Acceptance and Efficiency

Charm quarks are less frequently produced in hadronic collisions than strange quarks. It is therefore appropriate to test the secondary particle reconstruction scheme presented in the previous chapter with strange particles. The decay length has to be short to be able to reconstruct the secondary vertex within the limited region of 10.4 cm given by the distance between the first Silicon Drift Detector and the target area. The abundant K^0_S meson, decaying into two charged pions with a branching ratio of 68.95%, has a decay length of $c\tau = 2.68$ cm [66] and thus fulfills the required conditions.

The chapter starts with a detailed study of the acceptance and the efficiency using as reference the decay $K^0_S \to \pi^+\pi^-$. A measurement of the K^0_S rapidity density dN/dy and the inverse slope parameter T is presented and compared to existing measurements. In this way the systematic uncertainty of the efficiency is derived.

8.1 Acceptance

The acceptance in the CERES spectrometer is $8° < \theta < 14°$ for the polar angle at full azimuthal coverage. For the reconstruction of the secondary vertex it is in addition required that a particle decays upstream the first Silicon Drift Detector located 10.4 cm downstream the target system. The calculation of the number of particles falling in the acceptance of the spectrometer and passing SiDC1 is performed using a kinematic generator [81]. A schematic picture of the calculation is shown in figure 8.1. The decay point is marked with a small circle and has the coordinates (x_{sv}, y_{sv}, z_{sv}). Particles coming from $z_{sv} > 10.4$ cm are rejected. To consider the spectrometer acceptance one has to be aware that a simple cut on the polar angle is not suitable for secondary tracks. Therefore the angle θ is translated into a radius r at a distance

$$z_r = \frac{r_{max}}{\tan\theta_{max}} = \frac{130.8 \text{ cm}}{tan(14°)} = 542.61 \text{ cm}. \tag{8.1}$$

In this equation the maximal radius r_{max} is given by the outer barrel of the TPC. The minimal radius is given by $r_{min} = 73.7$ cm using $\theta_{min} = 8°$. Thus, a particle is accepted if its radius

$$r = \tan\theta_{sv} \cdot (z_r - z_{sv}) + r_{sv} \tag{8.2}$$

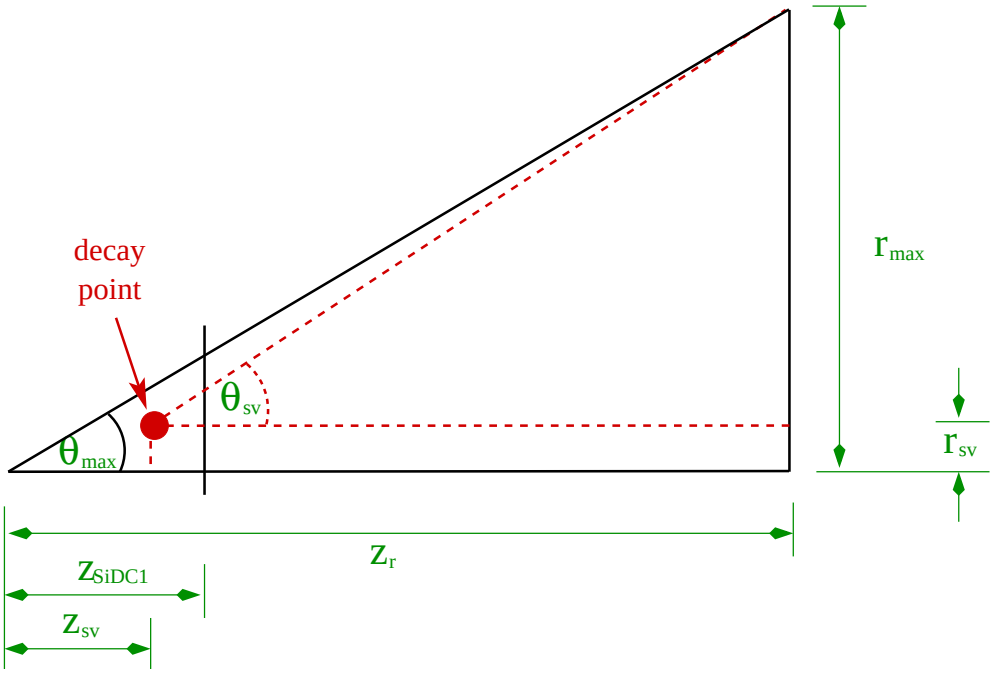

Figure 8.1: **Scheme for the calculation of the acceptance.** *The local angle θ_{sv} of a secondary track differs from the polar angle θ as determined from the origin of the coordinate system. Therefore the polar angle coverage of the spectrometer $\theta_{min} < \theta < \theta_{max}$ is translated into a radial coverage $r_{min} < r < r_{max}$ at the distance z_r.*

fulfills the condition 73.7 cm $< r <$ 130.8 cm at $z_r = 542.61$ cm.

8.2 Efficiency

The reconstruction efficiency of the $\overline{D}^0$ and the K^0_S meson is determined using a full overlay Monte Carlo simulation and applying the same cuts as in the analysis of the data. The error of the efficiency is given by the quality of the agreement between simulation and data which has to be verified.

This section starts with a description of the overlay Monte Carlo procedure, followed by a comparison of the relevant single track distributions between simulation and data. The momentum resolution is tested by measuring the mass resolution of the K^0_S. The vertex resolution is checked by reconstructing the targets using the secondary particle reconstruction scheme. Furthermore, a scan is performed for each individual cut and the results are compared to the simulation. The section ends with a description of the cut on the χ^2 probability of the straight line fits and its adjustment in the simulation.

8.2.1 Full Overlay Monte Carlo Simulation

The efficiency for the $\overline{D}^0$ analysis is determined with a full overlay Monte Carlo simulation. For this purpose 1 million $\overline{D}^0 \rightarrow K^+\pi^-$ decays are created using the aforemen-

tioned kinematic generator and requiring the conditions described in section 8.1. The transverse momentum distribution of the $\overline{D}^0$ is simulated with an inverse slope parameter of $T = 205$ MeV/c^2. The rapidity density is sampled with a Gaussian function of width $\sigma_y = 0.6$. These parameters are identical to those obtained from the PYTHIA event generator [47] described in more detail in section 9.2.

The decay kaons and pions are passed through a GEANT [68] simulation of the CERES spectrometer. The simulated particles are embedded into 50 different runs and reconstructed with the the C++ package COOL described in chapter 5. The selected runs sample the multiplicity distribution of the data taken during the beam time. The embedding of the simulation into real events is called overlay Monte Carlo. It provides a more realistic description of problems related to the large amount of background in a real event. The simulation is adjusted to describe the measured residuals of figure 6.22.

The rapidity density of the $\overline{D}^0$ meson, the opening angle and the secondary vertex distribution is shown in figure 8.2 as a function of the transverse momentum of the $\overline{D}^0$ meson. Within the acceptance of the CERES spectrometer the phase space between $2.1 < y < 2.5$ and $0 < p_T^{\overline{D}^0} < 1.6$ GeV/c^2 is occupied. The opening angle is large, starting at around 0.25 rad. The decay position of the $\overline{D}^0$ meson is in the range of few millimeters.

The efficiency is cross checked with the reference decay $K_S^0 \rightarrow \pi^+\pi^-$. The simulation of 1 million K_S^0 mesons is performed in the same way as described above. An inverse slope parameter of $T = 220$ MeV/c^2 is used, estimated from [82]. The width of the rapidity distribution is set to $\sigma_y = 1.2$ [83].

The same kinematic variables as in figure 8.2 are shown in figure 8.3 for the K_S^0 meson. The bulk of the K_S^0 mesons are reconstructed within a rapidity range of $2 < y < 2.5$ and a transverse momentum range of $0.1 < p_T^{K_S^0} < 1$ GeV/c. The opening angle in the spectrometer ranges from about 0.1 to 0.4 rad and is strongly anticorrelated with $p_T^{K_S^0}$. The decay position of the K_S^0 is reconstructable up to 5 cm.

8.2.2 Comparison of Single Track Variables

As starting point for efficiency checks the angular distribution of the tracks from the straight line fits (see section 7.1) are examined. This is shown in figure 8.4. The holes in the distribution are due to dead electronic devices either in SiDC1, SiDC2 or TPC. They are well reproduced by the simulation.

Another important issue is the number of single anode hits in the Silicon Drift Detectors. It has been shown in figure 7.7 that the resolution of single anode hits is worse than of multi anode hits. A different number of single anodes in the data than in the simulation would thus result in a different resolution of the secondary vertex and of the *bep* parameter. Although all dead anodes are included in the simulation, the distribution of the number of anodes shows differences between data and simulation. Therefore, 8% randomly selected anodes in SiDC1 are assigned to be a dead anode. SiDC2 is left unchanged. The distributions obtained after this adjustment are shown in figure 8.5.

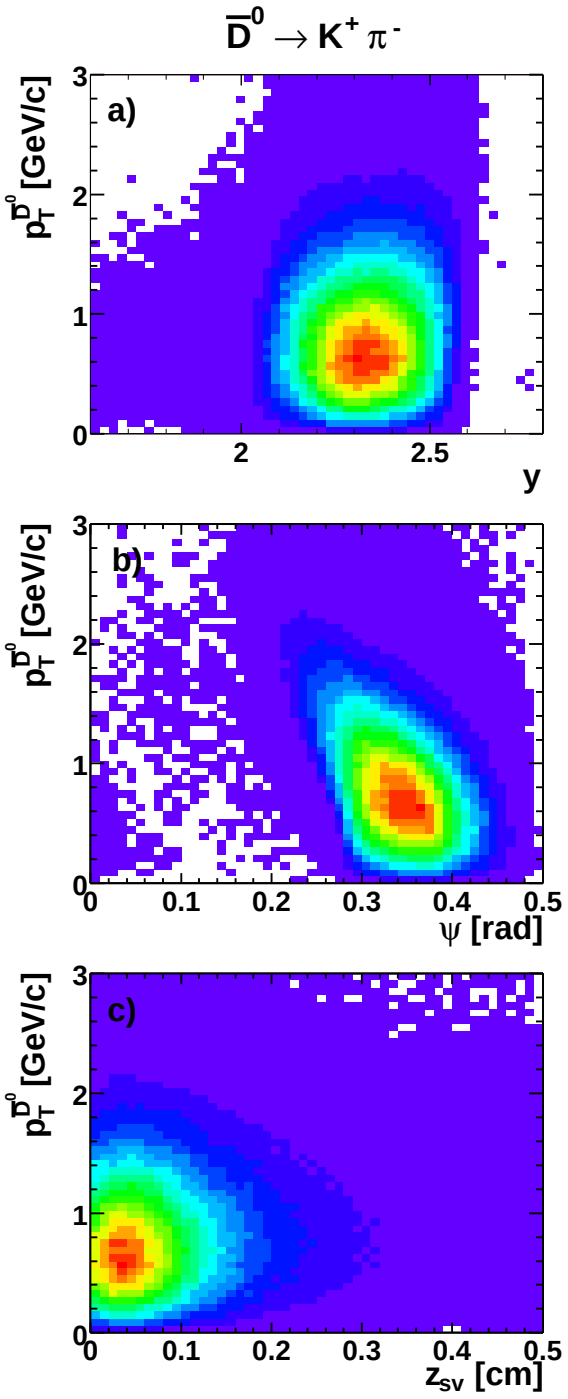

Figure 8.2: **Kinematic variables of the $\overline{\mathrm{D}}^0$.** *The plots show some kinematic variables of the $\overline{D}^0$ meson within the acceptance of the CERES spectrometer. (a) shows the rapidity, (b) the opening angle and (c) the decay point distribution versus the transverse momentum of the $\overline{D}^0$ meson.*

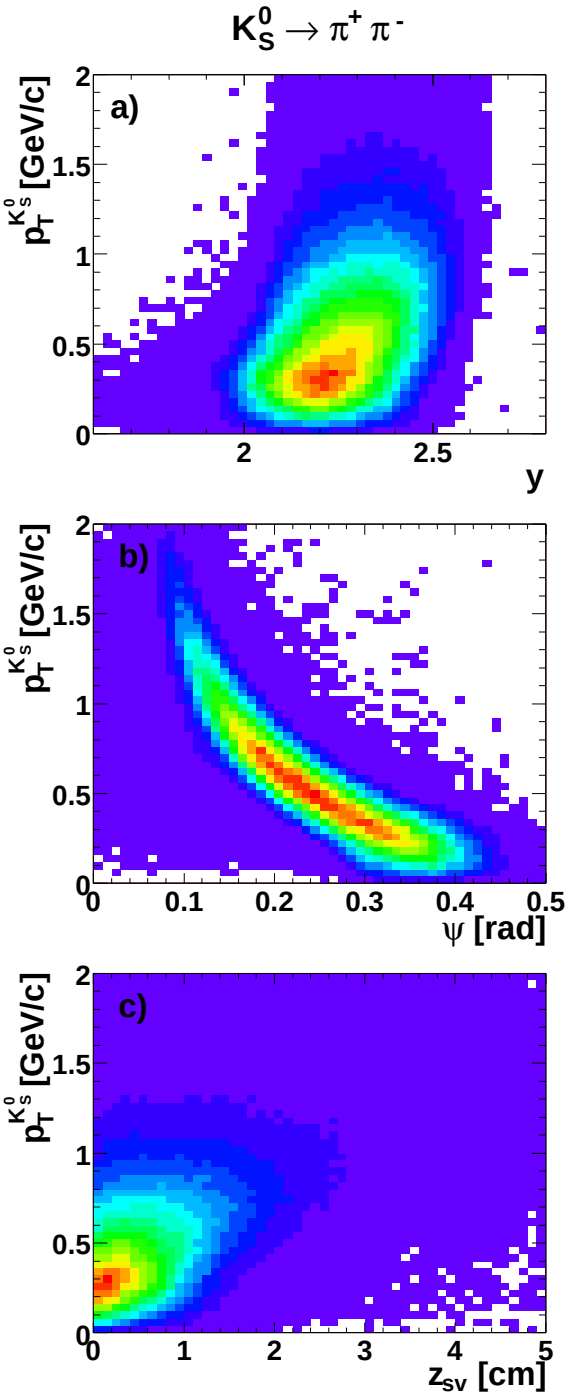

Figure 8.3: **Kinematic variables of the K_S^0.** *For comparison the plots show the same kinematic variables as figure 8.2 for the K_S^0 meson.*

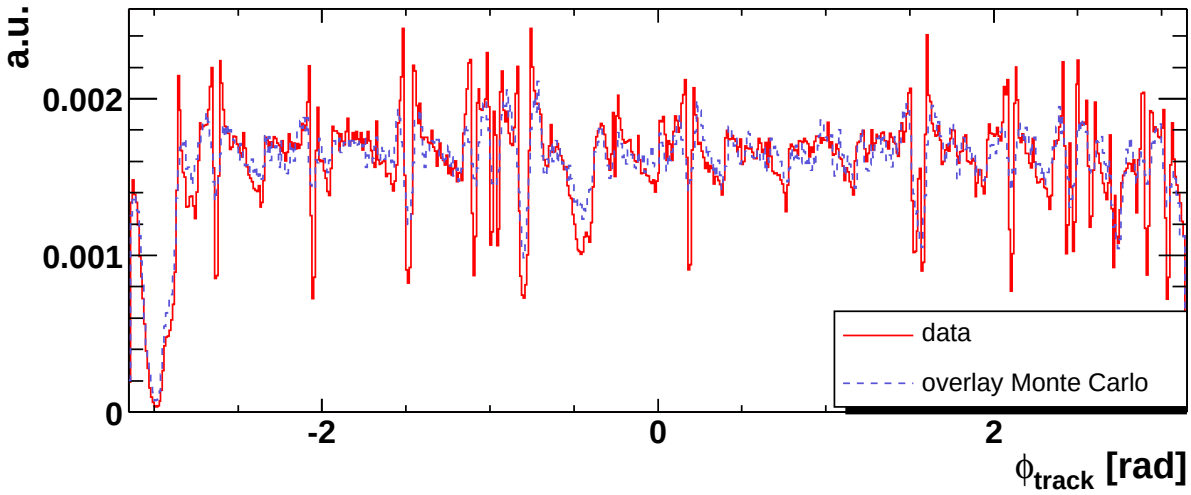

Figure 8.4: **Azimuthal distribution of the tracks.** *For the comparison of the azimuthal track distribution the same acceptance cut is used for the simulation and for the data. The acceptance cut depends on the number of fitted hits per track and is shown in figure 8.12.*

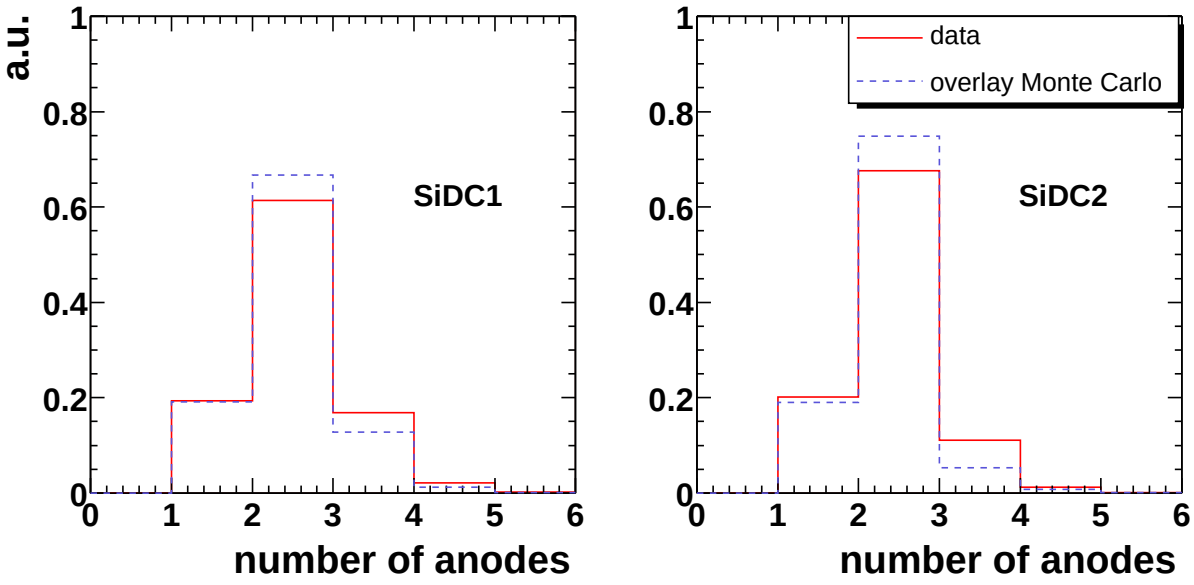

Figure 8.5: **Distribution of the Number of Anodes in a SiDC hit.** *For the secondary particle reconstruction scheme it is important that the amount of single anode hits in SiDC1 and SiDC2 is similar in the data and in the simulation.*

The ratio R of the number of tracks containing at least one single anode hit to the number of tracks containing only multi anode hits is $R = 0.52$ in the data. This large number shows how essential it is to include tracks with single anode hits in the analysis. The same ratio in overlay Monte Carlo is $R = 0.51$ after the adjustment of single anodes in SiDC1.

Another modification concerns the differential energy loss dE/dx in the Silicon Drift Detectors. The position of the mean and width of the distribution are adapted in the simulation to resemble the data. Originally a cut on the dE/dx of SiDC was planned to exclude unresolved double tracks. Such a cut becomes redundant once an opening angle cut is applied.

8.2.3 Comparison of Momentum Resolution

The momentum resolution of the CERES experiment given by equation (5.8) is determined by comparing the reconstructed momenta of tracks from an overlay Monte Carlo simulation with their true momenta. The momentum resolution obtained from the simulation can be verified using the decay $K^0_S \to \pi^+\pi^-$. The invariant mass of the K^0_S meson with $m_{K^0_S} = 497.65$ MeV/c^2 [66] is given by

$$m_{K^0_S} = \sqrt{m^2_{\pi^+} + m^2_{\pi^-} + 2E_{\pi^+}E_{\pi^-} - 2\vec{p}_{\pi^+} \cdot \vec{p}_{\pi^-}}, \tag{8.3}$$

where $m_\pi = 139.57$ MeV/c^2 [66] is the pion mass and E_π the pion energy. The contribution of the pion masses to the mass of the K^0_S is small. Thus, the mass resolution of the K^0_S is sensitive to the momentum resolution.

Figure 8.6 shows a comparison between the reconstructed invariant mass position and the width of the K^0_S between overlay Monte Carlo and data. For the comparison the cuts summarized in table 8.2 are used. The invariant mass position is displayed in form of an offset $\Delta\mu = m_{rec} - m_{K^0_S}$ between the reconstructed K^0_S mass m_{rec} and its nominal value $m_{K^0_S}$. The shape is well described by the simulation. A small mass offset of the order of few MeV/c^2 is observed at low and high $p_T^{K^0_S}$. The situation remains unchanged if the reconstructed angles θ_{rec} and ϕ_{rec} of the tracks are substituted in the simulation by the true angles θ_{true} and ϕ_{true}. If, on the other hand, the reconstructed momentum p_{rec} is substituted by the true momentum p_{true} the mass offset becomes flat over the whole $p_T^{K^0_S}$ range with $\Delta\mu_m \approx 0$. Furthermore, the same mass offset as shown in figure 8.6 is seen if a simulation is used where all the K^0_S mesons are forced to decay in the targets ($c\tau = 0$ cm). These observations indicate a bias in the momentum determination. However, the effect is small as compared to the average mass resolution of the K^0_S with $\sigma_m = 13.21 \pm 0.05$ MeV/c^2, indicating that the momentum bias is small as compared to the momentum resolution Δp.

The increase of the mass resolution with the transverse momentum of the K^0_S reflects the shape of the momentum resolution shown in figure 5.11. At low $p_T^{K^0_S}$ the mass resolution as obtained from data is somewhat worse than the simulation, although the overall agreement is satisfactory.

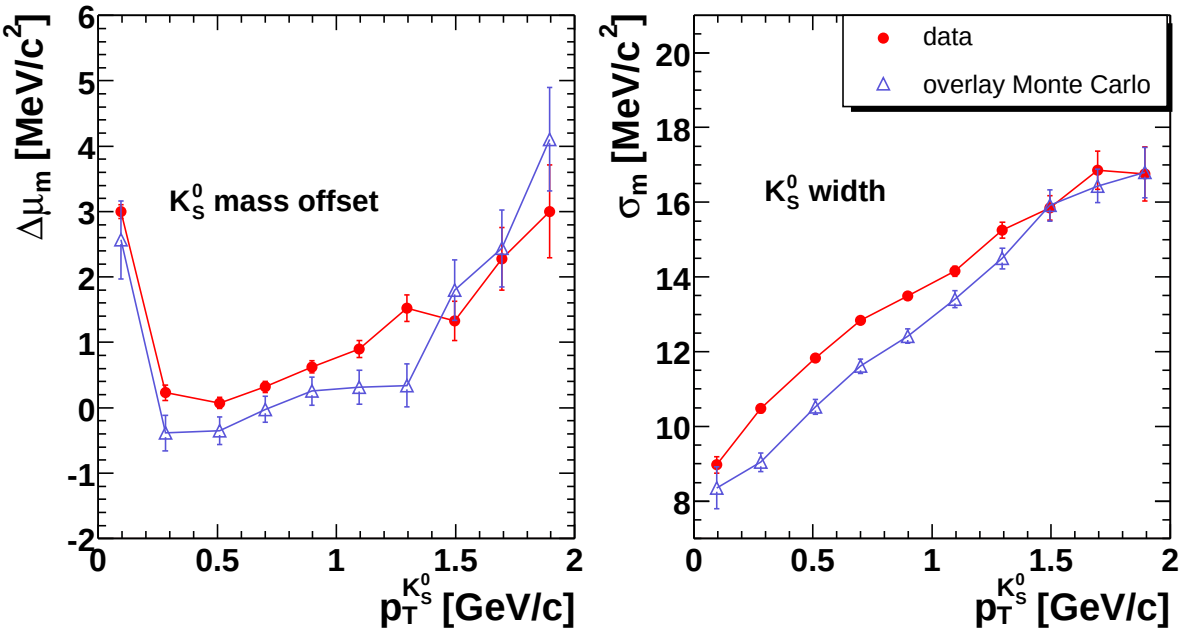

Figure 8.6: **K^0_S mass offset and width.** *The invariant mass offset and width of the K^0_S peak is plotted as a function of the transverse momentum of the K^0_S meson. The points are connected by a line to guide the eye.*

8.2.4 Comparison of Secondary Vertex Resolution

The presented analysis scheme is based on a secondary vertex cut to diminish the large contribution of target tracks. The resolution of the secondary vertex is determined in overlay Monte Carlo by comparing the reconstructed decay position of a simulated particle with its nominal value. For the $\overline{D}^0$ it is given by

$$(\Delta x_{sv}, \Delta y_{sv}, \Delta z_{sv}) = (49\ \mu\text{m}, 50\ \mu\text{m}, 348\ \mu\text{m}). \tag{8.4}$$

An improvement of about 7% is obtained if only tracks with multi anode hits in both SiDC detectors are considered. The K^0_S has a worse resolution of

$$(\Delta x_{sv}, \Delta y_{sv}, \Delta z_{sv}) = (132\ \mu\text{m}, 135\ \mu\text{m}, 1181\ \mu\text{m}), \tag{8.5}$$

due to the lower momentum range of the decay pions.

The secondary vertex resolution can be compared to the target width if the same reconstruction procedure is used. Figure 8.7 a) and d) show the 13 targets of the CERES experiment reconstructed by either using two or three points for the straight line fits of the tracks. An additional cut on the single track transverse momentum of $p_T > 500$ MeV/c is applied to the data in order to represent the same momentum region as the kaon and pion tracks from the $\overline{D}^0$ decay. Furthermore, only tracks with multi anode hits in both SiDC detectors are accepted to avoid effects related to a possible different number of single anode hits in the data and in the simulation which might result in different values for the resolution. A magnification of the target region is shown in figure 8.7 b) and e) together with a Gaussian fit. The target width obtained in this way is in good agreement with the

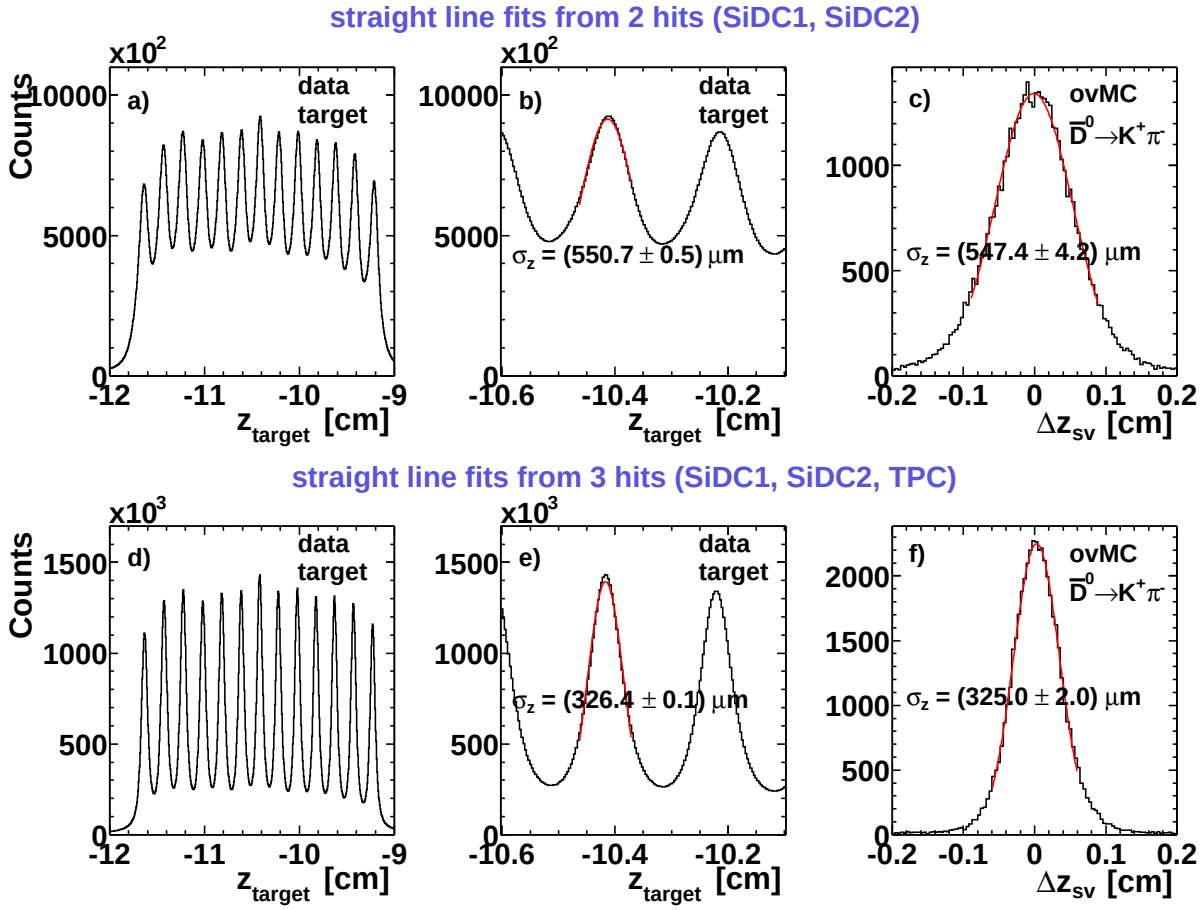

Figure 8.7: **Verification of the secondary vertex resolution.** *Plots a) and d) show the 13 targets of the CERES experiment reconstructed with the analysis scheme presented in chapter 7. Only tracks with multi anode hits in the SiDC detectors with $p_T > 500$ MeV/c are considered. Plots b) and e) show a magnification of the reconstructed targets. The target width obtained from a Gaussian fit agrees with the secondary vertex resolution of the $\overline{D}^0$ shown in c) and f).*

secondary vertex resolution of the $\overline{D}^0$ meson, shown in figure 8.7 c) and f). Remarkable is that the third point from the TPC on the straight line fits of the tracks improves the vertex resolution by 40%. This is expected because the high momentum tracks from the decay of the $\overline{D}^0$ meson have a very good pointing from the TPC to the SiDC.

8.2.5 Scan of Cut Parameters

Ideally, the correctness of the efficiency determination could be proven by showing that the fraction of the K^0_S yield lost by the application of a cut is the same in data as in simulation. This would imply the knowledge of the number of K^0_S without any cut. In this case, however, the significance of the K^0_S is too small, making such a measurement impossible. Still, it is possible to prove that the resolution of a cut parameter is understood

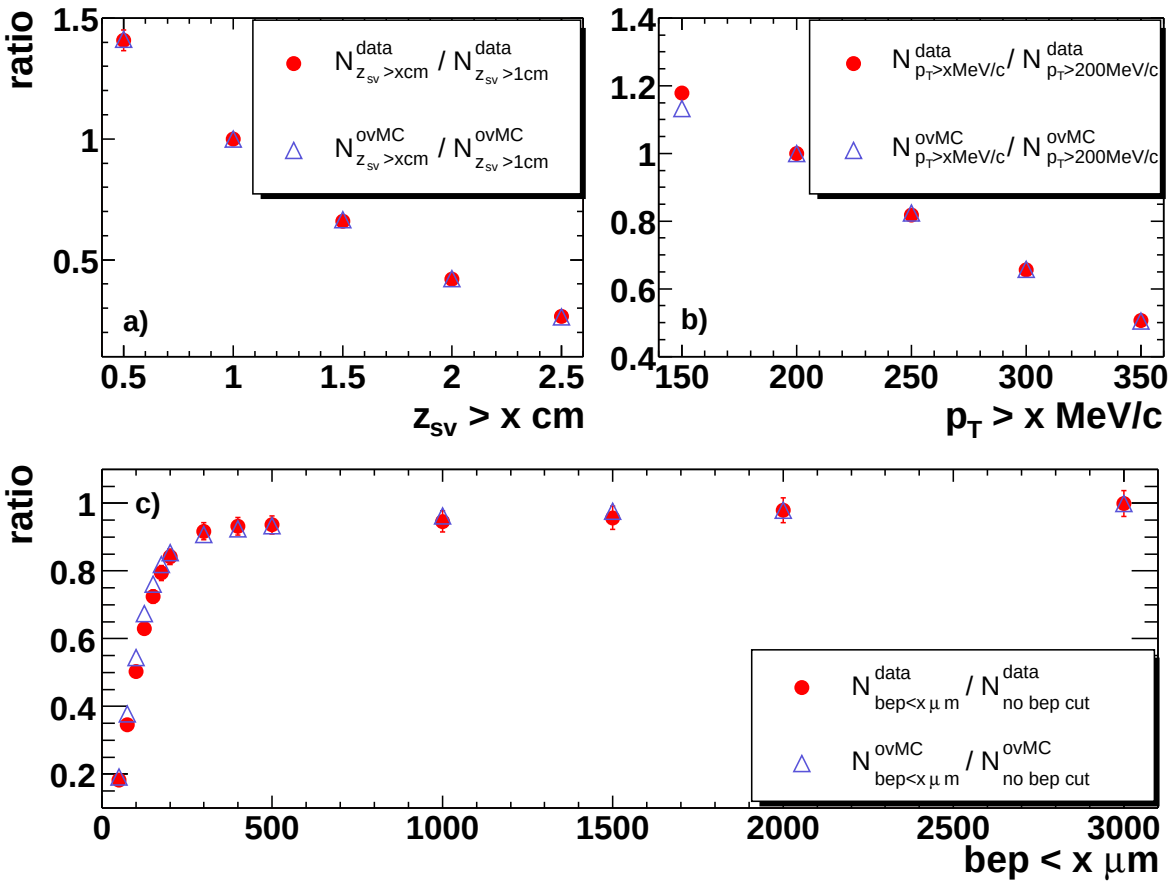

Figure 8.8: **Scan of z_{sv}, p_T, and bep cut parameter.** *To show the agreement between overlay Monte Carlo and data each cut parameter is scanned while fixing the others.*

by scanning this parameter, while fixing the others, and comparing the behavior of the data and the simulation under the the influence of this cut. This is shown in figure 8.8. Plot a) shows a scan of the secondary vertex cut for the values $z_{sv} > 0.5$, 1, 1.5, 2, and 2.5 cm, while the other cuts are fixed to $p_T > 150$ MeV/c and $bep < 200$ μm. For each set of cuts the K^0_S yield is determined. The yield obtained from the data and from the simulation is arbitrarily normalized to the corresponding yield obtained at $z_{sv} > 1$ cm. The figure shows that the data and simulation behave similarly.

In a similar way the single track transverse momentum cut is scanned in figure 8.8 b) for the values $p_T > 150$, 200, 250, 300, and 350 MeV/c, while fixing $bep < 200$ μm and $z_{sv} > 1$ cm. The yields are normalized to the yield at $p_T > 200$ MeV/c. Data and simulation show a good agreement except for the first point at 150 MeV/c. For this reason a single track transverse momentum cut of $p_T > 200$ MeV/c is chosen for the following K^0_S analysis. A harder cut of $p_T > 400$ MeV/c is chosen for the $\overline{D}^0$ analysis.

Unfortunately the same procedure fails if applied to scan the *bep* parameter while fixing $z_{sv} > 1$ cm and $p_T > 200$ MeV/c. Additional requirements on the quality of the track fit are needed. This is done by using a cut on the χ^2 probability of the straight line

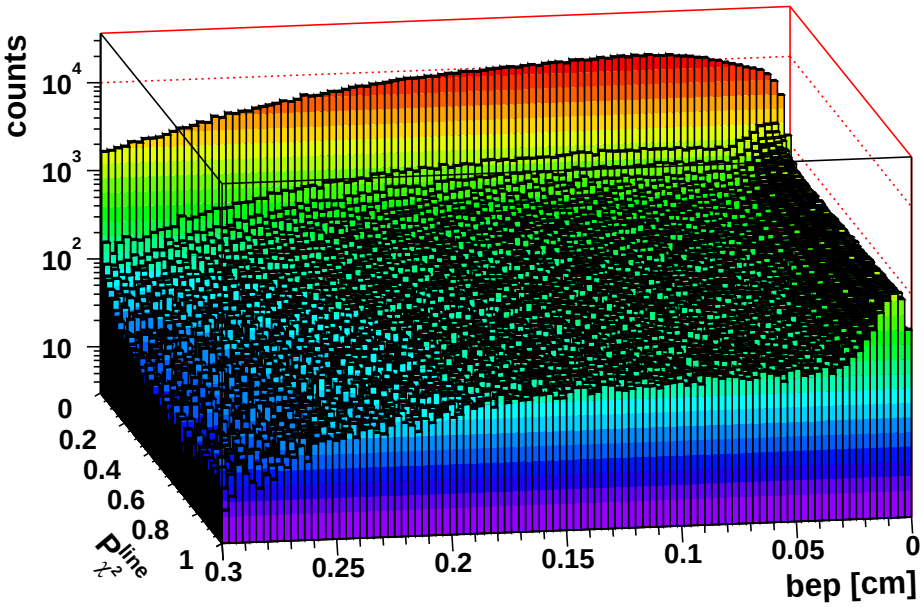

Figure 8.9: **Correlation between *bep* parameter and χ^2 probability of the straight line fits.** *The two components of the bep parameter cut seen in figure 7.8 emerge at different $P^{line}_{\chi^2}$ values. The broad component appears almost exclusively at $P^{line}_{\chi^2} \approx 0$. The narrow component at around 80 μm is equally distributed along all $P^{line}_{\chi^2}$ values.*

fits $P^{line}_{\chi^2}$, which will be explained in more detail in the next section.

As seen in figure 7.8 the *bep* parameter distribution has two components. The first component is narrow and peaks at 80 μm, while the second component is very broad and peaks at around 600 μm. The broad component is due to mismatches between the TPC and the SiDC track segments and disappears completely once a χ^2 probability cut is applied. If clean Monte Carlo is used, the second component is not even present because a mismatch between TPC and SiDC becomes rare. It has to be pointed out that the simulation only contains particles decaying upstream SiDC1.

The correlation between the *bep* parameter and $P^{line}_{\chi^2}$ is plotted in figure 8.9, using a logarithmic scale for the vertical axis. The broad component of the *bep* parameter appears mainly at $P^{line}_{\chi^2} \approx 0$, while the narrow component at around 80 μm is equally distributed along all $P^{line}_{\chi^2}$ values, as expected. Thus, using a *bep* parameter cut of $bep < 200$ μm implicitly rejects a large fraction of tracks with $P^{line}_{\chi^2} \approx 0$.

Once a cut of $P^{line}_{\chi^2} > 0.05$ is used to scan the *bep* parameter, the agreement between the data and the simulation is satisfactory, as seen in figure 8.8 c). In this case the yield obtained without applying a *bep* parameter cut is used for the normalization. Summarizing these results, it has been shown that the single track p_T cut, the secondary vertex cut z_{sv} and the *bep* parameter cut are understood. The remaining task is to study the agreement of the χ^2 probability between the data and the simulation.

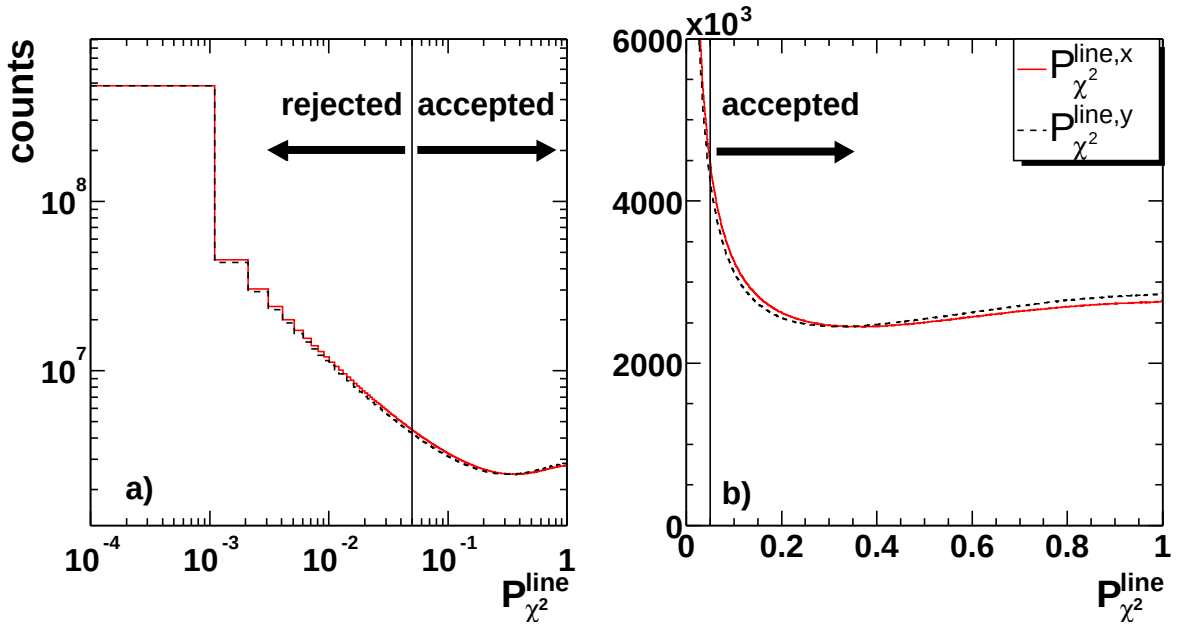

Figure 8.10: χ^2 **probability of the straight line fits.** *Plot a) shows the χ^2 probability of the straight line fits in the x-z plane and y-z plane in double logarithmic scale. The same is plotted in b) in linear scale. The distributions are obtained from the data. The vertical line indicates the cut used in the analysis.*

8.2.6 χ^2 probability

The χ^2 probability is a number between 0 and 1 that describes how likely it is that for a given number of degrees of freedom, the χ^2 could be greater than the reported χ^2. A very small χ^2 probability indicates that it is unlikely that the measurement is consistent with the expectation.

The straight line fits of the tracks are performed in the x-z plane and y-z plane. For both a χ^2 probability is defined, named as $P^{line,x}_{\chi^2}$ and $P^{line,y}_{\chi^2}$, respectively. Often the abbreviation $P^{line}_{\chi^2}$ is used to refer to both quantities. The distributions of $P^{line,x}_{\chi^2}$ and $P^{line,y}_{\chi^2}$ are plotted for data in figure 8.10, once in double logarithmic (a) and once in linear scale (b). The large peak at $P^{line}_{\chi^2} < 0.05$ arises from tracks, where the errors of the three points are too small to describe their distance to the fit. Thus, most of the mismatches between the TPC and the SiDC track segments will show up there. Also secondary tracks from particles decaying after SiDC1 or SiDC2 will have low $P^{line}_{\chi^2}$ values. By definition these tracks do not have a real match to the SiDC detectors. To significantly reduce the amount of mismatched tracks, and thus of background, a cut of $P^{line}_{\chi^2} > 0.05$ is used, as indicated by the vertical line in figure 8.10.

The χ^2 probability of the straight line fits is not well described by the simulation. The differences depend on the momentum and the polar angle θ of the tracks. Thus, the cut of $P^{line}_{\chi^2} > 0.05$ used in the data has to be adjusted in the simulation, such that the same number of tracks normalized to the total number of tracks in a given momentum and polar angle range is accepted.

The simulation has to describe the cocktail of particles arising from an ultrarelativistic heavy-ion collision in order to include all effects that might have an influence on the χ^2 probability of the straight line fits, for example late decays. For this purpose 9000 Pb-Au collisions at 6.5% centrality are generated with the **U**ltra**r**elativistic **Q**uantum **M**olecular **D**ynamics model (UrQMD) [84, 85], passed through a GEANT [68] simulation of the CERES spectrometer, and reconstructed with the C++ package COOL. The simulation is performed once in a clean mode, and once embedding it in real events. The clean UrQMD simulation underestimates the hit multiplicity in the TPC by a factor of 4, while the hit multiplicity in the SiDC is reproduced. On the other hand, the overlay UrQMD simulation overestimates the SiDC hit multiplicity by a factor of 2, while the TPC hit multiplicity is better described (factor 1.3).

The full circles and full lines in figure 8.11 show the $P_{\chi^2}^{line}$ cut as determined with the overlay UrQMD simulation. The corresponding cut of $P_{\chi^2}^{line} > 0.05$ as used in the data is indicated with the dashed line. The $P_{\chi^2}^{line}$ cut from the clean UrQMD simulation is drawn with dotted lines. The momentum dependence of the $P_{\chi^2}^{line}$ cut used in the simulation is fitted by the empirical function:

$$f(p) = C_0\, e^{-\sqrt{p}} + C_1 + C_2\, p. \tag{8.6}$$

The parameters are summarized in table 8.1. The steep rise at low momentum reflects the aforementioned underestimation of mismatches between the TPC and SiDC track segments. The dependence of the polar angle θ of the track becomes stronger with increasing hit multiplicity.

The adjustment of the $P_{\chi^2}^{line}$ cut gives rise to a systematic uncertainty in the determination of the efficiency, because neither the clean nor the overlay UrQMD simulation simultaneously describe the hit multiplicity in the SiDC and TPC. The two simulations thus allow to estimate the upper and lower boundary of the efficiency, the truth lying somewhere in between.

Besides the straight line fits of the track, also a secondary vertex fit is used in the analysis. This means that in addition a cut on the χ^2 probability of the secondary vertex fit is needed. This quantity is labeled $P_{\chi^2}^{vtx}$. The effect of this cut has been studied in the analysis of the K_S^0 described in the next section. If the analysis is performed with or without a cut of $P_{\chi^2}^{vtx} > 0.05$ the result changes by 5%.

8.3 p_T Spectrum of K_S^0

The efficiency is further cross-checked by measuring the K_S^0 p_T spectrum and comparing the results to a reference measurement from [86]. The reference measurement is performed with the CERES spectrometer, but only using the TPC and a reduced set of cuts. The centrality selection of both analyses are the same. The results will also be compared to measurements from the NA49 [83, 87] and the NA57 collaborations [88, 89].

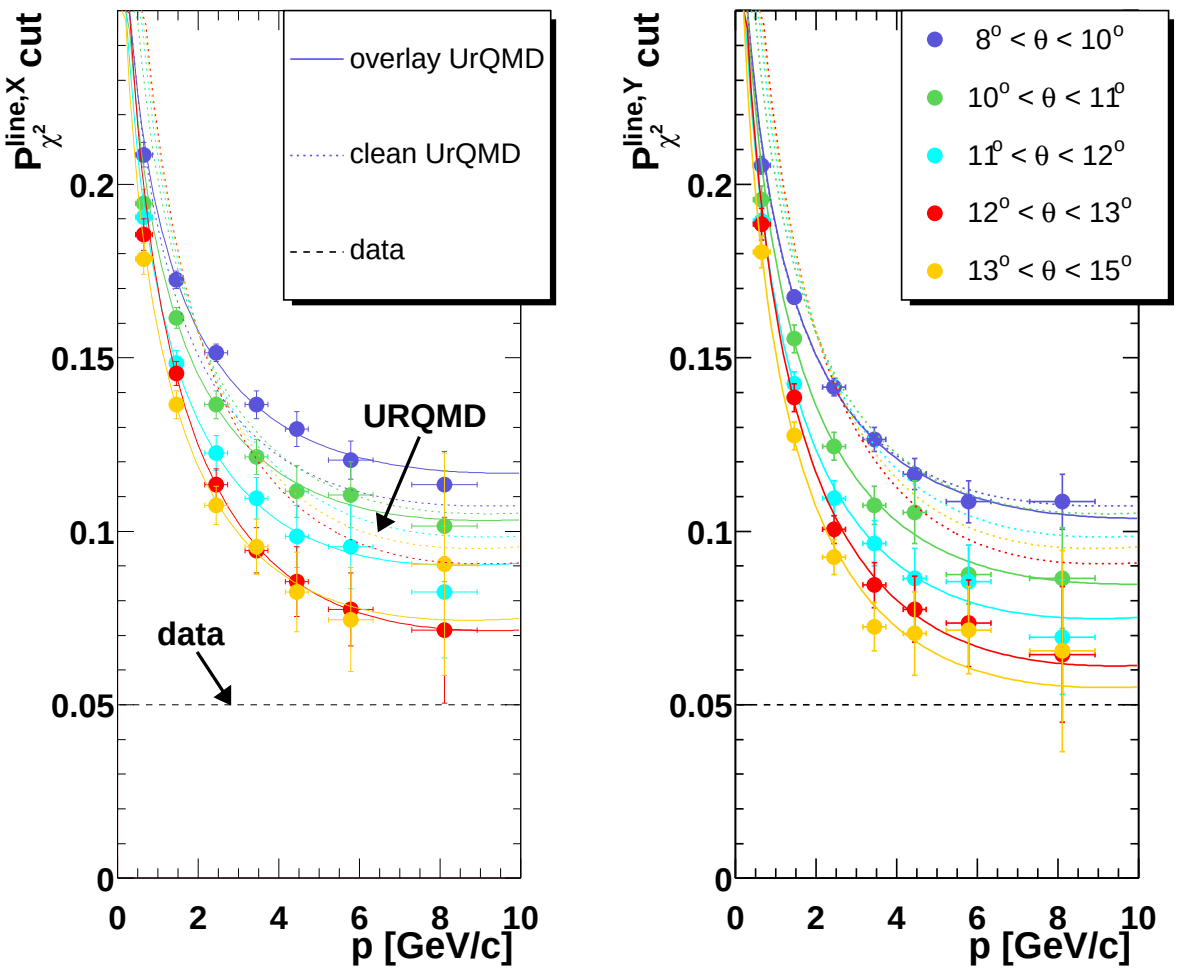

Figure 8.11: **Adjustment of the $P^{line}_{\chi^2}$ cut.** *A cut of $P^{line}_{\chi^2} > 0.05$ is used in the data. To reject the same fraction of tracks a momentum and polar angle dependent cut has to be applied in the simulation, as shown by the colored lines. The $P^{line}_{\chi^2}$ cut adjustment is determined using a UrQMD simulation. The simulation is performed once in a clean and once in an overlay mode.*

		$P^{line,x}_{\chi^2}$			$P^{line,y}_{\chi^2}$		
		C_0	C_1	C_2	C_0	C_1	C_2
clean UrQMD simulation	$8° < \theta < 10°$	0.3150	0.0691	0.0025	0.3548	0.0554	0.0025
	$10° < \theta < 11°$	0.3781	0.0592	0.0030	0.4044	0.0465	0.0030
	$11° < \theta < 12°$	0.4327	0.04531	0.0035	0.4495	0.0322	0.0035
	$12° < \theta < 13°$	0.4911	0.0301	0.0040	0.5215	0.0134	0.0040
	$13° < \theta < 15°$	0.4696	0.0356	0.0040	0.5284	0.0113	0.0040
overlay UrQMD simulation	$8° < \theta < 10°$	0.2846	0.0847	0.0020	0.3142	0.0704	0.0020
	$10° < \theta < 11°$	0.3080	0.0653	0.0025	0.3558	0.0447	0.0025
	$11° < \theta < 12°$	0.3241	0.0471	0.0030	0.3602	0.0299	0.0030
	$12° < \theta < 13°$	0.3856	0.0252	0.0030	0.3963	0.0145	0.0030
	$13° < \theta < 15°$	0.3379	0.0306	0.0030	0.3781	0.0091	0.0030

Table 8.1: **Fit parameters of the $P^{line}_{\chi^2}$ cut adjustment.** *The table contains the values for the fit parameters according to equation (8.6) and figure 8.11.*

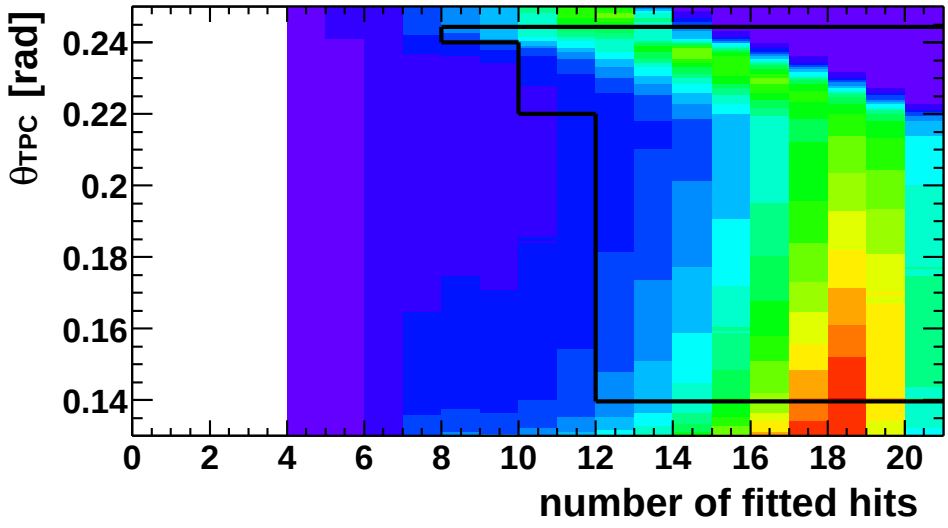

Figure 8.12: **Acceptance Cut in the TPC.** *The cut on the polar angle θ_{TPC} of the TPC track segment takes into account that at large θ_{TPC} the tracks leave the TPC earlier. These tracks have by definition a smaller number of hits per track.*

8.3.1 Analysis

The K^0_S analysis is based on 18.8 million events at 7% centrality, comprising the calibration units 146 to 415 (end of the run). The resolution of the data from the calibration units 1 to 145 does not satisfy the high requirements in pointing precision between TPC and SiDC needed for the secondary vertex reconstruction scheme. For the first 80 units the jitter of the TPC was not measured resulting in a worse drift time resolution. The data of the units 81 to 145 is rejected due to an unstable gas composition in the TPC during the beam time, which was monitored with less precision using a CO_2 analyzer instead of the drift velocity monitor.

The analysis is performed by combining all positive tracks with all negative tracks within each event. For both tracks the pion mass is assumed and the invariant mass $m_{\pi\pi}$ is calculated according to equation (8.3). Only events with an interaction position lying within 0.9 mm with respect to the closest target are considered, the distance between two targets being approximately 2 mm (compare figure 5.2). In the following this procedure is called same events analysis. The background distribution is obtained by combining the positive tracks of a given event with all negative tracks of ten other randomly chosen events within the same burst (1 burst $\approx$ 400 events), and vice versa. The mixing of two events is performed within the same target and the track multiplicity should not differ by more than 10%. This procedure is called mixed events analysis.

A polar angle cut is applied on the acceptance of the TPC according to figure 8.12. The upper and lower cut of 0.1396 rad $< \theta_{TPC} <$ 0.2443 rad considers the geometrical coverage of the spectrometer. In order to obtain a reasonable momentum fit at least 12 fitted hits are required for the TPC track segments. At large polar angles the tracks do not traverse the whole TPC barrel. Here the requirements for the number of fitted

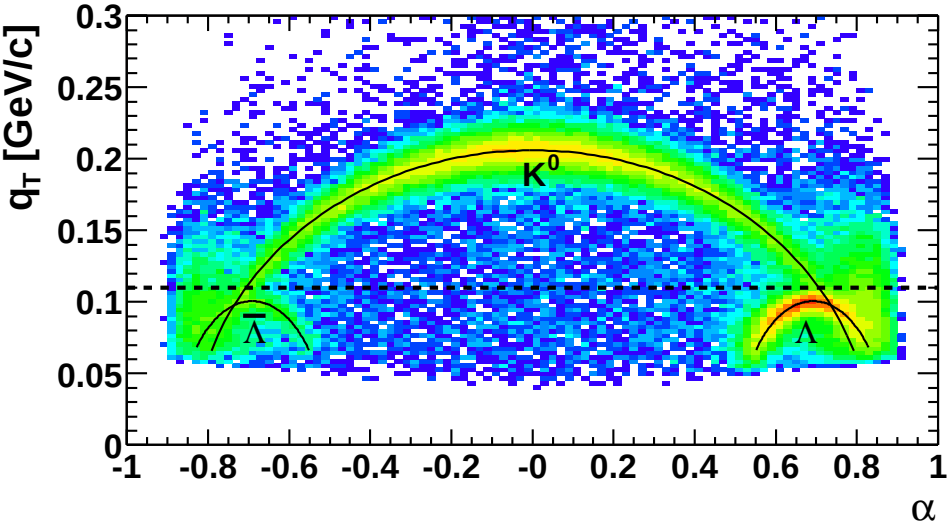

Figure 8.13: **Armenteros-Podolanski Plot for the K^0_S.** *The cuts $\psi > 0.1$ rad, bep < 200 μm, $z_{sv} < 1.5$ cm and $P_{\chi^2} > 0.01$ are used to obtain a clear K^0_S signal in the Armenteros-Podolanski plane. The small contribution of misidentified Λ baryons can be excluded by using a cut on the transverse momentum in flight direction of the mother particle of $q_T > 0.11$ GeV/c. The cut is drawn as dashed line. The solid lines for the K^0_S and Λ are calculated according to the formulas in appendix A.*

hits is relaxed to 10 fitted hits for the range 0.22 rad $< \theta_{TPC} <$ 0.24 rad and to 8 fitted hits for 0.24 rad $< \theta_{TPC}$.

Analyses performed without particle identification often suffer from the problem that misidentified resonances, which are reconstructed with the wrong mass assumption of the daughters, fall in the same mass range as the considered one. However, kinematical considerations still enable to suppress unwanted contributions. A powerful method is to apply a cut in the q_T-α plane of the Armenteros-Podolanski plot [90], where q_T is the transverse momentum with respect to the flight direction of the mother particle, and α is an asymmetry variable comprising the longitudinal momentum q_L. A detailed description about this topic can be found in appendix A. Figure 8.13 shows the Armenteros-Podolanski plot as obtained with an adequate choice of cuts from the data. The remaining contributions are mostly the K^0_S and the Λ meson. A cut of $q_T > 0.11$ MeV/c in the q_T-α plane is sufficient to suppress the Λ baryon. A summary of the cuts used in the K^0_S analysis can be found in table 8.2.

The total number of collected K^0_S mesons is 168315. The analysis is performed differentially in ten equidistant $p_T^{K^0_S}$ bins in the range $0 < p_T^{K^0_S} < 2$ GeV/c and three equidistant rapidity bins in the range $2.0 < y < 2.6$. Examples of the raw invariant mass spectra of the same and the normalized mixed events analyses are shown in figure 8.14. To extract the normalization constant the invariant mass distribution in the same events sample is divided by the analog distribution in the mixed events sample. The ratio is fitted by a Gaussian on top of the normalization constant. The mixed events distribution is then multiplied with this constant and subtracted from the same events distribution. The resulting signal spectrum is fitted with a Gaussian function for the K^0_S yield and a

polar angle	$0.1396 < \theta_{TPC} < 0.2443$
Armenteros-Podolanski	$q_T > 0.11$ GeV/c
single track transverse momentum	$p_T > 200$ MeV/c
opening angle	$\psi > 0.05$ rad
χ^2 probability of the line fit	$P_{\chi^2}^{line} > 0.05$
χ^2 probability of the vertex fit	$P_{\chi^2}^{vtx} > 0.05$
secondary vertex	$z_{sv} > 1$ cm
bep parameter	$bep < 200$ μm

Table 8.2: **Cuts for the K_S^0 analysis.** *The table contains a compilation of the cuts used in the K_S^0 analysis.*

polynomial of first order for a possible residual background contribution. The uncorrected K_S^0 yields obtained in this way are shown in figure 8.15 c) for each $p_T^{K_S^0}$ and y bin.

Also the acceptance and the efficiency are determined for each differential spectrum, as shown in figure 8.15 a) and b). Using further the number of analyzed events and the branching ratio for the decay $K_S^0 \to \pi^+\pi^-$, the quantity $dN/(p_T dy dp_T)$ is calculated and plotted versus the transverse momentum of the K_S^0 meson, as shown in figure 8.15 d). The p_T spectrum is fitted with the exponential function

$$\frac{d^2N}{p_T\, dy\, dp_T} = \frac{dN/dy}{T(T+m)} \cdot e^{-\frac{\sqrt{m^2+p_T^2}-m}{T}}. \tag{8.7}$$

For m the invariant mass of the K_S^0 meson $m_{K_S^0} = 497.65$ MeV/c^2 is used. The position of the data points within the bins are calculated according to [91]. The parameters obtained from the fits are the inverse slope parameter T and the rapidity density dN/dy. The results are discussed in the next section.

8.3.2 Results and Conclusions for the Efficiency

Figure 8.16 shows a compilation of the fit results from the K_S^0 p_T spectrum of figure 8.15 in comparison to other measurements. The three values for the rapidity density dN/dy obtained in this work are shown in figure 8.16 a) as circles. The corresponding values for the inverse slope parameter T are shown in plot b). The reference measurement from [86] is drawn as squares and the corresponding fit results as dashed lines. Both are CERES measurements for 158 AGeV/c Pb-Au collisions at 7% centrality, but using two different philosophies in the analysis scheme. The reference measurement is solely based on the information of the TPC. The triangles and dotted lines indicate the results obtained by the NA49 collaboration for Pb-Pb collisions at 5% centrality [83, 87]. The NA49 measurement is scaled by a factor of 0.938 using the number of participating nucleons N_{part} [92]. The dotted line is not a fit to the K_S^0 data points from NA49, but rather a fit to the mean of their measured K^+ and K^- rapidity density spectra. The measurement from the NA57 collaboration for the most 4.5% central Pb-Pb collisions [88, 89] is shown by the diamond symbols, using a scaling factor of 0.928. Although a disagreement is seen at mid-rapidity between the NA49 and NA57 rapidity density measurements, all four measurements are compatible within the narrow acceptance window of the CERES spectrometer.

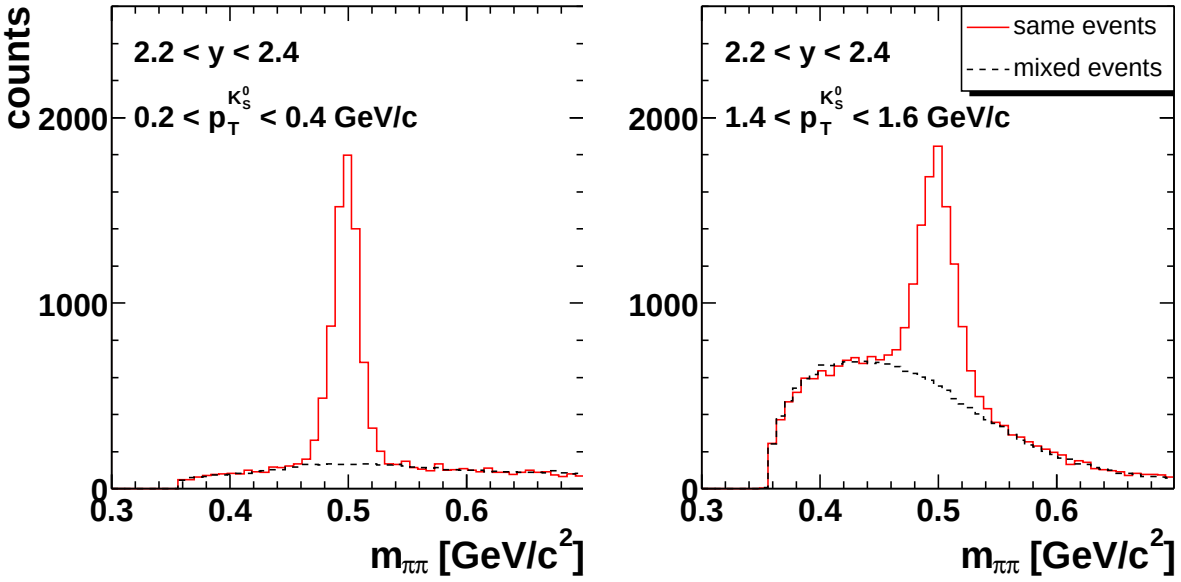

Figure 8.14: **Raw invariant mass spectra of the K^0_S meson.** *The plots show the raw invariant mass spectra of $K^0_S \to \pi^+\pi^-$ for two different $p_T^{K^0_S}$ bins in the rapidity range $2.2 < y < 2.4$. The contribution of the background is determined with the mixed events technique and is drawn as dashed line.*

The p_T spectrum integrated in the rapidity range $2.0 < y < 2.6$ is shown in figure 8.17 a). A fit according to equation (8.7) results in a rapidity density of $dN/dy = 19.75 \pm 0.23$ and an inverse slope parameter of $T = 227.97 \pm 1.47$ MeV/c^2. The measured rapidity density agrees within 5% if compared to the corresponding value obtained from the CERES fit from [86]. It agrees within the statistical errors with the corresponding value obtained from NA49 [83]. The difference of the data points to the dashed or dotted line is shown in figure 8.17 b) as a function of the transverse momentum of the K^0_S meson. The deviation towards larger $p_T^{K^0_S}$ reflects the larger fit value obtained for the inverse slope parameter T.

The results presented here are stable if the fit range in the K^0_S signal spectrum is varied or if the residual background is fitted with a constant instead of a polyomial of first order. As it was discussed in section 8.2.6, the efficiency is obtained by using the $P^{line}_{\chi^2}$ cut adjustment from the overlay UrQMD simulation, shown as full lines in figure 8.11. Using the adjustment from the clean UrQMD simulation, drawn as dashed lines in figure 8.11, increases the rapidity density by 7%.

As summary, it is concluded that the overall systematic uncertainties are dominated by the uncertainty of the efficiency determination. Systematic variations of the different cuts have shown that the uncertainty is dominated by the $P^{line}_{\chi^2}$ cut adjustment with 7% and the uncertainty of the $P^{vtx}_{\chi^2}$ cut with 5%, resulting in an systematic uncertainty of 8.6% for the final yields. Within this limit, the results for the K^0_S meson presented here are consistent with results from an independent analysis of the CERES data and results from the NA49 and NA57 collaborations.

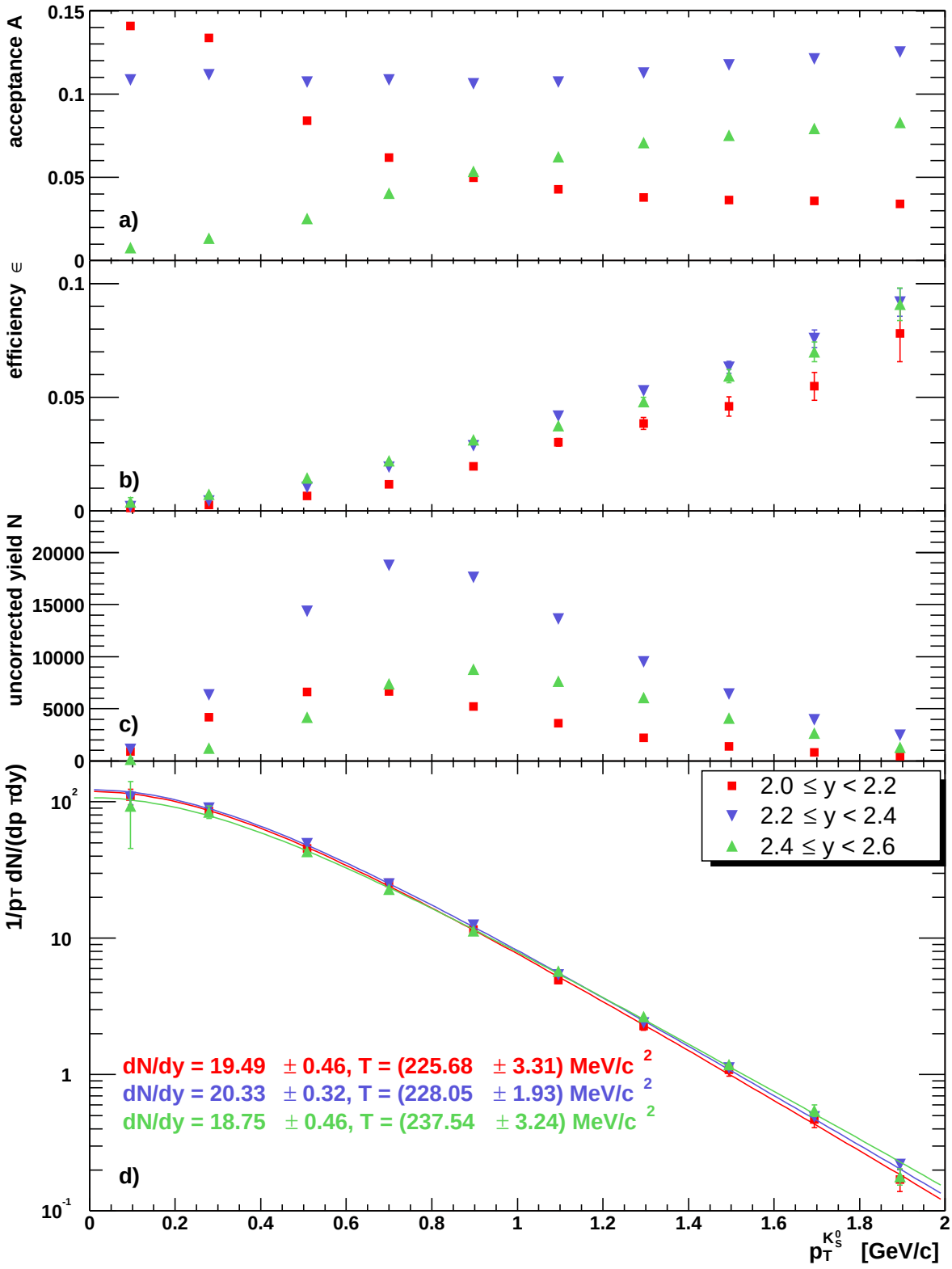

Figure 8.15: **K^0_S p_T spectra for different rapidity bins.** *The K^0_S p_T spectra (d) are fitted with function (8.7) in three rapidity bins. The corresponding uncorrected K^0_S yields (c), the efficiencies (b) and the acceptances (a) are also shown.*

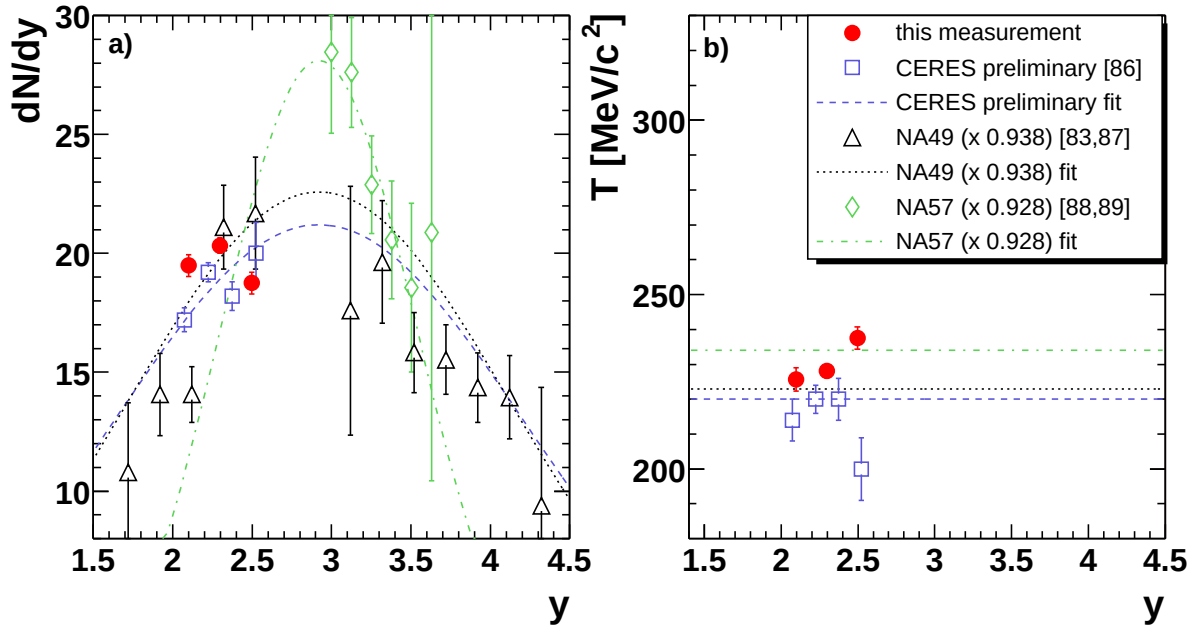

Figure 8.16: **Rapidity density and inverse slope parameter of the K^0_S.** *The plots show a compilation of the fit results from figure 8.15 (circles) in comparison to a second CERES measurement (squares) [86], a measurement from the NA49 collaboration (triangles) [83, 87], and a measurement from the NA58 collaboration [88, 89]. The fit parameters are the rapidity density dN/dy shown in a), and the inverse slope parameter T shown in b).*

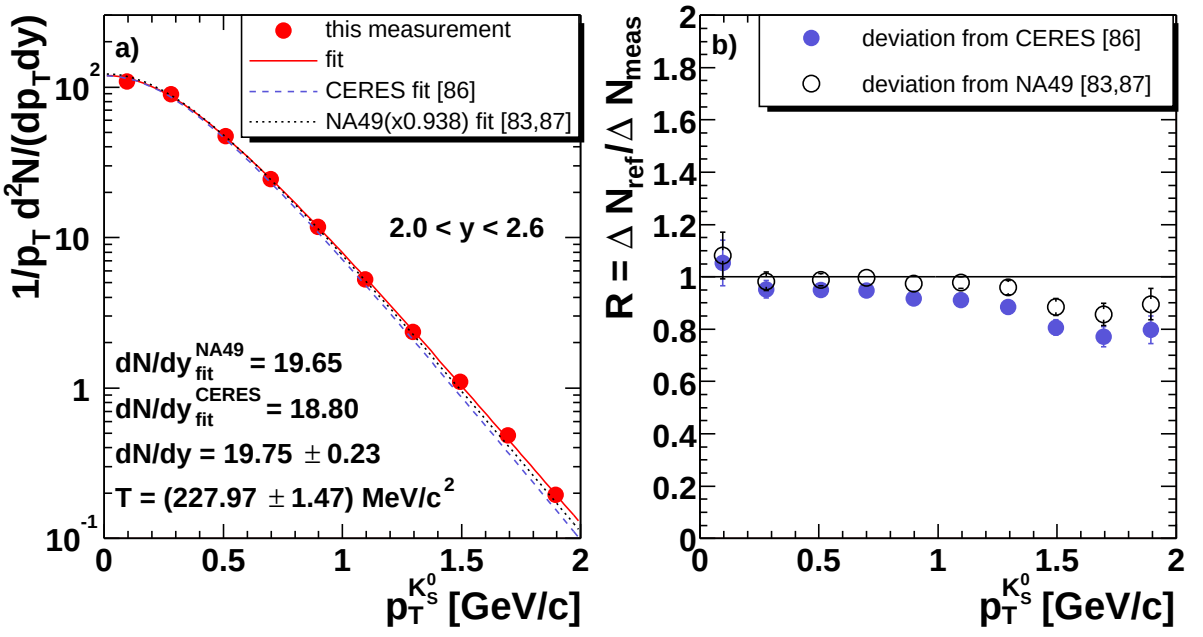

Figure 8.17: **Integrated K^0_S p_T Spectrum.** *Plot a) shows the K^0_S p_T spectrum integrated over the rapidity range $2.0 < y < 2.6$. The dashed and dotted lines are the corresponding dependencies obtained from the CERES and NA49 fits from [86] and [83, 87], respectively. Plot b) shows the deviation of the data points from the dashed (full circles) and the dotted (open circles) line.*

Chapter 9

Open Charm Analysis

The measurement of charmed mesons is an extremely difficult task in heavy-ion physics due to the low production cross-section and the huge amount of combinatorial background. For instance, 30 million collected events of 158 AGeV/c Pb-Au collisions would result in 3.6 million $\overline{D}^0$ mesons, if a yield of 0.12 $\overline{D}^0$ per event [26] is assumed. Measuring only the decay channel $\overline{D}^0 \rightarrow K^+\pi^-$ ($c\tau = 123.0$ μm) will further reduce this number by the branching ratio of 3.8% [66]. In only 3.4% of the cases both daughters will fall in the acceptance of the spectrometer, thus leading to an amount of 4650 detectable $\overline{D}^0$ mesons. This has to be multiplied by an efficiency of the order of 3%, resulting in roughly 140 $\overline{D}^0$ mesons. If an open charm enhancement factor of 3 is assumed, at most 420 $\overline{D}^0$ mesons would be expected. This number has to be further reduced by a factor 0.63 considering the fact that data of lower quality, i.e. with worse secondary vertex resolution, is sorted out for the analysis.

The situation is not promising either considering the three body decay $D^- \rightarrow K^+\pi^-\pi^-$ ($c\tau = 311.8$ μm) with a branching ratio of of 9.2% [66]. Assuming a yield of 0.036 D^- per event [26], an acceptance of 0.9% and again an efficiency of the order of 3% results in 27 expected D^- mesons in 30 million collected events of 158 AGeV/c Pb-Au collisions.

9.1 Suppression of Resonances

Without an effective particle identification many resonances will contribute to the invariant mass spectrum of the $\overline{D}^0$ meson. These contributions will remain after subtraction of the combinatorial background, and completely mask the tiny $\overline{D}^0$ peak.

The solution is again a cut in the q_T-α plane of the Armenteros-Podolanski plot. As derived in appendix A the semi-minor axis of the Armenteros-Podolanski ellipse is given by the center of mass momentum p_{cm}. If a mother particle at rest has the four-momentum $\mathbf{p_M} = (m_M, 0)$ and decays in two daughter particles with four-momenta $\mathbf{p_1} = (E_1, \vec{p}_1)$ and

decay	mass m_M [GeV/c^2]	semi-minor axis [GeV/c]
D^0,$\overline{D}^0 \to K\pi$	1.865	0.8609
$K^0_S \to \pi\pi$	0.498	0.2060
$\rho \to \pi\pi$	0.776	0.3619
$\omega \to \pi\pi$	0.783	0.3656
$\phi \to KK$	1.019	0.1269
$K^* \to K\pi$	0.892	0.2881
Λ,$\overline{\Lambda} \to \overline{p}\pi$	1.116	0.1006
$\Delta \to p\pi$	1.232	0.2272
$\Sigma \to \Lambda\pi$	1.383	0.2054
$\Xi^- \to \Lambda\pi$	1.321	0.1390
$\Omega^- \to \Lambda K$	1.672	0.2112

Table 9.1: **Semi-minor axes of Armenteros-Podolanski ellipses.** *The table contains examples of particle decays with the corresponding masses and semi-minor axes of the Armenteros-Podolanski ellipses. The semi-minor axis can be used as cut variable to suppress contributions from unwanted resonances in the invariant mass spectrum.*

$\mathbf{p_2} = (E_2, \vec{p}_2)$, then p_{cm} is given by

$$p_{cm} = |\vec{p}_1| = |\vec{p}_2| = \sqrt{\frac{(m_M^2 - (m_1 + m_2)^2) \cdot (m_M^2 - (m_1 - m_2)^2)}{4m_M^2}}, \tag{9.1}$$

applying the energy and momentum conservation law. Using equation (9.1) the semi-minor axis of the Armenteros-Podolanski ellipse is calculated for few examples in table 9.1. Figure 9.1 shows the Armenteros-Podolanski plot of the $\overline{D}^0$ meson obtained from an overlay Monte Carlo simulation.

It can be seen from equation (9.1) that a large mass m_M of the mother and small masses m_1 and m_2 of the daughters imply a large center of mass momentum p_{cm}. This is exactly the case for the $\overline{D}^0$ meson. A cut of $q_T > 0.5$ GeV/c, as indicated in figure 9.1, will thus reject most of the unwanted resonance contributions, except those from charm decays.

9.2 Fast Monte Carlo Simulation

To obtain the signal spectrum of all possible charm decays a fast Monte Carlo simulation based on the PYTHIA event generator [47] has been developed. The fast Monte Carlo simulation allows to make optimal use of the available computing time and disk space, and to reduce the statistical error dramatically compared to the limited statistics of a full overlay Monte Carlo simulation. Its precision is however not sufficient to determine the efficiency of the analysis method. For this purpose still a full overlay Monte Carlo simulation of $\overline{D}^0$ mesons is needed. This was already described in detail in section 8.2.1.

The input for the fast simulation is a sample of 158 GeV/c p-p collisions generated in fixed target mode with the PYTHIA event generator. The total number of collected

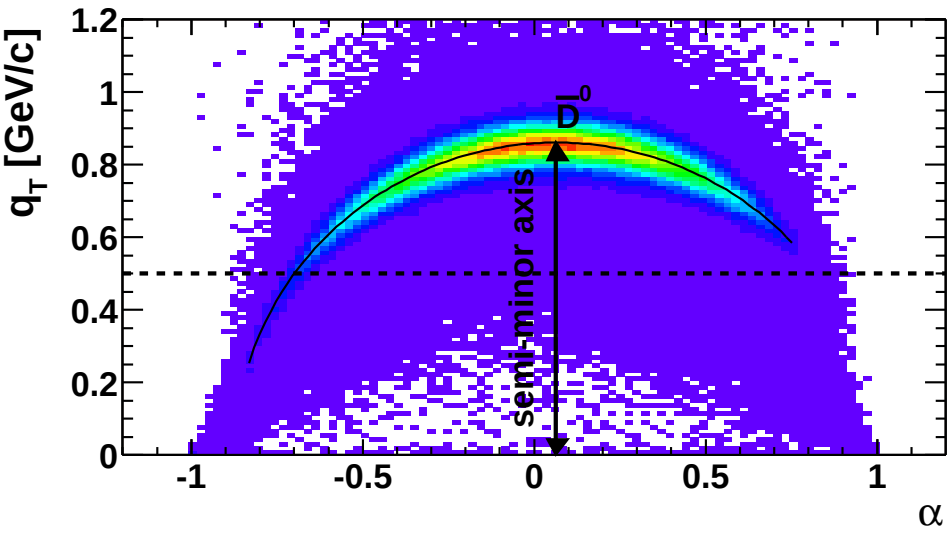

Figure 9.1: **Armenteros-Podolanski Plot for the $\overline{D}^0$ meson.** *The plot is obtained from an overlay Monte Carlo simulation. The solid line is calculated according to appendix A. The semi-minor axis of the $\overline{D}^0$ ellipse is larger than that of most of the other resonances. Only contribution from charm decays can pass the cut of $q_T > 0.5$, indicated by the dashed line.*

$c\overline{c}$ pairs is 3.2 million, obtained by only triggering on charm production processes. The charm mass is set to $m_c = 1.35$ GeV/c^2 [66]. The nucleon structure function is parameterized by MRS(G) [93]. The primordial k_T distribution inside the hadron is assumed to be Gaussian with $< k_T^2 >= 1$ (GeV/c)^2 and an upper cut-off at 3 GeV/c. The charm cross-section is scaled from p-p to A-A collisions using the number of binary collisions (see [25] for details).

The fast simulation tool processes all $\overline{D}^0$, D^0, D^-, D^+, Λ_c, D_s^- and D_s^+ decay channels from the PYTHIA simulation. Each two opposite charged particles having the same vertex are assumed to originate from a $\overline{D}^0 \to K^+\pi^-$ decay. The kaon mass is assigned to the positive particle, the pion mass to the negative one, respectively. The result is a continuous invariant mass spectrum $m_{K\pi}$. Some of the most important charmed resonance contributions are shown in figure 9.2. Remarkable is that the misidentified decay $D^0 \to K^-\pi^+$, i.e. where the kaon mass is assumed for the π^+ and the pion mass is assumed for the K^-, appears in the same invariant mass range as the $\overline{D}^0 \to K^+\pi^-$. The reason can be found in the similar momentum distributions of the decay kaon and pion $p_K \approx p_\pi$ (compare equation (8.3)).

To obtain a more realistic picture the momentum of a particle is smeared using equation (5.8) for the momentum resolution of the TPC. According to figure 8.5, 19.3% randomly chosen tracks are assigned to have a single anode hit in SiDC1, and respectively 20.1% in SiDC2. The three points (x_1, y_1, z_{SiDC1}), (x_2, y_2, z_{SiDC2}) and (x_3, y_3, z_{R2M}) on a given track are smeared according to the detector resolution described in section 7.3. Finally, the simulation is passed through the same secondary particle reconstruction scheme as used for the analysis of the data.

Figure 9.3 shows a comparison between the fast Monte Carlo and the full overlay Monte Carlo simulation for the decay channel $\overline{D}^0 \to K^+\pi^-$. The mass resolution of

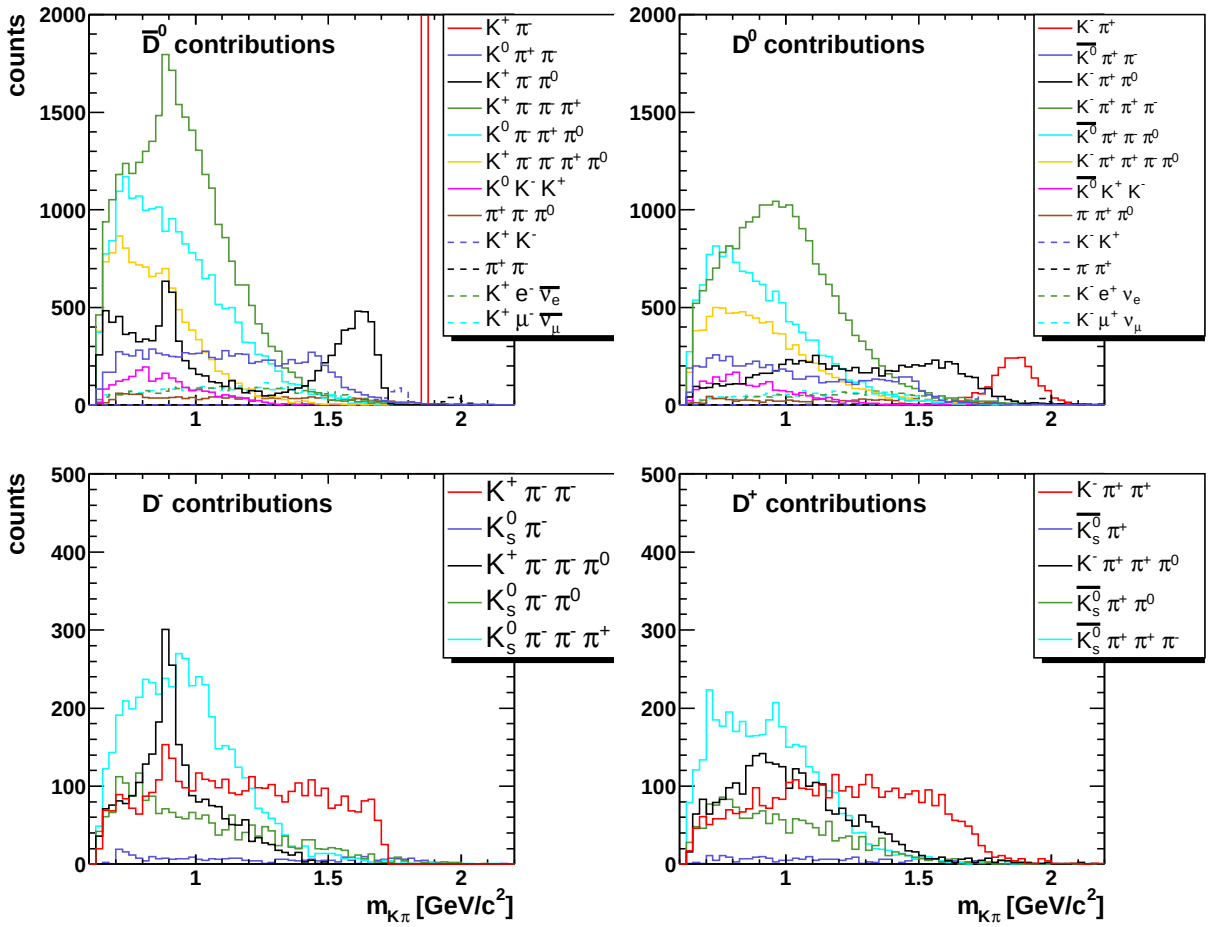

Figure 9.2: **Charmed resonance contributions to the invariant mass spectrum.** *The plots show some of the relevant contributions to the invariant mass spectrum of the* $\overline{D}^0 \to K^+\pi^-$ *decay.*

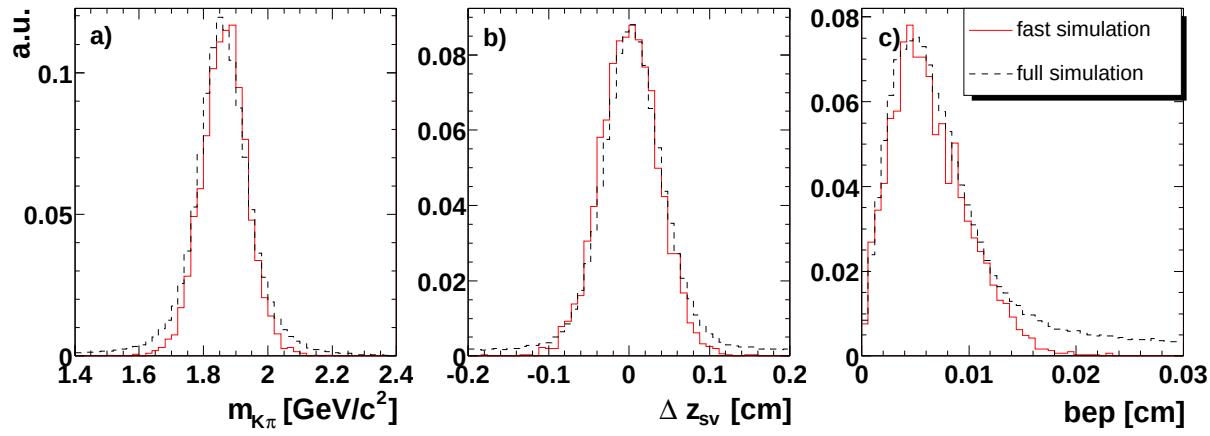

Figure 9.3: **Comparison between fast Monte Carlo and full overlay Monte Carlo.** *Plot a) shows the invariant mass distribution for the decay* $\overline{D}^0 \to K^+\pi^-$*. The full overlay Monte Carlo simulation is drawn as dashed line, the fast Monte Carlo simulation as solid line. Plot b) shows the resolution of the* z *coordinate of the decay point. The distribution of the bep parameter is shown in plot c).*

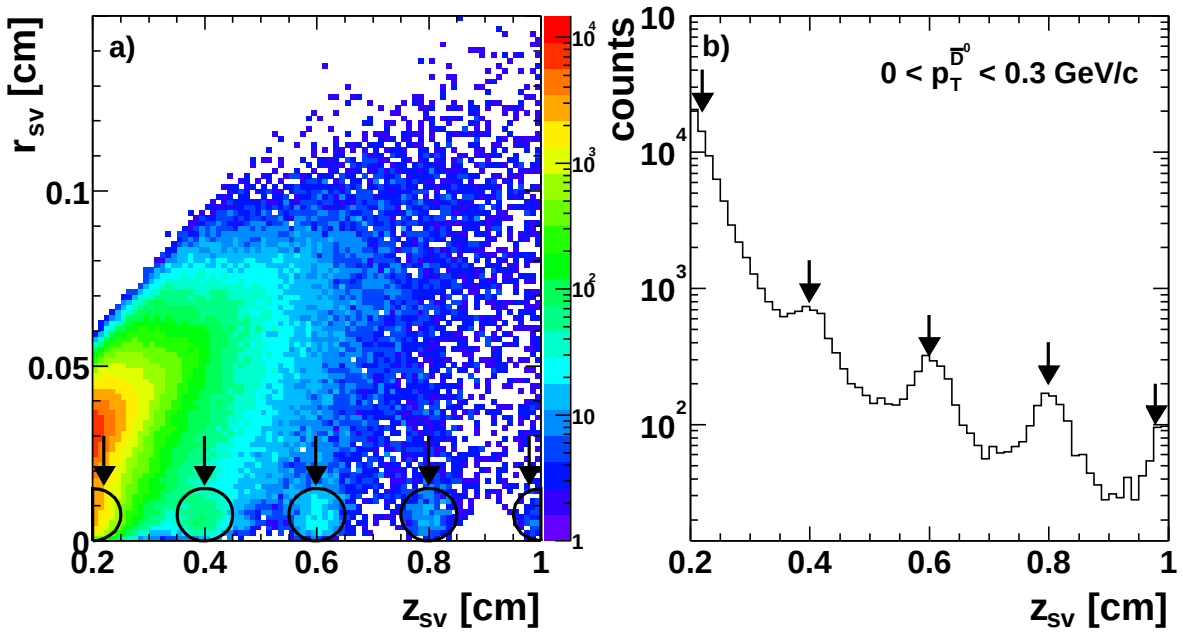

Figure 9.4: **Target structures in the secondary vertex distribution.** *The arrows and circles mark regions with enhanced secondary vertices. These might be tracks from secondary interactions of collision fragments in downstream targets. They are removed by cutting out a box of $z_{sv} > 1.5$ mm and $r_{sv} < 300$ μm in the r_{sv}-z_{sv} distribution of the secondary vertex.*

$\sigma_m = 70$ MeV/c^2 is reproduced by the fast Monte Carlo simulation. An additional smearing of the z coordinate with a width of $\sigma_z = 190$ μm had to be introduced to reproduce the secondary vertex resolution given in equation (8.4). The fast Monte Carlo simulation does not comprise the possibility of mismatches between the detectors. Thus, the distributions shown in figure 9.3 have only tails in the case of the full overlay Monte Carlo simulation.

9.3 Analysis

The analysis of the decay $\overline{D}^0 \rightarrow K^+\pi^-$ is similar to the K^0_S analysis described in section 8.3.1. Thus, only the differences will be explained here. The analysis of the $\overline{D}^0$ meson is is based on 18.9 million events at 7% centrality, comprising the calibration units 146 to 415 as explained in section 8.3.1. No effective particle identification is possible, meaning that the kaon mass is assigned to all positive tracks and the pion mass to all negative tracks. The combinatorial background is obtained with the mixed events technique.

A high single track transverse momentum cut of $p_T > 400$ MeV/c is possible for the $\overline{D}^0$ analysis due to the high momentum range of the decay kaon and pion. The decay length of the $\overline{D}^0$ meson with $c\tau = 123$ μm is short. Thus, the secondary vertex cut is chosen in the range of 1 mm (compare figure 8.2). In this scope interesting features become visible in the secondary vertex distribution as shown in figure 9.4. Plot a) shows

polar angle	$0.1396 < \theta_{TPC} < 0.2443$
Armenteros-Podolanski	$q_T > 0.5$ GeV/c
single track transverse momentum	$p_T > 400$ MeV/c
opening angle	$\psi > 0.25$ rad
χ^2 probability of the line fit	$P_{\chi^2}^{line} > 0.05$
χ^2 probability of the vertex fit	$P_{\chi^2}^{vtx} > 0.05$
secondary vertex	1 mm $< z_{sv} <$ 1 cm
bep parameter	$bep < 200$ μm
cleaning of target tracks	$z_{sv} < 1.5$ mm $\|\|$ $r_{sv} > 300$ μm

Table 9.2: **Cuts for the $\overline{\mathrm{D}}^0$ analysis.** *The table contains a compilation of the cuts used in the $\overline{D}^0$ analysis.*

the distribution of the transverse coordinate r_{sv} versus the longitudinal coordinate z_{sv} with logarithmic color code. The circles and arrows mark regions with enhanced secondary vertices. The distances of these structures are 2 mm in longitudinal direction, which is the distance between adjacent targets. These structures are target tracks which might originate from secondary interactions of collision fragments in downstream targets. Plot b) shows the distribution of z_{sv} for low values of $p_T^{\overline{D}^0}$. Here, the target structures appear as equidistant peaks marked with arrows. To obtain a clean track sample for the $\overline{D}^0$ analysis a box of $z_{sv} > 1.5$ mm and $r_{sv} < 300$ μm is cut out in the r_{sv}-z_{sv} distribution, taking into account that the radius of a target is 300 μm. A compilation of all cuts used for the $\overline{D}^0$ analysis is listed table 9.2. It has been shown in section 9.1 that the hard cut of $q_T > 0.5$ GeV/c^2 in the Armenteros-Podolanski plane removes all resonance contributions from the invariant mass distribution, except those from charmed mesons and baryons.

The normalization between the same and mixed events invariant mass distributions is obtained by fitting their ratio with a spectrum of charmed resonances on top of the normalization constant. The spectrum of charmed resonances is based on PYTHIA and simulated with the fast simulation described in section 9.2. The same cuts as used in the analysis of the data are applied to the simulation. As an example figure 9.5 shows a spectrum of charmed resonances for the cuts listed in table 9.2. The spectrum is normalized to the yield of the decay $\overline{D}^0 \to K^+\pi^-$. To fit the ratio between same and mixed events distributions the $\overline{D}^0$ yield is constraint to positive values.

The signal distribution, which is obtained after subtraction of the combinatorial background, is also fitted with the spectrum of charmed resonances, but now on top of a polynomial of first order to account for a possible residual background. In contrast to the fitting procedure for the ratio, the $\overline{D}^0$ yield is not constraint to positive values.

This procedure is repeated for different sets of cuts. The largest influence on the invariant mass spectrum of the $\overline{D}^0$ is observed, if the opening angle or the secondary vertex cut are varied. This is shown in figure 9.6 for three different opening angle cuts, $\psi > 0.24$, 0.25, and 0.26 rad, and two different secondary vertex cuts, $z_{sv} > 1.0$ and 1.1 mm. The six cut variations are labeled with numbers 1 to 6. The first row (a) shows the raw invariant mass spectra of the same events (solid line) and the normalized mixed events (dashed

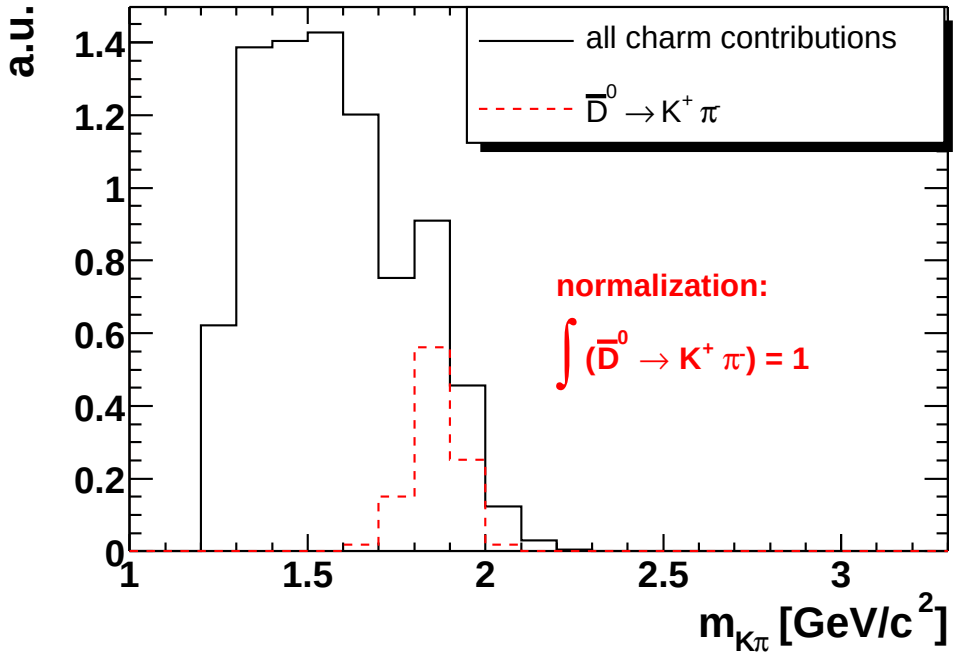

Figure 9.5: **Example of a spectrum of charmed resonances.** *The spectrum contains all contributions from charmed resonances, which pass the cuts listed in table 9.2. For comparison a bin size of 100 MeV/c^2 is chosen, as used in the analysis of the $\overline{D}^0$ meson. The red dashed-line indicates the contribution from the decay $\overline{D}^0 \to K^+\pi^-$.*

line) distributions in logarithmic scale with a bin size of 100 MeV/c^2. Remarkable is that, even though very hard cuts are applied (see table 9.2), the number of entries is still of the order of 10^6 per bin. The measurement of a tiny signal thus requires careful treatment of the normalization. The ratio between same and mixed events distributions is shown in the second row (b) of figure 9.6, together with the fit for the normalization as explained above. The signal distribution and the fit for the $\overline{D}^0$ yield is shown in the third row (c). The resulting fit parameters are the intercept and the slope for the residual background and the $\overline{D}^0$ yield N_{meas} in the considered decay channel. The fit parameters and the corresponding χ^2 per number of degrees of freedom are summarized in table 9.3 for the six sets of cuts. Except for the measurement number 2 with large χ^2/dof, all intercept and slope parameters are consistent with zero within the errors.

The efficiencies are calculated for each set of cuts using the full overlay Monte Carlo simulation described in section 8.2.1. The expected yields N_{exp} in the considered decay channel $\overline{D}^0 \to K^+\pi^-$ are calculated according to:

$$N_{exp} = N_{ev} \langle \overline{D}^0 \rangle \, B \, A \, \epsilon. \tag{9.2}$$

In this equation N_{ev} is the number of analyzed events, $\langle \overline{D}^0 \rangle = 0.12$ is the expected average number of $\overline{D}^0$ mesons per event according to [26], $B = 3.80\%$ [66] is the branching ratio, $A = 3.43\%$ is the acceptance and ϵ is the efficiency.

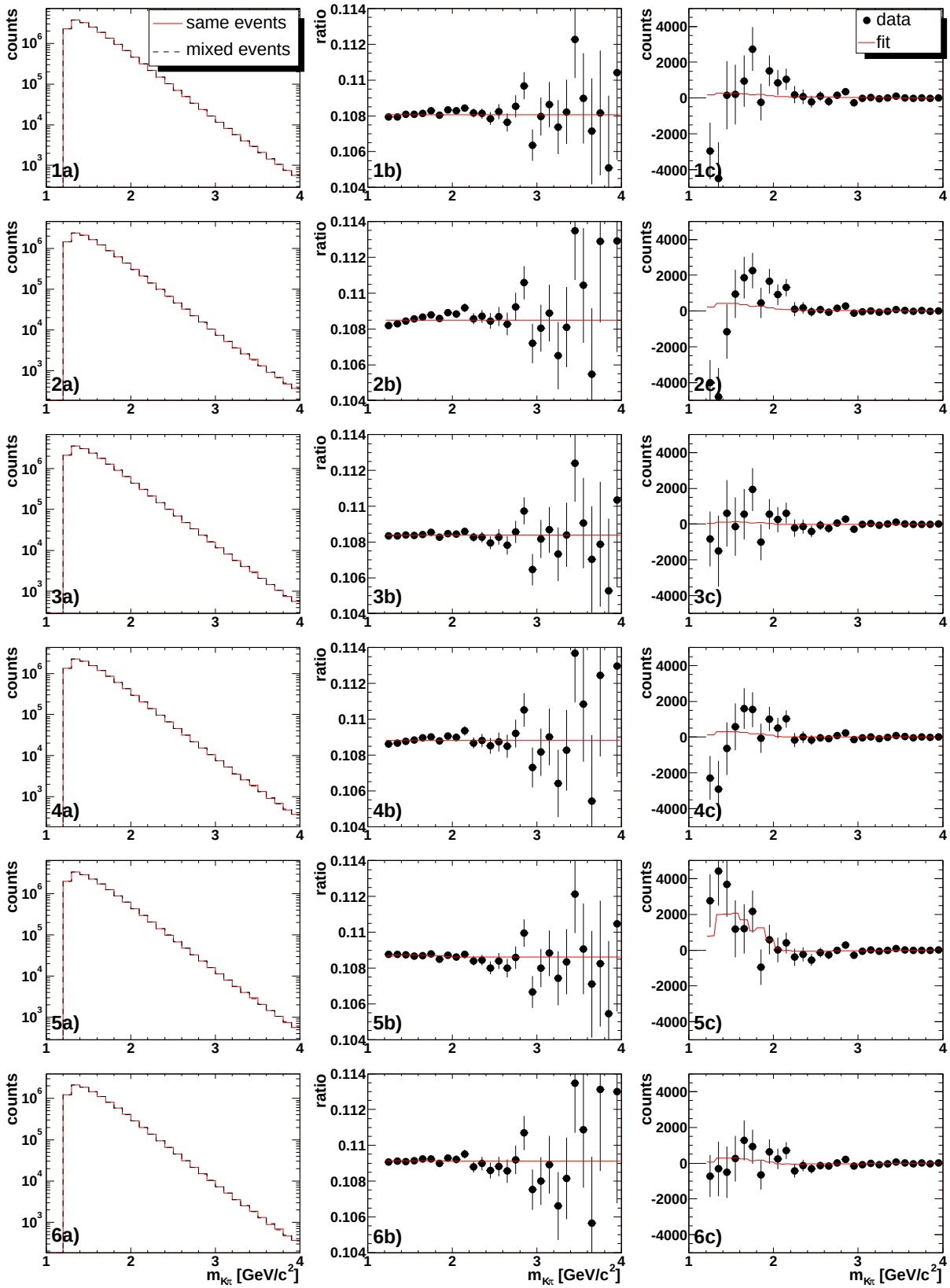

Figure 9.6: **$\overline{\mathrm{D}}^0$ invariant mass spectra for different sets of cuts.** *The numbers 1 to 6 label different sets of opening angle and secondary vertex cuts: $\psi > 0.24$ rad (1,2), $\psi > 0.25$ rad (3,4), and $\psi > 0.26$ rad (5,6), with $z_{sv} > 1.0$ mm (1,3,5) and $z_{sv} > 1.1$ mm (2,4,6). Plots a) show the raw invariant mass spectra, plots b) the ratio between same and mixed events distributions, and plots c) the signal spectra.*

spectrum	cuts	intercept	slope $[(\mathrm{GeV/c^2})^{-1}]$	N_{meas}	χ^2/dof
1	$\psi > 0.24$ rad $z_{sv} > 1.0$ mm	148 ± 175	-38 ± 47	130 ± 509	36.26/25
2	$\psi > 0.24$ rad $z_{sv} > 1.1$ mm	143 ± 140	-37 ± 38	224 ± 388	57.69/25
3	$\psi > 0.25$ rad $z_{sv} > 1.0$ mm	-44 ± 174	11 ± 47	105 ± 496	22.45/25
4	$\psi > 0.25$ rad $z_{sv} > 1.1$ mm	11 ± 140	-2 ± 38	200 ± 376	33.66/25
5	$\psi > 0.26$ rad $z_{sv} > 1.0$ mm	-163 ± 173	43 ± 47	1410 ± 456	27.81/25
6	$\psi > 0.26$ rad $z_{sv} > 1.1$ mm	-127 ± 139	34 ± 37	250 ± 366	22.84/25

Table 9.3: **Fit results for $\overline{\mathrm{D}}^0$ invariant mass spectra.** *The table summarizes the fit results from the signal spectra in figure 9.6. N_{meas} is the measured $\overline{D}^0$ yield.*

The efficiencies ϵ and the significances $S/\sqrt{B}$ are listed in the first two rows of table 9.4 for the six sets of cuts. The significances consider a range of $\pm 2.5\,\sigma_m$ around the nominal value of the $\overline{D}^0$ invariant mass. The expected $\overline{D}^0$ yields N_{exp} are given in the third row of table 9.4 according to equation (9.2). The first error of the expected yield is the statistical uncertainty coming from the acceptance and efficiency determination. The second error is the systematic uncertainty, containing the uncertainty of the branching ratio with 0.09% [66] and of the efficiency with 8.6%. The last row of table 9.4 contains the calculated enhancement factors E, i.e. the ratio between measured and expected yields, with the corresponding statistical and systematic uncertainties. The systematic uncertainties of the enhancement factors contain again the uncertainty of the branching ratio and of the efficiency. It is seen that this error is negligible as compared to the statistical error. Thus, this error is neglected in further considerations.

Within the statistical uncertainties the enhancement factors should remain robust against the variation of cuts. However, the delicate determination of the normalization constant between same and mixed events distributions could result in a systematic uncertainty in the measurement of the $\overline{D}^0$ yield. This systematic uncertainty is given by half of the largest variation between the enhancement factors, resulting in $\Delta E_{syst} \approx 7.3$.

9.4 Upper Limit in the Bayesian Approach

If the outcome of an experiment is a null result it is often interesting to set an upper limit in order to eliminate some of the proposed theories. This can be done either in the framework of Frequentist or Bayesian statistics. The two approaches attribute different meanings in the involved quantities and lead to different numerical results. The question which framework yields the better description is at present a hotly debated issue.

The determination of the upper limit in this thesis follows Bayesian philosophy, which

spectrum	ϵ	$S/\sqrt{B}$ $[10^{-3}]$	N_{exp}	E
1	3.2%	4.32	$94.95 \pm 0.06 \pm 8.47$	$1.4 \pm 5.4 \pm 0.1$
2	2.4%	4.07	$72.45 \pm 0.05 \pm 6.46$	$3.1 \pm 5.4 \pm 0.3$
3	3.1%	4.31	$92.87 \pm 0.06 \pm 8.28$	$1.1 \pm 5.3 \pm 0.1$
4	2.4%	4.05	$70.72 \pm 0.05 \pm 6.31$	$2.8 \pm 5.3 \pm 0.3$
5	3.1%	4.28	$90.37 \pm 0.05 \pm 8.06$	$15.6 \pm 5.0 \pm 1.4$
6	2.3%	4.02	$68.63 \pm 0.05 \pm 6.12$	$3.7 \pm 5.3 \pm 0.3$

Table 9.4: **Enhancement factors for different sets of cuts.** *The table contains the efficiencies ϵ, the significanes $S/\sqrt{B}$, the expected $\overline{D}^0$ yields N_{exp} and the enhancement factors E for the six different $\overline{D}^0$ spectra of figure 9.6. The expected yields are calculated according to equation (9.2). The enhancement factors are the ratios between the measured yields from table 9.3 and the expected yields. The errors are the statistical and systematic uncertainties, respectively.*

is very general and avoids unphysical confidence limits. Following [66, 94, 95] and [96] this section will describe some important features of Bayesian statistics and its conclusions for the upper limit determination of the $\overline{D}^0$ meson.

9.4.1 General Considerations

The starting point is Bayes' theorem:

$$p(hyp|data) = \frac{L(data|hyp)p(hyp)}{\int L(data|hyp')p(hyp')\,dhyp'}. \tag{9.3}$$

The degree of belief in a hypothesis, given the data, is summarized by the posterior **p**robability **d**ensity **f**unction (pdf) $p(hyp|data)$. It is proportional to the likelihood function $L(data|hyp)$ multiplied with the prior pdf $p(hyp)$. $L(data|hyp)$ gives the probability that the hypothesis, when true, just yields the data. The prior pdf $p(hyp)$ reflects the experimenters subjective degree of belief about the hypothesis before the measurement was carried out. The denominator in equation (9.3) normalizes the posterior pdf to unity.

As example, let's suppose that the measurement of a physical constant β results in the estimator b. Usually, no specific knowledge about the prior pdf $p(\beta)$ is at hand and the claim is that all physically reasonable values for β are equally probable. Thus, $p(\beta)$ is set to be constant over the region of interest and zero in the unphysical region. If β is assumed to by positive, the upper limit at $(1-\epsilon)$ confidence level is than given by:

$$1 - \epsilon = \int_0^M p(\beta'|b)\,d\beta' = \frac{\int_0^M L(b|\beta')p(\beta')\,d\beta'}{\int_0^\infty L(b|\beta')p(\beta')\,d\beta'}. \tag{9.4}$$

Figure 9.7 represents the outcome of several experiments measuring values for β, with significant probability of obtaining unphysical results. Assuming a step function for $p(\beta)$ would mean to just consider the shaded region, but renormalized to unity. By stating an upper limit at $(1-\epsilon)$ confidence level thus means that β lies in the grey shaded region.

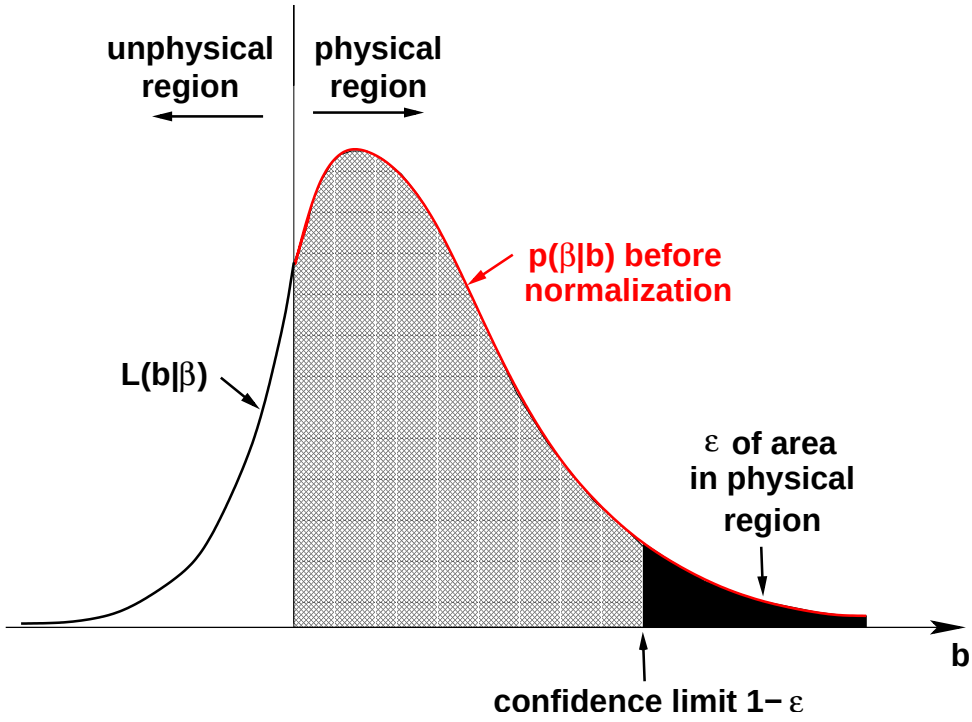

Figure 9.7: **Measurement of variables in bounded physical regions.** *Bayes' theorem says that the knowledge of the distribution of β, given the measurement b, is given by the function over the shaded region after appropriate renormalization.*

9.4.2 $\overline{\mathrm{D}}^0$ Upper Limit

In the following these considerations are applied to the measurement of the $\overline{D}^0$ yield. At first, a likelihood function is constructed. The measured invariant mass spectrum of the same and mixed events analysis is divided in bins i with bin content n_i^s and n_i^m, respectively. The bin contents are large and therefore taken to be real numbers which are Gaussian distributed. If so, than also the bin contents n_i of the invariant mass spectrum obtained after mixed events subtraction are Gaussian distributed with mean μ_i and width σ_i. The probability of the counts lying between n_i and $n_i + dn_i$ can then be written as:

$$L(n_i|\mu_i,\sigma_i)\,dn_i = \frac{1}{\sigma_i\sqrt{2\pi}}\,e^{-\frac{1}{2}\left(\frac{n_i-\mu_i}{\sigma_i}\right)^2}\,dn_i. \tag{9.5}$$

The invariant mass spectrum, obtained after mixed events subtraction, is described by a signal spectrum $W(m)$ on top of a first order polynomial describing the residual background

$$\mu(m;\mathbf{c}) = c_0 + c_1 m + c_2 W(m), \tag{9.6}$$

where $\mathbf{c} \equiv \{c_i\}$. The signal spectrum $W(m)$ is obtained from a PYTHIA simulation and contains all relevant resonances. It is normalized to the $\overline{D}^0$ peak, and thus c_2 gives the number of measured $\overline{D}^0 \to K^+\pi^-$ decays. The fit function $\mu(m;\mathbf{c})$ is linear in the

parameters $\mathbf{c}$ and can be expressed by

$$\mu(m;\mathbf{c}) = \sum_{j=0}^{2} c_j f_j(m), \tag{9.7}$$

where the f_j are a set of functions of m with $\mathbf{f} \equiv \{1, m, W(m)\}$.

Under the assumption that the bin contents n_i are statistically independent, the likelihood function of the data can be obtained by multiplying the probabilities of equation (9.5),

$$L(\mathbf{n}|\mathbf{c}) = \prod_i L(n_i|\mathbf{c}) = A\, e^{-\frac{1}{2}\sum_i \left(\frac{n_i - \mu(m_i;\mathbf{c})}{\sigma_i}\right)^2} = A\, e^{-\frac{1}{2}\chi^2(\mathbf{n}|\mathbf{c})}. \tag{9.8}$$

In this equation $\mathbf{n} \equiv \{n_i\}$, A is a normalization constant, and

$$\chi^2(\mathbf{n}|\mathbf{c}) = \sum_i \left(\frac{n_i - \mu(m_i;\mathbf{c})}{\sigma_i}\right)^2 = \sum_i \frac{1}{\sigma_i^2}\left(n_i - \sum_{j=0}^{2} c_j f_j(m_i)\right)^2. \tag{9.9}$$

The χ^2 can be expanded around the point $\overline{\mathbf{c}}$ where the likelihood becomes maximal or the χ^2 becomes minimal, thus leading to

$$\chi^2(\mathbf{n}|\mathbf{c}) = \chi^2(\mathbf{n}|\overline{\mathbf{c}}) + \sum_i \frac{\partial\chi^2(\mathbf{n}|\overline{\mathbf{c}})}{\partial c_k}\Delta c_k + \frac{1}{2}\sum_j\sum_k \frac{\partial^2\chi^2(\mathbf{n}|\overline{\mathbf{c}})}{\partial c_j \partial c_k}\Delta c_j \Delta c_k + \ldots, \tag{9.10}$$

with $\Delta c_k = c_k - \overline{c}_k$. The first derivative of equation (9.9) vanishes at the point $\overline{\mathbf{c}}$:

$$\frac{\partial\chi^2(\mathbf{n}|\overline{\mathbf{c}})}{\partial c_k} = -2\sum_i \frac{1}{\sigma_i^2}\left(n_i - \sum_j c_j f_j(m_i)\right) f_k(m_i) = 0. \tag{9.11}$$

This equation can be written in vector notation as

$$\mathbf{a} = \mathbf{W}\overline{\mathbf{c}} \quad \text{with} \quad a_k = \sum_i \frac{1}{\sigma_i^2} n_i f_k(m_i) \quad \text{and} \quad W_{jk} = \sum_i \frac{1}{\sigma_i^2} f_j(m_i) f_k(m_i). \tag{9.12}$$

The second derivative of equation (9.9), evaluated at the point $\overline{\mathbf{c}}$, yields an expression for the Hessian matrix

$$\mathbf{H} = H_{jk} = \frac{1}{2}\frac{\partial^2\chi^2(\mathbf{n}|\overline{\mathbf{c}})}{\partial c_j \partial c_k} = \sum_i \frac{1}{\sigma_i^2} f_j(m_i) f_k(m_i), \tag{9.13}$$

which is just equal to W_{jk} in equation (9.12). Higher derivatives vanish.

Inserting now the χ^2 expansion of equation (9.10) in equation (9.8), and considering proper normalization, results in

$$L(\mathbf{n}|\mathbf{c}) = \frac{1}{\sqrt{(2\pi)^3|\mathbf{V}|}}\, e^{-\frac{1}{2}(\mathbf{c}-\overline{\mathbf{c}})^T \mathbf{V}^{-1}(\mathbf{c}-\overline{\mathbf{c}})}, \tag{9.14}$$

where the covariance matrix $\mathbf{V}$ is the inverse of the Hessian matrix $\mathbf{H}$ with the determinant $|\mathbf{V}|$.

After deriving the likelihood function, the next step is to specify the prior pdf $p(\mathbf{c})$. Without having specific knowledge about the parameters the simplest choice is to set $p(c_0, c_1) = (2r)^{-2}$, where r defines the range in which the parameters are defined ($-r \leq c_0, c_1 \leq r$). The prior pdf $p(c_0, c_1)$ vanishes for $r \to \infty$ but the posterior pdf will remain finite because the normalization integral in the denominator contains the same factor $(2r)^{-2}$. Similar arguments apply to the choice of the remaining prior pdf $p(c_2)$, but now considering the knowledge that the $\overline{D}^0$ yield c_2 must be positive, that is ($0 \leq c_2 \leq r$):

$$p(c_2) = \begin{cases} 0 & \text{for } c_2 < 0 \\ r^{-1} & \text{for } c_2 \geq 0 \end{cases} \tag{9.15}$$

To obtain the posterior pdf, the likelihood function of equation (9.14) has to be multiplied with the prior pdf for the parameters, leading to

$$p(\mathbf{c}|\mathbf{n}) = \frac{B}{\sqrt{(2\pi)^3 |\mathbf{V}|}}\, p(c_2)\, e^{-\frac{1}{2}(\mathbf{c}-\overline{\mathbf{c}})^T \mathbf{V}^{-1} (\mathbf{c}-\overline{\mathbf{c}})}, \tag{9.16}$$

with the normalization constant B. The posterior pdf $p(c_2|\mathbf{n})$ can now be obtained by using the marginalization rule and integrating the joint pdf $p(\mathbf{c}|\mathbf{n})$ with respect to c_0 and c_1. In this way the posterior pdf is obtained as

$$p(c_2|\mathbf{n}) = \frac{B}{\delta\sqrt{2\pi}}\, p(c_2)\, e^{-\frac{1}{2}\left(\frac{c_2-\overline{c}_2}{\delta}\right)^2} = B\, p(c_2)\, g(c_2; \overline{c}_2, \delta), \tag{9.17}$$

where $g(c_2; \overline{c}_2, \delta)$ is used as abbreviation for the Gaussian function.

The upper limit for the $\overline{D}^0$ meson is thus given by

$$1 - \epsilon = \int_0^M p(c_2|\mathbf{n})\, dc_2 = \frac{\int_0^M g(c_2; \overline{c}_2, \delta)\, dc_2}{\int_0^\infty g(c_2; \overline{c}_2, \delta)\, dc_2} \tag{9.18}$$

at $(1 - \epsilon)$ confidence level.

9.5 Results and Discussion

The upper limit for the $\overline{D}^0$ yield is determined with measurement number 3 from figure 9.6, plot 3 c). This measurement is performed with the set of cuts listed in table 9.2. It fulfills the requirements of having one of the highest significances and at the same time $\chi^2/\text{dof} \approx 1$. The $\overline{D}^0$ yield N_{meas} obtained from this measurement is given by

$$N_{meas} = 105 \pm 496\ (\text{stat}) \pm 693\ (\text{syst}), \tag{9.19}$$

with a systematic uncertainty of 660%. The systematic uncertainty is obtained from the considerations in section 9.3 with $\Delta E_{syst}/E \approx 7.3/1.1$. Using further equation (9.18) with the parameters

$$\overline{c}_2 = N_{meas} = 105 \quad \text{and} \quad \delta = \sqrt{(\Delta N_{meas}^{stat})^2 + (\Delta N_{meas}^{syst})^2} = 852, \tag{9.20}$$

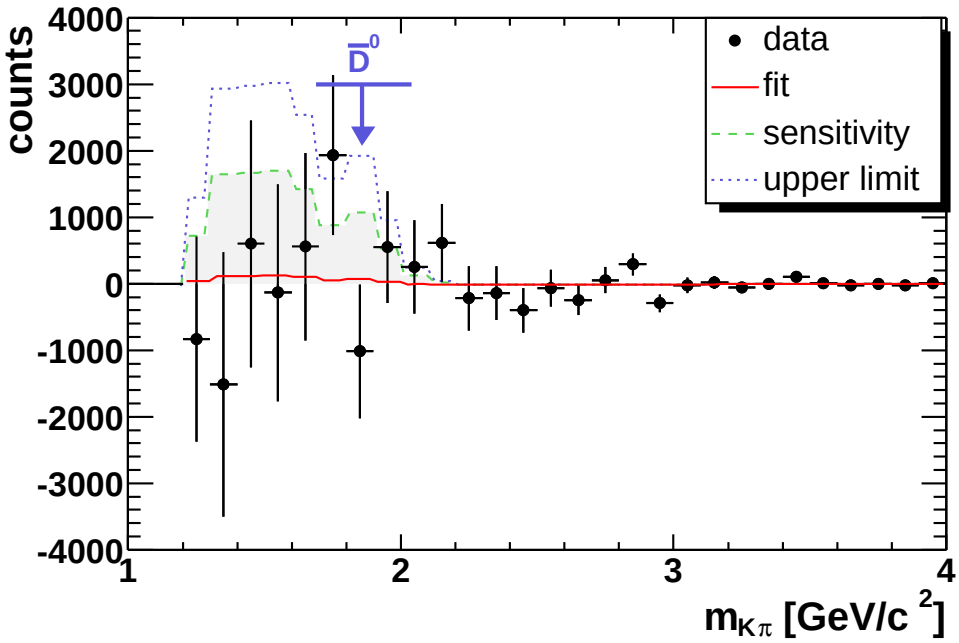

Figure 9.8: **$\overline{D}^0$ upper limit.** *The figure shows the final result for the measurement of the $\overline{D}^0$ yield. The data is based on 18.9 million analyzed events of 158 AGeV/c Pb-Au collisions. The red solid curve is the fit to the data with a measured enhancement factor of $E = 1$. The upper limit of $E_M = 22$ is indicated with the blue dotted line. The sensitivity of the experiment with $E_M^{sens} = 13$ is drawn as green dashed line. It is the best possible upper limit, which could be obtained with the available statistics if no systematic uncertainties would be present.*

an upper limit for the $\overline{D}^0$ yield of $M = 2058$ is obtained at 98% confidence level. As the expected number of $\overline{D}^0$ mesons is $N_{exp} = 93$, an upper limit for the enhancement factor of $E_M = M/N_{exp} = 22$ can be excluded. The same result is obtained if the measurement is fitted with a charmed resonance spectrum on top of a constant, instead of a polynomial of first order. If measurement number 6 from figure 9.6, plot 6 c) is used for the calculation, an upper limit for the open charm enhancement factor of $E_M = 24$ is obtained.

Figure 9.8 shows the final results for the measurement of the $\overline{D}^0$ yield in 158 AGeV/c Pb-Au collisions. The red solid curve is the fit to the data, resulting in an enhancement factor of $E = 1$. The blue dotted curve marks the upper limit for the enhancement factor with $E_M = 22$. The position of the $\overline{D}^0$ meson in the continuous spectrum of charmed resonances is indicated with an arrow and a horizontal line of $\pm 2.5\,\sigma_m$. The green dashed line marks the best possible upper limit of $E_M^{sens} = 13$, considering only the statistical uncertainty. This is denoted as sensitivity of the experiment. It is the upper limit that could be obtained with the available statistics, under the assumption that the systematic uncertainties in the determination of the normalization between same and mixed events distributions could be removed.

The result can be compared to two other measurements of the open charm enhancement factor E at the CERN SPS. The indirect measurement from the NA38/NA50 collaboration [17] has already been presented in section 3.1. It is conjectured that the observed excess in the intermediate mass range ($1 < m_{\mu\mu} < 3$ GeV/c^2) of the dimuon

spectrum could be due to an open charm enhancement. For 158 AGeV/c central Pb-Pb collisions an enhancement factor up to $E = 3.5$ is possible (compare figure 3.3). The upper limit of $E_M = 22$ obtained in this thesis is clearly not sensitive enough to reach the region below $E \approx 3.5$ and bring further light in the situation.

The second experiment is the direct open charm measurement of the decay channels $\overline{D}^0 \rightarrow K^+\pi^-$ and $D^0 \rightarrow K^-\pi^+$ from the NA49 collaboration [97, 98] for 158 AGeV/c Pb-Pb collisions. As result an upper limit for the combined yield per event of $M(\langle D^0 + \overline{D}^0 \rangle) = 1.5$ is obtained at 98% confidence level. The comparison to the expected yield per event $\langle D^0 + \overline{D}^0 \rangle = 0.21$ [26] gives an upper limit for the enhancement factor of $E_M^{NA49} = 7$.

The measurement in [97, 98] is based on two samples of tracks with and without kaon identification via the TPC dE/dx, respectively. The relative dE/dx-resolution is about 4%. The measurement of the particle momentum is precise with a resolution of $\Delta p/p^2 = 3 \cdot 10^{-5}$ (GeV/c)$^{-1}$. The decision weather kaon identification is performed or not depends on the track length and on weather the momentum of the track is low enough to make kaon selection via a dE/dx cut possible. The $\overline{D}^0$ and D^0 decay channels are analyzed separately and combined at the end. It is not clear how the contribution of D^0 mesons in the $\overline{D}^0$ spectrum, and vice versa, is treated for the track sample without kaon identification (compare herefore figure 9.2). This contribution might in fact be negligible compared to their $\overline{D}^0$ or D^0 mass resolution of $m_\Gamma = 6.2$ MeV/c^2, obtained from an overlay Monte Carlo simulation. However, in the absence of particle identification a careful study of contributing resonances to the invariant mass spectrum is advisable.

In [97, 98] the raw invariant mass spectra are directly fitted in a region of ± 90 MeV/c^2 around the position of the $\overline{D}^0$ or D^0 meson, using a Cauchy function for the signal distribution on top of a polynomial of fourth order for the background. The $\overline{D}^0$ or D^0 invariant masses and widths are kept fixed during the fitting procedure. This approach is not followed in this thesis. The reason is that, if the signal spectrum has a different shape than that predicted by a Monte Carlo simulation, it might easily be assigned to the background and thus included in the fit with the polynomial of high order. It is judged to be more safe to subtract the combinatorial background using the mixed events technique and describe the remaining signal spectrum with a simulation of the contributing resonances, as described in the course of this chapter.

Chapter 10

Conclusions

The development of a secondary particle reconstruction scheme using the combined information of the SiDC detectors and the TPC to reconstruct the secondary vertex is new for the CERES experiment. The analysis scheme allows to suppress a large fraction of target tracks by cutting on the longitudinal distance between the decay vertex of the secondary particle and the primary interaction region. The constraint of this method is, that the particle has to decay upstream SiDC1, i.e. within a distance of 10.4 cm. Consequently, it is applicable to reconstruct particles with relatively short decay length.

The method is optimal to reconstruct the decay $K^0_S \rightarrow \pi^+\pi^-$ ($c\tau = 2.68$ cm) and is already successfully incorporated in other CERES analyses, like the measurement of the elliptic flow of the K^0_S [99]. Within this thesis the K^0_S meson is used as reference measurement to study the efficiency for the subsequent measurement of the $\overline{D}^0$ yield. It is shown that the measurement of the integrated K^0_S rapidity density of $dN/dy = 19.75 \pm 0.23\,(\text{stat}) \pm 1.70\,(\text{syst})$ for $2.0 < y < 2.6$ is dominated by the uncertainty of the efficiency determination with 8.6%. Within this limit, the results obtained for the K^0_S agree with an alternative analysis of the CERES data and with measurements the NA49 and NA57 collaborations.

The secondary particle reconstruction scheme reaches its limits of applicability if the cut on the secondary vertex gets close to the target resolution of about $\sigma_z \approx 210$ μm. The analysis of the $\overline{D}^0$ meson ($c\tau = 123$ μm) is in this regime. However, a careful study of the combinatorial background and of contributing resonances to the invariant mass spectrum still allows to derive an upper limit for the $\overline{D}^0$ yield. Taking the ratio to the expected $\overline{D}^0$ yield per event of $\langle \overline{D}^0 \rangle = 0.21$ [25, 26], which is calculated by scaling the charm cross-section to nucleus-nucleus collisions, an upper limit of $E_M = 22$ is obtained at 98% confidence level for the open charm enhancement factor in 158 AGeV/c Pb-Au collisions.

Appendix A

The Armenteros-Podolanski Plot

A common problem of numerous experiments is the lack of particle identification. For a two body decay system this issue was addressed in 1954 by J. Podolanski and R. Armenteros [90]. They developed a method to distinguish between different hadrons using the transverse and longitudinal momenta q_T and q_L of the decay particles relative to the flight direction of their mother particle. In a so called Armenteros-Podolanski plot the transverse momentum q_T is plotted against an asymmetry variable α, which is a combination of the longitudinal momenta of the positive and the negative decay particles:

$$\alpha = \frac{q_L^+ - q_L^-}{q_L^+ + q_L^-}. \tag{A.1}$$

The transverse momenta of the decay particles are by definition equal:

$$q_T^+ = q_T^- = q_T. \tag{A.2}$$

The following derivations will show that each type of hadrons describe individual ellipses in the q_T-α plane.

In the center of mass system the transverse and longitudinal momentum of the positive decay particle and and its energy can be written as:

$$\begin{aligned} q_{T,cm}^+ &= p_{cm}\sin(\theta_{cm}) \\ q_{L,cm}^+ &= p_{cm}\cos(\theta_{cm}) \\ E_{cm}^+ &= \sqrt{(p_{cm})^2 + (m^+)^2}. \end{aligned} \tag{A.3}$$

In the laboratory system these quantities transform to

$$\begin{aligned} q_T^+ &= q_{T,cm}^+ = p_{cm}\sin(\theta_{cm}) \\ q_L^+ &= \gamma q_{L,cm}^+ + \gamma\beta E_{cm}^+ = \gamma p_{cm}\cos(\theta_{cm}) + \gamma\beta E_{cm}^+ \\ E^+ &= \gamma E_{cm}^+ + \gamma\beta q_{L,cm}^+ = \gamma E_{cm}^+ + \gamma\beta p_{cm}\cos(\theta_{cm}). \end{aligned} \tag{A.4}$$

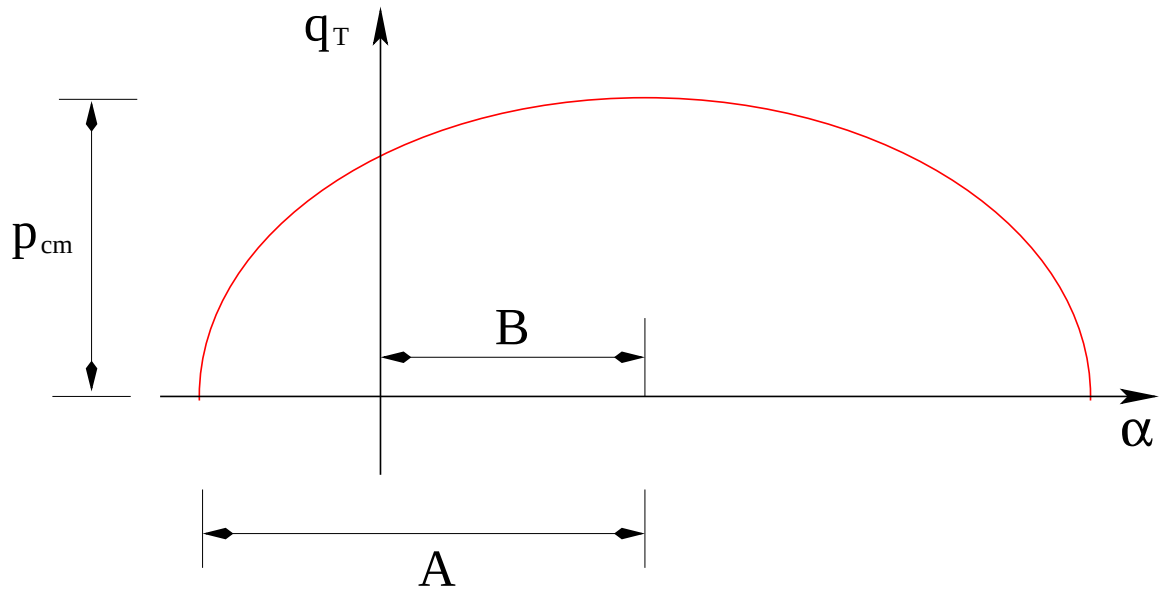

Figure A.1: **Armenteros-Podolanski Ellipse.** *Each particle has its individual ellipse in the q_T-α plane of the Armenteros-Podolanski plot with the semi-minor and semi-major axes given by p_{cm} and A as derived below. The point $(B, 0)$ is the center of the ellipse.*

Due to the relation $q^-_{L,cm} = -q^+_{L,cm}$, one arrives to

$$\begin{aligned} q^-_T &= q^-_{T,cm} = p_{cm}\sin(\theta_{cm}) \\ q^-_L &= -\gamma p_{cm}\cos(\theta_{cm}) + \gamma\beta E^-_{cm} \\ E^- &= \gamma E^-_{cm} - \gamma\beta p_{cm}\cos(\theta_{cm}) \end{aligned} \tag{A.5}$$

for the negative particle.

To derive the former defined variable α one has to form the difference

$$q^+_L - q^-_L = 2\gamma p_{cm}\cos(\theta_{cm}) + \gamma\beta(E^+_{cm} - E^-_{cm}) \tag{A.6}$$

and the addition

$$q^+_L + q^-_L = p_M = \gamma\beta m_M. \tag{A.7}$$

Here p_M denotes the momentum of the mother particle in the laboratory system and m_M its rest mass. According to equation (A.1), equations (A.6) and (A.7) can then be combined to form:

$$\alpha = \frac{2p_{cm}}{\beta m_M}\cos(\theta_{cm}) + \frac{E^+_{cm} - E^-_{cm}}{m_M} = A\cos(\theta_{cm}) + B. \tag{A.8}$$

Together with equation (A.4) or (A.5) this results in

$$\begin{aligned} \cos(\theta_{cm}) &= \frac{\alpha - B}{A} \quad \text{and} \\ \sin(\theta_{cm}) &= \frac{q_T}{p_{cm}} \end{aligned} \tag{A.9}$$

with

$$\sin^2(\theta_{cm}) + \cos^2(\theta_{cm}) = \left(\frac{\alpha - B}{A}\right)^2 + \left(\frac{q_T}{p_{cm}}\right)^2 = 1. \tag{A.10}$$

This is an ordinary ellipse equation in the q_T-α plane with the semi-minor axis given by p_{cm} and the semi-major axis by $A = 2p_{cm}/(\beta m_M)$. The ellipse is shifted along the α-axis by the amount $B = (E^+_{cm} - E^-_{cm})/m_M$. The geometry is depicted in figure A.1.

Bibliography

[1] G. Agakichiev et al.: *Enhanced Production of Low-Mass Electron Pairs in 200 GeV/Nucleon S-Au Collisions at the CERN Super Proton Synchrotron*, Phys. Rev. Lett. **75** (1995) 1272-1275.

[2] G. Agakichiev et al.: *Systematic study of low-mass electron pair production in p-Be and p-Au collisions at 450 GeV/c*, Eur. Phys. J. **C4** (1998) 231.

[3] G. Agakichiev et al.: *Low-mass e^+e^- pair production in 158 AGeV Pb-Au collisions at the CERN SPS, its dependence on multiplicity and transverse momentum*, Phys. Lett. **B422** (1998) 405-412.

[4] D. Adamová et al.: *Enhanced Production of Low-Mass Electron-Positron Pairs in 40 AGeV Pb-Au collisions at the CERN SPS*, Phys. Rev. Lett. **91** (2003) 042301, nucl-ex/0209024.

[5] G. Agakichiev et al.: *e^+e^--pair production in Pb-Au collisions at 158 GeV per nucleon*, Eur. Phys. J. **C41** (2005) 475-513.

[6] M. Masera: *Dimuon Prodution below Mass 3.1 GeV/c^2 in p-W and S-W Interactions at 200 GeV/c/A*, Nucl. Phys. **A590** (1995) 93c-102c.

[7] A. L. S. Angelis et al.: *Study of vector mesons in dimuon production in a large kinematic region in pW and SW interactions at 200 GeV/c/nucleon*, Eur. Phys. J. **C5** (1998) 63-75.

[8] E. Scomparin: *Intermediate mass muon pair continuum in Pb-Pb collisions at 158 GeV/c*, Nucl. Phys. **A610** (1996) 331c-341c.

[9] R. D. Pisarski: *Phenomenology of the Chiral Phase Transition*, Phys. Lett. **110B** (1982) 155-158.

[10] G. E. Brown and M. Rho: *Scaling effective Lagrangians in a dense medium*, Phys. Rev. Lett **66** (1991) 2720-2723.

[11] R. Rapp and J. Wambach: *Chiral Symmetry Restoration and Dileptons in Relativistic Heavy-Ion Collisions*, Adv. Nucl. Phys. **25** (2000) 1, hep-ph/9909229.

[12] A. Marín: J. Phys. **G30** (2004) 709-716, nucl-ex/0406007.

[13] J. Slívová (Bielčíková): *Azimuthal Correlations of High-p_T Pions in 158 AGeV/c Pb-Au Collisions Measured by the CERES Experiment*, Dissertation, Max-Planck-Institut für Kernphysik, Heidelberg, 2003.

[14] J. P. Wurm and J. Bielčíková: *Semi-Hard Scattering Unraveled from Collective Dynamics by Two-Pion Azimuthal Correlations in 158 AGeV/c Pb+Au Collisions*, Phys. Rev. Lett. **92** (2004) 032301, nucl-ex/0303014.

[15] D. Adamová et al.: *Beam Energy and Centrality Dependence of Two-Pion Bose-Einstein Correlations at SPS Energies*, Nucl. Phys. **A714** (2003) 124, nucl-ex/0207005.

[16] D. Adamová et al.: *Event-by-event fluctuations of the mean transverse momentum in 40, 80, and 158 AGeV/c*, Nucl. Phys. **A727** (2003) 97-119, nucl-ex/0305002.

[17] M. C. Abreu et al.: *Dimuon and charm production in nucleus-nucleus collisions at the CERN-SPS*, Eur. Phys. J. **C14** (2000) 443-455.

[18] P. Lévai, B. Müller and X.-N. Wang: *Open charm production in an equilibrating parton plasma*, Phys. Rev. **C51** (1995) 3326-3335.

[19] Z. Lin and X.-N. Wang: *Enhancement of intermediate mass dileptons from charm decays at SPS energies*, Phys. Lett. **B444** (1998) 245-251.

[20] P. Bordalo: *Dimuon enhancement in nucleus-nucleus ultrarelativistic interactions*, Nucl. Phys. **A661** (1999) 538c-541c.

[21] C. Spieles et al.: *A microscopic calculation of secondary Drell-Yan production in heavy ion collision*, Eur. Phys. J. **C5** (1998) 349-355.

[22] G. Q. Li and C. Gale: *Intermediate-Mass Dilepton Production in Heavy-Ion Collisions at 200 AGeV*, Phys. Rev. Lett. **81** (1998) 1572-1575.

[23] G. Q. Li and C. Gale: *Intermediate-mass dilepton spectra and the role of secondary hadronic processes in heavy-ion collisions*, Phys. Rev. **C58** (1998) 2914-2926.

[24] R. Rapp and E. Shuryak: *Thermal Dilepton Radiation at Intermediate Masses at the CERN-SpS*, Phys. Lett. **B473** (2000) 13-19, hep-ph/9909348.

[25] P. Braun-Munzinger et al.: *Open charm contribution to dilepton spectra produced in nuclear collisions at SPS energies*, Eur. Phys. **C1** (1998) 123-130.

[26] P. Braun-Munzinger and J. Stachel: *(Non) Thermal Aspects of Charmonium Production and a New Look at J/ψ Suppression*, Phys. Lett. **B490** (2000) 196, nucl-th/0007059.

[27] Cheuk-Yin Wong: *Introduction to High-Energy Heavy-Ion Collisions*, World Scientific (1994).

[28] P. E. Hodgson, E. Gadioli and E. Gadioli Erba: *Introduction to Nuclear Physics*, Oxford Science Publications (2000).

[29] J. Stachel and G. R. Young: *Relativistic Heavy Ion Physics at CERN and BNL*, Annu. Rev. Nucl. Part. Sci. **42** (1992) 537-597.

[30] P. Braun-Munzinger: *Towards the Quark-Gluon Plasma*, nucl-ex/9909014 (1999).

[31] U. Heinz and M. Jacob: *Evidence for a New State of Matter: An Assessment of the Results from the CERN Lead Beam Program*, nucl-th/0002042 (2000).

[32] ALICE collaboration: Technical Proposal CERN/LHC 95-71 (1995).

[33] F. Karsch: *Lattice Results on QCD Thermodynamics*, Nucl. Phys. **A698** (2002) 199c-208c, hep-ph/0103314.

[34] J. Stachel: *Towards the Quark-Gluon-Plamsa*, Nucl. Phys. **A654** (1999) 119c-135c, nucl-ex/9903007.

[35] P. Braun-Munzinger and J. Stachel: *Probing the Phase Boundary between Hadronic Matter and the Quark-Gluon-Plasma in Relativistic Heavy Ion Collisions*, Nucl. Phys **A606** (1996) 320-328, nucl-th/9606017.

[36] H. Heiselberg: *Hot Neutron Stars as a Source for Gamma Ray Bursts at Cosmological Distance Scales*, astro-ph/9711169 (1997).

[37] J. D. Bjorken: *Highly relativistic nucleus-nucleus collisions: The central rapidity region*, Phys. Rev. **D27** (1983), 140-151.

[38] J. Cleymans and K. Redlich: *Chemical and Thermal Freeze-Out Parameters from 1 to 200 AGeV*, Phys. Rev. **C60** (1999) 054908, nucl-th/9903063.

[39] M. Birse and J. McGovern: *Seeing the lighter side of quarks*, Physics World (1995).

[40] B. Müller: Rep. Prog. Phys. **58**(6) (1995) 611.

[41] H. Satz: *Colour Deconfinement in Hot and Dense Matter*, hep-ph/9611366 (1996).

[42] A. Chodos, R. L. Jaffe, K. Johnson, C. B. Thorn and V. F. Weisskopf: *New Extended Model of Hadrons*, Phys. Rev. **D9** (1974) 3471-3495.

[43] K. G. Wilson: *Confinement of Quarks*, Phys. Rev. **D10** (1974) 2445.

[44] J. Kapusta, P. Lichard and D. Seibert: *High energy photons from quark-gluon plasma versus hot hadronic gas*, Phys. Rev. **D44** (1991) 2774; *Erratum*, Phys. Rev. **D47** (1991) 4171.

[45] T. Matsui and H. Satz: *J/ψ Suppression by Quark-Gluon Plasma Formation*, Phys. Lett. **B178** (1986) 416-422.

[46] M. C. Abreu et al.: *J/ψ, ψ' and muon pair production in p-W and S-U collisions*, Nucl. Phys. **A566** (1994) 77c-85c.

[47] T. Sjöstrand: *PYTHIA 5.7 and JETSET 7.4 Physics and Manual*, Computer Physics Commun **82** (1994) 74, hep-ph/9508391.

[48] A. P. Kostyuk et al.: *Statistical Coalescence Model Analysis of J/ψ Production in Pb+Pb Collisions at 158 AGeV*, Phys. Lett. **B531** (2002) 195-202, hep-ph/0110269.

[49] A. P. Kostyuk et al.: *Heavy Flavor Enhancement as a Signal of Color Deconfinement*, Phys. Lett. **B519** (2001) 207, hep-ph/0103057.

[50] A. P. Kostyuk: *Statistical J/ψ production and open charm enhancement in Pb+Pb collisions at CERN SPS*, J. Phys. **G28** (2002) 2047-2050, hep-ph/0111096.

[51] K. Gallmeister et al.: *Is there a unique thermal source of dileptons in Pb(158 AGeV) + Au,Pb reactions?*, Phys. Lett. **B473** (2000) 20-24, hep-ph/9908269.

[52] K. Gallmeister et al.: *A unique large thermal source of real and virtual photons in the reaction Pb(158 AGeV) + Pb,Au*, hep-ph/0006134.

[53] K. Gallmeister et al.: *Can extended duality uniquely explain the dilepton data in HIC's at SPS?*, hep-ph/0001242.

[54] M. M. Aggarwal et al.: *Direct Photon Production in 158 AGeV ^{208}Pb+^{208}Pb Collisions*, nucl-ex/0006007.

[55] P. Braun-Munzinger et al.: *Chemical Equilibration in Pb+Pb Collisions at the SPS*, Phys. Lett. **B465** (1999) 15, nucl-th/9903010.

[56] P. Holl et al.: *Proposal: Study of Electron Pair and Photon Procution in Lead-Lead Collisions at the CERN SPS*, CERN/SPSLC 94-1.

[57] H. Appelshäuser: *Physics with the Upgraded CERES Detector*, Acta Physica Polonica **B**, Vol.29 (1998).

[58] E. Gatti, P. Rehak: *Semiconductor Drift Chamber - An Application of a Novel Charge Transport Scheme*, Nucl. Instr. and Meth. **A225** (1984) 608-614.

[59] O. Nix: *Einsatz und Lasertest von 4″ Siliziumdriftdetektoren*, Diploma Thesis, Universität Heidelberg, 1996.

[60] J. Séguinot and T. Ypsilantis: *Photo-Ionization and Cherenkov Ring Imaging*, Nucl. Instr. and Meth. **142** (1977) 377-391.

[61] G. Hering: *Dielectron Production in Heavy Ion Collisions at 158 GeV/c per Nucleon*, Dissertation, Technische Universität Darmstadt, 2001.

[62] K. Kleinknecht: *Detektoren für Teilchenstrahlung*, Teubner Studienbücher, Stuttgart, 1987.

[63] W. Schmitz: *Lambda-Produktion in Pb-Au-Kollisionen bei 40 AGeV*, Dissertation, Universität Heidelberg, 2001.

[64] G. Agakichiev et al.: *A New Robust Fitting Algorithm for Vertex Reconstruction in the CERES Experiment*, Nucl. Instr. and Meth. **A394** (1997) 225.

[65] F. Mosteller and W. Tukey: *Data Analysis and Regression: A Second Course in Statistic*, Addison - Wesley (1987).

[66] Particle Data Group, Review of Particle Physics, Phys. Lett. **B592** (2004) 1.

[67] S. Yurevich: *Low-mass e^+e^- pair production in Pb-Au collisions at 158 AGeV*, Dissertation, Universität Heidelberg, in preparation.

[68] CERN Geneva: *GEANT manual*, CERN Program Library Long Writeup W5013 (1993).

[69] H. Sako: private communication.

[70] W. Blum and L. Rolandi: *Particle Detection with Drift Chambers*, Springer-Verlag (1994).

[71] G. Agakichiev et al.: *The CERES/NA45 Radial Time Projection Chamber*, NIM in preparation.

[72] D. Miśkowiec: *Laser calibration system for the CERES Time Projection Chamber*, NIM in preparation.

[73] S. F. Biagi:*Monte Carlo simulation of electron drift and diffusion in counting gases under the influence of electric and magnetic fields*, Nucl. Instr. and Meth. **A421** (1999) 234-240.

[74] A. Marín: private communication.

[75] R. Renfordt et al., NA49 collaboration, IKF-58 Annual Report (1997) 4.

[76] K.-H. Rohe: *Elektronik für Physiker*, Teubner Studienbücher (1987).

[77] L. Dietrich: *Optimierung der Elektron-Pion-Separation in der CERES-TPC*, Diploma Thesis, Universität Heidelberg, 2001.

[78] J. Stachel: private communication about Thermal Model calculations.

[79] D. Antonczyk: Dissertation, Universität Heidelberg, in preparation.

[80] M. Sánchez García: *Momentum Reconstruction and Pion Production Analysis in the HADES Spectrometer at GSI*, Dissertation, Universidade de Santiago de Compostela, 2003.

[81] G. E. Brown et al.: *Pions from resonance decay in Brookhaven relativistic heavy-ion collisions*, Phys. Lett. **B253** (1991) 19-22.

[82] D. Röhrich: *Review of SPS experimental results on strangeness*, J. Phys. **G27** (2001) 355-366.

[83] C. Höhne: *Strangeness production in nuclear collisions - recent results from experiment NA49*, Nucl. Phys. **A661** (1999) 485c-488c.

[84] S. A. Bass et al.: *Microscopic Models for Ultrarelativistic Heavy Ion Collisions*, Prog. Part. Nucl. Phys **41** (1998) 225-370, nucl-th/9803035.

[85] M. Bleicher et al: *Relativistic Hadron-Hadron Collisions and the Ultra-Relativistic Quantum Molecular Dynamics Model (UrQMD)*, J. Phys. **G25** (1999), 1859-1896.

[86] S. Radomski: Dissertation, Technische Universität Darmstadt, in preparation.

[87] P. G. Jones et al.: *Hadron Yield and Hadron Spectra from the NA49 Experiment*, Nucl. Phys. **A610** (1996) 188c.

[88] F. Antinori et al.: *Study of the transverse mass spectra of the strange particles in Pb-Pb collisions at 158 A GeV/c*, J. Phys. **G**: Nucl. Phys. **30** (2004) 823-840, nucl-ex/0403016.

[89] F. Antinori et al.: *Rapidity distributions around mid-rapidity of strange particle in Pb-Pb collisions at 158 A GeV/c*, J. Phys. **G**: Nucl. Phys. **31** (2005) 1345-1357, nucl-ex/0509009.

[90] J. Podolanski and R. Armenteros: *Analysis of V-Events*, Phil. Mag. **45** (1954) 13-30.

[91] G. D. Lafferty and T. R. Wyatt: *Where to stick your data points: The treatment of measurements within wide bins*, Nucl. Instr. and Meth. **A355** (1995) 541-547.

[92] A. Białas et al.: *Multiplicity Distributions in Nucleus-Nucleus Collisions at High Energies*, Nucl. Phys. **B111** (1976) 461-476.

[93] H. Plothow-Besch, *PDFLIB: A library of all available parton density functions of the nucleon, the pion and the photon and the corresponding alpha-s calculations*, Computer Physics Commun **71** (1993) 396-416.

[94] Particles and Fields, Review of Particle Properties, Phys. Rev. **D50** (1994) 1275-1282.

[95] D. S. Sivia: *Data Analysis - A Bayesian Tutorial*, Oxoford Science Publications, 2005.

[96] M.Botje: *Open Charm Upper Limit from Bayes' Theorem*, NA49 collaboration, internal note (2005).

[97] M. van Leeuwen.: *Kaon and open charm production in central lead-lead collisions at the CERN SPS*, Dissertation, University Utrecht, 2003.

[98] C. Alt et al.: *Upper limit of D^0 production in Central Pb-Pb Collisions at 158 AGeV*, nucl-ex/0507031 (2005).

[99] J. Milošević: *Investigation of Azimuthal Asymmetries in Charged and Strange Particle Distributions from CERES*, Dissertation, Universität Heidelberg, in preparation.

The CERES Collaboration

P. Rehak
Brookhaven National Laboratory, Upton, USA

L. Musa, J. Schukraft
CERN, Geneva, Switzerland

A. Drees
Department for Physics and Astronomy, SUNY Stony Brook, USA

G. Agakichiev, D. Antonczyk, A. Andronic, P. Braun-Munzinger, O. Busch, C. Garabatos, G. Hering, J. Holeczek, M. Kalisky, A. Maas, A. Marín, D. Miśkowiec, S. Radomski, J. Rak, H. Sako, S. Sedykh, G. Tsiledakis
GSI, Darmstadt, Germany

H. Appelshäuser, M. Płoskoń, S. Kniege
IKF, Frankfurt, Germany

V. Belaga, K. Fomenko, Y. Panebrattsev, O. Petchenova, S. Shimansky, V. Yurevich
JINR, Dubna, Russia

J. P. Wurm
Max-Planck-Institut für Kernphysik, Heidelberg, Germany

D. Adamová, V. Kushpil, M. Šumbera
NPI/ASCR, Řež, Czech Republic

J. Bielčíková, R. Campagnolo, S. Damjanovic, T. Dietel, L. Dietrich, S. I. Esumi, K. Filimonov, P. Glässel, G. Krobath, W. Ludolphs, J. Milošević, R. Ortega, V. Petráček, W. Schmitz, W. Seipp, J. Stachel, H. Tilsner, T. Wienold, B. Windelband, S. Yurevich
Universität Heidelberg, Germany

J. P. Wessels
Universität Münster, Germany

A. Cherlin, Z. Fraenkel, I. Ravinovich, I. Tserruya
Weizmann Institute, Rehovot, Israel

Thank

Finally I finished reading and correcting all these pages and arrive to the nicest part.

Honestly, if this would have been a fantasy book instead of a thesis I would have chosen Ana as hero. I would even dare to say that these pages would not exist without her support. What a luck that I am sitting just right in the office next to hers, so that I can easily bother her with millions and millions of questions!

The next person on my list is Harry, my former office colleague and now professor in Frankfurt. He was an excellent supervisor during the time of the calibration of the TPC, and even agreed to continue the discussion after he had left to Frankfurt. That triggered a lot of progress in my analysis.

Not forgetting about Prof. Johanna Stachel, my boss. She gave me a lot of support and sent me around the world to attend many interesting conferences. I learned plenty of physics in these years of PhD!

From the CERES people of GSI I send special thank to Dariusz for all the wise e-mail advises. Also Gejdar Agakichiev and Christoph Blume contributed considerably to this work by providing me with helpful information about vertex fit algorithms or the calculation of upper limits.

I thank David, my present office colleague from ALICE, for diagnosing all computer entrapments, for suggesting every second day to go to the cinema, and for just being there. Not forgetting about Tarik, also from ALICE. Since he left, my rate of going to the pub decreased dramatically! I thank Rainer Schicker and Kurt Traxel for passing from time to time my office and remembering me how nice it is to talk about everything and nothing at the same time.

A huge thank goes to Rolf for listening to my physics problems, often till midnight, while drinking glass after glass of wine together. Amazingly, this resulted every single time in a solution!

I thank my sister Turid and my parents for believing so strongly in me. My best friend Nicole deserves a thank for just being my best friend, traveling around together and planing nonsense for the future. A lot of thank goes to my music band, the best vocalist Jens, the best guitarist Ross, and the best drummer Belle, for just preventing me from time to time to concentrate on physics.

And a thank to www.leo.org for providing me with such marvelous translations from German to English language. Unfortunately, non of these expressions did survive my correctors.